INVESTIGATIONS OF THE REDOX CHEMISTRY OF COLLOIDAL SEMICONDUCTOR QUANTUM DOTS

Carolyn L. Hartley

A dissertation submitted to the faculty at the University of North Carolina at Chapel Hill in partial fulfillment of the requirements for the degree of Doctor of Philosophy in the Department of Chemistry.

Chapel Hill
2021

Approved by:

Jillian L. Dempsey

Michel R. Gagné

Gerald J. Meyer

Joanna M. Atkin

James F. Cahoon

ABSTRACT

Carolyn L. Hartley: Investigations of the Redox Chemistry of Colloidal Semiconductor Quantum Dots
(Under the direction of Jillian L. Dempsey)

Quantum dots (QDs) are quantum-confined, nanometer-size semiconductor crystals that have gained popularity for their optical and charge transfer properties that make them strong candidates in many technologies. Though promising, QD-based device performance typically lags behind their expected potential. Much of this discrepancy is attributed to defects that arise at the QD surface; because of their small size and large surface area to volume ratio, it is established the presence of defects such as undercoordinated surface ions can markedly impact QD properties. Approaches to passivating such defects have been presented such as adding excess ligand or using a core/shell material. However, these efforts are inherently limited by a lack of molecular-level understanding of the QD surface.

To address these discrepancies, this dissertation presents studies of QD surface chemistry using a relatively new experimental tool: redox-active chemical probes. Chemical probes are attractive for studying QDs because they can be added stoichiometrically and provide insight into both the structure and reactivity of specific surface sites. Several projects utilizing redox-active probes are presented. First, the reactivity of oleate-capped CdSe QDs with added charge from a radical anion reductant is explored. We present the phenomenon of electron-promoted X-type ligand displacement, an important concept for understanding charge balance at QD surfaces. This concept was then expanded to another QD material: PbS. The influence of parameters including QD size, strength of reductant, and capping ligands are explored in order to gain substantial insight into the factors influencing QD surface defect reactivity. This work moves the field towards new insight into QD surface defects, which will ultimately enable researchers to design rational surface passivation strategies.

Finally, a secondary area of research that is critical to advancing QD-based optoelectronic devices is a firmer understanding of the dynamics of interfacial charge transfer from photoexcited QDs. Efforts to develop a system for testing the validity of semiclassical Marcus Theory in interfacial electron transfer between QDs and a molecular acceptor are presented. Realization of this work will help to shape understanding of photoinduced charge transfer in QD-based systems, ultimately helping QD-based devices to reach their full potential.

To my parents, who have been a constant source of love and support in my life.

ACKNOWLEDGEMENTS

I have many people and organizations to thank for helping me to succeed at UNC. Even though at times a PhD can be a very lonely endeavor, it truly takes a village.

First, to my advisor Jillian: I made the decision to come to UNC for graduate school while on my visitation weekend at Northwestern University. While the visit there was awesome, what stood out to me the most was that my host graduate student (the infamous Dr. Kedy Edme) who, after I mentioned I was also considering UNC's Chemistry program, couldn't stop talking about this amazing professor that I just had to meet named Jillian Dempsey. Kedy literally could not say enough about how you were not only an awesome scientist but also an incredibly compassionate person. Though he was supposed to be trying to sell me on Northwestern, Kedy's enthusiasm about your mentorship was off the charts. I was already leaning towards UNC, but that sealed the deal for me. Thankfully, my gut feeling and Kedy's recommendations stood to be true. Thank you for being the exact advisor that I needed in graduate school—for being incredibly supportive, for giving me every opportunity to go to conferences and never showing anything other than confidence in my abilities. It meant a great deal that even when I felt down and didn't believe in myself, you seemed to have total faith in me. Thank you also to my committee and to all of the inorganic faculty at UNC who are so incredibly supportive of graduate students.

I have been lucky to meet some of the best people on the 4th floor of Kenan. I've never felt anything other than welcome in the Dempsey lab, with older students always happy to chat about my research, answer my questions no matter how silly, and invite me to social events. I always remember how welcome I felt and have tried to pass that down to every new student who joins the group. Between the countless rounds of cornhole at He's Not, cookouts, and friendly Miller-Dempsey lab competitions, I couldn't imagine a better community for my graduate school time. To Hannah Starr, my flu shot buddy, co-Janus super user, safety pal and the first person to introduce me to quantum dots, thank you for your overflowing positivity

and generosity with baked goods. You have made my time at UNC a great one and I will probably have to return next year just so we can get flu shots together. To Melody: I think you take the cake for the person I've zoomed most with over the course of the pandemic! Starting up in the lab on the QD projects together was so fortunate, and I have deeply valued being able to bounce ideas and experimental plans off of each other, attend conferences together, start QD club to talk about QD papers when no one else wanted to, and push each other to be better writers in our joint publications.

To Dan: Thank you for being such a huge support and one of my best friends inside and outside of the lab. Thanks for being an outstanding first deputy safety officer with me, for always letting me run things by you when feeling uncertain, encouraging me to be more confident in myself and in the cool-ness of my data, sending me hilarious memes and being a great listener.

To the A-tower crew over the years, especially Dan, Debanjan, Tayliz, Brittany, Aldo and Ann Marie—thanks for keeping the lab fun and giving me a reliable dose of sass every time I ventured over to that part of the lab. Ann Marie, I have total faith that you will lead the lab and UNC Chemistry department towards an ever-improving safety culture. To the most recent Dempsey lab first years I overlapped with—Christian, Jennica, Gabi and Charlotte—I'm really excited about all the enthusiasm and new expertise you bring to the lab. I look forward to seeing what you all accomplish during your PhDs! Christian specifically, mentoring you during your REU in 2019 helped me to learn a lot about myself and pushed me to dig even more deeply into my research with your excellent questions and ideas.

To my communities outside of the chemistry department, thank you to all of my family and friends for the love and support and calls and spontaneous visits to Chapel Hill over the last five years. They have truly made all the difference for me. Thank you to my friend groups in Chapel Hill, especially who have helped me to grow so much as a person. To the UUMC Life group, our weekly bible study has been an amazing source of comfort and fruitful discussions. You all have helped me to grow in my faith so much over the last five years. To my Monday night group, my time with you all has been a significant source of support in my life. I will really miss the richness of conversations and perspectives on life you have shared with me.

To Javier: thank you for always making me feel loved, for running with me, for making me laugh and realize there's much more to life than studying. Although the long distance hasn't been easy, we've had so many fun adventures between Chapel Hill, the Tri-Cities area, Northern Virginia, Barcelona, and Juarez, and I can't wait for the many more adventures to come. You and Nugget are my guys—always able to make me smile with your ridiculousness (that you insist definitely isn't ridiculous). I love you.

Finally, to the people who have always had my back: my mom and dad. I could not have asked for better, more supportive, more selfless or more generous parents. Through your examples I learned from an early age to value hard work, faith, rational thinking, kindness, humility, and a killer sense of humor. I have no doubt that I inherited all of my positive qualities from you both, and I could not be where I am today without your endless support. I love you both more than I can express.

TABLE OF CONTENTS

LIST OF FIGURES

LIST OF TABLES

LIST OF SCHEMES

LIST OF ABBREVIATIONS AND SYMBOLS

ATR	Attenuated total reflection
CB	Conduction band
CdS	Cadmium sulfide
CdSe	Cadmium selenide
°C	Degrees Celsius
cm	Centimeter
$CoCp_2$	Cobaltocene
$CoCp^*_2$	Decamethylcobaltocene
CV	Cyclic voltammogram
2D	Two-dimensional
D	Diffusion coefficient
DFT	Density Functional Theory
DOSY	Diffusion ordered NMR spectroscopy
Δ	Change or difference
ε	Molar extinction coefficient
$E^{0\prime}$	Reduction Potential
equiv.	Equivalent
k_{ET}	Electron transfer rate constant
eV	Electron volts
Fc	Ferrocene
FT	Fourier transform
ΔG	Gibbs free energy
mg	Milligrams
Hz	Hertz
IR	Infrared

µL	Microliter
mL	Milliliter
M	Molar
mM	Millimolar
mol	Mole
mV	Millivolt
NC	Nanocrystal
nm	Nanometer
NMR	Nuclear magnetic resonance
NOESY	Nuclear Overhauser effect spectroscopy
ns	Nanosecond
OA	Oleic acid
ODE	Octadecene
PbS	Lead sulfide
pK_a	Logarithm of the acid dissociation constant
PL	Photoluminescence
ppm	Parts per million
ms	Millisecond
µ	Microsecond
QD	Quantum dot
TEM	Transmission electron microscopy
T1	Longitudinal relaxation time
T2	Spin-spin relaxation time
UDA	Undec-10-enoic acid
UDT	Undec-10-ene-1-thiol
UV-vis	Ultraviolet-visible

V	Volt
VB	Valence band
λ	Wavelength
XPS	X-ray photoelectron spectroscopy
ZnO	Zinc oxide

CHAPTER 1 : MOLECULAR-LEVEL INSIGHT INTO SEMICONDUCTOR NANOCRYSTAL SURFACES AND THEIR REDOX CHEMISTRY

This chapter was adapted with permission from *Hartley, C.L.; *Kessler, M.L.; Dempsey, J.L. Molecular-Level Insight into Semiconductor Nanocrystal Surfaces. *J. Am. Chem. Soc.* **2021**, *143*(3), 1251 – 1266.

1.1 Introduction

Semiconductor Nanocrystals: An Important Class of Materials Undergoing Continual Improvement. Semiconductor nanocrystals (NCs) are hybrid materials composed of a semiconductor lattice core terminated by exposed ions, many of which are passivated with molecular capping ligands. This hybrid structure imparts stability in colloidal solutions and enables processability. Broadly, NCs span multiple shapes and sizes. Of particular interest for applications, semiconductor NCs can exhibit a quantum confinement effect if one dimension is smaller than its exciton Bohr radius (e.g., two-dimensional quantum wells, one-dimensional nanowires, and zero-dimensional quantum dots). Selection of semiconductor material, size, capping ligand, and dimension therefore affords a high degree of tunability to the optical and electronic properties of the NC. These characteristics have made NCs promising candidates for implementation in technologies ranging from optoelectronic devices to biodiagnostics, and for photocatalysis.[1,2]

The last few decades have witnessed sweeping advancements in synthetic methods for accessing II–VI, IV–VI, and III–V semiconductor NCs, and an array of perovskite NCs due to their promise as next generation materials. Synthetic preparations have realized homogeneous NC morphologies including tetrapodal,[3] quasi-spherical,[4–7] platelet,[8,9] hexahedral,[10] and cuboidal structures,[11] among others.[12–15] Reproducible procedures yielding monodisperse NCs have afforded new opportunities to study material properties and reactivities, and to explore implementation in a variety of device architectures. However, unlike the exquisite level of control over shape and size dispersity achieved in NC syntheses, the field's

understanding of another key aspect of NCs, the surface structure (both physical and electronic), has been limited to vague descriptors until very recently.

Nanocrystal Surfaces and the Quest to Understand Them. In considering the properties and reactivities of semiconductor NCs, one of the most defining features is the surface. Compared to bulk semiconductors, NCs have much larger surface area-to-volume ratios. This results in a class of materials with properties that are heavily influenced by the structural and electronic character of the surface. The structural properties are dictated by the surface atoms which form the ligand–lattice interface and interact with solvent[16] or molecular reagents.[17] The strained surface of NCs is often a source of structural defects such as undercoordinated sites, missing atoms, and dimerized species (Figure 1.1). Additionally, the surface is well known to be a source of mid-band gap electronic "trap states" and to be intimately linked with the overall NC electronic structure.[18] Though commonly associated with undesirable properties such as low photoluminescence quantum yields (PLQY), structural defects and trap states have also been invoked as promoting desirable or controllable reactivity at the surface.[19] In sum, the role of the surface cannot be overstated, and in large part motivates the use of NCs in systems seeking to study interfacial reactivity.

Despite their importance in dictating NC reactivity and properties, NC surfaces are poorly understood due to a lack of molecular-level information. Analytical tools—especially tools that have traditionally been used by molecular chemists (e.g., nuclear magnetic resonance (NMR) and infrared (IR) spectroscopies, and inductively coupled plasma mass spectrometry/optical emission spectroscopy (ICP-MS/OES), etc.)—have been increasingly utilized in recent years to better characterize semiconductor stoichiometry and surface ligands. As a result, it is now routine to describe the NC surface by reporting the ligand packing density and coordination modes, in complement with the NC diameter obtained through optical spectroscopy and transmission electron microscopy (TEM) imaging. However, simply identifying the composition of ligands bound to the surface or estimating the general shape and size of the NC is not sufficient to fully account for experimental observations or thoughtfully engineer surfaces.

Instead, we argue that multiple techniques must be used in concert to analyze the molecular identities and reactivity of surface moieties and link these to the electronic properties of the material.

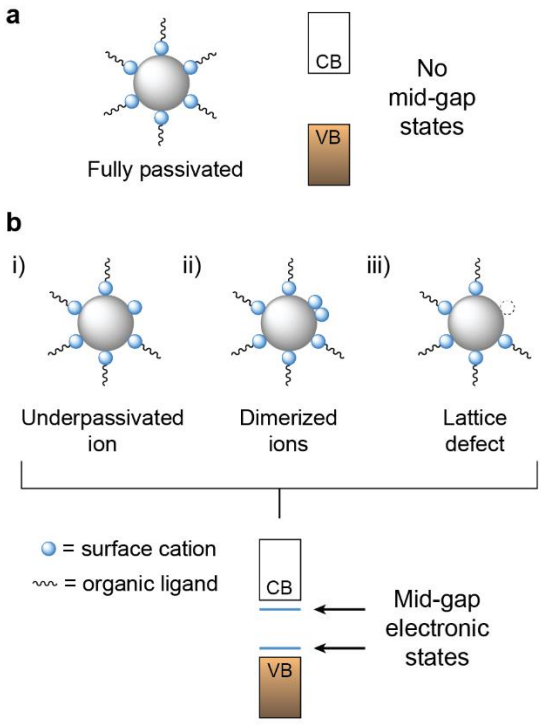

Figure 1.1 (a) Nanocrystals discussed herein are hybrid materials with an inorganic semiconductor lattice and molecular capping ligands. When a NC surface is fully passivated with ligands, the electronic structure is free of mid-gap states. (b) In the case of defects at the NC surface such as (i) underpassivated surface ions, (ii) surface ion dimerization, or (iii) stripped or missing surface atoms, electronic states may arise within the band gap. While these are common cases, we note that the defects depicted here are not an exhaustive list. The state below the conduction band (CB) corresponding to an electron trap is drawn for a cationic defect; analogously, the state above the valence band (VB) corresponding to a hole trap is drawn for an anionic defect.

Our Take. In this chapter, I outline what it means to take a molecular-level approach to probing semiconductor NC surfaces. Herein, we define 'molecular-level insight' into NC surfaces as an advance that provides clarity into the detailed physical or electronic structure (e.g., oxidation state, coordination number, or binding mode) of the capping ligands, the nanocrystalline lattice ions, or a combination of both constituents. Following the discussion of taking a molecular-level approach, we detail the growing toolbox of analytical techniques suited to this goal. We then highlight recent literature examples which

serve as case studies that have provided unprecedented insight into surface structure and reactivity by employing creative combinations of the analytical tools discussed. Finally, we provide an outlook on the state of the field and identify opportunities to expand molecular-level understanding in order to push the boundaries of current NC technologies.

1.2 Studying NC Surfaces with a Molecular-Level Approach

1.2.1 Defining the Nanocrystal Surface

To gain molecular-level understanding of (and ultimately control over) the NC surface, the structure and reactivity must be determined for each of the two inextricable components of a NC: the inorganic crystal lattice and the ligand shell. Several fundamental properties underpin the structure and reactivity of the inorganic lattice: the material crystal structure, the exposed facets, and the NC shape (morphology) (Figure 1.2a). These properties result from energy minimization of the surface during NC synthesis.[1] Synthetic conditions directly influence the crystal structure of the semiconductor material through coordination of the inorganic surface ions by molecular surfactants. For example, it has been shown that while carboxylates promote the formation of zinc blende CdSe NCs, the use of phosphonate ligands during synthesis instead induces the formation of the material in the wurtzite crystal structure due to a difference in preferred surface ion–ligand coordination.[20] Also resulting from surface energy minimization during NC growth, the exposed planar facets which comprise NC surfaces are directly linked to the underlying crystal structure. Different surface facets vary in their atomic arrangement, stoichiometry, and coordination environment. For example, in PbS NCs, the {111} facets that dominate in small NCs tend to be Pb-rich, whereas the {100} facets exposed in larger NC sizes are stoichiometric in Pb and S.[21,22] Finally, tuning the synthetic conditions can produce NCs of various morphologies, each of which display a unique distribution of exposed facets. For instance, quasi-spherical CdSe NCs are known to possess {100} and {111} facets, whereas the surface of CdSe nanoplatelets is dominated by {100} facets.[23] Together, the material crystal structure, exposed crystalline facets, and NC morphology are crucial properties to characterize, assess, and potentially exploit to probe the molecular-level coordination environment of the surface.

The inorganic ions arranged on NC facets constitute only one half of the NC surface; the ligand shell comprises the second, but equally important, half. In determining the structure and reactivity of the NC surface, ligand-based properties such as charge and binding motif are important to define and consider. Characterization of ligand binding is often interpreted within the framework of Green's covalent bond classification, which assigns ligands as L-, X-, or Z-type binding motifs.[24,25] L-type ligands are Lewis bases, contributing two electrons to the inorganic ion through a dative bond; X-type ligands are one-electron donors which bind covalently with inorganic ions; and Z-type (equivalently MX_n, M = metal) ligands act as Lewis acidic two-electron acceptors (Figure 1.2b). Additionally, neutral ion-paired X-type binding motifs have been reported for II–VI quantum belts,[26,27] perovskites,[28] and metal oxide NCs,[29] and can be exchanged for other neutral ligands.[27] Neutral ligands such as L-type amines or Z-type metal carboxylates are commonplace in colloidal NCs and serve a key role in both stabilizing NCs in laboratory solvents and passivating inorganic surface ions.[1] X-type ligands are anionic—in nonstoichiometric NCs that have metal-rich surfaces, X-type ligands serve to compensate the excess cationic charge, thereby providing net neutrality to the NCs and enabling dispersion in nonpolar solvents. In addition to classifying ligands in these categories, electronic passivation at the NC surface cannot be fully described without consideration of the binding geometry of the ligand anchoring group (Figure 1.2b). For instance, multidentate carboxylate ligands may bind through monodentate, chelating bidentate, or bridging bidentate coordination modes, providing an array of coordination numbers to the surface metal cations. Finally, site-specific ligand binding energies also contribute to the molecular-level depiction of the surface (Figure 1.2b).

Though researchers continue to describe colloidal semiconductor NCs as hybrid structures composed of an inorganic lattice and a coating of surfactants, it is increasingly apparent that such a distinction between the lattice and its ligands is an oversimplification.[18] While X- and L-type ligands are distinct from the inorganic semiconductor lattice, Z-type ligands bridge the ligand–lattice interface. They may either be considered as an MX_n unit (Z-type ligand), or viewed as a metal ion (M^{n+}) that terminates the semiconductor lattice and coordinates *n*X-type ligands. Both cases are indistinguishable from the

perspective of the NC-bound state, yet Z-type and X-type ligands display different reactivity towards various molecular reagents. Experimental evidence and computational treatment to distinguish between X-type ligands which are displaced as constituents of an MX_n moiety or through 1:1 X-type exchange are lacking. Recognizing that the information gained from ligand-based reactions does not necessarily yield insight into the coordination environments of species in their native, bound state is important. Since passivation of the NC surface as a function of the charge and coordination number of surface species is currently poorly understood, it is crucial to continue to interrogate the precise nature through which X- and Z-type ligand binding occurs in order to predict the chemical reactivity of the surface.

The lattice and ligand constituents of a NC's chemical composition does not fully describe the molecular-level structure or properties at the ligand–lattice interface. Importantly, chemical properties related to the surface inorganic ions such as coordination number, oxidation state,[30,31] or defects contribute to the molecular-level depiction of the surface (Figure 1.2c). Defects including metal dimers,[32] chalcogen dimers,[30] and undercoordinated ions can be intrinsic to the NC material or induced post-synthetically and should be considered during investigations of NC surfaces. Furthermore, defining NC surfaces with molecular-level precision must be contextualized with at least two factors: dynamic equilibria between the NC surface and its surrounding media, and heterogeneity across the surface of an individual NC as well as within the colloidal ensemble. As the presence of these factors is unavoidable to a certain extent, research questions should directly acknowledge and address equilibria and heterogeneity by exploiting new methods of obtaining, interpreting, and applying molecular-level insight. In light of these considerations, we discuss recent advances that elucidate the complex and dynamic nature of the NC surface within the broader context of single particle and ensemble heterogeneity to determine the structural origins of mid-gap charge carrier trap states. First, we highlight and briefly discuss the myriad of techniques currently available to answer these questions.

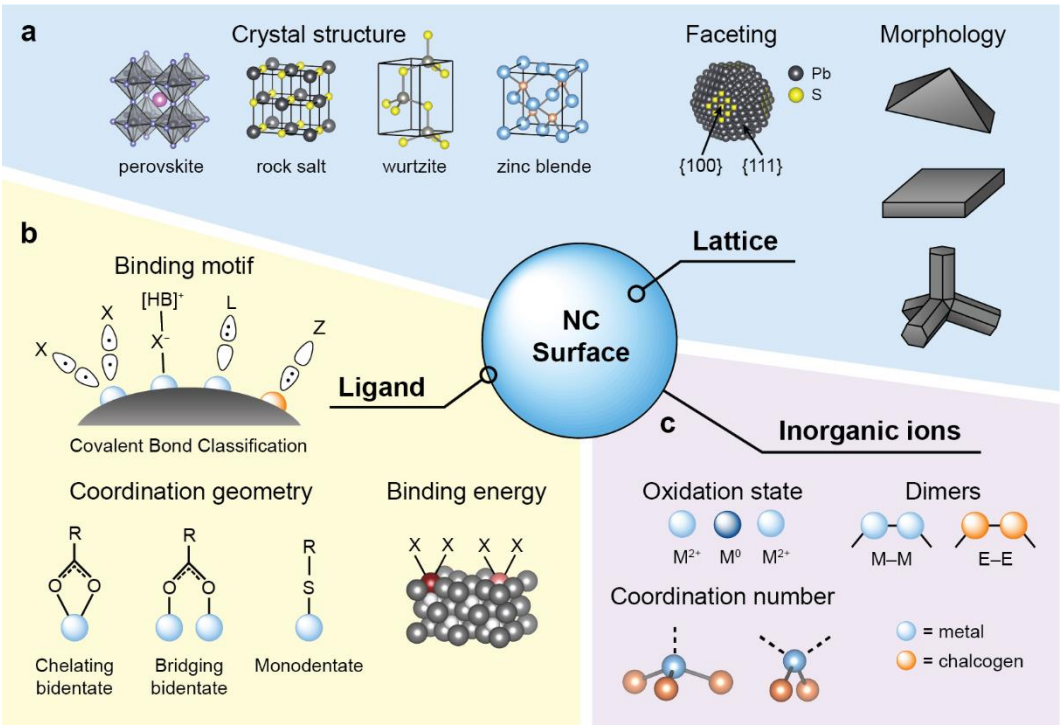

Figure 1.2 A molecular-level understanding of NC surfaces requires detailed knowledge of (a) lattice-based properties, (b) ligand-based properties, and (c) properties related to the surface inorganic ions (shown here for a II–VI NC; additional oxidation states and coordination numbers are possible for different systems, e.g., perovskites and III–V semiconductors).

1.2.2 How We Advance Understanding: A Growing Toolbox of Methods for Studying NC Surfaces

Over the last several decades, research has emphasized improved characterization of nanomaterials and their surfaces. In turn, a large number of tools used in the traditionally molecular research realm have been translated for the study of NCs. These tools can be grouped based on the surface component that they interrogate: the capping ligands, the ligand–lattice interface, or the electronic structure of the surface (Figure 1.3). Here we provide a general overview of the emerging toolbox for gaining molecular-level understanding of NC surfaces.

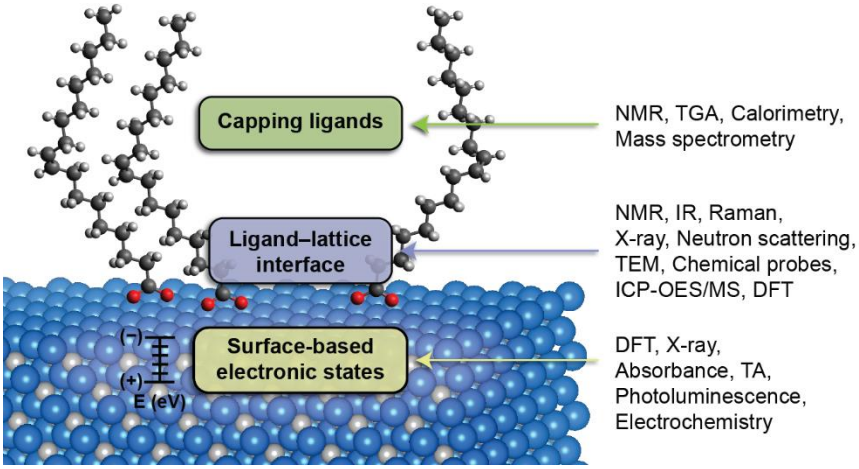

Figure 1.3 Current state-of-the-art analytical and computational techniques that yield molecular-level insight into NC surfaces.

Capping Ligands. The most common tool used to study the capping ligands at NC surfaces is solution-phase nuclear magnetic resonance (NMR) spectroscopy. NMR spectroscopy is a convenient, non-destructive tool for assessing ligand coverage and distinguishing between surface-bound and freely diffusing molecular species.[33,34] Furthermore, common NMR probes can detect a range of nuclei including ^{1}H, ^{13}C, ^{31}P, and ^{19}F, enabling detection of a wide variety of heteroatoms in the ligands bound to the surface. Beyond ligand characterization, 1D solution-phase NMR techniques can inform on the relative binding strengths of different ligand populations,[21,35,36] dynamic ligand exchange equilibria,[37–40] and the extent of solvent-ligand interactions.[16] 2D NMR techniques such as nuclear Overhauser effect spectroscopy (NOESY) and diffusion-ordered spectroscopy (DOSY) can interrogate ligand-ligand interactions and deconvolute overlapping ligand resonances, respectively.[41,42]

Additionally, thermal techniques such as thermogravimetric analysis (TGA)[43,44] and calorimetry[43,45] have been shown to provide valuable information on the identity and binding strength of the surface capping ligands. Mass spectrometry methods (e.g., electrospray ionization,[44] and simultaneous thermal analysis[46]) may also be used to confirm ligand identity. While useful, a downside of these techniques compared with NMR spectroscopy is the required decomposition of samples for the measurements.

Ligand–Lattice Interface. Most tools comprising the surface characterization toolbox reveal the structure and bonding configurations of lattice atoms with capping ligands at the interface. These tools can be broadly grouped into: (i) methods that reveal the as-synthesized NC surface structure (e.g., NMR and vibrational spectroscopies, X-ray techniques, small-angle neutron scattering (SANS), and TEM); (ii) tools that explore surface structure by assessing reactivity with added chemical reagents (e.g., chemical probes and ICP-MS/OES); and (iii) computational methods.

In addition to probing the capping ligands, NMR spectroscopy can also be used to study the ligand–lattice interface. This may be achieved by using probes corresponding to the nuclei that compose the material of interest (e.g., ^{207}Pb, ^{113}Cd, ^{133}Cs, $^{79/81}$Br, or ^{77}Se).[23,47–53] By directly studying the nuclei of lattice atoms, it is possible to learn about their local environment. For example, metal halide perovskites can be explored by halide NMR, or by nuclear quadrupole resonance (NQR) if composed of halides with large quadrupole moments (e.g., ^{127}I).[50] While these less traditional nuclei have been successfully probed by NMR spectroscopy, the sensitivity is often quite low.[23,50,51] Solid-state samples may produce better signal-to-noise ratios in some cases.[23,51] In further attempts to improve NMR feature resolution, several literature reports in recent years have used dynamic nuclear polarization (DNP)- and cross-polarization magic-angle spinning (CPMAS)-enhanced NMR to probe nanomaterials.[54,55] These NMR enhancement methods have resulted in spectra with exquisite resolution, enabling differentiation between core and surface atoms. Solid-state NMR experiments involving dipolar dephasing have further provided spatial resolution of $CsPbBr_3$ perovskite NC surfaces, yielding a comprehensive picture of lattice termination and ligand binding.[52] The use of NMR spectroscopy to study the ligand–lattice interface is therefore a promising avenue for gaining very specific structural insight, with the caveat that many of the more exotic methods noted here beyond 1D ^{1}H NMR are not widely available to most researchers.

Vibrational spectroscopy tools including infrared (IR) and Raman spectroscopies are effective for studying surface atom coordination environments and ligand binding modes. IR spectroscopy can be used to assess purity, confirm bound ligand identity,[27,35] gauge binding modes of multidentate ligands such as carboxylates,[23,47,56] and even characterize semiconductor surface atom bonding by monitoring heavy atom

vibrational signatures at low wavenumbers.[57] As a complementary method, Raman spectroscopy can probe features of interest related to lattice atom and ligand bonding. For example, Buhro and coworkers applied Raman spectroscopy in a recent study on CdSe quantum belts to differentiate between binding of protonated L-type thiol ligands vs. X-type thiolates by monitoring the S–H stretch at 2578 cm^{-1}.[58] Other works have used Raman signatures to characterize surface oxide defects[59,60] or detect the presence of oxidized chalcogenides.[61] Beyond probing static coordination environments at the surface, several research groups have turned to time-resolved infrared and Raman spectroscopies to better understand the dynamic nature of ligand coordination, especially in relation to the core exciton.[62,63] Benefits of both IR and Raman are their ease of use and relatively inexpensive instrumentation compared with NMR, though these spectroscopies are most helpful when used in complement with another technique to gain a comprehensive picture of the surface, as highlighted below (Section 1.2.3).

X-ray techniques provide insights into the structure at the ligand–lattice interface; one can learn about the lattice crystal structure using powder X-ray diffraction (PXRD), the coordination and local environment of surface atoms using X-ray absorption fine structure (XAFS), or the interparticle distance and size distribution of the particles with small-angle X-ray scattering (SAXS). Notably, SAXS provides indirect insight into the local environments at NC surfaces. The applications of these tools to study NCs have recently been reviewed in detail.[64–68] The insight provided by X-ray techniques—into both the underlying inorganic crystal structure and the local environments of surface atoms—is critical to developing a molecular-level understanding of NC surface structure.[69,70] While PXRD is typically available on university campuses, methods such as XAFS often require collaborations at specialized research institutes that have the necessary instrumentation and access to a synchrotron source, making them less commonly used despite their potential for high-value insight. In comparison to PXRD, XAFS, and SAXS, small-angle neutron scattering (SANS) has been less frequently utilized for probing the surface structure of NCs; however, SANS has the capability to analyze the inorganic lattice, surface capping ligands, and surrounding solvent simultaneously.[64,71–73] While incredibly useful for studying NC

surface chemistry with atomic-level detail and high spatial resolution, limited access to neutron scattering diffractometers has likely impeded the incorporation of SANS as a widespread technique.[71]

Characterization of NC surfaces through microscopy-based imaging techniques has also received attention in recent years. In particular, the resolution of transmission electron microscopy (TEM), traditionally used for gauging particle shape and size dispersity, has advanced such that the images collected can be used to improve understanding of surface atom bonding. An example by Alivisatos and coworkers illustrates the insight gained from powerful high-resolution TEM imaging.[74] High-resolution images elucidated the atomic attachment between fused wurtzite CdSe nanocrystal lattices, showing structural defects upon NC–NC dimer formation.[74] As resolution in TEM imaging and post-imaging processing continue to improve, we anticipate that TEM will be more commonly used for studying NC surface structure and bonding.

Beyond measurements on the native surface structure collected with the techniques described above, insights can be gained by inducing chemical changes at the NC surface. The use of chemical probes is an emerging tool for studying NC surfaces, wherein researchers add molecular reagents that react with predictable surface moieties to samples of NCs. Importantly, chemical probes must be coupled with another technique to monitor changes in either the NC, chemical reagent, or products formed to draw conclusions about surface chemistry. Because the use of chemical probes can be quantitative when done with precision, a remarkably detailed picture of the surface structure can emerge, as highlighted in Section 1.2.3. Two broad categories of chemical probes have emerged in the literature: redox-active probes and ligand-based probes. Redox-active probes report on surface species by reacting with surface sites via a reduction or oxidation reaction. The chemical products formed upon reaction with the probe can then serve as an indirect reporter on sterically accessible surface sites. In contrast to redox-active probes, ligand-based probes typically utilize a ligand displacement method (e.g., L-type-promoted Z-type displacement—see Section 1.2.3) to systematically and selectively remove bound ligands. The resulting byproducts of the reaction can be detected in solution and used to deduce a picture of the native surface species. The use of chemical probes has been reported across CdSe,[30,35,75] InP,[76,77] and PbS[21]

nanomaterials, providing key experimental understanding of bonding environments and reactivity at the surface.

Similarly, it is possible to learn about the NC surface by disrupting the native surface chemistry and then probing the resulting chemical species and NC composition by inductively coupled plasma (ICP)-based methods such as ICP-optical emission spectroscopy (ICP-OES) or ICP-mass spectrometry (ICP-MS). ICP-based tools are highly quantitative techniques for determining the stoichiometry of the inorganic lattice of NC materials (rather than the capping ligands). While these techniques are typically employed to reveal the core stoichiometry, the use of ICP-based techniques to quantify the reaction products of chemical probes or dopants can inform on the native surface structure and its reactivity. For example, both ICP-OES and ICP-MS can distinguish between cationic dopants incorporated at the surface or within the core lattice.[78,79] Additionally, the stoichiometry of surface moieties (e.g., Z-type ligands) liberated by ligand-based probes can be assessed by measuring the metal ion concentration using ICP-based techniques in tandem with ^{1}H NMR spectroscopy to quantify the organic constituents.[21] Because the detection limits for certain elements can be orders of magnitude higher when using ICP-OES than for ICP-MS, selection of the proper detection and sample digestion methods for each element is crucial to obtain trustworthy, highly quantitative data.[78]

Finally, the computational tool density functional theory (DFT) is an important and increasingly common approach to studying the physical structure of the NC surface on a molecular level. For example, studies rationalizing the presence of hydroxide ligands on PbS NCs,[80] preferred ligand packing arrangements,[81] differences in binding strengths of Z-type ligands on specific NC surface facets and sites, [36,82] and dimerization of surface atoms as a source of electronic traps[32,83] have provided immense structural insights. These computational works have in turn inspired new experiments and rationalized confounding experimental results, thus proving an indispensable tool for advancing the understanding of NC surfaces.

Surface-Based Electronic States. Both computational and experimental methods may be used to investigate the electronic structure at the surface with the goal of correlating mid-gap electronic states

with specific structural moieties. DFT is not only useful for predicting surface structure but can also correlate the expected physical structure with electronic states and surface reactivity.[84–86] The modeled electronic structure of the surface depends on the ligand coverage and surface charging, and has played a crucial role in understanding the precise nature of surface bonding and passivation strategies across different materials.[32,85] Unlike experimental tools, DFT may predict the formation of electronic states based on surface chemistry without convolution from the external environment (solvent) or possible impurities. To that end, application of computational methods to better understand links between the surface and electronic structure of less well-studied NC materials and morphologies (e.g., quantum dots vs. nanorods vs. nanoplatelets) will be critical. However, it is important that computational proposals be closely tied to experimental observations to ensure the validity of theoretical findings.

X-ray methods are also powerful tools to experimentally probe electronic states in materials. These include X-ray photoelectron spectroscopy (XPS), X-ray emission spectroscopy (XES), and X-ray absorption near edge structure (XANES), each of which can provide highly sensitive measurements of the oxidation state of surface atoms. By informing on the oxidation state of surface atoms (e.g., the presence of Pb^0 sites on perovskite NCs),[87] the correlation between reduced or oxidized surface atoms and the formation of mid-gap electronic states can be elucidated.[88] However, these spectroscopic tools are limited in that the penetration depth of the applied X-rays is often greater than the diameter of most NCs. As such, while surface atoms are indeed probed by these methods, they cannot be selectively monitored without significant spectral contribution from core atoms. The discrepancy between X-ray penetration depth and NC size therefore limits the possible information gained about sub-populations of surface defects. A related technique, ultraviolet photoelectron spectroscopy (UPS), can inform on the energetics of mid-gap and band-edge states, where changes in surface chemistry (e.g., ligand dipole moment) have been shown to influence the absolute energies.[89,90] The application of these tools to study NCs is an emerging area of research, and future work in this field may reveal the full power and limitations of these tools. For a thorough description of each method and the differences between them, I again direct readers to several helpful resources.[67,91,92]

UV-Vis-NIR absorbance spectroscopy is a commonly employed method to study NCs and may be used to gauge the impact of the surface electronic structure on the core exciton, though it does not provide the same explicit molecular-level detail as other techniques. Absorbance spectroscopy is frequently used to characterize NCs after ligand exchange procedures,[39,93–95] upon surface charging,[75,96,97] upon surface oxidation,[98] and after the addition of chemical probes.[21,35,99] The technique offers a non-destructive measurement that monitors blue- or red-shifts of the excitonic feature, gains or losses in absorbance, or appearances of new features resulting from reactivity with added chemical reagents. Many of these spectral changes arise from changes to the surface dipole, leading to an apparent change in semiconductor band gap without varying NC size.[1] The widespread use of absorbance spectroscopy, along with its sensitivity to changes in surface chemistry, highlights its value as a complementary method to more insightful techniques. As a stand-alone method, however, it does not offer molecular-level information on the surface, trap states, or ligands.

Unlike steady-state absorbance methods, time-resolved absorption spectroscopy coupled to pulsed laser photo-triggering methods (transient absorption, TA) can provide insight into the presence and types of surface trap states. Specifically, after NC excitation with a laser pulse, charge carrier dynamics can be analyzed by monitoring (i) the recovery of the electronic ground state, or (ii) the decay of excited state absorption features in the mid-IR. By monitoring the carrier dynamics over time as conduction band electrons and valence band holes recombine or localize in defect states, insight into the presence of mid-gap states can be gleaned. Importantly, studies performed on ultrafast timescales (femtosecond to picosecond) are often needed to resolve carrier trapping and interfacial charge transfer processes. In the case of a NC with no defects or mid-gap trap states, the ground state bleach recovery can be fit with a single exponential function. However, when mid-gap states are present (i.e. multiple recombination centers) within either a single NC or across an ensemble of particles, the recovery is described by a multiexponential function. By deconvoluting the multiexponential expression, the data can reveal details of ensemble-averaged recombination pathways. Additionally, the usefulness of TA spectroscopy for assessing the types of traps (i.e. electron vs. hole traps) varies by material. For example, TA spectroscopy

of CdSe NCs is well established to be more sensitive to the conduction band electron dynamics than to valence band hole movement due to the lower degeneracy of the conduction band states.[100,101] Conversely, TA spectroscopy of NC materials that have similar conduction band and valence band degeneracies results in spectra with approximately equal contributions from both carriers, making it difficult to assign the fast recombination pathways. In such cases, creative methods to systematically induce or eliminate possible trap states can be employed to study the impact on the TA spectra. While TA spectroscopy alone does not yield molecular-level information, it is a powerful tool for studying charge carrier dynamics on short timescales and may be correlated with ligand etching or passivation treatments to identify the dominant trap states present.

In contrast to absorbance spectroscopy, photoluminescence (PL) spectroscopy has traditionally been considered the primary tool to assess the presence of surface defects through three key measurements: steady-state PL, time-resolved PL, and PL quantum yields (PLQY). These measurements reveal the presence, or lack thereof, of mid-gap trap states (both radiative and non-radiative) at the NC surface. A loss of steady-state PL intensity, a shortening of the emission lifetime, or a low PLQY resulting from various surface treatments may indicate the formation of defect sites that yield electronic mid-gap trap states. Additionally, the observation of low-energy emission features in the steady-state spectra of some NC materials such as CdSe and CdS quantum dots has been correlated with the presence of emissive surface defects.[102–104] Importantly, PL spectra do not provide direct molecular-level insight into the surface structure or electronic trap states, but are revealing when combined with other techniques as described below (Section 1.2.3).

Finally, electrochemical techniques have been popularized in recent years to analyze the electronic structure of NCs. A variety of methods including voltammetry (e.g., cyclic voltammetry, CV, and differential pulse voltammetry, DPV), spectroelectrochemistry, and electroluminescence have been applied to quantify the energetics of band-edge and mid-gap electronic states, and their application has been described in several recent articles.[105–107] A challenge of using these methods is that insulating aliphatic ligands hinder electronic contact between the electrodes and the redox-active NC.[105] This has

been circumvented in some studies by utilizing redox shuttles to perform measurements on colloidal solutions or performing electrochemical measurements with thin films of NCs.[88,108–112] However, the difference in environment between colloidal and thin-film NC samples undoubtedly impacts the absolute redox potentials of both band-edge and surface electronic states. Thus, reported electrochemical values from thin films may not translate directly to colloidal systems.[112] Additionally, the use of common electrolytes such as perchlorate salts in electrochemical measurements has been shown to promote unexpected reactivity with NC materials, stressing the importance of designing such systems with great care.[109]

1.2.3 Recent Advances in Gaining Molecular-Level Insight into the NC Surface

Revealing the heterogeneity of binding sites. NC surfaces undergo dynamic ligand exchange and displacement reactions and can be selectively perturbed using molecular reagents to induce quantifiable changes, which are measurable via spectroscopic, imaging, and computational techniques. X-type ligand exchange equilibria have been extensively studied for various materials in recent years,[37–40,113] yet Z-type ligand reactivity has recontextualized the way the field thinks about ligand-based reactions. First characterized by Owen and coworkers, L-type-promoted Z-type displacement occurs when Lewis bases (L) added to solutions of NCs shift the equilibrium of surface-bound Z-type moieties toward liberated L–Z complexes.[114] The discovery of L-type-promoted Z-type displacement has broad implications ranging from the use of various solvents (e.g., tetrahydrofuran or alcohols) in purification protocols to post-synthetic treatments intended to enhance device performance, demonstrating that apparently innocent species in solution can interact with the NC surface through unexpected pathways. The loss of Z-type ligands from the NC surface has since been extensively correlated with a decrease in PLQY, consistent with vacancies that act as hole traps.[77,115–117]

To better understand the coordination environment of such vacant sites, research teams led by Beaulac and Hens utilized carefully controlled L-type-promoted Z-type ligand displacement to chemically probe CdSe NC surfaces.[35,36] Both works relied on ^{1}H NMR spectroscopy to quantify the absolute number

of bound and free Z-type ligands in equilibrium with the NC surface upon titration of L-type amines, including *N*, *N*, *N*′, *N*′-tetramethylethane-1,2-diamine (TMEDA), benzylamine, and *n*-butylamine. From nonlinear regression analysis of these ^{1}H NMR spectroscopy data, a coupled, two-site displacement (binding) isotherm was proposed to describe the equilibrium reactions at the NC surface. Scheme 1.1 illustrates this concept, showing Z-type binding to two chemically distinct sites on the NC surface, B_1 and B_2. The displacement of an L–Z complex from sites B_1 and B_2 is governed by equilibrium constants K_1 and K_2, respectively. The numbers of vacant (binding) sites were therefore experimentally determined concomitantly with the Z-type displacement (binding) equilibrium constants for the two distinct populations.

While immense insight was gained from identifying and quantifying simultaneous L-type-promoted Z-type equilibrium processes at the surfaces of CdSe NCs, each research team extended the impact of their conclusions by using different tools to correlate the two Z-type binding sites, B_1 and B_2, with facet-specific molecular structure. Zinc blende CdSe NCs have a morphology which falls between that of a truncated octahedron and a cuboctahedron, with the lattice terminating in {100} and {111} facets. On the {100} facet, the Z-type cadmium ion is coordinated to two selenium ions, while on the {111} facet, the Z-type cadmium ion is coordinated to one selenium ion (Figure 1.4a). Beaulac and coworkers recorded the PL quenching of CdSe NCs upon addition of TMEDA, and then applied a Stern–Volmer analysis to elucidate the quenching efficiency of the B_1 and B_2 sites (Figure 1.5).[35] They found that vacancies on {111} facets (at B_1 sites) minimally impacted the overall PLQY, whereas the vacancies on {100} facets (at B_2 sites) efficiently quenched the PL, suggesting that displacement of Z-type ligands from sites coordinating the cadmium ion through two selenium bonds is associated with hole trapping at the exposed Se^{2-} ions. The assignment of Z-type populations on the {100} and {111} facets treats each crystallographic facet as a uniform distribution, yet possible heterogeneity across edge and vertex sites may complicate this picture.

Scheme 1.1 L-Type-Promoted Z-type Displacement from Distinct Binding Sites on a NC Surface

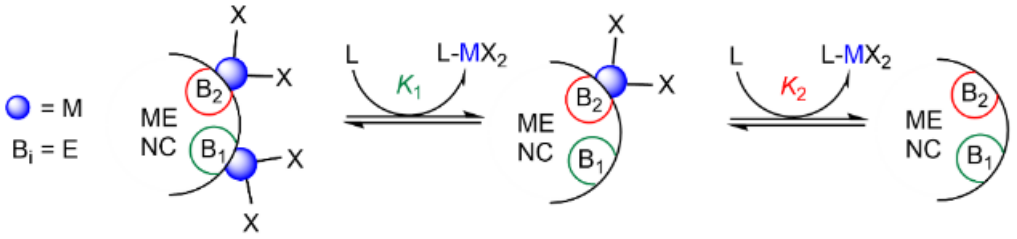

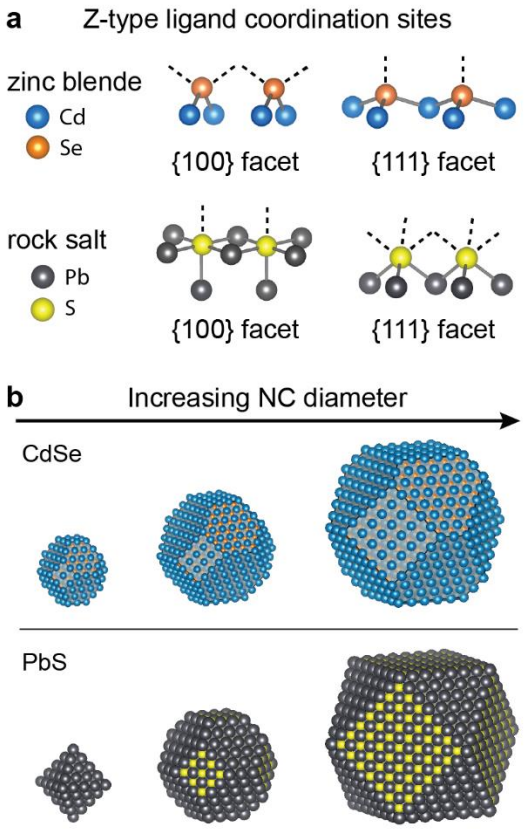

Figure 1.4 (a) On zinc blende NC surfaces, Z-type ligands are coordinated through two bonds on the {100} facet or one bond on the {111} facet (bonds are represented by dashed black lines). Ball-and-stick models represent the lattice structure of the Z-type ligand coordination site; Z-type ligands are not shown. Other crystal structures provide different Z-type coordination environments, as shown for rock salt. (b) With increasing size, zinc blende CdSe NCs largely retain a consistent morphology and distribution of exposed facets. Conversely, rock salt PbS NCs expose {100} facets with increasing diameter as the morphology changes.

Investigating the heterogeneity of Z-type binding sites on a single nanocrystalline facet, Hens and coworkers combined NMR studies with density functional theory (DFT) calculations.[36] Displacement

energy calculations of Z-type ligands positioned at center, edge, and vertex sites on the {100} facet of CdSe NCs indicated that the location of the binding site for a Z-type ligand on a given crystal facet dictates the thermodynamic descriptors governing Z-type displacement (Figure 1.6). Consistent with conclusions from Beaulac and coworkers, this study argues that large numbers of Z-type binding sites are located at vertices and edges relative to facet centers, thereby exacerbating the heterogeneity of ligand displacement (binding) energies across the NC surface.

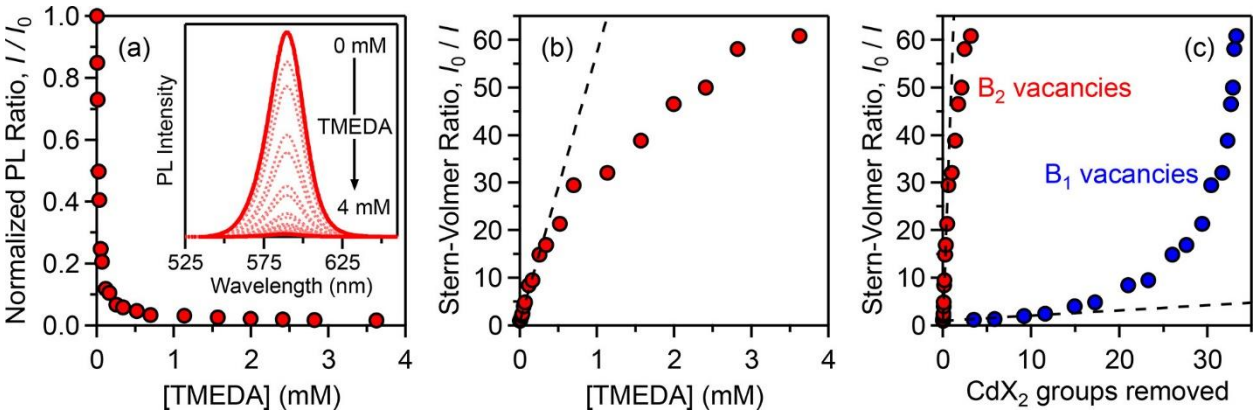

Figure 1.5 (a) Titration of TMEDA into CdSe NCs quenches the PL intensity. (b) Quenching of the PL is represented as a function of the Stern-Volmer ratio. (c) Deconvolution of the quenching efficiencies for B1 and B2 vacancies indicates that displacement of CdX2 from sites on the {100} facets (B2 vacancies) contributes significantly to PL quenching. Reprinted with permission from ref 35. Copyright 2018 American Chemical Society.

These works demonstrate that the assignment of multiple populations of Z-type binding sites to facet- or site-specific locations is complicated by heterogeneity of the NC surface, but the study of multiple NC sizes or morphologies can prove useful to elucidate the locations of Z-type binding sites. Beaulac and coworkers examined three sizes of CdSe NCs—3.0, 3.8, and 4.1 nm in diameter—to evaluate whether the relative proportions of the two Z-type populations depend on size. NC diameter was not found to influence the displacement (binding) equilibria or the distribution of reactive Z-type sites. However, CdSe NCs are not predicted to deviate from their quasi-spherical shape (described above) as a function of diameter. By contrast, PbS NCs undergo size-dependent shape transitions below 5 nm in diameter, changing from octahedral to truncated octahedral shapes with increasing diameter (Figure

1.4b).[21,22,80,118] Work in our lab demonstrated that TMEDA-promoted Pb(oleate)$_2$ displacement is also well-modeled by a two-site displacement isotherm, but that small vs. large PbS NCs show significant differences in the relative populations of Z-type binding sites, consistent with size-dependent topology.[21] Mapping displacement isotherm parameters to topological models revealed that Z-type ligands at vertex sites are the most labile, and that Z-displacement from edge sites with inequivalent coordination environments proceeds according to distinct equilibria. The development of an experimental, quantitative analysis to deconvolute multiple simultaneous surface equilibrium reactions represents a necessary and key advance into gaining molecular-level information.

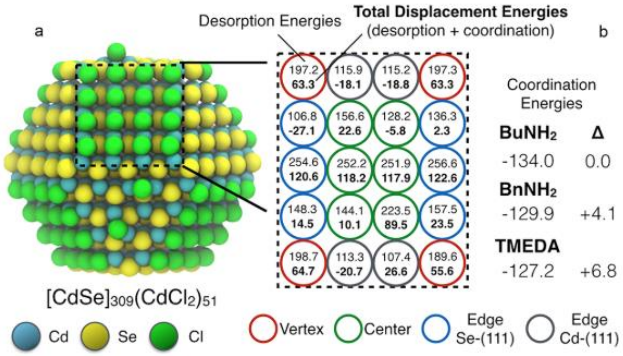

Figure 1.6 (a) Representation of a CdSe NC ligated with Z-type $CdCl_2$ ligands. (b) Displacement energies display significant heterogeneity depending on the binding location of each Z-type ligand, represented as vertex, center, and edge sites. Reprinted with permission from ref 36. Copyright 2018 American Chemical Society.

Interpreting facet-specific ligand coordination geometries. The preferred binding mode of multidentate ligands represents another poorly understood aspect of NC surface chemistry. Carboxylic acids and phosphonic acids are routinely employed in synthetic procedures, and both can coordinate one or more metal cations on the NC surface. An early computational report of carboxylate ligands on CdSe NCs showed that chelating and bridging bidentate geometries are energetically favorable.[119] This report additionally established the thermally activated mobility of carboxylate anchoring groups, which oscillate between right- and left-tilted-bridge configurations at room temperature. While atomically precise stoichiometries and ligand coordination geometries have been determined for InP magic-size clusters

using single-crystal X-ray diffraction,[120] colloidal NCs are too large and heterogeneous to characterize with such methods.[121] The coordination of carboxylate anchoring groups on NCs has proven challenging to characterize precisely by experimental methods—early contributions utilized the energy difference between the asymmetric and symmetric O–C–O stretching features ($\Delta\nu$) in FTIR spectra to deconvolute the binding modes of palmitate ligands on InP NCs[47] and oleate ligands on PbS NCs.[56] The $\Delta\nu$ values of these two sets of peaks suggested that carboxylates bind these types of NCs through both bridging and chelating bidentate modes, consistent with computational predictions. However, researchers were unable to determine the preference of different facets for each type of binding mode using only the $\Delta\nu$ values obtained from FTIR spectroscopy.

More recently, Peng and coworkers critically reexamined the assignment of these O–C–O stretching frequencies through a resourceful combination of NMR and FTIR spectroscopies, alongside complementary DFT.[23] A series of zinc blende CdSe NCs was synthesized to access shapes with unique distributions of surface facets: nanoplatelets, hexahedrons, and spheroids (quantum dots). The surface area of the nanoplatelets is dominated by {100} facets, whereas hexahedrons are terminated by three {100} facets, two {111} facets, and one {110} facet (Figure 1.7). Spheroidal NCs ~3 nm in diameter display {100} and {111} facets, yet heterogeneity of the surface due to the large number of edge and vertex sites, as discussed above, results in an ill-defined distribution of facets compared with nanoplatelets and hexahedrons. Because the surface facets are terminated by Cd ions, the chemical environment of surface Cd was investigated through ^{113}Cd CPMAS NMR spectroscopy. Comparison of the ^{113}Cd NMR resonances for each morphology demonstrated a qualitative difference in the environment of the surface Cd ions, wherein peak broadening indicated the presence of multiple types of facets for hexahedral and spheroidal NCs.

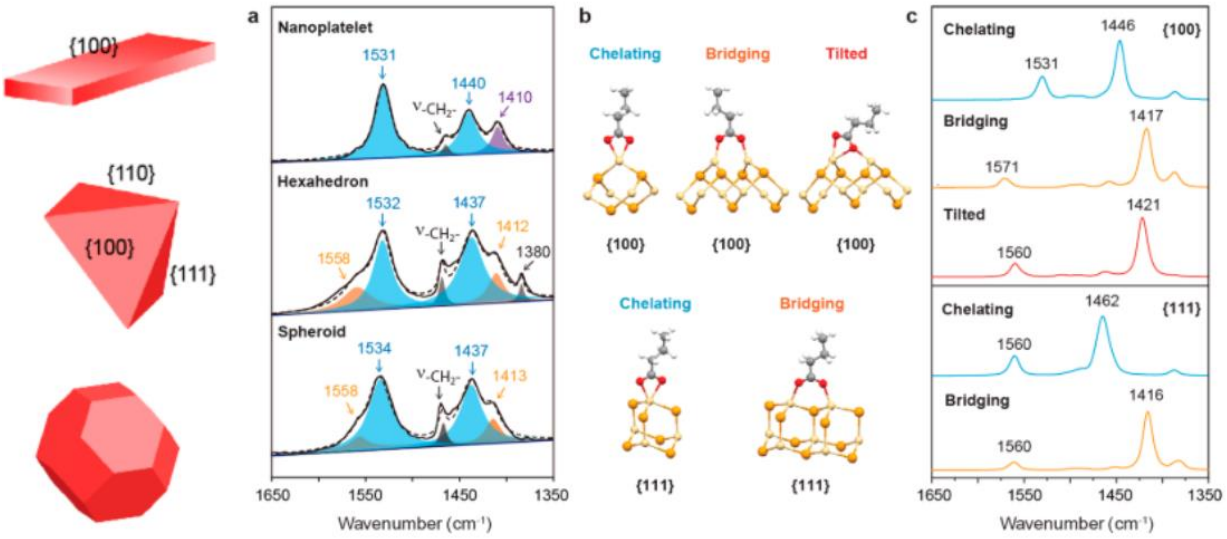

Figure 1.7 Left-most panel: Nanoplatelet, hexahedral, and spheroidal NCs and corresponding facets. (a) Experimental FTIR spectra of CdSe NCs. (b) Possible coordination geometries of carboxylate ligands on {100} and {111} facets of zinc blende CdSe NCs. (c) Calculated FTIR stretches for each carboxylate coordination geometry on each NC facet. Reproduced with permission from ref 23. Copyright 2019 American Chemical Society.

After establishing that surface Cd environments are shape- and facet-dependent, the authors applied a similar analysis to investigate carboxylate binding modes on the distinct surface facets using a combination of experimental and calculated FTIR spectra collected for each material. The symmetric O–C–O stretching features near 1530 and 1440 cm^{-1} in the FTIR spectrum of nanoplatelets (Figure 1.7a) agreed well with the chelating binding mode computed for carboxylate ligands on {100} facets (Figure 1.7b,c). These IR features are present for all three materials, supporting the dominance of the chelating geometry on CdSe NCs and confirming the prediction that the surface area of each morphology displays a large proportion of {100} facets. From the molecular-level perspective, the coordination environment of the chelating configuration on the {100} facet provides two ligand-based bonds to a Cd ion, which is also coordinated to two underlying Se ions (Figure 1.7b). Assignment of the FTIR features to the chelating binding mode is also consistent with computed binding energies that support the stability of this tetrahedral configuration.

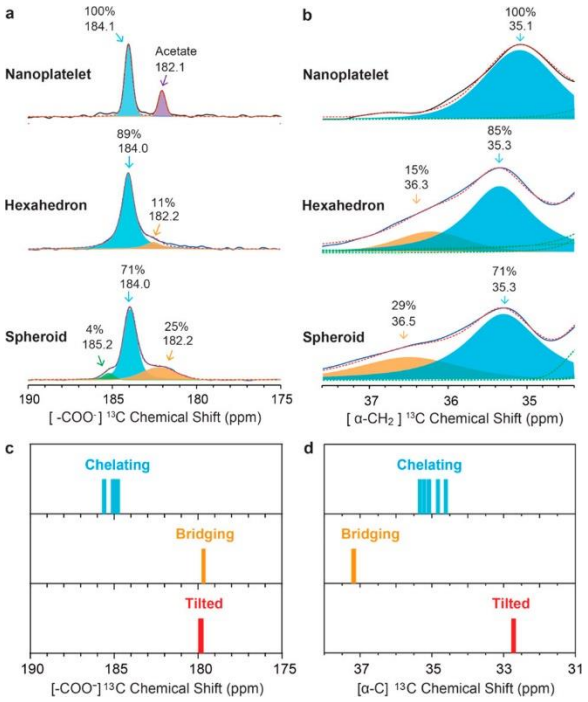

Figure 1.8 (a) Experimental ^{13}C NMR spectra for nanoplatelet, hexahedral, and spheroidal CdSe NCs, showing the carboxylate region with a dominant peak attributed to the chelating geometry (calculated, panel c). (b) The α-CH_2 regions of the ^{13}C NMR spectra shows peaks attributed to the chelating coordination mode and a minor feature attributed to the bridging bidentate geometry (calculated, panel d). Reprinted with permission from ref 23. Copyright 2019 American Chemical Society.

For hexahedrons and spheroids, the FTIR spectra indicate that additional binding configurations exist on the NC surface, yet the computed IR spectra are not sufficient to assign the experimental peaks to specific modes. Utilizing techniques including solution-phase ^{13}C NMR and solid-state ^{13}C CPMAS NMR spectroscopies, resonances at 184 ppm and 35 ppm ascribed to the dominant chelating binding mode were identified on CdSe {100} facets (Figure 1.8a,b). Comparing with computed ^{13}C NMR chemical shifts (Figure 1.8c,d), minor features in the spectra of hexahedrons and spheroids were assigned to the bridging configuration on {111} facets. The features in the FTIR spectra for these materials near 1560 and 1415 cm^{-1} are also consistent with this assignment. The bridging configuration satisfies the tetrahedral coordination of the {111} surface Cd ions, which coordinate a single oxygen of the carboxylate group as well as three underlying Se ions (Figure 1.7b).

Finally, the feature at 1380 cm^{-1} in the FTIR spectrum of hexahedrons (Figure 1.7a) was reasoned to originate from coordination of Z-type cadmium carboxylates to neutral {110} facets, which comprise about 25% of the total surface area of these NCs. However, the calculated binding energy of Z-type ligands on the {110} facets was found to be an order of magnitude less than that for X-type carboxylate binding on {111} and {100} facets. Indeed, the Z-type contribution to the total bound carboxylate density was much lower than the predicted ~25%. Through a clever combination of experimental and computational techniques as well as the use of distinct nanocrystalline morphologies, this study provided robust and quantitative support for facet-specific binding configurations of carboxylate ligands on semiconductor NCs.

Elucidating metal-based surface defects. Important insight into facet-specific ligand displacement (binding) equilibria and coordination geometries has significantly advanced our understanding of the ligand–lattice interface. However, implementation of NCs into high performance devices also requires knowledge of the relationship between the NC surface and the electronic structure of the material. The electronic structure of the surface is difficult to probe experimentally, and as such computations can aid in linking chemical and redox reactivity at the surface with observed experimental phenomena. For example, in 2013 Owen and coworkers observed significant losses in PLQY upon removal of Z-type ligands from CdSe and CdS NCs.[114] In a follow-up work in collaboration with Sfeir, it was proposed that these losses in PLQY could be attributed to Z-type ligand loss from {100} facets, forming two-coordinate selenium ions that participate in hole trapping processes.[115] Complementary computational work by Infante and co-workers has also demonstrated the impact of ligand binding motif on the formation of mid-gap trap states through systematic ligand removal from CdSe NC models.[86] Removal of X- and L-type ligands from CdSe NC models did not result in trap state formation, whereas Z-type ligand displacement did yield mid-gap trap states. DFT modeling of the exposed Se ions after Z-type ligand removal revealed that the newly formed mid-gap states localize on two-coordinate Se ions, consistent with experimental findings (Figure 1.9a). Considering the molecular orbital diagram of the Z-type binding site, the authors proposed that the mid-gap state is localized on a nonbonding Se 4p orbital (Figure 1.9b). The understanding of the

relationship between ligand passivation and the electronic structure of NCs is in its infancy, emphasizing the need for molecular orbital explanations of charge carrier trapping processes for a variety of semiconductor materials as well as experimental validation.

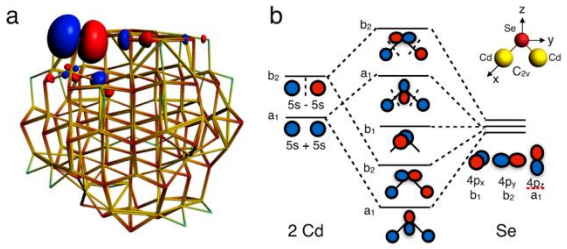

Figure 1.9 (a) The molecular orbital localized on the 4p nonbonding orbital of a two-coordinate Se ion resulting from displacement of a Z-type ligand. (b) The MO diagram for the C2v arrangement of atoms shown in the upper right diagram. Reprinted with permission from ref 86. Copyright 2017 American Chemical Society.

While many computational studies have concluded that chalcogenide defects on NC surfaces are a major source of performance-limiting trap states, fewer studies have explored metal-based defects. Metal-based trap states have been hypothesized to form when a NC is charged with excess electrons, yet they are difficult to probe experimentally and their contribution to the electronic structure is not well-understood. Current experimental evidence for localization of excess charge at the surface suggests that reduction of surface metal ions is intimately linked to ligand binding and displacement. For example, addition of the molecular reductant sodium naphthalenide to CdSe NCs led to the liberation of X-type oleate ligands from the surface as evinced by ^{1}H NMR and FTIR spectroscopies.[75] Because experimental avenues to probe metal-based traps are limited, Houtepen and coworkers relied upon DFT studies to investigate how the oxidation state of surface metal ions as well as ligand passivation impact overall electronic structure.[32] Using a series of neutral, completely ligated (fully passivated) $M_{68}E_{55}Cl_{26}$ (M = Cd, Zn; E= S, Se, Te) zinc blende NCs, up to four electrons were sequentially injected into each NC. Addition of one or two electrons did not markedly impact the electronic structure of the NCs. However, three and

four excess electrons created mid-gap states localized on the three-coordinate Cd ions on {111} facets. Concomitantly with trap state formation, structural rearrangement of the {111} facet resulted in ejection of Cd^0 from the lattice plane. Interestingly, the formation of metal-based trap states was found to vary not only with number of electrons injected, but also with semiconductor material.

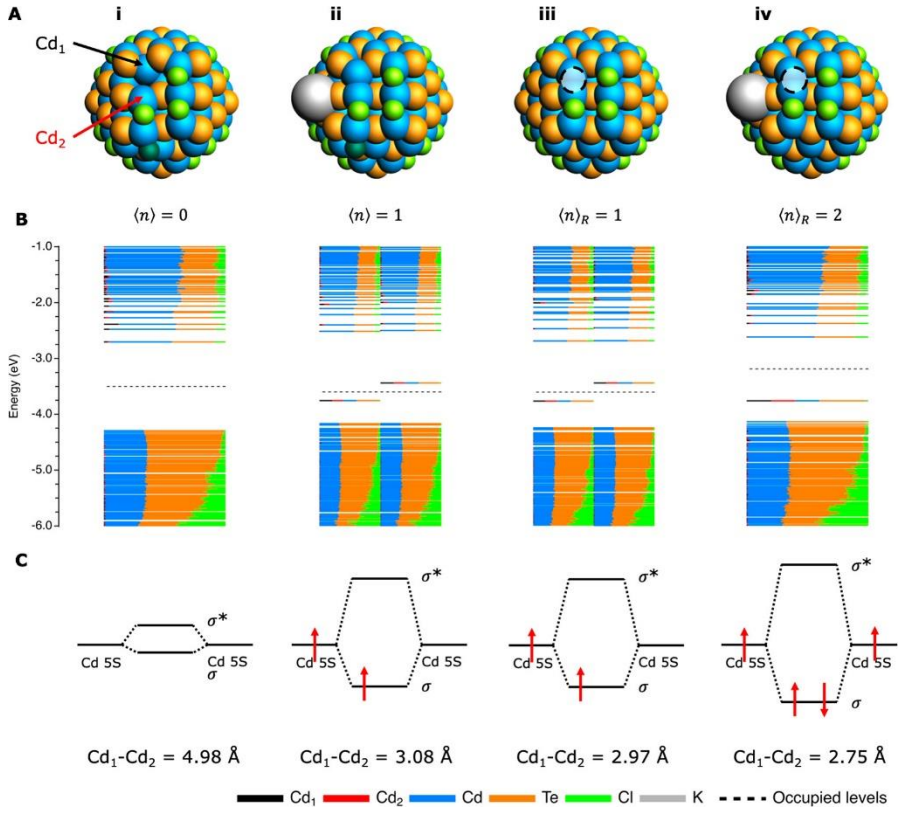

Figure 1.10 (a) Imperfectly passivated CdTe NC models (i and ii) upon moving an X-type chloride ligand to a different facet (dark green sphere) and injecting 0 or 1 electrons (i and ii, respectively). (iii and iv) NC models upon removing an X-type chloride ligand from the system (dashed circle) and injecting 1 or 2 electrons (iii and iv, respectively). (b) The density of states, where solid lines represent molecular orbitals and the MOs below the dashed line are occupied. Mid-gap electronic states appear when 1 or 2 electrons are injected. (c) MO diagrams show that increasing the number of excess electrons results in Cd–Cd dimers with decreasing bond lengths due to stabilization of the 5s bonding MO. Reprinted with permission from ref 32. Copyright 2019 American Chemical Society.

In addition to the study of fully passivated NCs, Houtepen and coworkers considered surface charging in NCs that had an X-type chloride ligand from a {100} facet moved to a different facet or removed from the system entirely (imperfectly passivated). Unlike in the case of fully passivated NCs, the

authors proposed that addition of one or two excess electrons to an imperfectly passivated CdTe NC induced Cd−Cd dimerization (Figure 1.10a). Further analysis predicted that the overlap of Cd 5s orbitals resulting from dimerization led to the formation of a mid-gap electronic state (Figure 1.10b,c). Moreover, the authors showed that addition of excess charge to CdTe NCs that substituted a neutral L-type amine ligand for a Cl^0 atom did not result in Cd−Cd dimerization. This finding highlighted how reduction of the NC surface may lead to charge imbalance and subsequent metal-based defects (e.g., metal ion dimerization), and presented a possible experimental means to limit defect formation related to surface charging by employing neutral L-type capping ligands.[32] In summary, these theory-based findings directly complement experimental observations of X-type ligand loss from CdSe NCs,[75] both of which suggest that metal-based trap states exist on NC surfaces and are likely induced by charging.

1.3 Outlook

Limitations. While the case studies considered in Section 1.2.3 showcase the level of detail with which researchers can understand NC surfaces through thoughtful and creative applications of complementary tools, it is important to recognize that only recently has this type of molecular-level understanding become accessible. Looking towards the potential discoveries in this area of study, it is key to recognize several limitations that require intentional solutions to further understanding of NC surfaces. A first limitation is the normalization of vague descriptors of NC surfaces. It is not uncommon in the literature to attribute irreproducibility or unexpected behavior to surface moieties or defect sites without specific descriptors of their molecular-level identity. This may be common in part due to the complex and dynamic nature of the NC surface, especially given that NC batches contain particle-to-particle heterogeneities in size, shape, surface properties, and ligand coverage. It can therefore be difficult to know precisely which defects exist on each individual NC; however, a more detailed understanding of the types of defects that exist on certain materials, even if obtained through an ensemble measurement, can aid in directing strategies for defect passivation and surface engineering. As the normalization of vague language to describe NC surfaces limits the field by establishing literature precedent for invoking the

surface without directly probing it, an intentional effort by researchers and peer reviewers to demand more specific language and exploratory studies of NC surface chemistry will help mitigate this first concern.

Second, there remains a major challenge in comparing results between NC studies in solution with those in thin films or the solid state. This is in large part due to the differences in local environment of NC surfaces between the two phases, as well as a lack of characterization of NC surface chemistry once the NCs are assembled in a thin film. It is critical that the field moves toward improved understanding not only of NC surface chemistry in general, but also of differences that arise between colloidal vs. solid-state NC samples. Overcoming this limitation will require systematic and fundamental studies of NC surface chemistry before and after thin film assembly and may be further enlightened by computational simulations. Closing this gap will be critical from both a fundamental surface science as well as a device applications perspective.

A final limitation towards improved molecular-level understanding of NC surfaces is poor accessibility to many of the most useful tools highlighted above (Section 1.2.2). XANES, XAFS, and heteroatom or solid-state NMR are just a few examples of highly revealing tools that are only available in a handful of national labs or research institutes across the world. Without access to such instruments, strategic use of the other tools highlighted above may still prove fruitful for answering many surface-related questions. However, this limitation may be overcome through collaborative works, and we encourage those as possible.

Opportunities for Advancing the Field. With these limitations in mind, it is important to recognize that the field has made major strides towards understanding NC surfaces. The broader NC community can continue these advances by undertaking complementary tool-based studies. An expanded library of such works in the literature will greatly improve overall understanding of surfaces across various materials and morphologies. The growth of the analytical toolbox will also advance ways to probe NC surface chemistry. In tandem, the sensitivity and resolution of existing techniques can be further improved, and

new combinations of tools can be constructed to answer important questions about the molecular-level chemical and electronic structure of NC surfaces.

Additionally, there are limitless opportunities for synergies between theory and experiment. Experimentalists may take inspiration from proposed computational findings; similarly, theorists should apply computational tools to elucidate puzzling experimental results. For example, the majority of studies linking the formation of structural defects (e.g., metal dimers, oxidized chalcogenide dimers, etc.) with electronic trap states, especially as a result of surface charging, have been computational (see Section 1.2.3). There remains a need for a body of experimental evidence to confirm these proposed connections. Such knowledge will benefit the scientific community by helping to explain poorly understood phenomena arising at NC surfaces, and establishing a foundation for rational design and passivation to achieve the full potential of NCs in chemical systems and optoelectronic devices.

As researchers set out to deepen their understanding of NC surfaces in their own systems, we urge them to perform detailed optical and surface characterization of NC samples, regardless of the specific focus of a given study. Thorough characterization may illuminate reasons for discrepancies between investigations performed in different laboratories and help rationalize unexpected behavior. Materials such as metal halide perovskite NCs that have advanced rapidly due to their favorable properties, but lag behind II–VI and III–V NCs in molecular-level surface studies, would benefit in particular from intensive characterization. Additionally, to the extent possible we encourage the use of complementary tools that probe each aspect of the surface—the capping ligands, ligand-lattice interface, and surface-based electronic states.

As these critical advances are made, outstanding gaps in knowledge in the field can be addressed. These include but are not limited to: (i) Almost all molecular-level insights to date have focused on quasi-spherical zinc blende CdSe NCs; how will our understanding of the surface change upon exploring other NC materials and morphologies? (ii) Facet-dependent behavior has been reported in various NC-based systems for catalysis;[122,123] how do the exposed facets of a particular NC morphology impact surface trap state populations, redox reactivity, etc.? To what extent can surfaces be engineered to promote desired

reactivity? (iii) Once the nature of defect sites is better characterized, what are direct and targeted post-synthetic chemical modifications that can induce or passivate such sites on NC surfaces? While not an exhaustive list of all avenues worth exploring, these questions serve as a launchpad for further discoveries into surface states across NC-based systems.

1.4 Concluding Remarks on Quantum Dot Surface Chemistry

In the last several years, major strides have been made towards gaining a detailed, molecular-level understanding of the physical and electronic structure of semiconductor NC surfaces. In large part, progress has been aided by an emerging toolbox of methods that can identify components of the NC surface with increasing specificity and can also measure changes to the surface coordination environment through carefully designed systems utilizing chemical probes. Additionally, computational models can complement experimental findings to rationalize or even predict the structural origins of mid-gap trap states when analytical methods fall short. The case studies highlighted in this chapter demonstrate that deep molecular-level insight into NC surfaces can be gained by a creative combination of tools. While metrics obtained under the presence of ensemble heterogeneity are ultimately representative averages of NC properties, they allow the field to progress by proposing new links between the physical and the electronic structure of the surface. As the field continues to move forward, these critical links will be key to achieving rational surface passivation and functional modification strategies, ultimately leading to more efficient NC technologies.

1.5 Overview of Dissertation

In this dissertation, I specifically focus on expanding molecular-level understanding of the QD surface through the use of redox-active chemical probes in tandem with a wide range of spectroscopic tools. In so doing, this work provides critical insight into the nature of defect sites on CdSe and PbS QD surfaces. In Chapter 2 I present a model system to probe electron-accepting defect sites on CdSe QDs and propose an electron-promoted X-type ligand displacement mechanism as a new approach for

understanding charge balance at the QD surface. In Chapter 3, I expand upon our understanding of the redox reactivity of surface defects with PbS QDs using a range of QD sizes and redox-active chemical probes. In Chapter 4, I investigate the impact of varying surface capping ligands on the reactivity with added reducing agent to gain further insight into how the native surface chemistry (i.e., ligand identity and coverage) impact the reactivity and stability of the QD surface to charging. Finally, a new approach to understanding the redox chemistry of the QD core is presented in Chapter 5. Within this chapter I explore the light-promoted charge transfer of QDs with molecular donors and acceptors with the goal of assessing whether it is possible to access the Marcus inverted region in electron transfer from QDs.

REFERENCES

(1) Boles, M. A.; Ling, D.; Hyeon, T.; Talapin, D. V. The Surface Science of Nanocrystals. *Nat. Mater.* **2016**, *15*, 141–153.

(2) Kovalenko, M. V; Manna, L.; Cabot, A.; Hens, Z.; Talapin, D. V; Kagan, C. R.; Klimov, V. I.; Rogach, A. L.; Reiss, P.; Milliron, D. J.; et al. Prospects of Nanoscience with Nanocrystals. *ACS Nano* **2015**, *9*, 1012–1057.

(3) Manna, L.; Milliron, D. J.; Meisel, A.; Scher, E. C.; Alivisatos, A. P. Controlled Growth of Tetrapod-Branched Inorganic Nanocrystals. *Nat. Mater.* **2003**, *2*, 382–385.

(4) Hines, M. A.; Scholes, G. D. Colloidal PbS Nanocrystals with Size-Tunable Near-Infrared Emission: Observation of Post-Synthesis Self-Narrowing of the Particle Size Distribution. *Adv. Mater.* **2003**, *15*, 1844–1849.

(5) Murray, C. B.; Norris, D. J.; Bawendi, M. G. Synthesis and Characterization of Nearly Monodisperse CdE (E = Sulfur, Selenium, Tellurium) Semiconductor Nanocrystallites. *J. Am. Chem. Soc.* **1993**, *115*, 8706–8715.

(6) Hendricks, M. P.; Campos, M. P.; Cleveland, G. T.; Jen-La Plante, I.; Owen, J. S. A Tunable Library of Substituted Thiourea Precursors to Metal Sulfide Nanocrystals. *Science* **2015**, *348*, 1226–1230.

(7) Campos, M. P.; Hendricks, M. P.; Beecher, A. N.; Walravens, W.; Swain, R. A.; Cleveland, G. T.; Hens, Z.; Sfeir, M. Y.; Owen, J. S. A Library of Selenourea Precursors to PbSe Nanocrystals with Size Distributions near the Homogeneous Limit. *J. Am. Chem. Soc.* **2017**, *139*, 2296–2305.

(8) Ithurria, S.; Tessier, M. D.; Mahler, B.; Lobo, R. P. S. M.; Dubertret, B.; Efros, A. L. Colloidal Nanoplatelets with Two-Dimensional Electronic Structure. *Nat. Mater.* **2011**, *10*, 936–941.

(9) Cho, W.; Kim, S.; Coropceanu, I.; Srivastava, V.; Diroll, B. T.; Hazarika, A.; Fedin, I.; Galli, G.; Schaller, R. D.; Talapin, D. V. Direct Synthesis of Six-Monolayer (1.9 Nm) Thick Zinc-Blende CdSe Nanoplatelets Emitting at 585 Nm. *Chem. Mater.* **2018**, *30*, 6957–6960.

(10) Zhou, J.; Pu, C.; Jiao, T.; Hou, X.; Peng, X. A Two-Step Synthetic Strategy toward Monodisperse Colloidal CdSe and CdSe/CdS Core/Shell Nanocrystals. *J. Am. Chem. Soc.* **2016**, *138*, 6475–6483.

(11) Lu, H.; Zhu, X.; Miller, C.; San Martin, J.; Chen, X.; Miller, E. M.; Yan, Y.; Beard, M. C. Enhanced Photoredox Activity of CsPbBr 3 Nanocrystals by Quantitative Colloidal Ligand Exchange. *J. Chem. Phys.* **2019**, *151*, 204305.

(12) Chang, J.; Waclawik, E. R. Colloidal Semiconductor Nanocrystals: Controlled Synthesis and Surface Chemistry in Organic Media. *RSC Adv.* **2014**, *4*, 23505–23527.

(13) Ginterseder, M.; Franke, D.; Perkinson, C. F.; Wang, L.; Hansen, E. C.; Bawendi, M. G. Scalable Synthesis of InAs Quantum Dots Mediated through Indium Redox Chemistry. *J. Am. Chem. Soc.* **2020**, *142*, 4088–4092.

(14) van Embden, J.; Chesman, A. S. R.; Jasieniak, J. J. The Heat-Up Synthesis of Colloidal Nanocrystals. *Chem. Mater.* **2015**, *27*, 2246–2285.

(15) Murray, C. B.; Kagan, C. R.; Bawendi, M. G. Synthesis and Characterization of Monodisperse Nanocrystals and Close-Packed Nanocrystal Assemblies. *Annu. Rev. Mater. Sci.* **2000**, 545–610.

(16) De Roo, J.; Yazdani, N.; Drijvers, E.; Lauria, A.; Maes, J.; Owen, J. S.; Van Driessche, I.; Niederberger, M.; Wood, V.; Martins, J. C.; et al. Probing Solvent–Ligand Interactions in Colloidal Nanocrystals by the NMR Line Broadening. *Chem. Mater.* **2018**, *30*, 5485–5492.

(17) Frederick, M. T.; Amin, V. A.; Cass, L. C.; Weiss, E. A. A Molecule to Detect and Perturb the Confinement of Charge Carriers in Quantum Dots. *Nano Lett.* **2011**, *11*, 5455–5460.

(18) Giansante, C. Surface Chemistry Control of Colloidal Quantum Dot Band Gap. *J. Phys. Chem. C* **2018**, *122*, 18110–18116.

(19) Harvie, A. J.; Smith, C. T.; Ahumada-Lazo, R.; Jeuken, L. J. C.; Califano, M.; Bon, R. S.; Hardman, S. J. O.; Binks, D. J.; Critchley, K. Ultrafast Trap State-Mediated Electron Transfer for Quantum Dot Redox Sensing. *J. Phys. Chem. C* **2018**, *122*, 10173–10180.

(20) Gao, Y.; Peng, X. Crystal Structure Control of CdSe Nanocrystals in Growth and Nucleation: Dominating Effects of Surface versus Interior Structure. *J. Am. Chem. Soc.* **2014**, *136*, 6724–6732.

(21) Kessler, M. L.; Dempsey, J. L. Mapping the Topology of PbS Nanocrystals through Displacement Isotherms of Surface-Bound Metal Oleate Complexes. *Chem. Mater.* **2020**, *32*, 2561–2571.

(22) Choi, H.; Ko, J.-H.; Kim, Y.-H.; Jeong, S. Steric-Hindrance-Driven Shape Transition in PbS Quantum Dots: Understanding Size-Dependent Stability. *J. Am. Chem. Soc.* **2013**, *135*, 5278–5281.

(23) Zhang, J.; Zhang, H.; Cao, W.; Pang, Z.; Li, J.; Shu, Y.; Zhu, C.; Kong, X.; Wang, L.; Peng, X. Identification of Facet-Dependent Coordination Structures of Carboxylate Ligands on CdSe Nanocrystals. *J. Am. Chem. Soc.* **2019**, *141*, 15675–15683.

(24) Green, M. L. H. A New Approach to the Formal Classification of Covalent Compounds of the Elements. *J. Organomet. Chem.* **1995**, *500*, 127–148.

(25) De Roo, J.; De Keukeleere, K.; Hens, Z.; Van Driessche, I. From Ligands to Binding Motifs and beyond; the Enhanced Versatility of Nanocrystal Surfaces. *Dalt. Trans.* **2016**, *45*, 13277–13283.

(26) Zhou, Y.; Buhro, W. E. Reversible Exchange of L-Type and Bound-Ion-Pair X-Type Ligation on Cadmium Selenide Quantum Belts. *J. Am. Chem. Soc.* **2017**, *139*, 12887–12890.

(27) Yao, Y.; DeKoster, G. T.; Buhro, W. E. Interchange of L-, Z-, and Bound-Ion-Pair X-Type Ligation on Cadmium Selenide Quantum Belts. *Chem. Mater.* **2019**, *31*, 4299–4312.

(28) Nenon, D. P.; Pressler, K.; Kang, J.; Koscher, B. A.; Olshansky, J. H.; Osowiecki, W. T.; Koc, M. A.; Wang, L.-W.; Alivisatos, A. P. Design Principles for Trap-Free CsPbX3 Nanocrystals: Enumerating and Eliminating Surface Halide Vacancies with Softer Lewis Bases. *J. Am. Chem. Soc.* **2018**, *140*, 17760–17772.

(29) De Keukeleere, K.; Coucke, S.; De Canck, E.; Van Der Voort, P.; Delpech, F.; Coppel, Y.; Hens, Z.; Van Driessche, I.; Owen, J. S.; De Roo, J. Stabilization of Colloidal Ti, Zr, and Hf Oxide Nanocrystals by Protonated Tri-n-Octylphosphine Oxide (TOPO) and Its Decomposition Products. *Chem. Mater.* **2017**, *29*, 10233–10242.

(30) Tsui, E. Y.; Hartstein, K. H.; Gamelin, D. R. Selenium Redox Reactivity on Colloidal CdSe Quantum Dot Surfaces. *J. Am. Chem. Soc.* **2016**, *138*, 11105–11108.

(31) Zhao, J.; Holmes, M. A.; Osterloh, F. E. Quantum Confinement Controls Photocatalysis: A Free Energy Analysis for Photocatalytic Proton Reduction at CdSe Nanocrystals. *ACS Nano* **2013**, *7*, 4316–4325.

(32) du Fossé, I.; ten Brinck, S.; Infante, I.; Houtepen, A. J. Role of Surface Reduction in the Formation of Traps in n -Doped II–VI Semiconductor Nanocrystals: How to Charge without Reducing the Surface. *Chem. Mater.* **2019**, *31*, 4575–4583.

(33) Hens, Z.; Martins, J. C. A Solution NMR Toolbox for Characterizing the Surface Chemistry of Colloidal Nanocrystals. *Chem. Mater.* **2013**, *25*, 1211–1221.

(34) Moreels, I.; Fritzinger, B.; Martins, J. C.; Hens, Z. Surface Chemistry of Colloidal PbSe Nanocrystals. *J. Am. Chem. Soc.* **2008**, *130*, 15081–15086.

(35) Saniepay, M.; Mi, C.; Liu, Z.; Abel, E. P.; Beaulac, R. Insights into the Structural Complexity of Colloidal CdSe Nanocrystal Surfaces: Correlating the Efficiency of Nonradiative Excited-State Processes to Specific Defects. *J. Am. Chem. Soc.* **2018**, *140*, 1725–1736.

(36) Drijvers, E.; De Roo, J.; Martins, J. C.; Infante, I.; Hens, Z. Ligand Displacement Exposes Binding Site Heterogeneity on CdSe Nanocrystal Surfaces. *Chem. Mater.* **2018**, *30*, 1178–1186.

(37) Smock, S. R.; Williams, T. J.; Brutchey, R. L. Quantifying the Thermodynamics of Ligand Binding to CsPbBr 3 Quantum Dots. *Angew. Chemie Int. Ed.* **2018**, *57*, 11711–11715.

(38) Kessler, M. L.; Starr, H. E.; Knauf, R. R.; Rountree, K. J.; Dempsey, J. L. Exchange Equilibria of Carboxylate-Terminated Ligands at PbS Nanocrystal Surfaces. *Phys. Chem. Chem. Phys.* **2018**, *20*, 23649–23655.

(39) Knauf, R. R.; Lennox, J. C.; Dempsey, J. L. Quantifying Ligand Exchange Reactions at CdSe Nanocrystal Surfaces. *Chem. Mater.* **2016**, *28*, 4762–4770.

(40) Ritchhart, A.; Cossairt, B. M. Quantifying Ligand Exchange on InP Using an Atomically Precise Cluster Platform. *Inorg. Chem.* **2019**, *58*, 2840–2847.

(41) De Roo, J.; Ibáñez, M.; Geiregat, P.; Nedelcu, G.; Walravens, W.; Maes, J.; Martins, J. C.; Van Driessche, I.; Kovalenko, M. V.; Hens, Z. Highly Dynamic Ligand Binding and Light Absorption Coefficient of Cesium Lead Bromide Perovskite Nanocrystals. *ACS Nano* **2016**, *10*, 2071–2081.

(42) Bronstein, N. D.; Martinez, M. S.; Kroupa, D. M.; Vörös, M.; Lu, H.; Brawand, N. P.; Nozik, A. J.; Sellinger, A.; Galli, G.; Beard, M. C. Designing Janus Ligand Shells on PbS Quantum Dots Using Ligand–Ligand Cooperativity. *ACS Nano* **2019**, *13*, 3839–3846.

(43) Webber, D. H.; Brutchey, R. L. Nanocrystal Ligand Exchange with 1,2,3,4-Thiatriazole-5-Thiolate and Its Facile in Situ Conversion to Thiocyanate. *Dalt. Trans.* **2012**, *41*, 7835.

(44) Buckley, J. J.; Greaney, M. J.; Brutchey, R. L. Ligand Exchange of Colloidal CdSe Nanocrystals with Stibanates Derived from Sb 2 S 3 Dissolved in a Thiol-Amine Mixture. *Chem. Mater.* **2014**, *26*, 6311–6317.

(45) Shen, Y.; Tan, R.; Gee, M. Y.; Greytak, A. B. Quantum Yield Regeneration: Influence of Neutral Ligand Binding on Photophysical Properties in Colloidal Core/Shell Quantum Dots. *ACS Nano* **2015**, *9*, 3345–3359.

(46) Seo, H.; Bang, M.; Kim, Y.; Son, C.; Jeon, H. B.; Kim, S.-W. Unprecedented Surface Stabilized InP Quantum Dots with Bidentate Ligands. *RSC Adv.* **2020**, *10*, 11517–11523.

(47) Cros-Gagneux, A.; Delpech, F.; Nayral, C.; Cornejo, A.; Coppel, Y.; Chaudret, B. Surface Chemistry of InP Quantum Dots: A Comprehensive Study. *J. Am. Chem. Soc.* **2010**, *132*, 18147–18157.

(48) Aebli, M.; Piveteau, L.; Nazarenko, O.; Benin, B. M.; Krieg, F.; Verel, R.; Kovalenko, M. V. Lead-Halide Scalar Couplings in 207Pb NMR of APbX3 Perovskites (A = Cs, Methylammonium, Formamidinium; X = Cl, Br, I). *Sci. Rep.* **2020**, *10*, 8229.

(49) Lee, D.; Wolska-Pietkiewicz, M.; Badoni, S.; Grala, A.; Lewiński, J.; De Paëpe, G. Disclosing Interfaces of ZnO Nanocrystals Using Dynamic Nuclear Polarization: Sol-Gel versus Organometallic Approach. *Angew. Chemie Int. Ed.* **2019**, *58*, 17163–17168.

(50) Piveteau, L.; Aebli, M.; Yazdani, N.; Millen, M.; Korosec, L.; Krieg, F.; Benin, B. M.; Morad, V.; Piveteau, C.; Shiroka, T.; et al. Bulk and Nanocrystalline Cesium Lead-Halide Perovskites as Seen by Halide Magnetic Resonance. *ACS Cent. Sci.* **2020**, *6*, 1138–1149.

(51) Piveteau, L.; Ong, T.-C.; Walder, B. J.; Dirin, D. N.; Moscheni, D.; Schneider, B.; Bär, J.; Protesescu, L.; Masciocchi, N.; Guagliardi, A.; et al. Resolving the Core and the Surface of CdSe Quantum Dots and Nanoplatelets Using Dynamic Nuclear Polarization Enhanced PASS–PIETA NMR Spectroscopy. *ACS Cent. Sci.* **2018**, *4*, 1113–1125.

(52) Chen, Y.; Smock, S. R.; Flintgruber, A. H.; Perras, F. A.; Brutchey, R. L.; Rossini, A. J. Surface Termination of CsPbBr 3 Perovskite Quantum Dots Determined by Solid-State NMR Spectroscopy. *J. Am. Chem. Soc.* **2020**, *142*, 6117–6127.

(53) Piveteau, L.; Morad, V.; Kovalenko, M. V. Solid-State NMR and NQR Spectroscopy of Lead-Halide Perovskite Materials. *J. Am. Chem. Soc.* **2020**, *142*, 19413–19437.

(54) Xie, Y.; Du, N.; Yu, S.; Zhang, L.; Yang, M. Unraveling the Structure-Dependent Radiative and Nonradiative Decays in (CdSe) 13 Clusters through First-Principles Calculations. *J. Phys. Chem. C* **2019**, *123*, 30714–30722.

(55) Piveteau, L.; Ong, T.-C.; Rossini, A. J.; Emsley, L.; Copéret, C.; Kovalenko, M. V. Structure of Colloidal Quantum Dots from Dynamic Nuclear Polarization Surface Enhanced NMR Spectroscopy. *J. Am. Chem. Soc.* **2015**, *137*, 13964–13971.

(56) Cass, L. C.; Malicki, M.; Weiss, E. A. The Chemical Environments of Oleate Species within Samples of Oleate-Coated PbS Quantum Dots. *Anal. Chem.* **2013**, *85*, 6974–6979.

(57) Protesescu, L.; Nachtegaal, M.; Voznyy, O.; Borovinskaya, O.; Rossini, A. J.; Emsley, L.; Copéret, C.; Günther, D.; Sargent, E. H.; Kovalenko, M. V. Atomistic Description of Thiostannate-Capped CdSe Nanocrystals: Retention of Four-Coordinate SnS4 Motif and Preservation of Cd-Rich Stoichiometry. *J. Am. Chem. Soc.* **2015**, *137*, 1862–1874.

(58) Yao, Y.; Buhro, W. E. Thiol Versus Thiolate Ligation on Cadmium Selenide Quantum Belts. *Chem. Mater.* **2020**, *32*, 205–214.

(59) Blackburn, J. L.; Chappell, H.; Luther, J. M.; Nozik, A. J.; Johnson, J. C. Correlation between Photooxidation and the Appearance of Raman Scattering Bands in Lead Chalcogenide Quantum Dots. *J. Phys. Chem. Lett.* **2011**, *2*, 599–603.

(60) Stadelmann, K.; Elizabeth, A.; Martín Sabanés, N.; Domke, K. F. The SERS Signature of PbS Quantum Dot Oxidation. *Vib. Spectrosc.* **2017**, *91*, 157–162.

(61) Pala, I. R.; Arachchige, I. U.; Georgiev, D. G.; Brock, S. L. Reversible Gelation of II-VI Nanocrystals: The Nature of Interparticle Bonding and the Origin of Nanocrystal Photochemical Instability. *Angew. Chemie Int. Ed.* **2010**, *49*, 3661–3665.

(62) Leger, J. D.; Friedfeld, M. R.; Beck, R. A.; Gaynor, J. D.; Petrone, A.; Li, X.; Cossairt, B. M.; Khalil, M. Carboxylate Anchors Act as Exciton Reporters in 1.3 Nm Indium Phosphide Nanoclusters. *J. Phys. Chem. Lett.* **2019**, *10*, 1833–1839.

(63) Kennehan, E. R.; Munson, K. T.; Doucette, G. S.; Marshall, A. R.; Beard, M. C.; Asbury, J. B. Dynamic Ligand Surface Chemistry of Excited PbS Quantum Dots. *J. Phys. Chem. Lett.* **2020**, *11*, 2291–2297.

(64) Weir, M. P.; Toolan, D. T. W.; Kilbride, R. C.; Penfold, N. J. W.; Washington, A. L.; King, S. M.; Xiao, J.; Zhang, Z.; Gray, V.; Dowland, S.; et al. Ligand Shell Structure in Lead Sulfide–Oleic Acid Colloidal Quantum Dots Revealed by Small-Angle Scattering. *J. Phys. Chem. Lett.* **2019**, *10*, 4713–4719.

(65) Lee, B.; Littrell, K.; Sha, Y.; Shevchenko, E. V. Revealing the Effects of the Non-Solvent on the Ligand Shell of Nanoparticles and Their Crystallization. *J. Am. Chem. Soc.* **2019**, *141*, 16651–16662.

(66) Holder, C. F.; Schaak, R. E. Tutorial on Powder X-Ray Diffraction for Characterizing Nanoscale Materials. *ACS Nano* **2019**, *13*, 7359–7365.

(67) Rao, C. N. R.; Biswas, K. Characterization of Nanomaterials by Physical Methods. *Annu. Rev. Anal. Chem.* **2009**, *2*, 435–462.

(68) Li, T.; Senesi, A. J.; Lee, B. Small Angle X-Ray Scattering for Nanoparticle Research. *Chem. Rev.* **2016**, *116*, 11128–11180.

(69) Boldt, K.; Bartlett, S.; Kirkwood, N.; Johannessen, B. Quantification of Material Gradients in Core/Shell Nanocrystals Using EXAFS Spectroscopy. *Nano Lett.* **2020**, *20*, 1009–1017.

(70) Pejova, B.; Sherif, E.; Minde, M. W. Sonochemically Synthesized Quantum Nanocrystals of Cubic CuInS2 : Evidence for Multifractal Surface Morphology, Size-Dependent Structure, and Particle Size Distribution. *J. Phys. Chem. C* **2020**, *124*, 20240–20255.

(71) Hollamby, M. J. Practical Applications of Small-Angle Neutron Scattering. *Phys. Chem. Chem. Phys.* **2013**, *15*, 10566.

(72) Winslow, S. W.; Liu, Y.; Swan, J. W.; Tisdale, W. A. Quantification of a PbCl x Shell on the Surface of PbS Nanocrystals. *ACS Mater. Lett.* **2019**, *1*, 209–216.

(73) Winslow, S. W.; Shcherbakov-Wu, W.; Liu, Y.; Tisdale, W. A.; Swan, J. W. Characterization of Colloidal Nanocrystal Surface Structure Using Small Angle Neutron Scattering and Efficient Bayesian Parameter Estimation. *J. Chem. Phys.* **2019**, *150*, 244702.

(74) Ondry, J. C.; Philbin, J. P.; Lostica, M.; Rabani, E.; Alivisatos, A. P. Resilient Pathways to Atomic Attachment of Quantum Dot Dimers and Artificial Solids from Faceted CdSe Quantum Dot Building Blocks. *ACS Nano* **2019**, *13*, 12322–12344.

(75) Hartley, C. L.; Dempsey, J. L. Electron-Promoted X-Type Ligand Displacement at CdSe Quantum Dot Surfaces. *Nano Lett.* **2019**, *19*, 1151–1157.

(76) Kirkwood, N.; Monchen, J. O. V.; Crisp, R. W.; Grimaldi, G.; Bergstein, H. A. C.; du Fossé, I.; van der Stam, W.; Infante, I.; Houtepen, A. J. Finding and Fixing Traps in II–VI and III–V Colloidal Quantum Dots: The Importance of Z-Type Ligand Passivation. *J. Am. Chem. Soc.* **2018**, *140*, 15712–15723.

(77) Stein, J. L.; Mader, E. A.; Cossairt, B. M. Luminescent InP Quantum Dots with Tunable Emission by Post-Synthetic Modification with Lewis Acids. *J. Phys. Chem. Lett.* **2016**, *7*, 1315–1320.

(78) Morrison, C.; Sun, H.; Yao, Y.; Loomis, R. A.; Buhro, W. E. Methods for the ICP-OES Analysis of Semiconductor Materials. *Chem. Mater.* **2020**, *32*, 1760–1768.

(79) Kirkwood, N.; De Backer, A.; Altantzis, T.; Winckelmans, N.; Longo, A.; Antolinez, F. V.; Rabouw, F. T.; De Trizio, L.; Geuchies, J. J.; Mulder, J. T.; et al. Locating and Controlling the Zn Content in In(Zn)P Quantum Dots. *Chem. Mater.* **2020**, *32*, 557–565.

(80) Zherebetskyy, D.; Scheele, M.; Zhang, Y.; Bronstein, N.; Thompson, C.; Britt, D.; Salmeron, M.; Alivisatos, P.; Wang, L. Hydroxylation of the Surface of PbS Nanocrystals Passivated with Oleic Acid. *Science* **2014**, *344*, 1380–1384.

(81) De Nolf, K.; Cosseddu, S. M.; Jasieniak, J. J.; Drijvers, E.; Martins, J. C.; Infante, I.; Hens, Z. Binding and Packing in Two-Component Colloidal Quantum Dot Ligand Shells: Linear versus Branched Carboxylates. *J. Am. Chem. Soc.* **2017**, *139*, 3456–3464.

(82) Singh, S.; Tomar, R.; ten Brinck, S.; De Roo, J.; Geiregat, P.; Martins, J. C.; Infante, I.; Hens, Z. Colloidal CdSe Nanoplatelets, A Model for Surface Chemistry/Optoelectronic Property Relations in Semiconductor Nanocrystals. *J. Am. Chem. Soc.* **2018**, *140*, 13292–13300.

(83) Voznyy, O.; Thon, S. M.; Ip, A. H.; Sargent, E. H. Dynamic Trap Formation and Elimination in Colloidal Quantum Dots. *J. Phys. Chem. Lett.* **2013**, *4*, 987–992.

(84) Zhao, Q.; Kulik, H. J. Electronic Structure Origins of Surface-Dependent Growth in III–V Quantum Dots. *Chem. Mater.* **2018**, *30*, 7154–7165.

(85) Giansante, C.; Infante, I. Surface Traps in Colloidal Quantum Dots: A Combined Experimental and Theoretical Perspective. *J. Phys. Chem. Lett.* **2017**, 5209–5215.

(86) Houtepen, A. J.; Hens, Z.; Owen, J. S.; Infante, I. On the Origin of Surface Traps in Colloidal II–VI Semiconductor Nanocrystals. *Chem. Mater.* **2017**, *29*, 752–761.

(87) Dang, Z.; Shamsi, J.; Palazon, F.; Imran, M.; Akkerman, Q. A.; Park, S.; Bertoni, G.; Prato, M.; Brescia, R.; Manna, L. In Situ Transmission Electron Microscopy Study of Electron Beam-Induced Transformations in Colloidal Cesium Lead Halide Perovskite Nanocrystals. *ACS Nano* **2017**, *11*, 2124–2132.

(88) van der Stam, W.; de Graaf, M.; Gudjonsdottir, S.; Geuchies, J. J.; Dijkema, J. J.; Kirkwood, N.; Evers, W. H.; Longo, A.; Houtepen, A. J. Tuning and Probing the Distribution of Cu + and Cu 2+ Trap States Responsible for Broad-Band Photoluminescence in CuInS 2 Nanocrystals. *ACS Nano* **2018**, *12*, 11244–11253.

(89) Brown, P. R.; Kim, D.; Lunt, R. R.; Zhao, N.; Bawendi, M. G.; Grossman, J. C.; Bulović, V. Energy Level Modification in Lead Sulfide Quantum Dot Thin Films through Ligand Exchange. *ACS Nano* **2014**, *8*, 5863–5872.

(90) Volk, S.; Yazdani, N.; Wood, V. Manipulating Electronic Structure from the Bottom-Up: Colloidal Nanocrystal-Based Semiconductors. *J. Phys. Chem. Lett.* **2020**, *11*, 9255–9264.

(91) Sarma, D. D.; Santra, P. K.; Mukherjee, S.; Nag, A. X-Ray Photoelectron Spectroscopy: A Unique Tool To Determine the Internal Heterostructure of Nanoparticles. *Chem. Mater.* **2013**, *25*, 1222–1232.

(92) Stevie, F. A.; Donley, C. L. Introduction to X-Ray Photoelectron Spectroscopy. *J. Vac. Sci. Technol. A* **2020**, *38*, 063204.

(93) Kroupa, D. M.; Vörös, M.; Brawand, N. P.; Bronstein, N.; McNichols, B. W.; Castaneda, C. V; Nozik, A. J.; Sellinger, A.; Galli, G.; Beard, M. C. Optical Absorbance Enhancement in PbS QD/Cinnamate Ligand Complexes. *J. Phys. Chem. Lett.* **2018**, *9*, 3425–3433.

(94) Giansante, C.; Infante, I.; Fabiano, E.; Grisorio, R.; Suranna, G. P.; Gigli, G. "Darker-than-Black" PbS Quantum Dots: Enhancing Optical Absorption of Colloidal Semiconductor Nanocrystals via Short Conjugated Ligands. *J. Am. Chem. Soc.* **2015**, *137*, 1875–1886.

(95) Frederick, M. T.; Weiss, E. a. Relaxation of Exciton Confinement in CdSe Quantum Dots by Modification with a Conjugated Dithiocarbamate Ligand. *ACS Nano* **2010**, *4*, 3195–3200.

(96) Shim, M.; Guyot-Sionnest, P. N-Type Colloidal Semiconductor Nanocrystals. *Nature* **2000**, *407*, 981–983.

(97) Houtepen, A. J.; Vanmaekelbergh, D. Orbital Occupation in Electron-Charged CdSe Quantum-Dot Solids. *J. Phys. Chem. B* **2005**, *109*, 19634–19642.

(98) Tariq, M.; Koch, M. D.; Andrews, J. W.; Knowles, K. E. Correlation between Surface Chemistry and Optical Properties in Colloidal Cu2O Nanoparticles. *J. Phys. Chem. C* **2020**, *124*, 4810–4819.

(99) Knowles, K. E.; Malicki, M.; Parameswaran, R.; Cass, L. C.; Weiss, E. A. Spontaneous Multielectron Transfer from the Surfaces of PbS Quantum Dots to Tetracyanoquinodimethane. *J. Am. Chem. Soc.* **2013**, *135*, 7264–7271.

(100) Hughes, K. E.; Stein, J. L.; Friedfeld, M. R.; Cossairt, B. M.; Gamelin, D. R. Effects of Surface Chemistry on the Photophysics of Colloidal InP Nanocrystals. *ACS Nano* **2019**, *13*, 14198–14207.

(101) Hunsche, S.; Dekorsy, T.; Klimov, V.; Kurz, H. Ultrafast Dynamics of Carrier-Induced Absorption Changes in Highly-Excited CdSe Nanocrystals. *Appl. Phys. B Lasers Opt.* **1996**, *62*, 3–10.

(102) Veamatahau, A.; Jiang, B.; Seifert, T.; Makuta, S.; Latham, K.; Kanehara, M.; Teranishi, T.; Tachibana, Y. Origin of Surface Trap States in CdS Quantum Dots: Relationship between Size Dependent Photoluminescence and Sulfur Vacancy Trap States. *Phys. Chem. Chem. Phys.* **2015**, *17*, 2850–2858.

(103) Karan, S.; Majumder, M.; Mallik, B. Controlled Surface Trap State Photoluminescence from CdS QDs Impregnated in Poly(Methyl Methacrylate). *Photochem. Photobiol. Sci.* **2012**, *11*, 1220.

(104) Palato, S.; Seiler, H.; McGovern, L.; Mack, T. G.; Jethi, L.; Kambhampati, P. Electron Dynamics at the Surface of Semiconductor Nanocrystals. *J. Phys. Chem. C* **2017**, *121*, 26519–26527.

(105) Amelia, M.; Lincheneau, C.; Silvi, S.; Credi, A. Electrochemical Properties of CdSe and CdTe Quantum Dots. *Chem. Soc. Rev.* **2012**, *41*, 5728.

(106) Guyot-Sionnest, P. Charging Colloidal Quantum Dots by Electrochemistry. *Microchim. Acta* **2008**, *160*, 309–314.

(107) Fedin, I.; Talapin, D. V. Probing the Surface of Colloidal Nanomaterials with Potentiometry in Situ. *J. Am. Chem. Soc.* **2014**, *136*, 11228–11231.

(108) van der Stam, W.; du Fossé, I.; Grimaldi, G.; Monchen, J. O. V; Kirkwood, N.; Houtepen, A. J. Spectroelectrochemical Signatures of Surface Trap Passivation on CdTe Nanocrystals. *Chem. Mater.* **2018**, *30*, 8052–8061.

(109) Gudjonsdottir, S.; Van Der Stam, W.; Kirkwood, N.; Evers, W. H.; Houtepen, A. J. The Role of Dopant Ions on Charge Injection and Transport in Electrochemically Doped Quantum Dot Films. *J. Am. Chem. Soc.* **2018**, *140*, 6582–6590.

(110) Chen, M.; Guyot-Sionnest, P. Reversible Electrochemistry of Mercury Chalcogenide Colloidal Quantum Dot Films. *ACS Nano* **2017**, *11*, 4165–4173.

(111) Brozek, C. K.; Hartstein, K. H.; Gamelin, D. R. Potentiometric Titrations for Measuring the Capacitance of Colloidal Photodoped ZnO Nanocrystals. *J. Am. Chem. Soc.* **2016**, *138*, 10605–10610.

(112) Carroll, G. M.; Brozek, C. K.; Hartstein, K. H.; Tsui, E. Y.; Gamelin, D. R. Potentiometric Measurements of Semiconductor Nanocrystal Redox Potentials. *J. Am. Chem. Soc.* **2016**, *138*, 4310–4313.

(113) Kroupa, D. M.; Anderson, N. C.; Castaneda, C. V.; Nozik, A. J.; Beard, M. C. In Situ Spectroscopic Characterization of a Solution-Phase X-Type Ligand Exchange at Colloidal Lead Sulphide Quantum Dot Surfaces. *Chem. Commun.* **2016**, *52*, 13893–13896.

(114) Anderson, N. C.; Hendricks, M. P.; Choi, J. J.; Owen, J. S. Ligand Exchange and the Stoichiometry of Metal Chalcogenide Nanocrystals: Spectroscopic Observation of Facile Metal-Carboxylate Displacement and Binding. *J. Am. Chem. Soc.* **2013**, *135*, 18536–18548.

(115) Busby, E.; Anderson, N. C.; Owen, J. S.; Sfeir, M. Y. Effect of Surface Stoichiometry on Blinking and Hole Trapping Dynamics in CdSe Nanocrystals. *J. Phys. Chem. C* **2015**, *119*, 27797–27803.

(116) Kirkwood, N.; Monchen, J. O. V.; Crisp, R. W.; Grimaldi, G.; Bergstein, H. A. C.; Du Fossé, I.; Van Der Stam, W.; Infante, I.; Houtepen, A. J. Finding and Fixing Traps in II-VI and III-V Colloidal Quantum Dots: The Importance of Z-Type Ligand Passivation. *J. Am. Chem. Soc.* **2018**, *140*, 15712–15723.

(117) Boehme, S. C.; Azpiroz, J. M.; Aulin, Y. V.; Grozema, F. C.; Vanmaekelbergh, D.; Siebbeles, L. D. A.; Infante, I.; Houtepen, A. J. Density of Trap States and Auger-Mediated Electron Trapping in CdTe Quantum-Dot Solids. *Nano Lett.* **2015**, *15*, 3056–3066.

(118) Beygi, H.; Sajjadi, S. A.; Babakhani, A.; Young, J. F.; van Veggel, F. C. J. M. Surface Chemistry of As-Synthesized and Air-Oxidized PbS Quantum Dots. *Appl. Surf. Sci.* **2018**, *457*, 1–10.

(119) Voznyy, O. Mobile Surface Traps in CdSe Nanocrystals with Carboxylic Acid Ligands. *J. Phys. Chem. C* **2011**, *115*, 15927–15932.

(120) Friedfeld, M. R.; Stein, J. L.; Ritchhart, A.; Cossairt, B. M. Conversion Reactions of Atomically Precise Semiconductor Clusters. *Acc. Chem. Res.* **2018**, *51*, 2803–2810.

(121) Hens, Z.; De Roo, J. Atomically Precise Nanocrystals. *J. Am. Chem. Soc.* **2020**, *142*, 15627–15637.

(122) Xu, Y.; Wang, H.; Yu, Y.; Tian, L.; Zhao, W.; Zhang, B. Cu 2 O Nanocrystals: Surfactant-Free Room-Temperature Morphology-Modulated Synthesis and Shape-Dependent Heterogeneous Organic Catalytic Activities. *J. Phys. Chem. C* **2011**, *115*, 15288–15296.

(123) Huang, W.-C.; Lyu, L.-M.; Yang, Y.-C.; Huang, M. H. Synthesis of Cu 2 O Nanocrystals from Cubic to Rhombic Dodecahedral Structures and Their Comparative Photocatalytic Activity. *J. Am. Chem. Soc.* **2012**, *134*, 1261–1267.

CHAPTER 2 : ELECTRON-PROMOTED X-TYPE LIGAND DISPLACEMENT AT CDSE QUANTUM DOT SURFACES

This chapter was adapted with permission from Hartley, C.L.; Dempsey, J.L. Electron-Promoted X-Type Ligand Displacement at CdSe Quantum Dot Surfaces. *Nano Lett.* **2019**, *19*, 1151 – 1157.

2.1 Introduction

Semiconductor nanocrystals that are quantum confined in all three dimensions, commonly called quantum dots (QDs), have gained popularity in recent years for applications in optoelectronic devices ranging from next generation solar cells to light-emitting diodes and lasers.[1–4] The appeal lies in their strong absorption and emission features, the ease of solution processability, and the tunability of their properties through nanocrystal size, semiconductor material, and surface-capping ligands.[1,5,6] The tunable nature of these nanomaterials can be further extended through addition of excess charge carriers (doping).[1,2,6–8] A precise control of QD doping is pivotal in the development of technologies that operate through an electronic gradient using p- and n-type nanocrystals, as well as enhancing charge carrier transport in those materials.[2,7,9]

Over the last several decades, four primary methods of QD doping have been established: *defect doping* by addition of impurity heteroatoms into the nanocrystal lattice analogous to bulk semiconductor doping; *electrochemical doping* by an applied potential to QD films or colloidal solutions; *photodoping* via photoinduced exciton formation followed by valence band hole filling by donor molecules; and *remote chemical doping*, achieved by use of a chemical reductant capable of reducing band edge states through outer-sphere electron transfer.[1,2,7,9–15,16,17] Of these methods, remote chemical doping provides a direct chemical means of systematically studying stoichiometric QD charging.

Guyot-Sionnest and coworkers first reported n-type doping of CdSe QDs by addition of excess sodium biphenyl.[2] Since this report in 2000, remote chemical doping has expanded in scope with a wide

range of reductants reported to dope a variety of QD materials.[1,2,10,12,16] In all published systems, a significant excess of reductant is required in order to observe delocalized charge carriers.[1,6,11,14,16,19,20] To rationalize this, the QD surface is often invoked as a reservoir for excess carriers that localize in surface-based electron and hole trap states (Scheme 2.1).[2,10,20] Reduction of localized surface states is supported by a host of experimental evidence including the growth of new absorbance features attributable to filled trap states,[2,8,10] detection of oxidized reagents by a dark reduction of Se moieties prior to CdSe photodoping,[17,20] as well as the appearance of localized surface plasmon resonances in doped QDs.[21,22] The exact nature of these mid-gap states that act as charge carrier reservoirs is rarely well-defined, though several redox-active surface species on CdSe QDs have been identified. For example, reduction of Cd^{2+} ions to Cd^0 has been observed in systems for photocatalysis employing Cd-based QDs.[20,23] Additionally, oxidized Se^{1-} defects that may be dimerized (i.e. diselenides) are known to occur on CdSe surfaces and their reduction to Se^{2-} by molecular reductants has been reported.[17,20,24,25]

Scheme 2.1 Conventional interpretation of the role of surface trap states as reservoirs for excess electrons.[a]

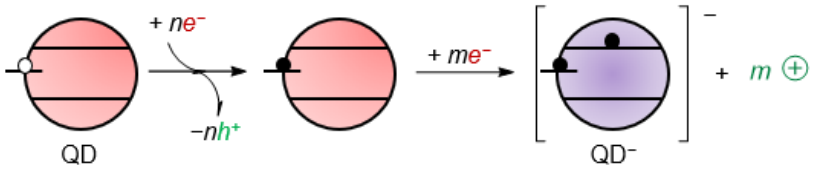

a. The atomic nature of mid-gap trap states is often not clearly defined, but generally a certain number of electron-deficient mid-gap states may accept *n* electrons. Typically, a different additional number of electrons (*m*) is then needed to reduce band edge states.

While the addition of electrons to QDs is known to lead to surface localization of these charge carriers, the resulting changes in surface composition are not well understood. To address this, we present a case study probing changes in surface coordination chemistry upon doping oleate-capped CdSe QDs with a strong one-electron reductant, sodium naphthalenide ($Na[C_{10}H_8]$) ($E^{\circ\prime} = -3.1$ V vs. $Fc^{+/0}$ in THF).[26] UV-Vis absorption, ^{1}H NMR, and FTIR spectroscopies are utilized to reconcile changes in the QD optical properties upon n-type doping with a measurable decrease in surface ligand coverage. Our studies reveal a

mechanism in which QD reduction proceeds through surface Cd^{2+} and Se^{1-} ions, as has been invoked previously.[2,10,20] However, we show that in order to maintain a charge-balanced surface, reduction is coupled with dissociation of a portion of anionic oleate ligands when electrons localize on surface Cd^{2+} ions. Though the importance of surface chemistry in impacting electronic structure has been highlighted in recent years,[6,24,27–31] this work is the first example we are aware of that experimentally probes changes in the ligand shell of semiconductor QDs upon remote chemical doping.

2.2 Results and Discussion

Oleate-capped CdSe QDs of 3.4 nm diameter were synthesized and purified according to a modified literature procedure;[32] the average ligand packing density of as-prepared nanocrystals is approximately 3.4 oleates/nm^2. To systematically study the mechanism of remote chemical doping, aliquots of $Na[C_{10}H_8]$ (0–100 equivalents/QD) were added to samples of QDs in THF (Figure 2.1a). Upon n-type doping, QDs are typically characterized by changes in their absorbance profile. Injection of electrons into the lowest energy CB state ($1S_e$) results in an absorbance bleach and slight red shift of the excitonic feature.[2,10,11,14] A low-energy tail is also often visible upon QD reduction and may be attributed to formation of Cd^0 sites,[33–36] or alternatively excitation of electrons in optically-active mid-gap surface states.[2,10] This diagnostic absorbance feature has been observed in other remote chemical doping studies as well as photocatalysis experiments with both CdS and CdSe QDs in which Cd^0 formation is postulated to be a key initial step for catalysis on QD surfaces.[2,10,34–36] From the bleach magnitude, the average number of CB electrons $\langle n \rangle$ is estimated using the method of Guyot-Sionnest (Figure 2.2).[10]

Estimated values of $\langle n \rangle$ as a function of reductant shows $\langle n \rangle$ plateaus around 1–2 CB electrons (Figure 2.1b). Similar to previously reported systems, there is little or no excitonic bleach with less than ~10 equivalents of reductant.[2,10,17,20,37] This suggests that initial reducing equivalents localize in optically silent surface states, though UV-Vis absorption spectroscopy alone cannot distinguish between states with Cd^{2+} or Se^{1-} character. With higher equivalents ($\geq$ 20 equiv.), there is a significant bleach of the excitonic feature as well as growth of a lower-energy tail. Because this tail feature is not observed until

there is a significant bleach of the excitonic absorbance as well as previous reports of Cd^0 formation by CB electrons,[33,34] we hypothesize that the optically active reduced surface states may be in exchange with CB electrons.

To investigate the reversibility of reduction by $Na[C_{10}H_8]$, the mild oxidant ferrocenium tetrakis[3,5-bis(trifluoromethyl)phenyl]borate ($[Fc][BAr^F{}_4]$) ($E^{\circ\prime}$= 0.0 V vs. $Fc^{+/0}$) was titrated into samples of doped QDs (QD^-) (Figure 2.1c). Addition of ~2–3 equivalents of $[Fc][BAr^F{}_4]$ results in complete restoration of the $1S_e$ feature while the lower-energy tail remains. This is in close agreement with the estimated $\langle n \rangle$ = 1–2 electrons at the end of the reductive titration. Upon further addition of $[Fc][BAr^F{}_4]$ (and only after the excitonic feature has been fully restored), the lower-energy tail returns to baseline, supporting assignment of this feature to electrons in surface-localized trap states that may be oxidized.

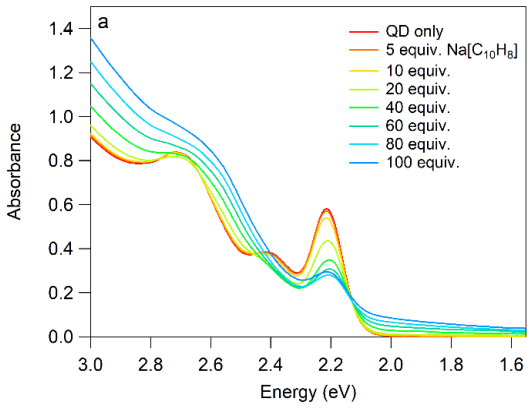

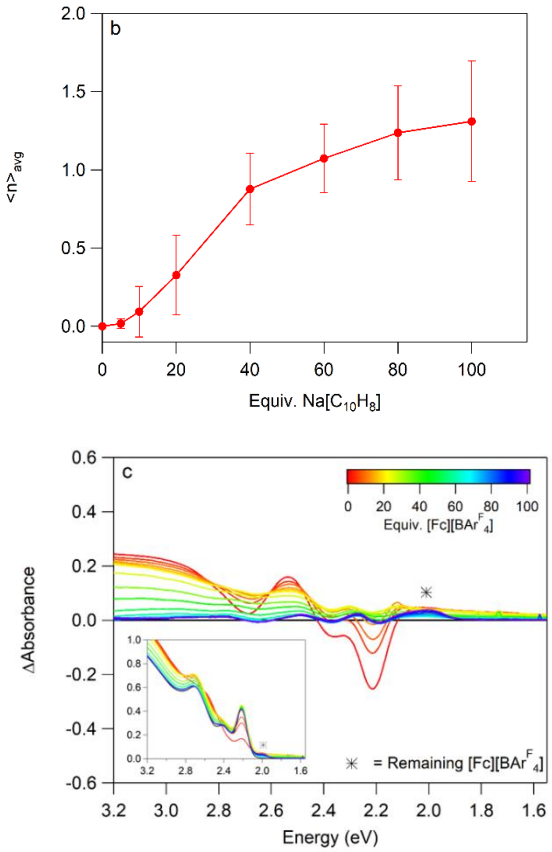

Figure 2.1 (a) UV-Vis absorption titration of 3.4 nm CdSe QDs in THF (~2.8 µM) with addition of 0–100 equiv./QD of $Na[C_{10}H_8]$; (b) Average number of estimated CB electrons, $\langle \boldsymbol{n} \rangle$ with addition of reductant; (c) Difference in absorbance ($A - A_0$) with 100 equiv. $Na[C_{10}H_8]$ and re-oxidation of QDs by $[Fc][BAr^F{}_4]$ with absorbance spectra shown as inset.

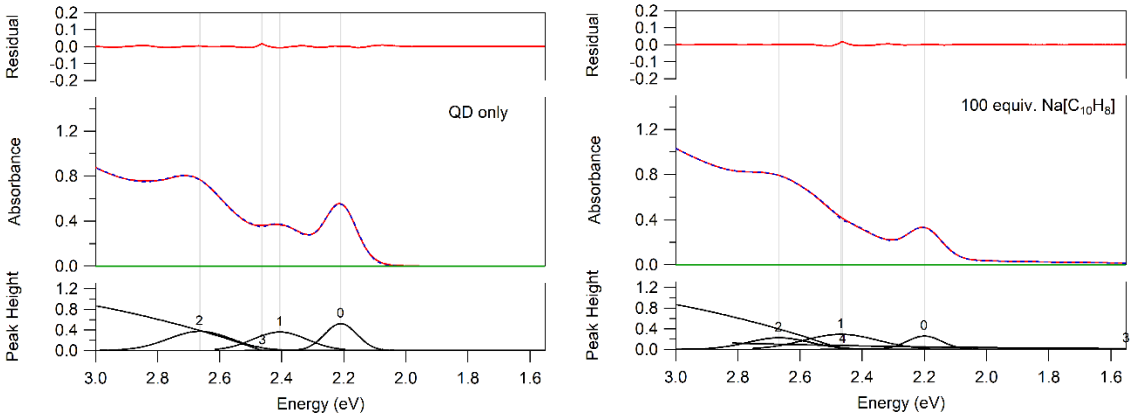

Figure 2.2 Example spectra of UV-Vis absorbance features fit via the method of Shim et al. to estimate number of CB electrons showing the original trace (red) and fit trace (dotted blue line) with the residual from the fit (top).[2] Note that the fitted curve labeled as trace 3 in the QD only spectrum is labeled as trace 4 in the 100 equiv. $Na[C_{10}H_8]$ spectrum.

Interestingly, re-oxidation of QD^- requires fewer equivalents of $[Fc][BAr^F{}_4]$ to recover the original QD-only absorbance trace than equivalents of reductant added. As shown in Figure 2.1c for a sample of QD^- reduced with 100 equiv. $Na[C_{10}H_8]$, only ~50 equiv. $[Fc][BAr^F{}_4]$ were titrated in before both the excitonic absorbance recovered and the visible tail diminished to baseline. Further addition of oxidant (up to ~100 equiv.) led to growth of a $[Fc][BAr^F{}_4]$ absorbance feature at ~2.0 eV, indicating further equivalents of $[Fc]^+$ are unreactive. Reversibility studies thereby provide a method of confirming the estimated number of CB electrons by spectral fitting (1–2) as well as the number of electrons that are localized on oxidizable surface states that are quantifiable by optical handles (~48–49). The discrepancy in equivalents of oxidant needed to recover the original trace versus reductant added suggests that a portion of excess $Na[C_{10}H_8]$ irreversibly reduces a population of surface atoms (or these species are unable to be oxidized with $[Fc][BAr^F{}_4]$). These irreversibly reduced species lack distinct spectral handles, suggestive of oxidized Se-based dimers that could, upon reduction, rearrange on the surface.[20,24] Both oxidized diselenides and reduced Se^{2-} species are optically silent and therefore cannot be directly detected in these experiments.[20,24] Finally, we note that on the minutes-long timescale of these experiments, there is evidence of slow trapping of CB electrons at the surface, consistent with previous reports (Figure 2.3).[17] This background effect would result in an increasing number of reduced surface atoms over the course of the titration.[17,20]

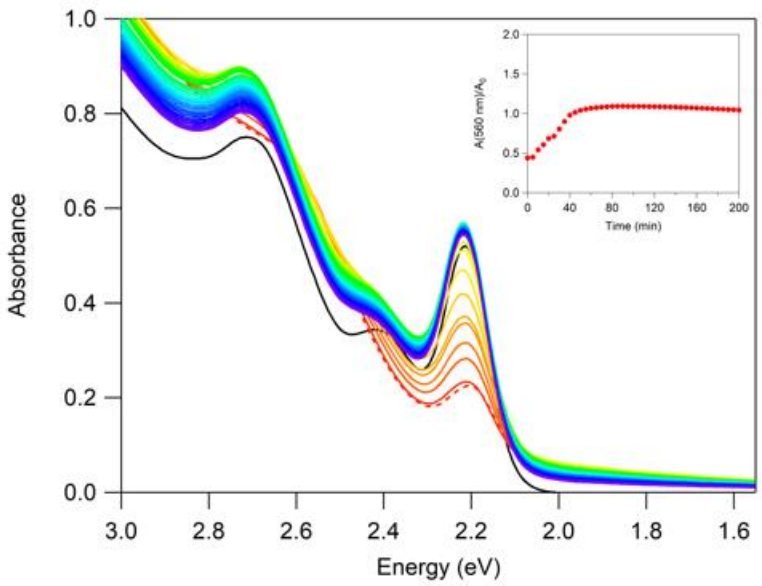

Figure 2.3 Sample of 2.6 µM 3.4 nm CdSe QDs in THF alone (black trace) and then with 100 equiv. $Na[C_{10}H_8]$ (dashed red line) under N_2 atmosphere. Over the course of minutes (see inset), recovery of the excitonic feature is observed, consistent with surface trapping of CB electrons proposed by Tsui et al.[20] This trapping of CB electrons over the course of minutes likely contributes to the larger error bars observed towards the end of reductive UV-Vis spectroscopy titrations (as in Figure 2.1b) with increasing equivalents of $Na[C_{10}H_8]$ added. At later time points, rearrangement of reduced surface species or trace impurities may result in oxidation of surface states and return of the low energy tail to baseline, as proposed by Shim et al.[2]

Collectively, the systematic titration studies by UV-Vis absorption spectroscopy provide an important starting point for understanding the mechanism of QD doping by chemical reductants. Consistent with previously reported works, the first 5–10 electrons added per QD are not directly injected into the $1S_e$ state, as evidenced by lack of an excitonic bleach; we argue that these initial equivalents reduce surface Cd^{2+} and Se^{1-} ions. With further equivalents of reductant added, a bleach is observed suggesting that following surface charging, the CB is populated. This bleach is observed in tandem with growth of a low energy tail, hinting at a thermal equilibrium between optically active mid-gap surface trap states with CB electrons. Finally, reversibility studies offer compelling evidence for oxidation of both the CB and a subpopulation of reduced surface states. Consistent with previous observations, these studies suggest that when the doped QD^- is oxidized, electrons are removed first from the CB, followed by the surface.[10] It is important to note that while a subpopulation of reduced surface states is oxidized, a

portion of the added electrons remain in surface moieties that cannot be oxidized by [Fc][BAr^F_4], perhaps due to surface atom rearrangement. While absorption studies allow for the quantification of CB and some surface-based electrons, this technique is limited as it cannot probe the nature of reduced surface species.

To directly probe changes in surface composition with doping, complementary titrations were performed via ^{1}H NMR spectroscopy. Changes in QD ligand coverage were monitored by using the oleate alkene resonance as a handle for differentiating between surface-bound ligands (δ 5.37) versus those free in solution (δ 5.33). The resonances corresponding to bound ligands are considerably broadened compared with the sharp resonances of free molecules, enabling distinct quantification of the bound and free species (Figure 2.5).[31,32,38] NMR spectra of the as-prepared QDs in THF-d_8 show ~2% free ligand relative to the bound oleate signal. Upon addition of Na[$C_{10}H_8$], the ratio of free to bound ligands increases with up to ~20 equivalents of reductant (Figure 2.4). After the addition of ~40 equivalents of Na[$C_{10}H_8$], free ligand signals are lost (Figure 2.4). We speculate that this is due to a side reaction between excess Na[$C_{10}H_8$] and liberated oleate ligands (Figure 2.6). The consumption of some reductant from interaction with dissociated oleate ligands at high equivalents may account partially for the excess of Na[$C_{10}H_8$] required to observe saturation of CB electrons. At the high sample concentrations needed for NMR measurements, further aliquots of Na[$C_{10}H_8$] added at long sample intervals (hours) result in precipitation of a dark red solid concurrent with loss of the bound oleate resonances. This observation highlights the instability of the reduced QD species over the course of hours. However, precipitation of QDs is not observed in UV-Vis titration experiments run over the course of minutes and at lower concentrations.

Concurrent with the increase in free oleate signal, resonances corresponding to naphthalene grow in at 7.83 and 7.44 ppm. The resonances are sharp, indicating that naphthalene does not adsorb to the nanocrystal surface nor associate with tightly bound ligands. Though the naphthalene resonances provide a convenient means of confirming consumption of the paramagnetic reductant, the long T1 relaxation time needed for absolute quantification of those protons requires very long d1 delays for use as a quantitative handle in NMR experiments (Figure 2.7). Approximate equivalents of Na[$C_{10}H_8$] added and

the resulting bound-ligand loss in Figure 2.4 show a qualitative progression of ligand loss upon QD doping. Quantitative studies are consistent with these observations (Table 2.1 and Table 2.2).

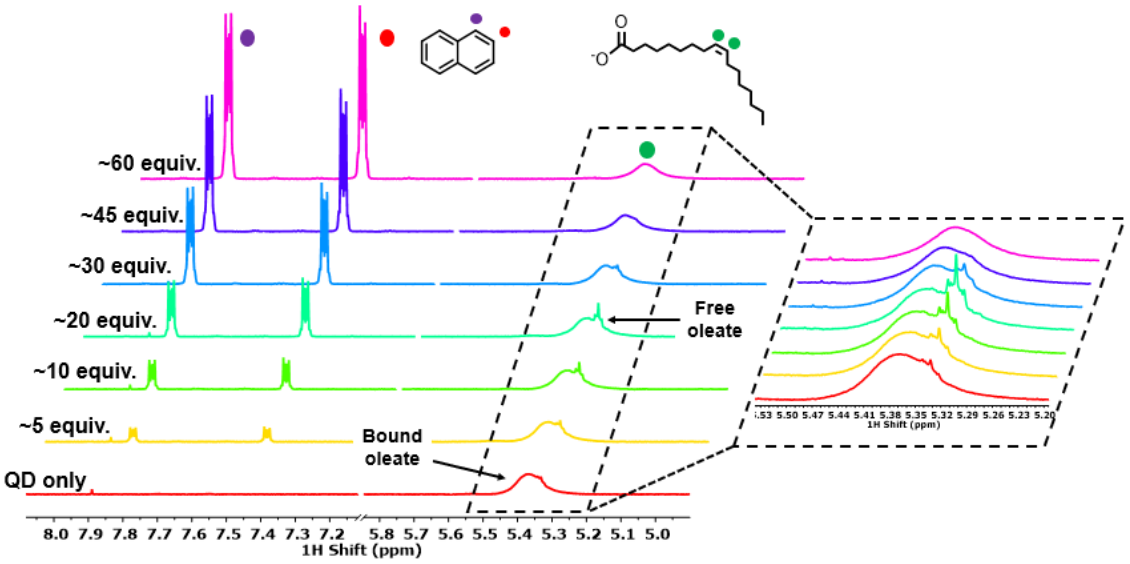

Figure 2.4 ^{1}H NMR titration shows qualitatively the dissociation of oleate ligands from 3.4 nm CdSe QDs (112 µM) in THF-d_8 with addition of Na[$C_{10}H_8$]. At high equivalents of Na[$C_{10}H_8$], loss of the free ligand signal is observed.

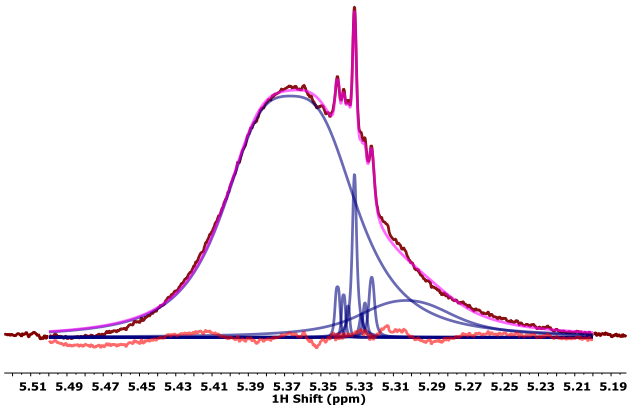

Figure 2.5 Example spectrum of fitting the alkene resonance of the oleate ligands to quantify the number of bound and free ligands with added reductant. The maroon trace is the sample spectrum, the pink trace is the sum of the fits (blue peaks), and the red trace is the fit residual.

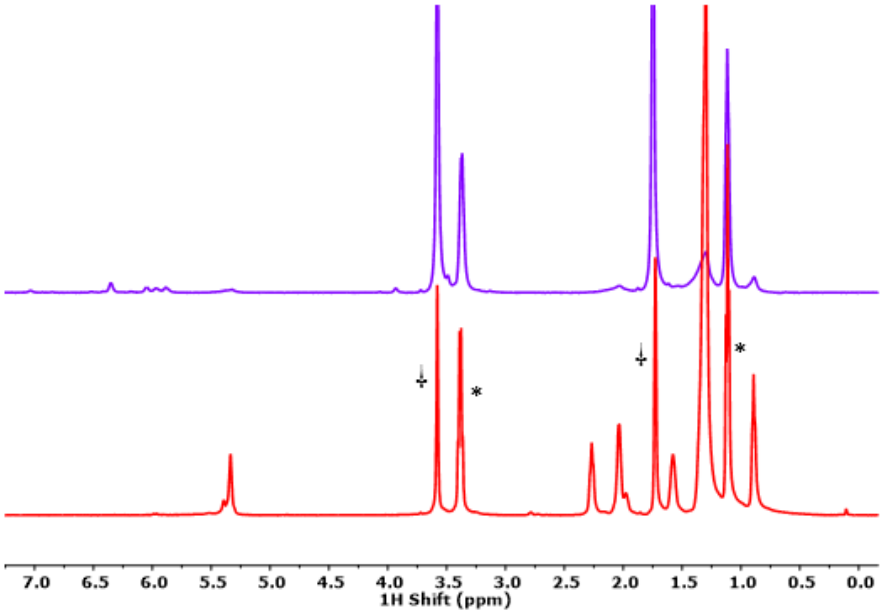

Figure 2.6 ^{1}H NMR spectra of independently synthesized Cd(oleate)$_2$ before (red) and after (purple) addition of an excess of Na[$C_{10}H_8$] in THF-d_8. Upon gradual addition of reductant, a white solid precipitates from solution, and the NMR resonances corresponding to oleate protons are lost. With further addition of reductant, a dark solution with brown precipitate forms. This suggests a side reaction between excess Na[$C_{10}H_8$] and dissociated oleate ligands leading to loss of the free oleate resonances observed at high equivalents of reductant. Solvent residuals are labeled with a ⏚ symbol and diethyl ether peaks labeled with an asterisk (*).

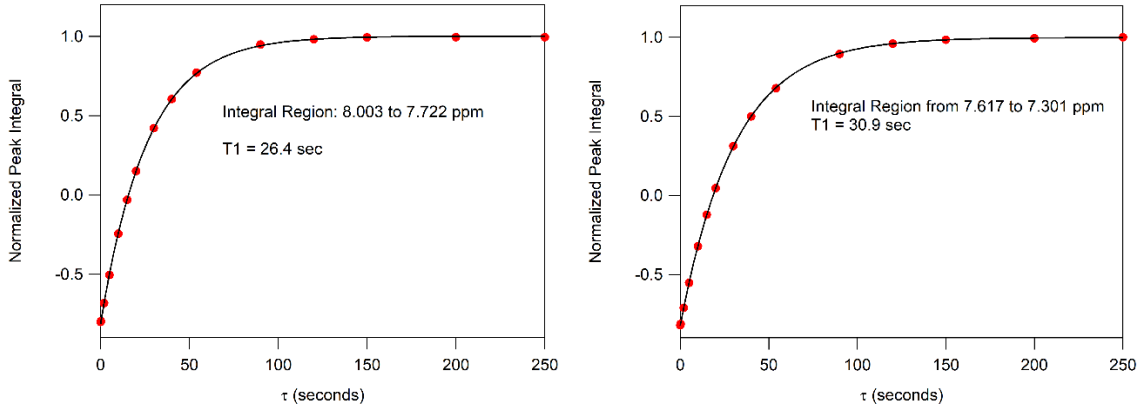

Figure 2.7 Plots of the normalized peak integrals of naphthalene protons versus delay time determined from an inversion recovery experiment of naphthalene in THF-d_8 in the presence of 65 µM 3.4 nm CdSe QDs show very long T1 delay times of naphthalene protons. The experiment was run on a 500 MHz Bruker NMR spectrometer with a calibrated pulse width of 8.7 at delay times of 0.001 seconds up to 250 seconds.

Table 2.1 Quantitative NMR titration performed on a 600 MHz Bruker NMR spectrometer on a solution of 109 µM 3.4 nm CdSe QDs in THF-d_8 with aliquots of Na[$C_{10}H_8$] added using 1,3,5-trimethoxybenzene as an internal standard. A d1 delay time of 155 seconds was used to ensure the complete relaxation of naphthalene protons for accurate quantification.

Equivalents Na[$C_{10}H_8$]	**Bound Ligands (per mole QD)**	**Free Ligands (per mole QD)**	**Total Ligand Count**
QD only*	123	2	125
12.2	121	7	128
18.0	118	8	126
24.1	113	4	117
34.2	98	-	98
59.0	84	-	84

*The QD only NMR trace with no naphthalene present was run using a d1 time of 7.5 seconds.

Table 2.2 Repeated quantitative NMR titration performed on a 600 MHz Bruker NMR spectrometer on a solution of 109 µM 3.4 nm CdSe QDs in THF-d_8 with aliquots of Na[$C_{10}H_8$] added using 1,3,5-trimethoxybenzene as an internal standard. A d1 delay time of 155 seconds was used to ensure the complete relaxation of naphthalene protons for accurate quantification.

Equivalents Na[$C_{10}H_8$]	**Bound Ligands (per mole QD)**	**Free Ligands (per mole QD)**	**Total Ligand Count**
QD only*	125	2	127
12.6	119	8	127
18.4	121	7	128
24.6	120	4	124
36.6	98	-	98
59.9	83	-	83

*The QD only NMR trace with no naphthalene present was run using a d1 time of 7.5 seconds.

Notably, addition of [Fc][BAr^F_4] to samples of QD^- does not result in rebinding of desorbed oleate ligands to the QD surface, suggesting that re-oxidized surface Cd species are charge-balanced by $BAr^F_4{}^-$ anions. This finding stands in contrast with the optical reversibility shown by UV-Vis absorption spectroscopy and emphasizes that changes in QD composition are not fully captured by monitoring optoelectronic changes.

It has been demonstrated that small alkali metal ions can intercalate into nanocrystal lattices and could therefore adversely affect ligand binding.[15,16] To confirm that oleate dissociation was not caused by cation intercalation, studies were conducted monitoring ligand coverage upon addition of Na[BAr^F_4]. ^{1}H NMR spectra showed no significant changes in ligand coverage with the addition of up to 40 equiv. of Na[BAr^F_4], confirming that Na^+ cations alone do not promote ligand dissociation (Figure 2.8).

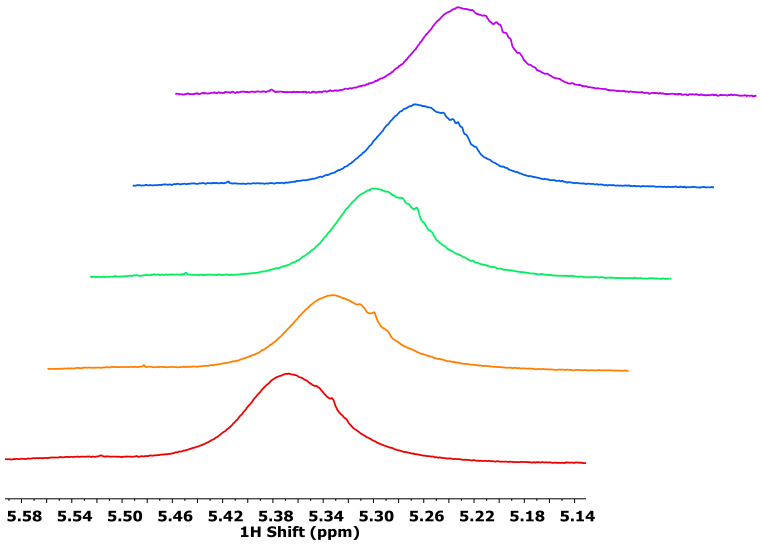

Figure 2.8 ^{1}H NMR spectra of similarly prepared and purified 194 µM 3.1 nm CdSe QDs (red) with addition of 5 equivalents (orange), 10 equivalents (green), 20 equivalents (blue), and 40 equivalents (purple) Na[BAr^F_4] salt in THF-d_8. The spectra do not show evidence of significant ligand loss with addition of Na[BAr^F_4], indicating that ligand loss observed upon addition of Na[$C_{10}H_8$] is not caused primarily by the effects of possible Na^+ intercalation into the nanocrystal lattice. Though this control study was performed on a QD size different from the batch of focus, its results should not be affected by changes in QD reduction potentials with size as it involves no redox reactivity.

Together, NMR studies provide a direct probe of surface chemistry changes upon addition of $Na[C_{10}H_8]$. The observation of dissociated oleate ligands from the QD surface with ≤20 equivalents of reductant indicate conclusively that the first electrons added indeed reduce surface states. We suggest these species are likely Cd^{2+} ions, as it has been established that oleate ligands ligate surface Cd^{2+}.[39–41] The quantified oleate loss therefore serves as a handle for reduction of Cd^{2+} surface moieties. This chapter further shows that ligand loss is a result of surface reduction rather than interaction with Na^+. Finally, oxidation of QD^- by $[Fc][BAr^F{}_4]$ indicates that the changes in ligand coverage caused by reduction of the surface are irreversible (Figure 2.9).

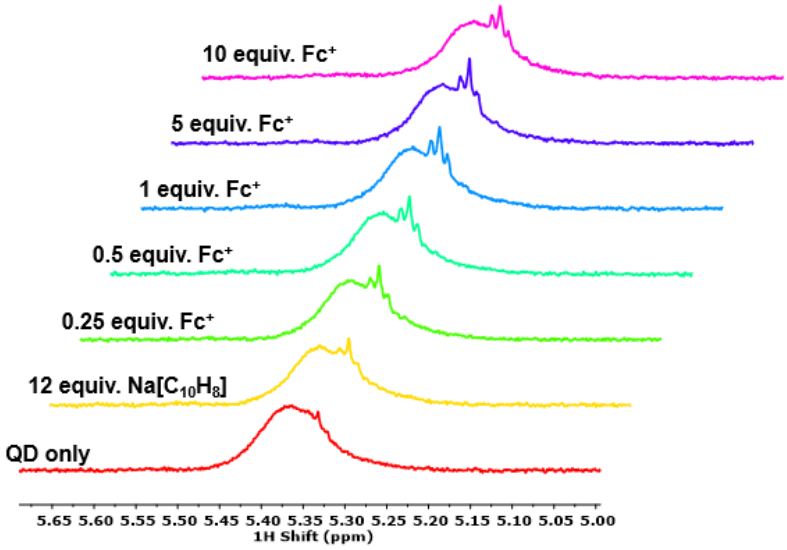

Figure 2.9 ^{1}H NMR spectra of 82 µM 3.4 nm CdSe QDs in THF-d_8 alone (red), with addition of ~12 equivalents of $Na[C_{10}H_8]$ (orange) followed by increasing equivalents of $[Fc][BAr^F{}_4]$ (green to pink traces). Oxidation of the reduced QDs by ferrocenium does not result in re-binding of dissociated oleate ligands.

To gain a more complete picture of surface chemistry changes upon QD doping, the nature of the dissociated oleates was assessed via FTIR. The ligand binding mode of oleate ligands on as-synthesized QDs was determined by taking the difference between the asymmetric and symmetric carboxylate stretching frequencies ($\Delta\nu = \nu_{asymmetric} - \nu_{symmetric}$), as carboxylate binding modes each have characteristic $\Delta\nu$ values.[42] In as-prepared QDs, prominent carboxylate stretches are observed at 1530 cm^{-1} ($\nu_{asymmetric}$), and 1434 cm^{-1} and 1410 cm^{-1} (both potential $\nu_{symmetric}$, yielding $\Delta\nu$ = 96 and 120 cm^{-1}, respectively),

indicating that a major binding mode of oleate ligands is chelating bidentate.[42] Changes in oleate binding modes were monitored with addition of Na[$C_{10}H_8$]. Samples were prepared under an inert atmosphere and oxidized by exposure to air prior to measurement. We note that because of exposure to air, we do not expect electric fields from localized surface electrons to influence the collected spectra. Additionally, consistent with chemical re-oxidation studies by ^{1}H NMR spectroscopy, ligand dissociation is not expected to be reversed by QD^- oxidation in air.

Comparison of the spectra containing added Na[$C_{10}H_8$] with that of QDs alone shows the progressive appearance of new carboxylate stretches at 1560 cm^{-1} and 1426 cm^{-1}. The energy difference between these new stretches ($\Delta\nu$ = 134 cm^{-1}) is characteristic of an ionic carboxylate binding mode, suggestive of the formation of a sodium oleate salt (Na[oleate]) (Figure 2.10).[42] This was confirmed by analysis of independently synthesized Na[oleate], which shows carboxylate stretches within 2 cm^{-1} of these values (Figure 2.11). Comparison to the IR spectrum of $Cd(oleate)_2$ ($\Delta\nu$ = 120 cm^{-1}) rules out the possibility that the free oleate signal in ^{1}H NMR spectra is from loss of Z-type $Cd(oleate)_2$ ligands (Figure 2.11). The observation of Na[oleate] provides further evidence that oleates dissociate as X-type ligands upon addition of reductant. Importantly, these experiments suggest that with QD reduction, anionic ligands necessarily dissociate to maintain a charge-balanced surface.

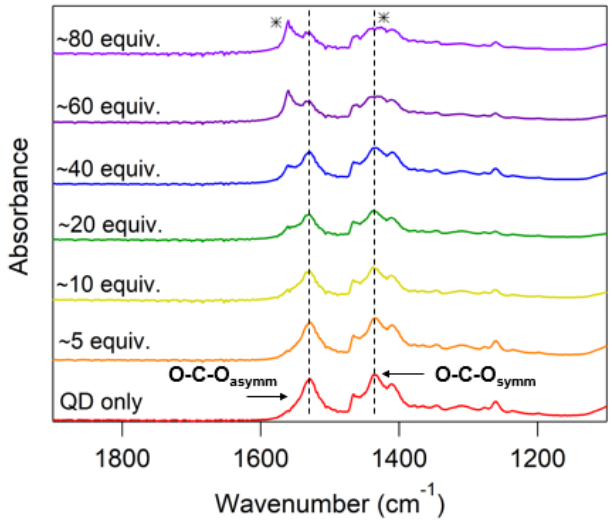

Figure 2.10 FTIR spectra of 3.4 nm CdSe QD with added Na[$C_{10}H_8$] show a corresponding increase in carboxylate stretches at 1560 and 1426 cm^{-1} corresponding to the formation of Na[oleate], indicated by asterisks (*).

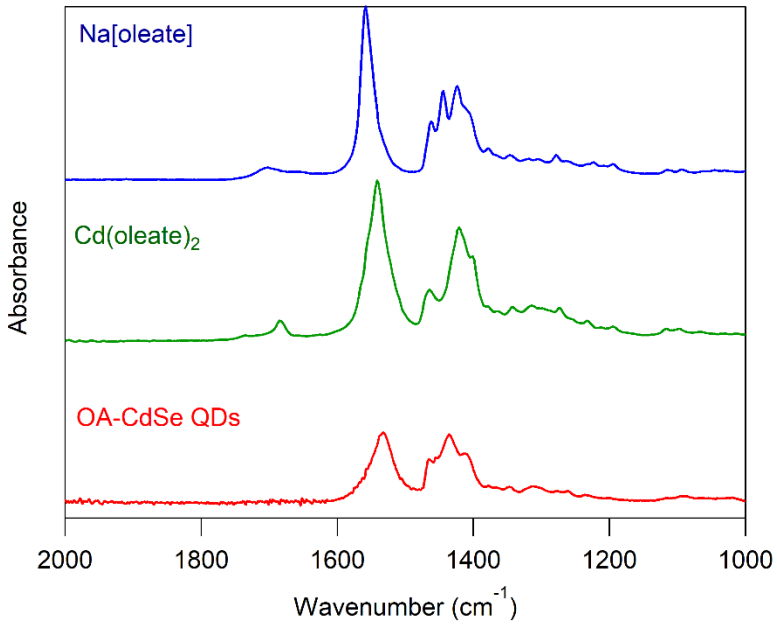

Figure 2.11 ATR-FTIR spectra of independently synthesized $Cd(oleate)_2$ (green) and Na[oleate] (blue) compared with OA-capped CdSe QDs (red). $Cd(oleate)_2$ shows carboxylate stretches at 1542 and 1422 cm^{-1} ($\Delta\nu$= 120 cm^{-1}). Na[oleate] shows prominent carboxylate stretches at 1558 and 1424 cm^{-1} ($\Delta\nu$= 134 cm^{-1}).

Together, UV-Vis absorption, NMR, and FTIR data provide an emerging picture of how QD doping is coupled to changes in surface coordination chemistry—and more broadly, insight into the mechanism of QD doping. Optical studies show that there is minimal evidence of CB electrons until 10–20 equivalents of Na[$C_{10}H_8$] are added. ^{1}H NMR data show that at these lower equivalents, a portion of bound oleate ligands dissociate from the surface in response to added electrons. By FTIR, it is clear that these freed oleates associate with Na^+ ions as Na[oleate]. These methods provide strong complementary evidence for reduction of surface Cd^{2+} with little-to-no filling of the CB with ≤10 equivalents of Na[$C_{10}H_8$]. This mechanism thus suggests charge balance on the surface, in agreement with previous proposals of maintaining overall charge neutrality in metal-rich QDs passivated with X-type ligands.[41,43,44]

Indeed, Valdez et al. recently reported charge-balancing CB electrons in a study of remote chemical doping of ZnO nanocrystals by adding a variety of monatomic and inorganic cations into their doped samples.[16] The authors demonstrated that the reduction of ZnO nanocrystals prepared with trioctylphosphine oxide is roughly stoichiometric with the cations in solution (which are presumed to intercalate into the nanocrystal lattice), and furthermore that the achievable number of CB electrons tracks with cation valency.[16] In the present work, another mechanism of charge balancing doped QDs is revealed through redox reactivity at the surface by anionic ligand loss with added electrons (Scheme 2.2a). We note that because the mechanism presented here is inherently different from that studied by Valdez et al. by using QDs coated in X-type ligands rather than neutral L-type, our studies provide an additional picture of charge balance at QD surfaces.

While it is possible to monitor reduction of surface Cd^{2+} atoms by loss of oleate ligands, there is a discrepancy between the oleates lost per QD and equivalents of reductant added prior to observation of CB electrons (Table 2.1 and Table 2.2). For example, with few equivalents of $Na[C_{10}H_8]$ where CB reduction is not observed, we find by ^{1}H NMR that an average of ~5% of initially bound oleates dissociate, notably less than if all added electrons reduced Cd^{2+} ions bound to oleate ligands. This discrepancy suggests the reduction of surface species that are not detectable by the techniques employed. Notably, underpassivated Cd ions on the QD surface could be reduced without loss of oleate ligands. Energy-dispersive X-ray spectroscopy of the sample used in this work suggests a Cd-rich stoichiometry (Table 2.3).

Given the relatively low ligand coverage (3.4 oleates/nm^2), this suggests that there are likely underpassivated Cd species that, if reduced, would be charge balanced by Na^+ ions and could contribute to a portion of the discrepancy between equivalents of reductant added and oleates lost. Additionally, we hypothesize that Se^{1-} defects on the surface are reduced by excess $Na[C_{10}H_8]$, though reduction of these species is expected to occur with a large energetic cost associated with surface rearrangement upon reduction to Se^{2-}.[17] These oxidized Se species are established to be prevalent on CdSe surfaces and postulated to be an active electron-accepting species.[17,20,24] For example, Tsui et al. recently demonstrated

that CdSe QDs could be photodoped after a dark reduction of the surface by strong reductants.[20] In this work, the authors invoked the reduction of diselenides in these dark redox reactions at the surface.[20] We propose a similar mechanism for reduction of Se^{1-} species that likely occurs in parallel or sequential to a Cd^{2+} reduction pathway (Scheme 2.3b).[17,20]

Further addition of $Na[C_{10}H_8]$ results in a bleach of the $1S_e$ feature, indicating reduction of the CB to yield n-type QDs. The resulting n-type QDs are presumably charge-balanced by Na^+ ions not paired with freed oleate ligands. We anticipate that this finding may be extended to doping QDs passivated with other commonly employed X-type ligands.

Scheme 2.3 More detailed understanding of reduction of surface species in remote chemical doping: (a) Proposed reduction pathway of Cd^{2+} moieties on QD surfaces. (b) Proposed reduction pathway of surface diselenide species.

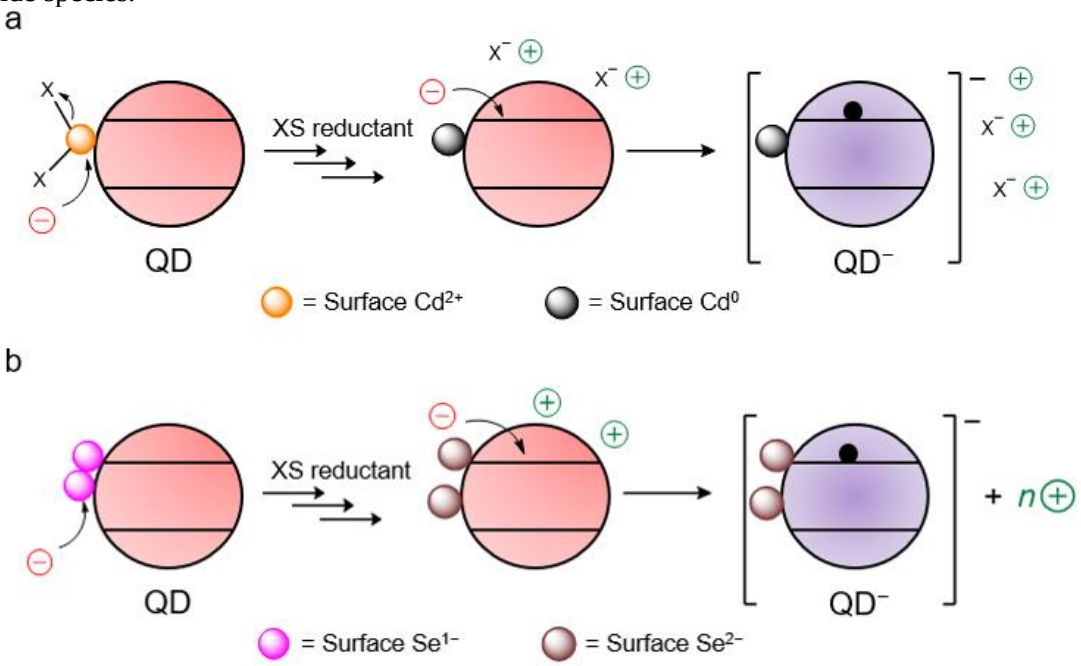

Table 2.3 Elemental analysis of TEM sample by Energy-dispersive X-ray spectroscopy

Element	Peak area	Area Sigma	k factor	Weight %	Weight % Sigma	Atomic %
C	15630	209	2.504	76.36	0.46	90.81
O	1555	74	1.871	5.68	0.26	5.07
Si	865	56	1.000	1.69	0.11	0.86
Cu	4177	101	1.393	11.35	0.27	2.55
Se	391	37	2.146	1.64	0.15	0.30
Cd	936	76	1.803	3.29	0.26	0.42

Previous reports studying oleate ligand binding modes on QD surfaces have shown that different nanocrystal facets may favor specific ligand binding modes depending on whether the facet is metal- or chalcogen-rich.[31,45] For example, on zinc-blende CdSe QDs Se-rich surfaces are passivated by Z-type $Cd(oleate)_2$ with monodentate oleate binding to Cd atoms while (100) Cd-rich surfaces are more likely to have oleates bound in a bridging fashion across multiple Cd sites that are part of the core stoichiometry.[40] Alternatively, oleates may bind in a chelating bidentate geometry to surface metal atoms.[40,42] While this work cannot distinguish between loss of oleate ligands among specific populations, it is notable that our studies demonstrate only a small fraction (5-10%) of bound oleates are lost even with tens of equivalents of reductant added. This indicates that only a subpopulation of oleate-bound Cd^{2+} surface moieties act as traps. Clearly, a detailed understanding of changes in surface chemistry is imperative for improved doping and will be an important area of study in future works.

2.3 Conclusion

To conclude, UV-Vis absorption, NMR, and FTIR spectroscopic studies provide unifying evidence for reduction of the QD surface upon addition of excess charge carriers and indicate that reduction of a portion of surface Cd^{2+} atoms is accompanied by loss of anionic ligands. Parallel ^{1}H NMR and UV-Vis absorption spectroscopy titrations consistently show that the first 10–20 equiv. of reductant reduce surface

species rather than directly engage in electron transfer to the CB. The approximate number of Cd^{2+} surface species reduced in this initial surface reduction may be roughly estimated by the number of dissociated ligands per QD. Furthermore, the discrepancy between the quantified Cd^{2+} ion reduction (via ligand loss) and equivalents of $Na[C_{10}H_8]$ added prior to evidence of CB electrons may provide an indirect handle of the number of reducible Se species on the surface. This mechanistic understanding highlights the importance of charge compensation in remote chemical doping of QDs, whether it is manifested in anionic ligand loss, surface reorganization, or charge balance in the presence of excess ions (Na^+, $BAr^F{}_4^-$).

While the exact number of surface sites that are reduced prior to CB filling will vary across QDs prepared with different synthesis and purification methods, the presented work demonstrates a general method for quantifying reduction of surface species by chemical doping. QD size will also undoubtedly affect the surface reduction studied in this system not only by varying band edge potentials of the nanocrystals, but also by changing the surface area to volume ratio and thus influencing the number of surface sites. In a broader sense, this enhanced understanding not only yields insight into the mechanism of remote chemical doping but also a more detailed picture of redox reactivity at the QD surface. Importantly, this provides a method of accounting for unintentional ligand loss, and therefore unrecognized changes in QD electronics, in the presence of redox reagents in studies of doping, catalysis, sensing applications, and device preparation methods.[1,20] Moreover, these data provide the first example of electron-promoted loss of X-type oleate ligands via reduction of surface $Cd(oleate)_2$ moieties. This bettered understanding of charge balance at the QD surface through anionic ligand loss presents a new, controllable method of X-type ligand displacement and surface passivation promoted not by incoming ligands, but rather by electrons. Ongoing work is focused on investigating surface reduction across a wide range of QD sizes, nanocrystal materials and redox agents.

REFERENCES

(1) Schimpf, A. M.; Knowles, K. E.; Carroll, G. M.; Gamelin, D. R. Electronic Doping and Redox-Potential Tuning in Colloidal Semiconductor Nanocrystals. *Acc. Chem. Res.* **2015**, *48*, 1929–1937.

(2) Shim, M.; Guyot-Sionnest, P. N-Type Colloidal Semiconductor Nanocrystals. *Nature* **2000**, *407*, 981–983.

(3) Talapin, D. V.; Lee, J.-S.; Kovalenko, M. V.; Shevchenko, E. V. Prospects of Colloidal Nanocsrystals for Electronic and Optoelectronic Applications. *Chem. Rev.* **2010**, *110*, 389–458.

(4) Pietryga, J. M.; Park, Y.; Lim, J.; Fidler, A. F.; Bae, W. K.; Brovelli, S.; Klimov, V. I. Spectroscopic and Device Aspects of Nanocrystal Quantum Dots. *Chem. Rev.* **2016**, *116*, 10513–10622.

(5) Kamat, P. V. Quantum Dot Solar Cells. The Next Big Thing in Photovoltaics. *J. Phys. Chem. Lett.* **2013**, *4*, 908–918.

(6) Harris, R. D.; Bettis Homan, S.; Kodaimati, M.; He, C.; Nepomnyashchii, A. B.; Swenson, N. K.; Lian, S.; Calzada, R.; Weiss, E. A. Electronic Processes within Quantum Dot-Molecule Complexes. *Chem. Rev.* **2016**, *116*, 12865–12919.

(7) Mocatta, D.; Cohen, G.; Schattner, J.; Millo, O.; Rabani, E.; Banin, U. Heavily Doped Semiconductor Nanocrystal Quantum Dots. *Science* **2011**, *332*, 77–81.

(8) Wang, C.; Shim, M.; Guyot-Sionnest, P. Electrochromic Nanocrystal Quantum Dots. *Science* **2001**, *291*, 2390–2392.

(9) Carey, G. H.; Abdelhady, A. L.; Ning, Z.; Thon, S. M.; Bakr, O. M.; Sargent, E. H. Colloidal Quantum Dot Solar Cells. *Chem. Rev.* **2015**, *115*, 12732–12763.

(10) Shim, M.; Wang, C.; Guyot-Sionnest, P. Charge-Tunable Optical Properties in Colloidal Semiconductor Nanocrystals. *J. Phys. Chem. B* **2001**, *105*, 2369–2373.

(11) Rinehart, J. D.; Schimpf, A. M.; Weaver, A. L.; Cohn, A. W.; Gamelin, D. R. Photochemical Electronic Doping of Colloidal CdSe Nanocrystals. *J. Am. Chem. Soc.* **2013**, *135*, 18782–18785.

(12) Koh, W.; Koposov, A. Y.; Stewart, J. T.; Pal, B. N.; Robel, I.; Pietryga, J. M.; Klimov, V. I. Heavily Doped N-Type PbSe and PbS Nanocrystals Using Ground-State Charge Transfer from Cobaltocene. *Sci. Rep.* **2013**, *3*, 2004.

(13) Erwin, S. C.; Zu, L.; Haftel, M. I.; Efros, A. L.; Kennedy, T. A.; Norris, D. J. Doping Semiconductor Nanocrystals. *Nature* **2005**, *436*, 91–94.

(14) Araujo, J. J.; Brozek, C. K.; Kroupa, D.; Gamelin, D. R. Degenerately N-Doped Colloidal PbSe Quantum Dots: Band Assignments and Electrostatic Effects. *Nano Lett.* **2018**, *18*, 3893–3900.

(15) Gudjonsdottir, S.; Van Der Stam, W.; Kirkwood, N.; Evers, W. H.; Houtepen, A. J. The Role of Dopant Ions on Charge Injection and Transport in Electrochemically Doped Quantum Dot Films. *J. Am. Chem. Soc.* **2018**, *140*, 6582–6590.

(16) Valdez, C. N.; Delley, M. F.; Mayer, J. M. Cation Effects on the Reduction of Colloidal ZnO Nanocrystals. *J. Am. Chem. Soc.* **2018**, *140*, 8924–8933.

(17) Tsui, E. Y.; Carroll, G. M.; Miller, B.; Marchioro, A.; Gamelin, D. R. Extremely Slow Spontaneous Electron Trapping in Photodoped N-Type CdSe Nanocrystals. *Chem. Mater.* **2017**, *29*, 3754–3762.

(18) Brozek, C. K.; Hartstein, K. H.; Gamelin, D. R. Potentiometric Titrations for Measuring the Capacitance of Colloidal Photodoped ZnO Nanocrystals. *J. Am. Chem. Soc.* **2016**, *138*, 10605–10610.

(19) Chávez, I.; Alvarez-Carena, A.; Molins, E.; Roig, A.; Maniukiewicz, W.; Arancibia, A.; Arancibia, V.; Brand, H.; Manuel Manríquez, J. Selective Oxidants for Organometallic Compounds Containing a Stabilising Anion of Highly Reactive Cations: (3,5(CF3)2C6H3)4B−)Cp2Fe+ and (3,5(CF3)2C6H3)4B−)Cp*2Fe+. *J. Organomet. Chem.* **2000**, *601*, 126–132.

(20) Tsui, E. Y.; Hartstein, K. H.; Gamelin, D. R. Selenium Redox Reactivity on Colloidal CdSe Quantum Dot Surfaces. *J. Am. Chem. Soc.* **2016**, *138*, 11105–11108.

(21) Schimpf, A. M.; Thakkar, N.; Gunthardt, C. E.; Masiello, D. J.; Gamelin, D. R. Charge-Tunable Quantum Plasmons in Colloidal Semiconductor Nanocrystals. *ACS Nano* **2014**, *8*, 1065–1072.

(22) Routzahn, A. L.; White, S. L.; Fong, L.-K.; Jain, P. K. Plasmonics with Doped Quantum Dots. *Isr. J. Chem.* **2012**, *52*, 983–991.

(23) Zhao, J.; Holmes, M. A.; Osterloh, F. E. Quantum Confinement Controls Photocatalysis: A Free Energy Analysis for Photocatalytic Proton Reduction at CdSe Nanocrystals. *ACS Nano* **2013**, *7*, 4316–4325.

(24) Voznyy, O.; Thon, S. M.; Ip, A. H.; Sargent, E. H. Dynamic Trap Formation and Elimination in Colloidal Quantum Dots. *J. Phys. Chem. Lett.* **2013**, *4*, 987–992.

(25) Giansante, C.; Infante, I. Surface Traps in Colloidal Quantum Dots: A Combined Experimental and Theoretical Perspective. *J. Phys. Chem. Lett.* **2017**, *8*, 5209–5215.

(26) Connelly, N. G.; Geiger, W. E. Chemical Redox Agents for Organometallic Chemistry. *Chem. Rev.* **1996**, *96*, 877–910.

(27) Houtepen, A. J.; Hens, Z.; Owen, J. S.; Infante, I. On the Origin of Surface Traps in Colloidal II–VI Semiconductor Nanocrystals. *Chem. Mater.* **2017**, *29*, 752–761.

(28) Veamatahau, A.; Jiang, B.; Seifert, T.; Makuta, S.; Latham, K.; Kanehara, M.; Teranishi, T.; Tachibana, Y. Origin of Surface Trap States in CdS Quantum Dots: Relationship between Size Dependent Photoluminescence and Sulfur Vacancy Trap States. *Phys. Chem. Chem. Phys.* **2015**, *17*, 2850–2858.

(29) Palato, S.; Seiler, H.; McGovern, L.; Mack, T. G.; Jethi, L.; Kambhampati, P. Electron Dynamics at the Surface of Semiconductor Nanocrystals. *J. Phys. Chem. C* **2017**, *121*, 26519–26527.

(30) Krause, M. M.; Jethi, L.; Mack, T. G.; Kambhampati, P. Ligand Surface Chemistry Dictates Light Emission from Nanocrystals. *J. Phys. Chem. Lett.* **2015**, *6*, 4292–4296.

(31) Boles, M. A.; Ling, D.; Hyeon, T.; Talapin, D. V. Erratum: The Surface Science of Nanocrystals. *Nat. Mater.* **2016**, *15*, 364–364.

(32) Knauf, R. R.; Lennox, J. C.; Dempsey, J. L. Quantifying Ligand Exchange Reactions at CdSe Nanocrystal Surfaces. *Chem. Mater.* **2016**, *28*, 4762–4770.

(33) Rajh, T.; Micic, O. I.; Lawless, D.; Serpone, N. Semiconductor Photophysics. 7. Photoluminescence and Picosecond Charge Carrier Dynamics in Cadmium Sulfide Quantum Dots Confined in a Silicate Glass. *J. Phys. Chem.* **1992**, *96*, 4633–4641.

(34) Shiragami, T.; Ankyu, H.; Fukami, S.; Pac, C.; Yanagida, S.; Mori, H.; Hiroshi, F. Semiconductor Photocatalysis: Visible Light Induced Photoreduction of Aromatic Ketones and Electron-Deficient Alkenes Catalyzed by Quantised Cadmium Sulfide. *J. Chem. Soc. Faraday Trans.* **1992**, *88*, 1055–1061.

(35) Nedoluzhko, A. I.; Shumilin, I. A.; Nikandrov, V. V. Coupled Action of Cadmium Metal and Hydrogenase in Formate Photodecomposition Sensitized by CdS. *J. Phys. Chem.* **1996**, *100*, 17544–17550.

(36) Zhao, J.; Holmes, M. A.; Osterloh, F. E. Quantum Confinement Controls Photocatalysis: A Free Energy Analysis for Photocatalytic Proton Reduction at CdSe Nanocrystals. *ACS Nano* **2013**, *7*, 4316–4325.

(37) Rinehart, J. D.; Weaver, A. L.; Gamelin, D. R. Redox Brightening of Colloidal Semiconductor Nanocrystals Using Molecular Reductants. *J. Am. Chem. Soc.* **2012**, *134*, 16175–16177.

(38) Hens, Z.; Martins, J. C. A Solution NMR Toolbox for Characterizing the Surface Chemistry of Colloidal Nanocrystals. *Chem. Mater.* **2013**, *25*, 1211–1221.

(39) Tamukong, P. K.; Peiris, W. D. N.; Kilina, S. Computational Insights into CdSe Quantum Dots' Interactions with Acetate Ligands. *Phys. Chem. Chem. Phys.* **2016**, *18*, 20499–20510.

(40) Chen, P. E.; Anderson, N. C.; Norman, Z. M.; Owen, J. S. Tight Binding of Carboxylate, Phosphonate, and Carbamate Anions to Stoichiometric CdSe Nanocrystals. *J. Am. Chem. Soc.* **2017**, *139*, 3227–3236.

(41) Anderson, N. C.; Hendricks, M. P.; Choi, J. J.; Owen, J. S. Ligand Exchange and the Stoichiometry of Metal Chalcogenide Nanocrystals: Spectroscopic Observation of Facile Metal-Carboxylate Displacement and Binding. *J. Am. Chem. Soc.* **2013**, *135*, 18536–18548.

(42) Cass, L. C.; Malicki, M.; Weiss, E. A. The Chemical Environments of Oleate Species within Samples of Oleate-Coated PbS Quantum Dots. *Anal. Chem.* **2013**, *85*, 6974–6979.

(43) Moreels, I.; Fritzinger, B.; Martins, J. C.; Hens, Z. Surface Chemistry of Colloidal PbSe Nanocrystals. *J. Am. Chem. Soc.* **2008**, *130*, 15081–15086.

(44) Drijvers, E.; De Roo, J.; Martins, J. C.; Infante, I.; Hens, Z. Ligand Displacement Exposes Binding Site Heterogeneity on CdSe Nanocrystal Surfaces. *Chem. Mater.* **2018**, *30*, 1178–1186.

(45) Smith, A. M.; Nie, S. Semiconductor Nanocrystals: Structure, Properties, and Band Gap Engineering. *Acc Chem Res.* **2010**, *43*, 190–200.

CHAPTER 3 : REVEALING THE MOLECULAR IDENTITY OF DEFECT SITES ON PBS QUANTUM DOT SURFACES WITH REDOX-ACTIVE CHEMICAL PROBES

This chapter was adapted with permission from Hartley, C.L.; Dempsey, J.L. Revealing the Molecular-Level Identity of Defect Sites on PbS Quantum Dot Surfaces with Redox-Active Chemical Probes. *Chem. Mater.* **2021**, *33* (7), 2655 – 2665.

3.1 Introduction

Colloidal semiconductor quantum dots (QDs) are a promising class of materials with potential applications in photovoltaics,[1,2] commercial displays,[3] and photoredox catalysis systems,[4,5] to name a few. However, commercialization of many QD-based optoelectronic devices has seen only limited success; this is largely due to the low charge transport efficiencies observed relative to bulk semiconductor materials. The cause for these low efficiencies can in part be attributed to performance-limiting defects at QD surfaces, such as underpassivated metal or chalcogenide ions, and can result in mid-gap electronic trap states.[6,7] Such states can trap excited electrons or holes, leading to low photochemical quantum yields and hindered charge transfer between nanocrystals within a device. Surface defects are present on as-synthesized QDs, and their occurrence and routes for passivation have consequently been a major area of study.[6–11] For instance, techniques such as emission spectroscopy and electrochemistry have traditionally been used to establish the presence and approximate energies of mid-gap trap states.[12–18] Though useful, such methods are limited by the insight they may provide regarding the *molecular identity* and *reactivity* of specific defects at the QD surface. [19]

Indeed, QD surface defects are often ill-defined, making targeted passivation approaches challenging. One tactic to elucidate the molecular-level details of QD surfaces—with the aim of controlling these defects sites—is the use of chemical probes. Chemical probes are molecular reagents that react predictably with specific sites at the QD surface, and the resulting reactivity in turn can reveal details about the native QD surface structure.[20–25] Chemical probes may be classified as either ligand-

based probes, or redox-active probes depending on the type of reactivity they engage in at the QD surface (Scheme 3.1).[19]

Scheme 3.1. Approaches to studying surfaces defects through reaction of QDs with (i) ligand-based (shown here for metal ion defects) or (ii) redox-active chemical probes

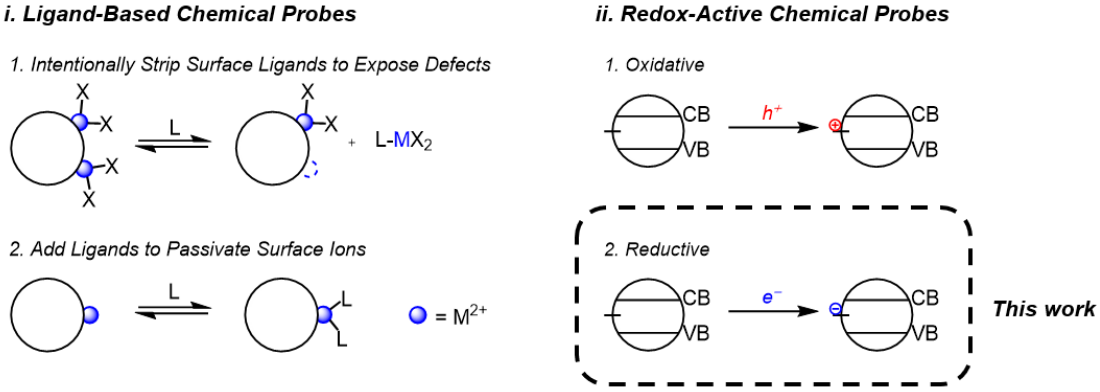

Substantial insight into the structural and electronic properties of QD surfaces has been revealed using both ligand-based and redox-active probes. Redox-active probes in particular have yielded new understanding of both chalcogenide- and metal ion-derived defects that occur natively or that may be induced upon reduction or oxidation (charging) of the surface. For example, Tsui et al. demonstrated that oxidized diselenide species are a common defect motif on CdSe surfaces by investigating surface reactivity with organometallic redox reagents that are known to selectively reduce chalcogenide dimers.[24] Redox probes were also used to better understand anionic chalcogenide defects in PbS QDs. Knowles et al. used a molecular acceptor, tetracyanoquinodimethane (TCNQ), to probe spontaneous electron transfer from undercoordinated S^{2-} sites on QD surfaces using FTIR and UV-Vis-NIR absorbance spectroscopies.[26]

Similarly, redox reactivity has been key to elucidating the nature of metal-based surface defects. A recent study by our group revealed that addition of $Na[C_{10}H_8]$ ($E^{o\prime} = -3.1$ V vs. $Fc^{+/0}$) to CdSe QDs led to reduction of surface Cd^{2+} ions with concomitant displacement of charge-balancing anionic ligands, yielding putative Cd^0 sites on the QD surfaces.[23] This example illustrates the redox reactivity of surface

Cd^{2+} sites and the displacement of anionic ligands via an electron-promoted X-type ligand displacement mechanism in response to surface metal ion charging. The reduction of Cd^{2+} surface sites was also recently reported by Pu et al. upon applying an electrochemical bias to CdSe QD thin films passivated with cadmium carboxylate ligands.[27] DFT studies by Voznyy et al. and du Fossé et al. have explored the impact of charging at the surfaces of semiconductor QDs and predicted that the dimerization of surface metal ions induced by charging serves as a source of mid-gap trap states.[28,29] Collectively, these examples highlight how redox-active chemical probes may be employed to better understand QD surface structure, as well as inform on accessible redox-active surface moieties.

While the combined efforts of the aforementioned studies have yielded insight into QD surface structure, there remains a need for a systematic investigation of the molecular nature (atomic identity, bonding environment, oxidation state, or reduction potential) and reactivity of these surface defects . Indeed, many of the examples noted above focused on identifying the structure or oxidation state of likely defect sites but stopped short of exploring their redox reactivity—an important indicator of the specific environment of a given defect—in tandem. Additionally, QD size is known to impact which bonding environments—and therefore which possible defects—may exist at the surface, yet this variable has been underexplored to date.[22,30,31] Importantly, the redox properties of defect sites are expected to have significant influence on QD reactivity in multi-component systems, as well as have major implications in QD charging or remote chemical doping processes.

To this end, we herein report systematic investigations of defect sites on PbS QD surfaces using a series of redox-active chemical probes. PbS was selected as it is a widely studied and well understood QD material, and thereby serves as a relevant platform for redox-active defect sites. We first establish the reactivity between a moderately reducing organometallic reductant, cobaltocene, with metal-based surface sites on 4.1 nm PbS QDs and then study the impact of varying QD size and potency of the reductant. Finally, we explore other redox-active defect sites at the surface by employing selective trialkylphosphine reagents to selectively probe chalcogenide defects. Our studies reveal the presence of both metal and chalcogenide defect structures at PbS QD surfaces. By studying the reactivity of these defect sites with

redox-active chemical probes, we elucidate their molecular-level nature and reduction potentials. In doing so, we deepen understanding of QD surface defects and routes to intentionally passivate or induce them.

3.2 Experimental Methods

General Considerations. All syntheses were performed under a nitrogen environment using standard Schlenk techniques. All experiments were performed or set up in a dry nitrogen-filled glovebox (MBraun) unless otherwise noted. Solvents used in the glovebox (toluene, tetrahydrofuran, acetonitrile) were purified over an alumina column and dispensed from a dry argon-atmosphere solvent system (Pure Process Technologies) and then dried over activated 3 Å molecular sieves. NMR solvents were similarly stored over activated 3 Å molecular sieves, and in the case of THF-d_8 further dried over an alumina plug.

Chemicals. Lead(II) oxide (PbO) (99.999% trace metals basis), oleic acid (OA) (90%), 1-octadecene (ODE) (90%), hexamethyldisilathiane ($(TMS)_2S$) (synthesis grade), tri-*n*-butylphosphine (Bu_3P) (mixture of isomers, 97%), and 1,3,5-trimethoxybenzene (TMB) (Reagent Plus ≥99%) were purchased from Sigma-Aldrich and used as received. Sodium hydroxide was purchased from Fisher Scientific and used as received. Cobaltocene ($CoCp_2$) (≥98%) was purchased from VWR and purified by dissolving in toluene in a glovebox in the dark, filtering off insoluble particulates, and removing solvent under vacuum, followed by sublimation of the solid in the dark prior to use. Purified cobaltocene was stored in a −30 ºC freezer under inert atmosphere. Decamethylcobaltocene ($CoCp^*_2$) was purchased from Sigma-Aldrich and recrystallized from cold pentane before use and then stored in a −30 ºC freezer in a glovebox. Toluene-d_8 and THF-d_8 were purchased from Cambridge Isotope Laboratories. All other solvents used were purchased from Fisher Scientific or VWR.

PbS Synthesis and Purification. PbS QDs were synthesized using a previously reported literature procedure.[22] QDs ranging in diameter from 2.6 to 4.9 nm were prepared by varying the molar ratio of OA to PbO used to prepare the $Pb(oleate)_2$ precursor as well as the injection temperature of the $(TMS)_2S$. In

general, higher OA:PbO ratios and higher injection temperatures resulted in larger nanocrystals (Table 3.1 Conditions employed to synthesize PbS QDs of varying diameter.Table 3.1). The QDs were purified rigorously by repeated precipitation and centrifugation cycles to isolate the nanocrystals from excess ligand, solvent and reaction byproducts. For QDs used in direct size comparison studies, purification procedures were the same across all batches. For these batches (2.6 nm, 3.8 nm, 4.1 nm, 4.9 nm, featured in Section 3.3), the crude reaction mixture was precipitated with acetone and divided among centrifuge tubes and centrifuged. The supernatant was decanted, and the QD solid was dispersed in 1 – 2 mL pentane or toluene and precipitated with 12 mL acetone, sonicated, and centrifuged. This step was repeated once. The resulting solid was dispersed in 1 mL pentane and precipitated with a 1:1 mixture of acetone and methanol, sonicated, and centrifuged. This step was repeated a total of three to four times. The QDs were dispersed in 1 mL pentane, precipitated with 12 mL methanol and centrifuged. The QDs were then dispersed in 1 mL pentane and precipitated with 9 mL of a 1:2 mixture of acetone:methanol, sonicated, and centrifuged. This step was repeated a total of two to three times. Finally, the QDs were dispersed in 1 mL pentane, precipitated with 12 mL acetone, and centrifuged a total of three times. For the largest batch of QDs (4.9 nm) prepared with a large excess of oleic acid, we found that filtering the QD solution over a glass fiber filter paper plug between purification steps further helped to get rid of excess $Pb(oleate)_2$. The purified solid was then dispersed in pentane, transferred to a 20 mL vial, and dried via evaporation.

For samples used in other studies, purification proceeded with minor variations to the procedure described above. The QDs were stored as a solid in an inert-atmosphere glovebox. QD size and extinction coefficients at 400 nm were determined using the sizing curve reported by Moreels et al.[32]

Table 3.1 Conditions employed to synthesize PbS QDs of varying diameter.

Diameter (nm)	**OA:PbO ratio**	**Injection Temperature**
2.6	2.02	88 ºC
3.8	4.21	153 ºC
4.1	8.09	139 ºC

4.9	8.33	139 ºC

All reactions proceeded for 3 min after injection of hexamethyldisilathiane before growth was halted by removing heating mantle and reaction mixture was rapidly cooled via immersion of flask in room temperature oil bath. The crude reaction mixture was then transferred to centrifuge tubes for purification as described in chapter 3.

UV-Vis-NIR Absorbance Studies. UV-Vis-NIR absorbance data was collected on an Agilent Cary 60 or Cary 5000 spectrophotometer. Samples of QDs were prepared in toluene (1 – 5 μM) and ~3 mL of this solution were added to a custom-made quartz cuvette with an adapted 14/20 ground-glass joint. The cuvette was equipped with a micro stir bar and then capped with a rubber septum that was secured with electrical tape and copper wire. A solution of cobaltocene was prepared in toluene (15 mM) and then loaded into a gas-tight locking Hamilton syringe. The charged needle was locked and the end stuck into a separate rubber septum to avoid exposure to air. The cuvette and syringe were then brought out of the glovebox and the cobaltocene was added incrementally by syringe, stirring for approximately 30 seconds after each addition to ensure thorough mixing before collecting a spectrum. Samples for long timescale studies were prepared in cuvettes sealed with Kontes valves and shielded from light.

NMR Studies. ^{1}H NMR spectra were collected on a 600 MHz Bruker NMR spectrometer with a cryoprobe. Unless noted otherwise, titration studies were prepared by adding 600 μL of a 30 μM QD stock solution in toluene-d_8 to J-Young NMR tubes. An internal standard stock solution was then prepared by dissolving ~15 mg of 1,3,5-trimethoxybenzene in 1.5 mL toluene-d_8, and then 50 μL was added to each NMR tube. A 50 mM solution of redox reagent was prepared in toluene-d_8 and added in increments of 0, 50, 100, 500, and 1000 equivalents per QD to the NMR tubes at staggered times to ensure that all samples mixed for the same amount of time (3 hours) before collecting NMR spectra. Spectra were collected with 12 scans and a d1 delay time of 30 seconds. The absolute number of bound and free ligands per QD were determined by spectral fitting with MestReNova software (Figure 3.1). ^{31}P{^{1}H} NMR spectra were collected on a 500 or 600 MHz Bruker NMR spectrometer.

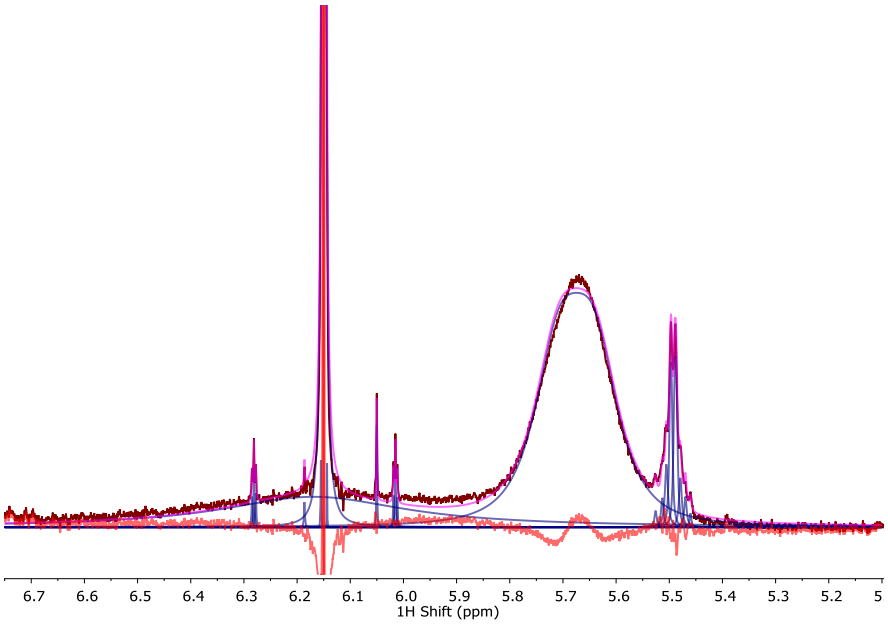

Figure 3.1 Representative fitting of bound and free oleate resonances in ^{1}H NMR spectra (maroon). The bound oleate peak is fit to one broad feature at ~5.65 ppm and the free oleate peak to the multiplet centered at ~5.48 ppm. Multipeak features are depicted in blue and the overall fit is in pink. The residual is shown in red. At high equivalents of $CoCp_2$, a broad feature is present at 6.2 ppm corresponding to $[CoCp_2]^+$. This feature is fit to account for a slight overlap with the bound oleate feature. The signal at 6.15 ppm overlapping with the broad $[CoCp_2]^+$ resonance is from the 1,3,5-trimethoxybenzene internal standard. Data shown is from addition of 500 eq. $CoCp_2$ to the 4.9 nm PbS QDs.

XPS Sample Preparation. Samples for X-ray photoelectron spectroscopy (XPS) analysis were measured on gold-coated silicon wafers that had been sonicated for 2 minutes in 190 proof ethanol and dried in air prior to use to remove residual carbon species. Solutions of QDs in toluene (typically ~10 μM) reacted with 0, 50, 100, 500 or 1000 equiv. cobaltocene for 21 hours and then the QDs isolated by precipitation with acetonitrile. The isolated nanocrystals were redispersed in toluene and were drop cast onto the wafers until a brown film was visible by eye. The XPS samples were loaded onto a sample holder in a nitrogen-filled glovebox and transported to the XPS facility in a sealed glass tube, which was then loaded onto the instrument in an inert-environment glovebag. X-ray photoelectron spectroscopy (XPS) was performed using a Kratos Axis Ultra DLD X-ray photoelectron spectrometer with a monochromatic Al Kα X-ray source. Survey scans and high-resolution scans were obtained with pass energies of 80 and 20 eV, respectively. Spectra were corrected to the C 1s peak at 284.6 eV.

TEM Sample Preparation. Samples for Transmission electron microscopy (TEM) imaging were prepared by drop casting dilute solutions of QDs in pentane that were filtered through 2 μm PTFE syringe filters onto TEM grids (Ultrathin carbon film on lacey carbon support film, 400 mesh, copper) under ambient conditions. The grids dried in air and were then conditioned overnight under vacuum to remove any trace volatiles. Images were collected on a Thermo Scientific Talos F200X S/TEM at an accelerating voltage of 200 kV and with a 70 μm objective aperture.

3.3 Results and Discussion

3.3.1 A System for Studying Redox-Active Defect Sites on PbS Surfaces

Oleate-capped PbS QDs ranging in size from 2.6 to 5.1 nm in diameter provide a versatile platform for interrogating redox-active defects on QD surfaces. The size range explored here provides a means to access QDs with a range of band edge potentials as well as different morphologies, surface facets and stoichiometries which are known to vary as a function of QD size for PbS.[22,30,31,33] Varying QD size in our studies thereby provides additional insight into the molecular nature of reactive surface species.

Redox-active chemical probes were selected to span potency from strong ($E^{o\prime} = -1.9$ V vs. $Fc^{+/0}$) to weak ($E^{o\prime} = -0.48$ V vs. $Fc^{+/0}$) (Table 3.4). As other works have investigated oxidation of PbS QD surfaces,[26] we focus here on the impact of reductive chemical probes. With this wide array of reductants, we demonstrate that it is possible to vary the driving force of surface reduction and, in effect, target specific sites to rationally passivate undesired surface defects.

3.3.2 PbS QDs Display Surface Reactivity with $CoCp_2$

The reactivity between a mid-size batch of PbS QDs (4.1 nm diameter) was first established with the moderate reductant cobaltocene ($CoCp_2$, $E^{o\prime} = -1.3$ V vs. $Fc^{+/0}$). $CoCp_2$ has been previously shown to undergo ground state charge transfer with PbS QDs and does not display any deleterious side

chemistry.[34,35] Upon reduction of a colloidal QD by $CoCp_2$, the donated electron can either occupy a delocalized conduction band electronic state or be confined to localized electronic states at the surface (Figure 3.2a). In order to assess whether $CoCp_2$ is able to reduce the 4.1 nm PbS QD conduction band (CB) edge state, the electron transfer reaction was monitored using UV-Vis-NIR absorbance spectroscopy. Absorbance spectroscopy is commonly employed to gauge band edge charging with excess electrons or holes; upon reduction of the CB or oxidation of the valence band (VB), a bleach of the excitonic absorbance feature will be observed due to the lowered probability of exciting a carrier into an already-filled state.[35,36] The absorption spectra of the 4.1 nm QDs in toluene before and after addition of 500 equiv. $CoCp_2$ (per mol QD) are shown in Figure 3.2b. No excitonic bleach (λ_{max} = 1186 nm) is observed, indicating that band edge reduction by $CoCp_2$ is energetically unfavorable even with a large excess of reductant. While previous studies observed interfacial electron transfer from $CoCp_2$ into CB states of similarly sized oleate-capped PbS QDs ($\geq \sim$ 4.2 nm in diameter),[35] our observations likely differ from this prior report as this previous work was performed on QD thin films rather than in solution.

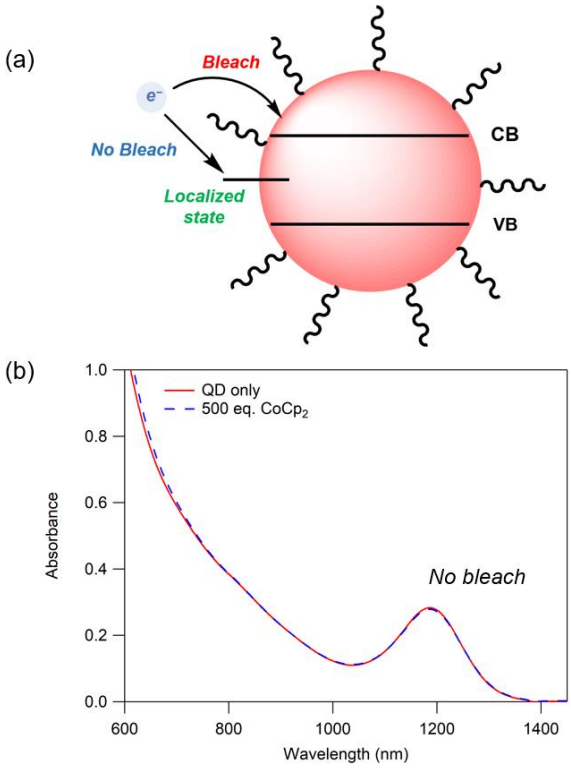

Figure 3.2 (a) Diagram depicting the optical response observed by absorbance spectroscopy upon reduction of either the band edge state or a localized surface state. (b) UV-Vis-NIR absorption spectrum of 4.1 nm QDs (2.5 μM) in toluene before (red) and after (blue) addition of 500 equiv. $CoCp_2$.

Although no band edge reduction was observed by UV-Vis-NIR absorbance spectroscopy, we anticipated that $CoCp_2$ was a sufficiently strong reductant to reduce localized surface states, as has been postulated previously.[35] In order to interrogate reduction of the surface directly, titration studies were performed using ^{1}H NMR spectroscopy. NMR spectroscopy is a convenient method to probe QD surface chemistry as it allows for quantification of the capping oleate ligands bound to surface Pb ions. The alkene proton resonance of the oleate ligands may be used to differentiate between bound vs. free ligands in solution. The bound oleate ligand resonance is broad and appears at 5.66 ppm, whereas the free oleate resonance are sharper and shifted up-field (5.48 ppm).[22,37–39] Characterization of as-synthesized 4.1 nm QDs reveal an average bound ligand coverage of 173 ± 5 oleates per QD.

Addition of excess $CoCp_2$ (0 – 1000 equiv.) to the PbS QDs in toluene-d_8 results in dissociation of a portion of bound oleate ligands that increases with equivalents of reductant added (Figure 3.3). The 4.1 nm QDs lose an average of 14.7 ± 3.2% of initially bound oleate ligands with addition of up to 1000 equiv. $CoCp_2$; this corresponds to approximately 25 oleate ligands displaced per QD. Importantly, the total number of ligands (bound + free) remains constant throughout the course of the titration, indicating that the QDs remain stable in solution even in the presence of large excesses of reductant (Figure 3.4). X-ray photoelectron spectroscopy (XPS) studies confirm that isolated PbS QDs reacted with an excess of $CoCp_2$ do not have any significant changes in their Pb:S ratio (Table 3.2). The observed ligand loss without a corresponding loss of surface Pb atoms therefore suggests that the detected free ligand is due to liberation of X-type anionic oleates, and not Z-type $Pb(oleate)_2$ fragments, upon reduction. This observation is consistent with the electron-promoted X-type ligand displacement phenomenon previously reported for CdSe QDs,[23] and these data thereby provide direct evidence that surface Pb^{2+} ions are reduced by $CoCp_2$.

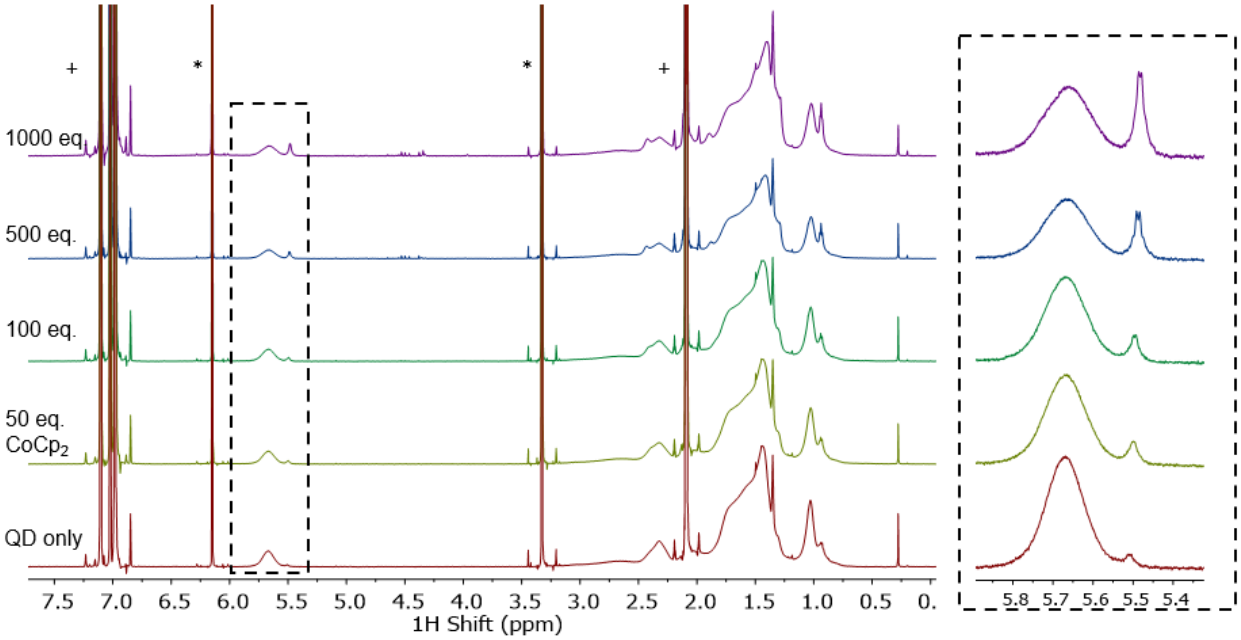

Figure 3.3 ^{1}H NMR titration of 4.1 nm QDs (27.7 µM) in toluene-d_8 upon addition of 0 (red), 50 (yellow), 100 (green), 500 (blue), and 1000 equiv. $CoCp_2$ (violet). Internal standard of 1,3,5-trimethoxybenzene is indicated by (*) and solvent residual by (+).

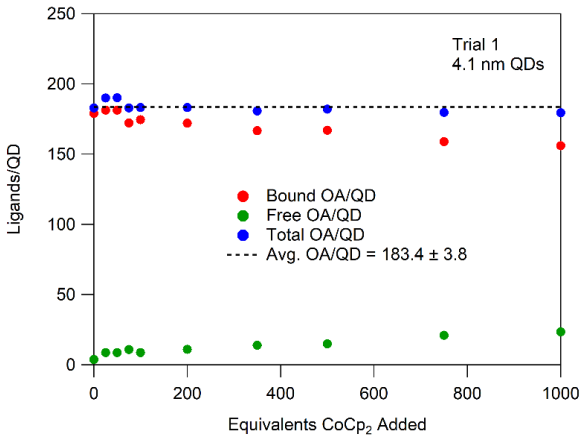

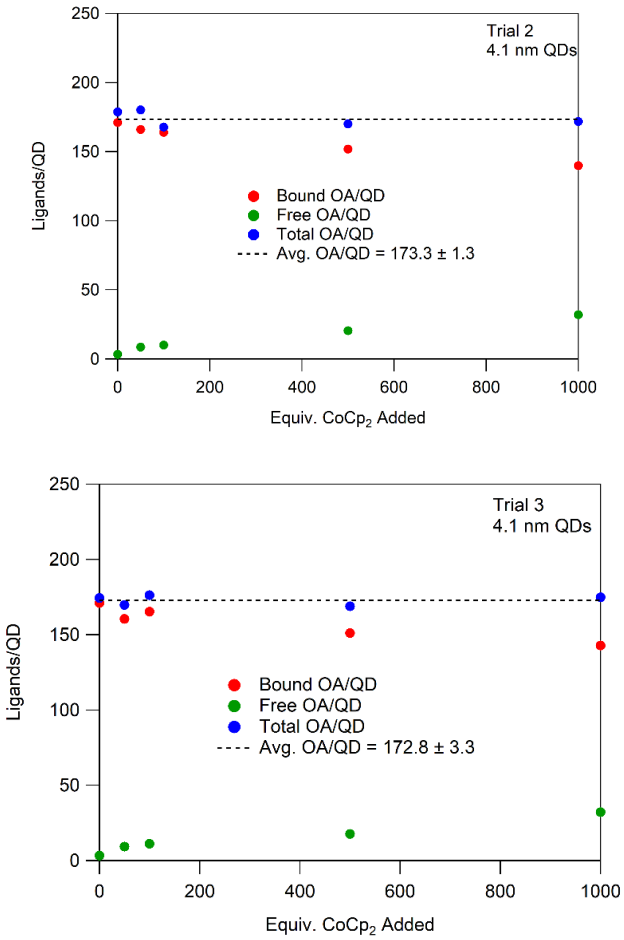

Figure 3.4 Example of calculated ligand coverage from three titrations of $CoCp_2$ with 4.1 nm PbS QDs using the fitting method described in above. The total oleate ligands calculated in solution remained constant up to 1000 eq. $CoCp_2$ added, with an increasing proportion dissociated from the surface.

Table 3.2 Average Pb:S ratios of 4.3 nm PbS QDs before and after mixing with excess $CoCp_2$ in toluene solution for 21 hours, as quantified by X-ray Photoelectron Spectroscopy. Average and standard deviation determined from two identical samples drop cast on Au-coated Si wafers and sampling of two different spots on each wafer for a total of four measurements in each sample.

Sample	**Average Pb:S Ratio**	**Standard Deviation**
QD stock solution	1.81	0.12
QD precipitated control	1.67	0.12
50 eq. $CoCp_2$	1.89	0.20
100 eq. $CoCp_2$	1.71	0.07
500 eq. $CoCp_2$	1.62	0.08

1000 eq. $CoCp_2$	1.72	0.05

Within our system we propose that oleate-bound Pb^{2+} surface ions are reduced to Pb^0 concurrent with ejection of bound anionic oleate ligands; reduction to form surface Pb^0 sites is expected to be stable and would be consistent with reports of Cd^0 formation upon reduction of Cd^{2+} ions at the surfaces of CdSe nanocrystals.[23,40–43] Though formally plausible, Pb^{1+} ions are anticipated to be unstable and, if formed, would likely dimerize with neighboring Pb ions as has been postulated in recent computational studies.[28,29] We were unable to detect direct evidence for Pb-Pb dimers or formation of Pb^0 atoms using XPS spectroscopy (Figure 3.5); however, this could be due to the limited sensitivity of XPS to minor surface subpopulations on QDs. Therefore, the formation of these surface structures upon reduction of Pb^{2+} ions and displacement of oleate ligands cannot be ruled out.

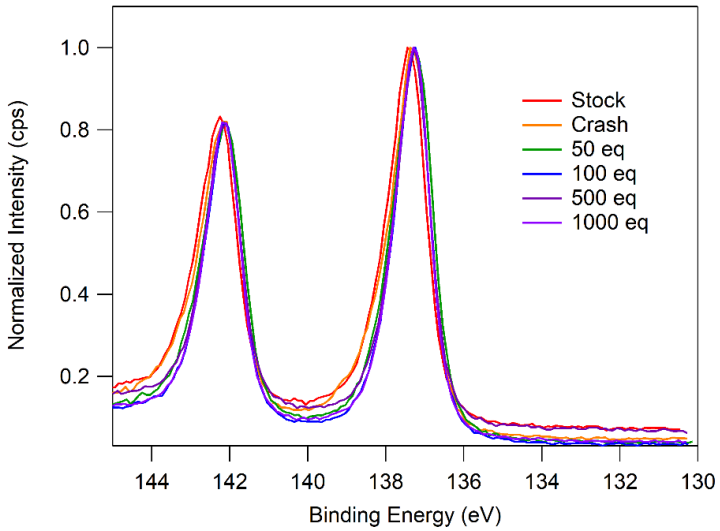

Figure 3.5 Pb 4f XPS spectra of 4.3 nm QDs with ca. 50, 100, 500 and 1000 equiv. $CoCp_2$ added. These changes are not significant enough to indicate formation of Pb-Pb dimers or reduced Pb^0 populations (Pb^0 expected as a new peak at 136.9 eV).[3]

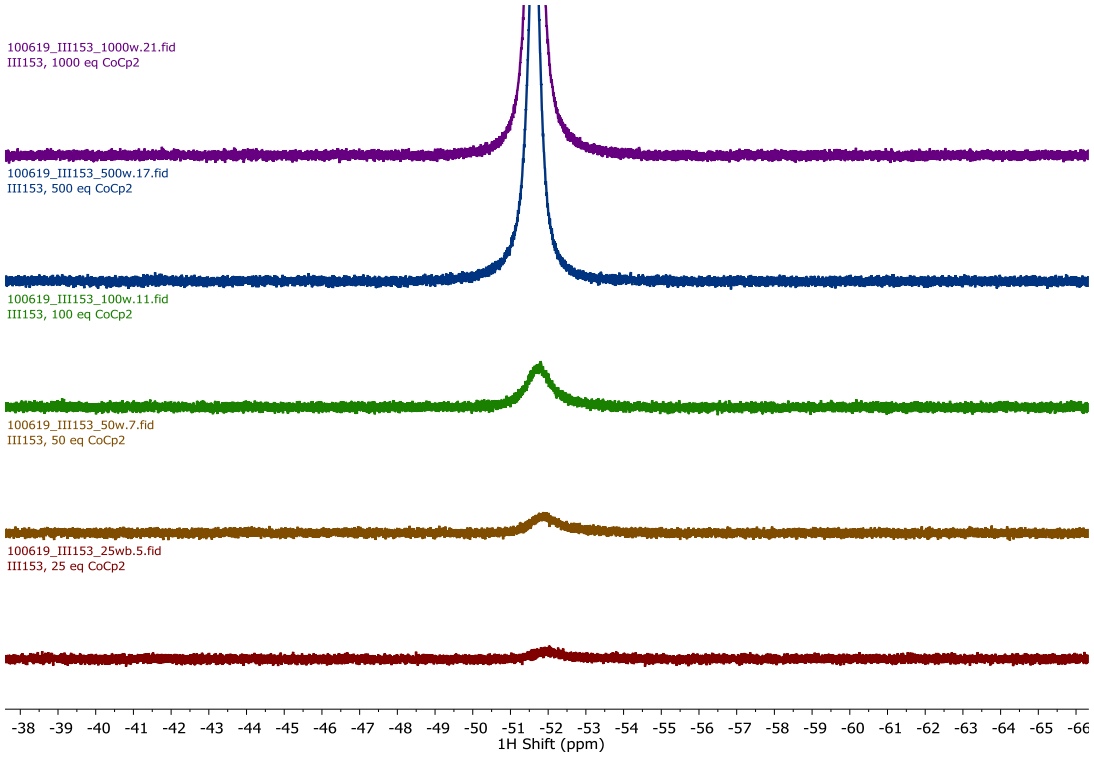

Figure 3.6 ^{1}H NMR spectra of 4.1 nm QDs with added $CoCp_2$ in toluene-d_8, monitoring the paramagnetic $CoCp_2$ resonance at ca. −52 ppm. The presence of unreacted paramagnetic $CoCp_2$ is evident at additions of 25 eq. (red), 50 eq. (orange), 100 eq. (green), 500 eq. (blue), and 1000 eq. (purple).

In addition to monitoring resonances corresponding to the surface capping ligands in the ^{1}H NMR spectra, the reductant $CoCp_2$, and its oxidized product $[CoCp_2]^+$, are also readily detected in the ^{1}H NMR spectra. At all equivalents added (50 – 1000 equiv.), the NMR resonance for paramagnetic $CoCp_2$ is observed at −52 ppm (Figure 3.6). The presence of $CoCp_2$ in the QD samples indicates that while a portion of the reducing agent reacts with the QD (as evidenced by liberation of X-type oleate ligands), not all of the $CoCp_2$ added reacts on the hours-long timescale. Furthermore, a new broad feature is observed at 6.2 ppm after $CoCp_2$ is added (Figure 3.1). We tentatively assign this to the NMR resonance of the cyclopentadienyl protons of the oxidized cobaltocenium ion ($[CoCp_2]^+$). In support of this assignment, we isolated the putative $[CoCp_2]$[oleate] from a mixture of PbS QDs with excess $CoCp_2$ (see **SI**). $[CoCp_2]^+$ is expected to act as a counterion to both reduced surface sites as well as to liberated oleates as a cobaltocenium oleate salt, $[CoCp_2]$[oleate] (Figure 3.7-Figure 3.8).[44]

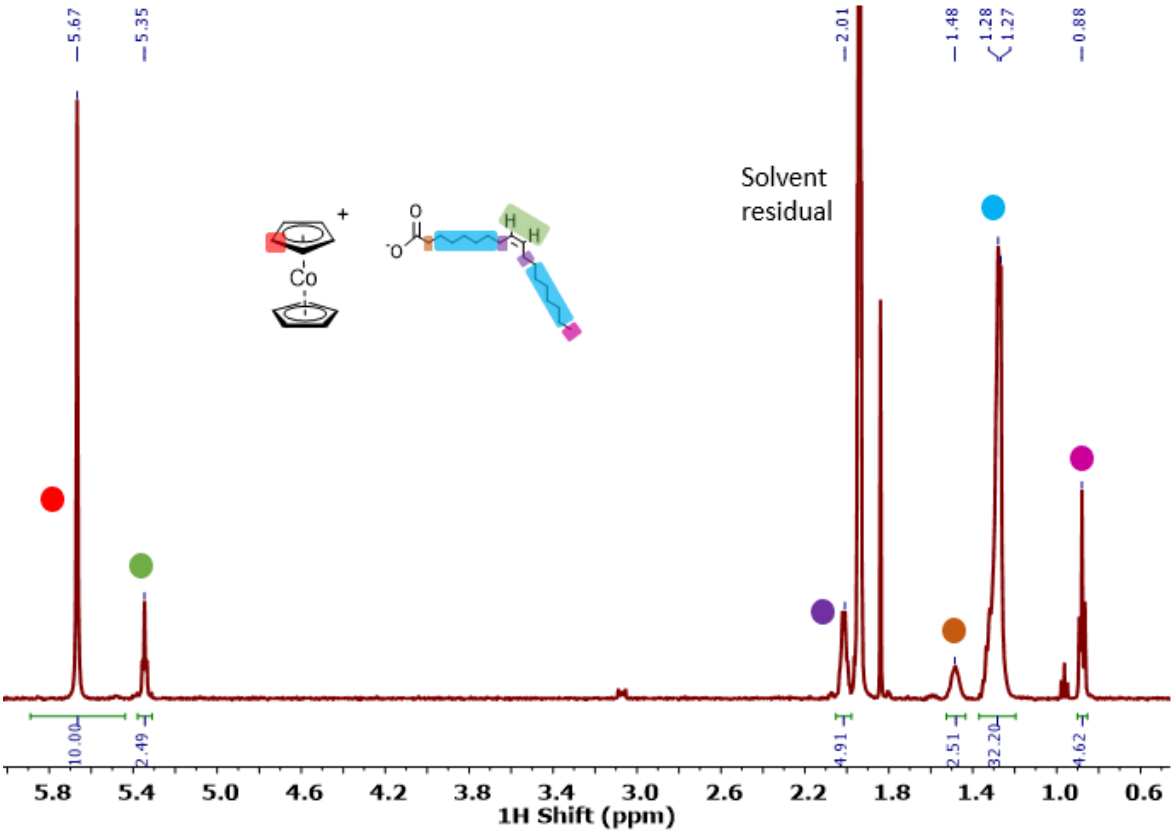

Figure 3.7 ^{1}H NMR in acetonitrile-d_3. Ratio of Cp protons to oleate alkene protons is 10:2.5 (expected ratio is 10:2 for a 1:1 $CoCp_2^+$: OA^- salt) indicating a slight excess of oleate, likely from small amount of $Pb(oleate)_2$ etched during isolation procedure. We anticipate that the integration of the alkyl (blue) and methyl group (pink) resonance integrations are slightly higher than expected due to underlying solvent impurities such as pentane that have overlapping resonances at the same shift..

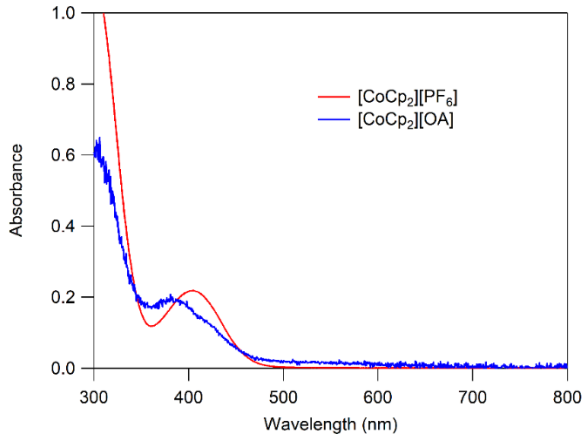

Figure 3.8 UV-Vis absorbance spectra of isolated product $[CoCp_2][OA]$ and $[CoCp_2][PF_6]$ in acetonitrile under N_2 environment.

When samples are allowed to react over the course of days, the relative integration of the paramagnetic $CoCp_2$ resonance decreases (Figure 3.9). Concurrently, oleate ligands continue to dissociate from the QD surface. The slow and continued reactivity over hours and days point towards a gradual equilibration between $CoCp_2$ and surface Pb^{2+} ions. Therefore, all NMR titrations were carefully timed to ensure that all samples mixed for exactly the same period of time (3 hours) prior to collecting spectra to enable precise comparisons in the extent of surface reduction and oleate loss.

Additionally, it is important to note that ^{1}H NMR- silent redox processes are expected to occur in tandem with oleate displacement. For example, underpassivated Pb^{2+} sites or hydroxide-ligated Pb^{2+} ions have been postulated as PbS surface defects in the literature, though these would not be observable by our NMR experiments.[28,29,45] Attempts to detect the presence and reduction of these postulated Pb^{2+} surface sites by XPS (Figure 3.10) and FTIR (Figure 3.11) spectroscopies were inconclusive; however, we cannot eliminate the possibility of small subpopulations of these and similar metal-based sites on the surface reacting with added excess reductant.

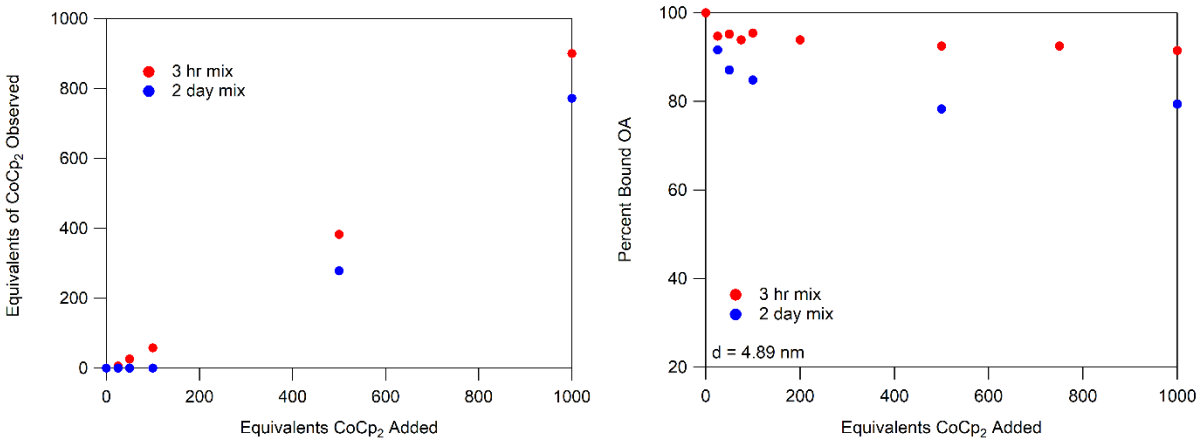

Figure 3.9 (Left) Approximate quantification of $CoCp_2$ using integration of ^1H NMR resonance at −52 ppm relative to internal standard, as determined after 3 hours or 2 days of mixing. (Right) Percentage of bound oleate ligands on 4.9 nm QDs with excess $CoCp_2$ added, determined after 2 hours or 2 days of mixing.

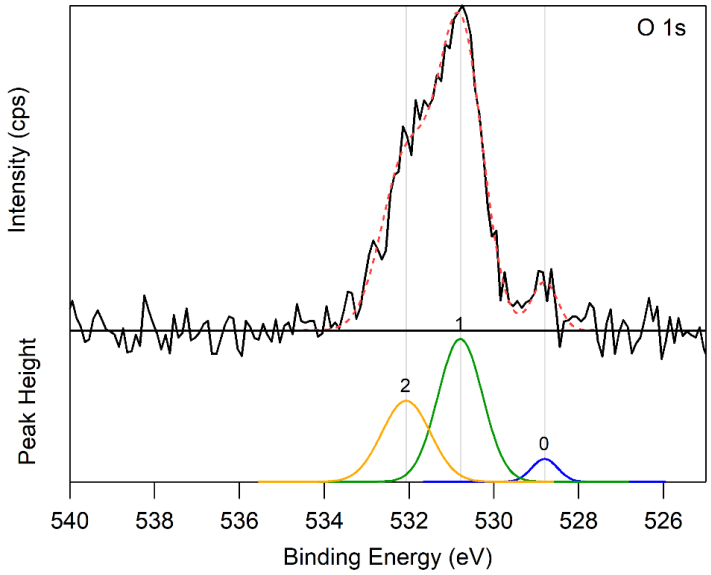

Figure 3.10 O 1s XPS spectrum for 4.3 nm QD (black trace) and fit (dotted red line) with gaussians. Underlying features are evident at 528.8, 530.8, and 532.1 eV (blue, green, and yellow peaks, respectively). These features may be attributed to PbO_x species, and a mixture of contributions from possible Pb-OH and Pb-carboxylate species with multiple binding modes present, respectively.[5,6] This data provides inconclusive evidence for the presence of Pb-OH species in our samples due to the spectral overlap of Pb-OH and Pb-carboxylate species.

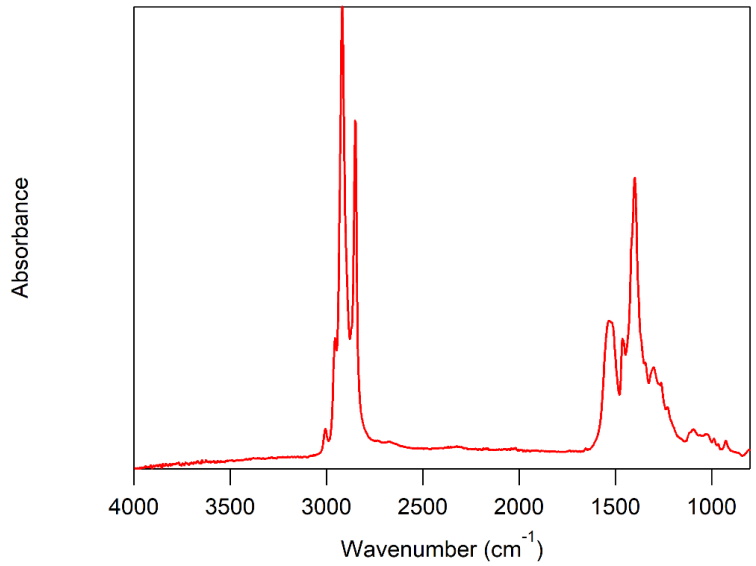

Figure 3.11 ATR-FTIR spectrum of 4.1 nm QD that is representative of the data obtained for the QD batches studied throughout this work. The data shows no evidence of significant hydroxide populations present (expected in the range of ca. 3600 – 3000 cm^{-1}).

3.3.3 QD Surface Reactivity Has A Marked Size Dependence

Having established measurable reactivity (i.e., surface Pb^{2+} ion reduction and oleate displacement) at the surfaces 4.1 nm PbS QDs upon addition of excess $CoCp_2$, we next sought to understand the dependence of surface redox reactivity on QD size. For PbS, QD diameter is known to influence the band edge potentials as well as the morphology and surface facets exposed.[22,30,31] To investigate the influence of these parameters, we prepared several batches of QDs that varied in diameter. Each batch was handled and purified similarly for relevant comparison. To that end, we found that samples prepared by another method[46] did not precisely follow the trends observed below, and we thus restrict our discussion to these samples prepared by the method reported by Hines and Scholes.[47] Three additional sizes of QDs—2.6, 3.8, and 4.9 nm—were prepared and characterized by UV-Vis-NIR absorbance spectroscopy, ^{1}H NMR spectroscopy, TEM, and XPS methods (Table 3.3, Figure 3.12 – Figure 3.15). QDs larger than 5 nm are not compared herein due to problems with solubility and stability of those sizes prepared by the method of Hines and Scholes.[47]

Table 3.3 Data characterizing 2.6, 3.8, 4.1, 4.9 nm QDs used in size-dependence studies

Approximate QD Diameter	**λ_{max}**	**Approximate surface ligand packing density (OA/nm^2)**	**Pb: S ratio as determined by XPS**
2.6 nm	812 nm	3.73 ± 0.13	2.05 ± 0.06
3.8 nm	1120 nm	3.98 ± 0.14	1.84 ± 0.05
4.1 nm	1186 nm	3.34 ± 0.09	1.64 ± 0.13
4.9 nm	1356 nm	2.66 ± 0.12	1.84 ± 0.07

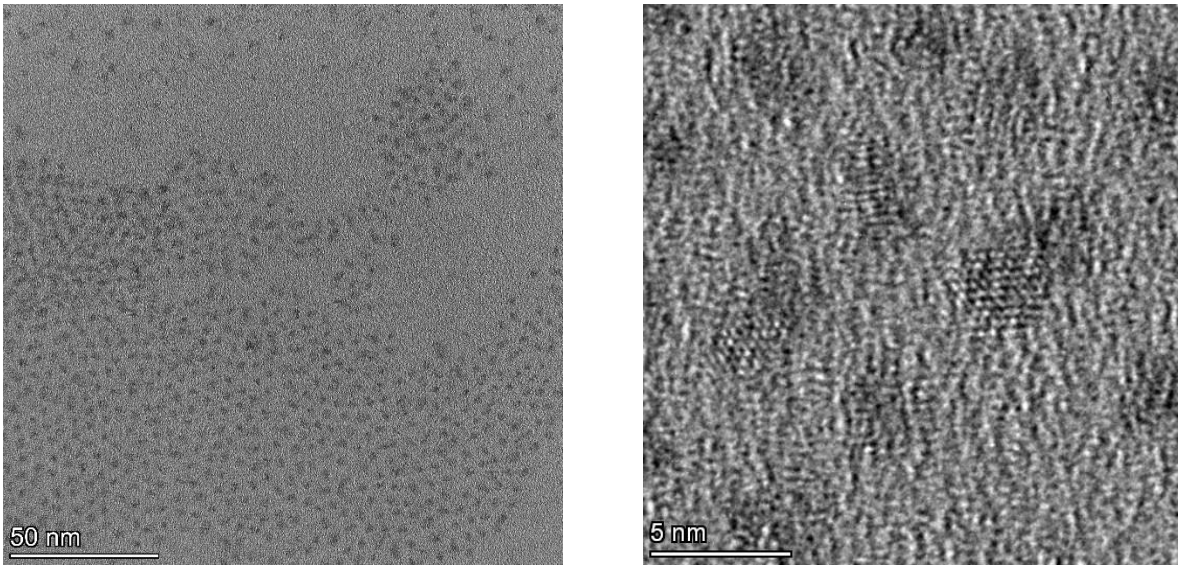

Figure 3.12 TEM images of 2.6 nm PbS QDs

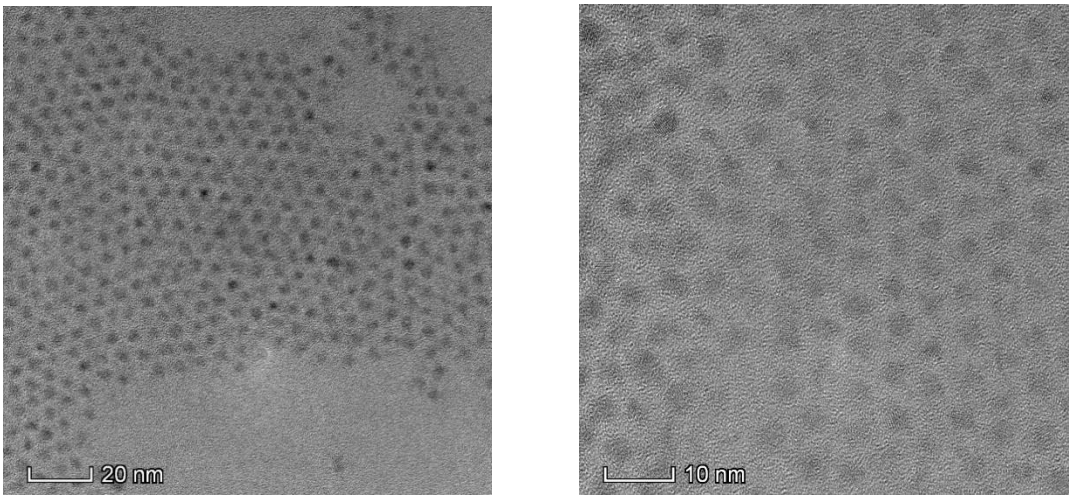

Figure 3.13 TEM images of 3.8 nm PbS QDs.

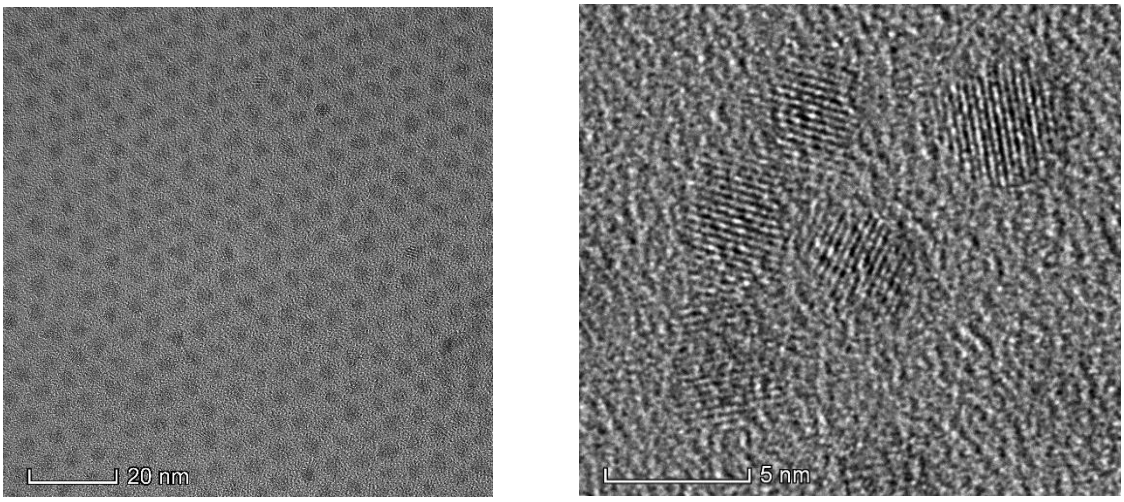

Figure 3.14 TEM images of 4.1 nm PbS QDs.

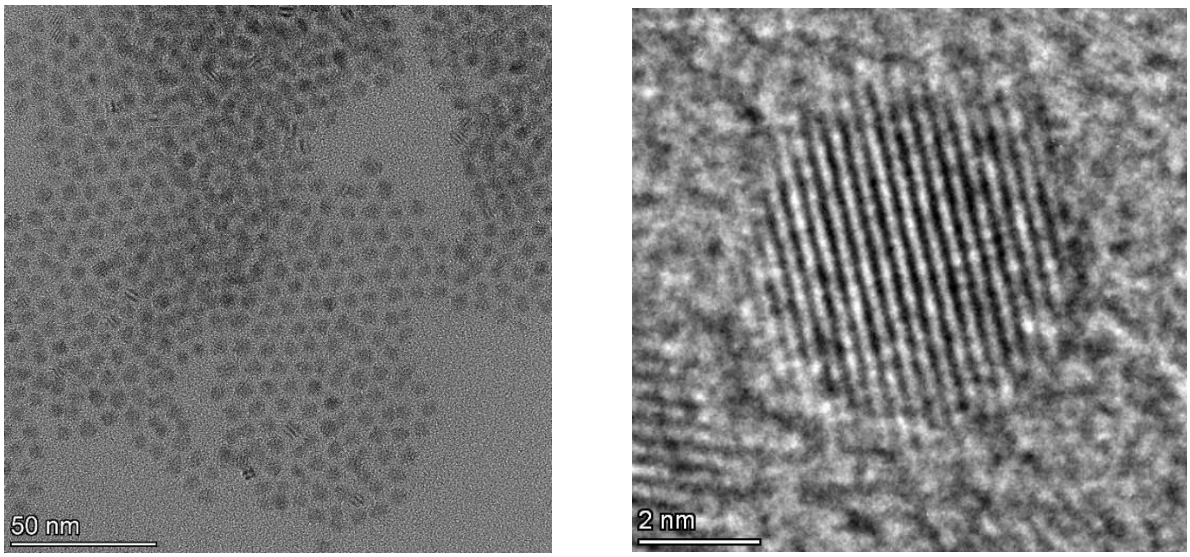

Figure 3.15 TEM images of 4.9 nm PbS QDs

In order to first probe whether $CoCp_2$ is able to directly reduce the CB states of any of these QDs, each sample was titrated with aliquots of $CoCp_2$ and the absorbance monitored via UV-Vis-NIR absorbance spectroscopy (Figure 3.16 – Figure 3.20). As the 4.1 nm QDs did not show any evidence of CB charging, it was not expected that the smaller QDs (2.6 and 3.8 nm) would show an excitonic bleach, as their conduction band edge states are higher in energy. Notably, no excitonic bleach was observed for any of these four samples, indicating that even for the larger 4.9 nm QDs, $CoCp_2$ is too weak of a reductant to engage in ground state electron transfer to the CB edge states of PbS. Many of the PbS QD samples did display a minor red-shift (1 – 4 nm) of the excitonic absorbance feature. This red shift is an indicator of surface charging resulting from Coulombic repulsion with the delocalized exciton or a Stark effect.[48]

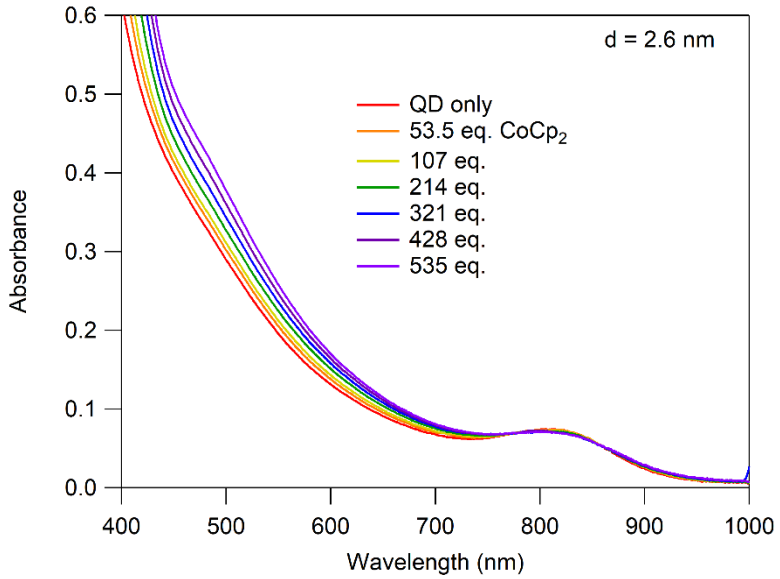

Figure 3.16 UV-Vis-NIR absorbance spectra of 2.6 nm PbS QDs (1.5 µM) with added $CoCp_2$ in toluene.

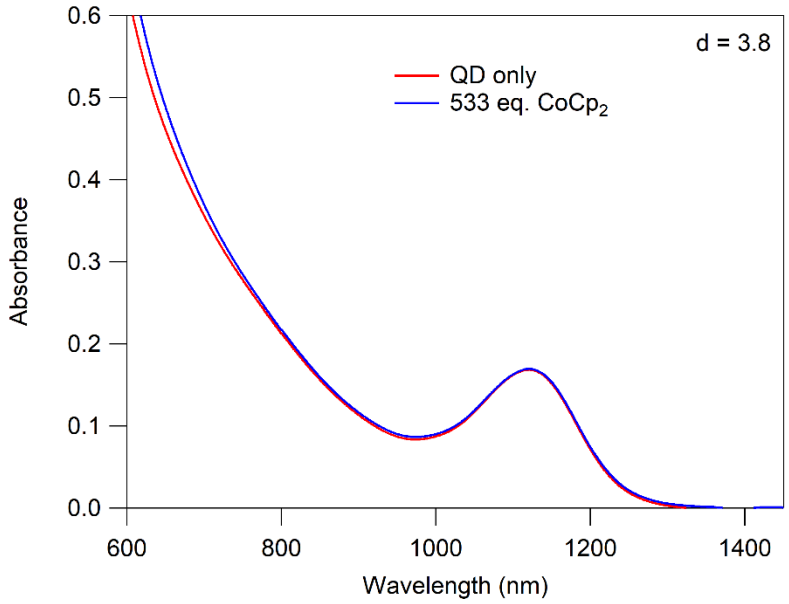

Figure 3.17 UV-Vis-NIR absorbance spectra of 3.8 nm PbS QDs (2 µM) with added $CoCp_2$ in toluene.

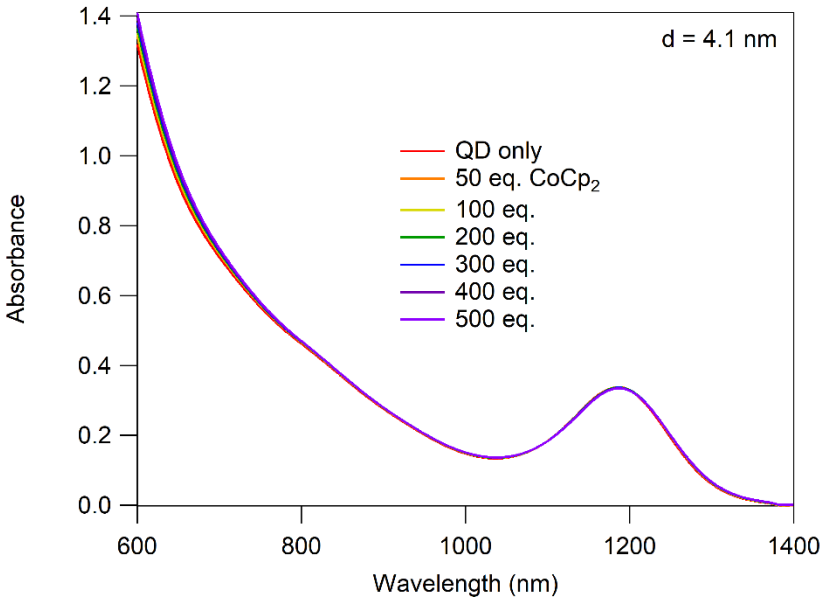

Figure 3.18 UV-Vis-NIR absorbance spectra of 4.1 nm PbS QDs (3.1 µM) with added $CoCp_2$ in toluene.

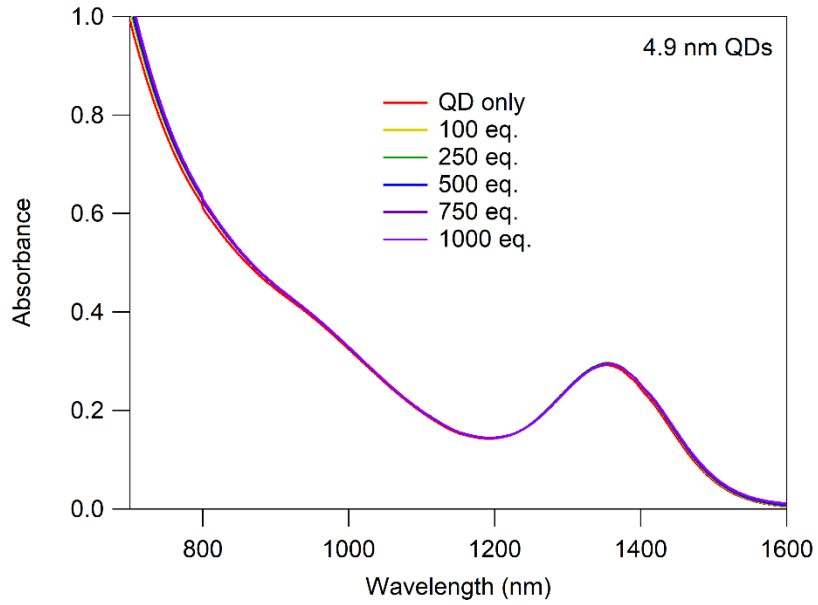

Figure 3.19 UV-Vis-NIR absorbance spectra of 4.9 nm PbS QDs (2.5 µM) with added $CoCp_2$ in toluene.

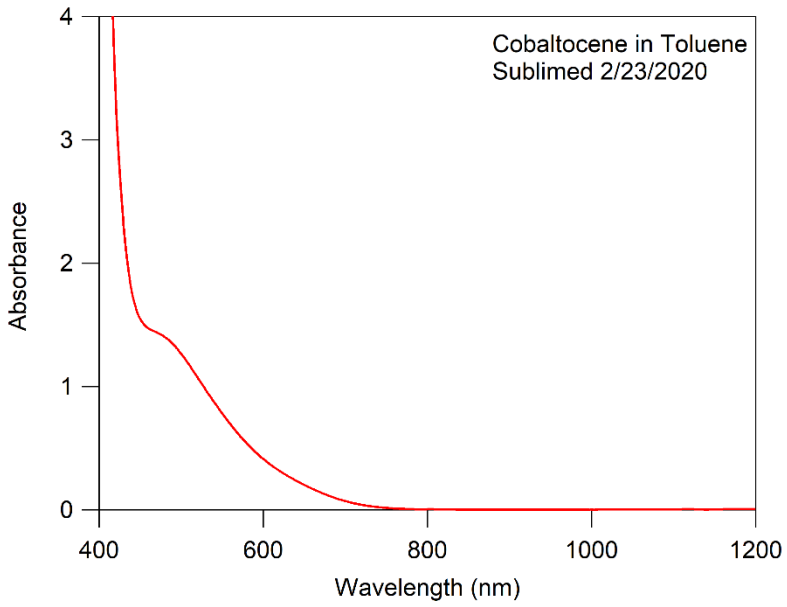

Figure 3.20 UV-Vis-NIR absorbance spectra of $CoCp_2$ in toluene. Increase in absorbance at shorter wavelength shoulder in absorbance spectra above is likely a result of absorbance from unreacted $CoCp_2$ remaining in solution at higher equivalents added.

Titrations of these three additional QD samples with $CoCp_2$ were then monitored with ^{1}H NMR spectroscopy in order to compare the extent of reactivity with added charge. Addition of excess of $CoCp_2$ (0 – 1000 equiv.) resulted in varying degrees of oleate displacement for the different sizes (see Appendix B). The average percentages of bound oleate ligands (normalized for any minor amounts of free ligand present in the as-synthesized QD sample) are presented in Figure 3.21. The data show a clear trend of greater oleate loss with increasing QD size: after mixing for 3 hours with 1000 equiv. $CoCp_2$, 1.2 ± 1.1% of the bound oleates are displaced from 2.6 nm QDs, 3.5 ± 1.4% from 3.8 nm QDs, 14.7 ± 3.2% from 4.1 nm QDs, and 11.1 ± 2.1% from 4.9 nm QDs. The broad feature at 6.2 ppm attributed to $[CoCp_2]^+$ is observed in all QD samples with $CoCp_2$ added, as is the presence of paramagnetic $CoCp_2$ at −52 ppm.

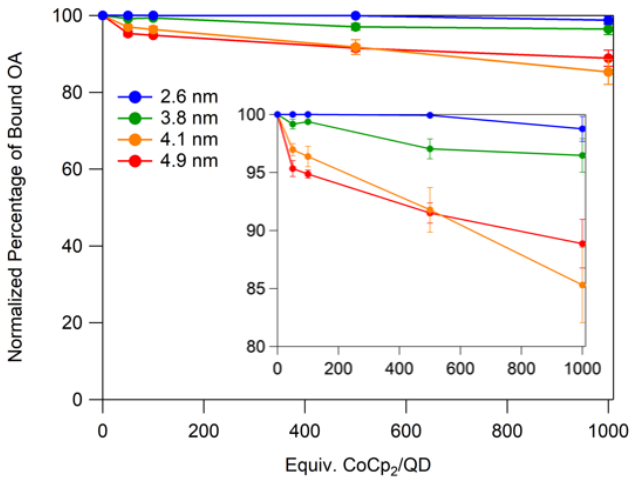

Figure 3.21 Comparison of different sizes of QDs with added $CoCp_2$, normalized for minor amounts of free ligand in QD only ^1H NMR spectra. Data points are the average of three repeated trials with standard deviation included as error bars. The lines between data points are a guide to the eye. Inset: Data plotted with smaller y-axis range for clearer depiction of trends.

We interpret the trend of greater amounts of displaced oleates observed for larger QDs by considering changes in the PbS QD surface environments with size. Several recent compelling works have demonstrated that PbS QDs transition from an octahedral morphology to a cuboctahedral shape with increasing diameter.[22,30,31] This in turn impacts the types of facets and bonding environments at the surface that are exposed. For example, small octahedral PbS QDs (< 3 nm) are known to be lead-rich with polar (111) facets exposed. Conversely, larger QDs tend to be more stoichiometric in Pb and S ions, and it has been proposed that additional neutral (100) facets begin to appear on QDs larger than ~3 nm diameter.[22,30,31] Additionally, the larger QD sizes in this study possess lower ligand packing densities than the smaller QDs (Table 3.3) which suggests that the surfaces of larger QDs may be more accessible to reducing agents.

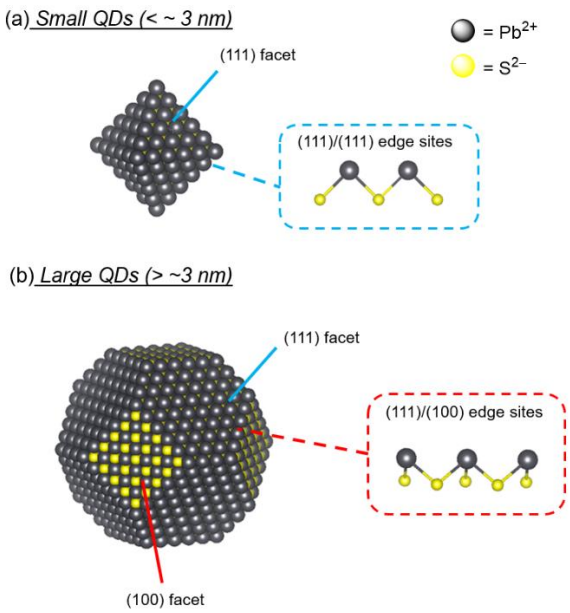

Figure 3.22 PbS QDs have been shown to exhibit a size dependent morphology where (a) small QDs possess an octahedral shape and (b) larger QDs a cuboctahedral shape. (100) facets are present on surfaces of large PbS QDs, and new Pb environments emerge at these facets as well as at (111)/(100) facet edge sites.

The size dependence of exposed Pb coordination environments at the surface likely impacts the extent of ligand displacement observed upon reduction by $CoCp_2$. Importantly, surface Pb^{2+} ions that are reduced by $CoCp_2$ to liberate oleate ligands are anticipated to be at approximately the same free energy (as quantified by their reduction potential) regardless of QD size. Therefore, the greater proportion of oleates displaced in larger QD sizes suggests that there is a larger relative number of those specific types of Pb^{2+} sites in larger QDs. While the NMR studies themselves cannot indicate distinct ligand bonding environments, the size dependence observed here suggest that the Pb^{2+} sites most likely to be reduced by $CoCp_2$ may be those at the edges between (111) and (100) facets as those appear on larger size QDs (Figure 3.22). Reduction of Pb^{2+} ions within the (100) facets present on the larger QDs is less likely due to the overall charge neutrality of those facets as well as being less sterically accessible than edge sites.[22,45].

3.3.4 The Extent of QD Surface Charging Tracks with Reductant Strength

In order to gain a more holistic understanding of the redox reactivity of the surfaces of PbS QDs, we next probed the dependence of surface reactivity on the potency of the reductant employed. To do this, both milder and stronger reductants than $CoCp_2$ (Table 3.4) were reacted with PbS QDs and the extent of reactivity (i.e., oleate displacement in ^{1}H NMR studies) compared. For these redox-reagent dependence experiments, additional batches of PbS QDs ranging in size from ca. 3 – 5 nm were employed in addition to those studied in the size-dependence experiments above. These studies provide insight into the effect of driving force on surface reduction.

We first employed two reductants milder than $CoCp_2$, decamethylferrocene ($FeCp^*_2$) and Co(Cp)(dppe), and monitored their reactivity with 4.3 nm PbS QDs. Upon reaction of 4.3 nm QDs with ca. 500 equiv. of each redox agent, less ligand loss was observed compared with $CoCp_2$ as shown with ^{1}H NMR spectroscopy). Specifically, <1% oleate loss was observed upon addition of excess $FeCp^*_2$ and ~2.5 – 4% with added Co(Cp)dppe, compared with ~6% ligand displaced with added $CoCp_2$. This diminished reactivity with milder reducing agents illustrates the influence that the reductant strength has on the extent of surface charging.

Table 3.4 Chemical Redox Probes Used in This Chapter[34,49]

Chemical Probe	Reduction Potential ($E^{o\prime}$, V vs. $Fc^{+/0}$)	Energy vs. Vacuum[d] (eV)
Decamethylcobaltocene, $CoCp^*_2$	−1.91[a]	−3.22
Cobaltocene, $CoCp_2$	−1.33[b]	−3.80
Co(Cp)(dppe)[c]	−0.93[b]	−4.20
Decamethylferrocene, $FeCp^*_2$	−0.48[a]	−4.65

a. Reported conditions in CH_3CN with $[Bu_4N][PF_6]$
b. Reported conditions in CH_2Cl_2 with $[Bu_4N][PF_6]$
c. dppe = 1,2-bis(diphenylphosphino)ethane
d. Conversion to energy from reduction potential shown in SI

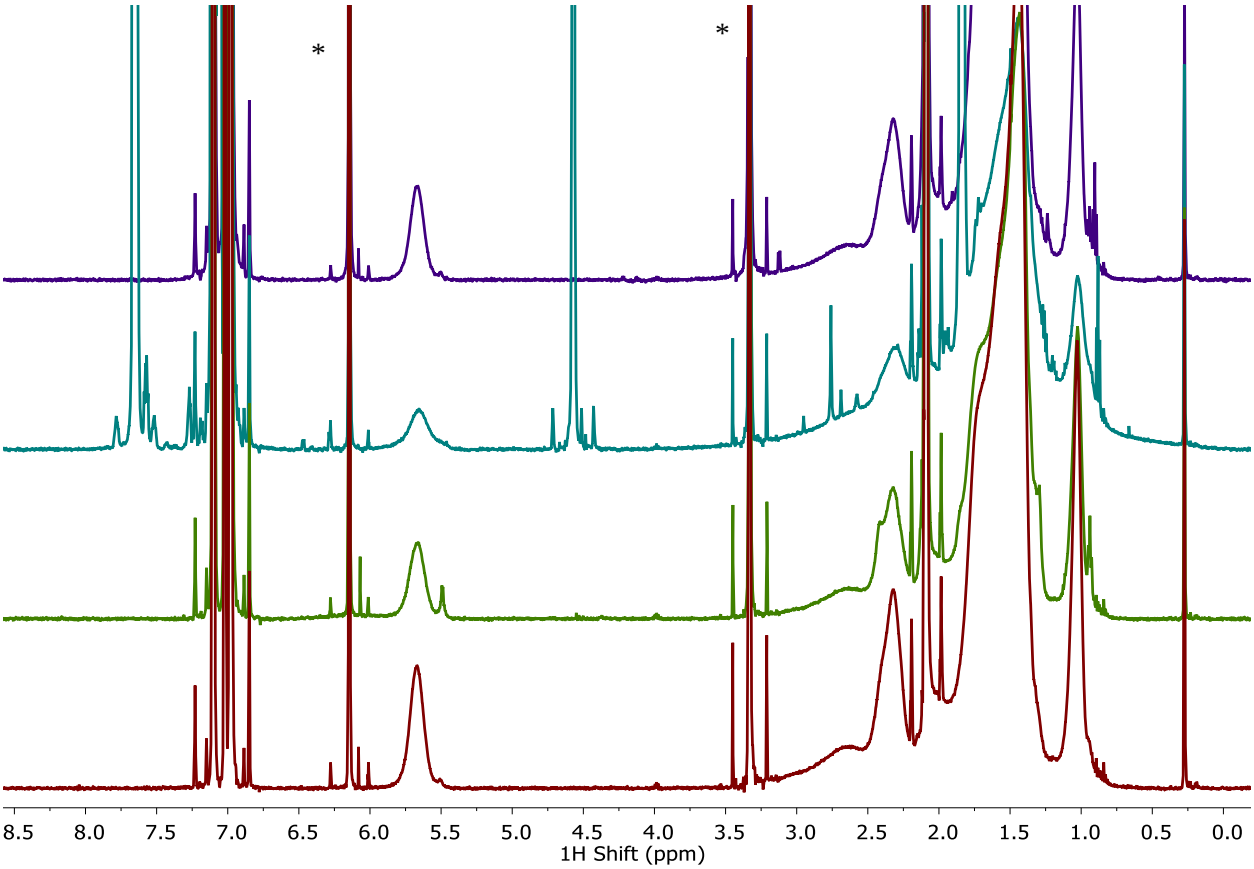

Figure 3.23 ^{1}H NMR titration of 27.7 µM PbS QDs (4.3 nm) alone (red) or with ~ 500 eq. $CoCp_2$ (green), Co(Cp)(dppe) (blue) or $FeCp^*_2$ (purple) in toluene-d_8. (*) denotes internal standard 1,3,5-trimethoxybenzene. NMR spectra collected on 600 MHz NMR with cryoprobe utilizing d1 delay of 30 seconds with 12 scans.

To further establish the relationship between surface charging and reductant strength, we next moved to a reductant stronger than $CoCp_2$, decamethylcobaltocene ($CoCp^*_2$). Due to the strongly reducing nature of $CoCp^*_2$ and estimated literature values for PbS CB edge potentials—ranging from −3 eV to ca. −4.2 eV (with respect to vacuum) across sizes from 2 nm to 8 nm, respectively—we anticipated that $CoCp^*_2$ could directly inject electrons into QD CB edge states.[33,35] Addition of 50 equiv. $CoCp^*_2$ to 4.9 nm PbS QDs in 1:1 THF: toluene resulted in a significant bleach of the excitonic absorption feature, as detected by UV-Vis-NIR absorbance spectroscopy, consistent with electron injection into the CB states (Figure 3.24a). Notably, the excitonic bleach recovers within minutes (Figure 3.25). This observation is consistent with a previous report by Koh et al. that suggested that delocalized CB electrons in PbS QDs may localize at surface sites over time.[35]

^{1}H NMR titrations were next performed to assess whether the more negative reduction potential of $CoCp^*_2$ has an impact on the amount of oleate displacement observed. Incremental addition of $CoCp^*_2$ (5 – 100 equiv.) to 4.9 nm QDs leads to a dramatic decrease in oleate coverage, with up to 60% of bound oleates lost (Figure 3.24b). Interestingly, the quantification of displaced oleate ligands corresponds closely with a 1:1 loss for each equivalent of $CoCp^*_2$ added up to 10 equiv., and then slightly greater ratio of approximately 1.2 – 1.4 oleates lost per equiv. $CoCp^*_2$ added with 25 – 100 equiv. (Table 3.5). The excess oleate ligands displaced per equivalent of $CoCp^*_2$ added suggests that there may be a more complex ligand displacement mechanism at play in the higher equivalent regime. For example, $CoCp^*_2$ may be capable of reducing spectroscopically silent surface states, the reduction of which could promote surface rearrangement leading to some Z-type ligand dissociation.

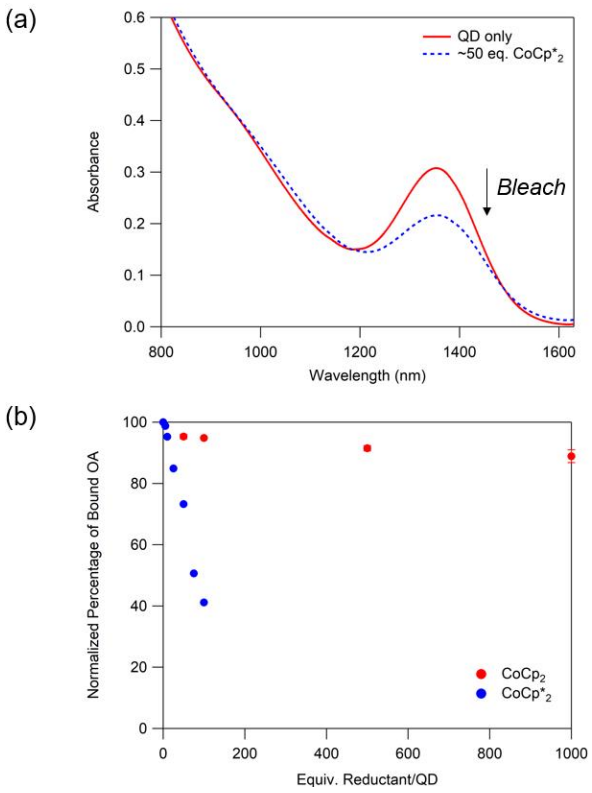

Figure 3.24 (a) UV-Vis-NIR absorption spectra of 4.9 nm QDs (2.5 µM) in 1:1 THF:toluene before (red) and after (blue) addition of ca. 50 equiv. $CoCp^*_2$. (b) Comparison of the percentage of bound oleate per

QD in 4.9 nm PbS QDs (27.7 µM) with added $CoCp_2$ (red) and $CoCp^*_2$ (blue). NMR spectra of $CoCp^*_2$ titration in Figure 3.26.

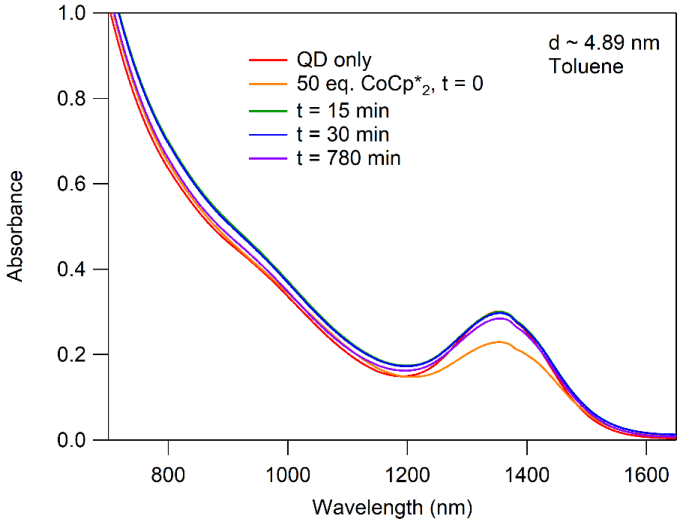

Figure 3.25 UV-Vis-NIR absorbance spectra of 4.9 nm PbS QDs (2.5 µM) with 50 eq. $CoCp^*_2$ in toluene recorded at various time points after mixing.

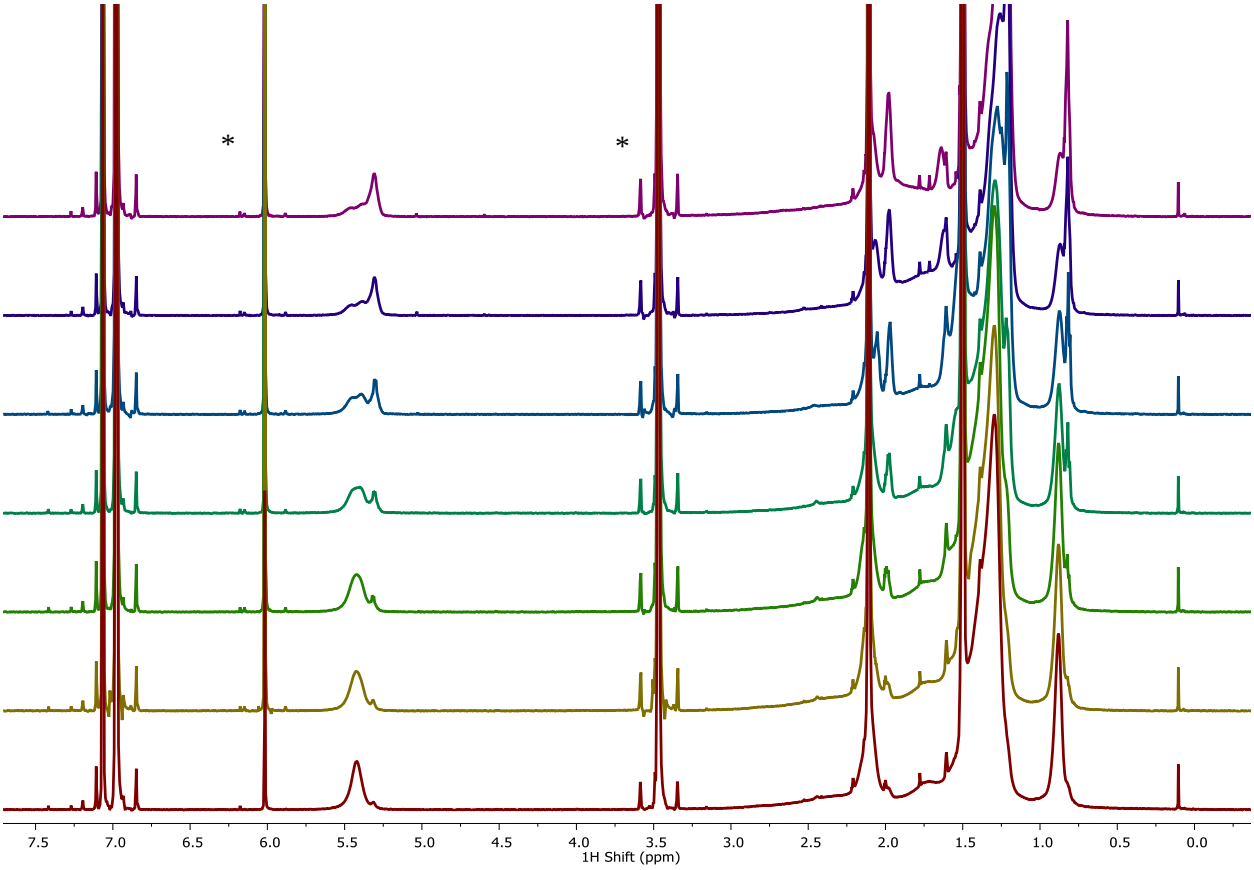

Figure 3.26 Full ^{1}H NMR titration of 27.7 µM PbS QDs (4.9 nm) with 0 (red), 5 (orange), 10 (light green), 25 (dark green), 50 (blue), 75 (purple), and 100 (magenta) eq. $CoCp^{*}_{2}$ added in 1:1 toluene-d_8: THF-d_8 corresponding to Figure 3.24. (*) denotes internal standard 1,3,5-trimethoxybenzene. NMR spectra collected on 600 MHz NMR with cryoprobe utilizing d1 delay of 30 seconds with 12 scans.

Table 3.5 Bound oleate ligand loss of 4.9 nm QDs upon addition of $CoCp^{*}_{2}$

Equivalents $CoCp^{*}_{2}$/QD	**Displaced ligands per QD from addition of reducing agent**
0	0
5	2.5
10	9.9
25	31
50	58
75	103
100	122

Furthermore, unlike for milder reductants and $CoCp_2$, we observe complete consumption of the $CoCp^{*}_{2}$ as evidenced by lack of a paramagnetic resonance for $CoCp^{*}_{2}$ expected at ca. 45 ppm. Addition of $CoCp^{*}_{2}$ in greater excess (>100 equiv./QD) results in rapid QD precipitation, indicating that loss of a large percentage of passivating surface ligands leads to QD instability. The dramatic increase in oleate displacement observed with $CoCp^{*}_{2}$ addition is likely a direct result of the greater driving force for reduction of the same Pb surface sites that react with $CoCp_2$, as well as reduction of higher energy populations of Pb ions that are perhaps inaccessible to milder reductants even at high concentrations. Additionally, another pathway for surface reduction by $CoCp^{*}_{2}$ is also possible wherein electrons initially injected into the CB edge are subsequently trapped at lower energy surface sites as evidenced by the recovery of the excitonic bleach on a minutes-long timescale,[35] leading to further oleate ligand displacement upon localization at the surface. These surface reduction pathways may occur simultaneously and are not necessarily mutually exclusive.

Overall, these studies reveal the marked impact of reductant strength on the extent of surface charging as indicated by the extent of oleate loss. The lesser degree of reactivity of the QD surface sites with reductants milder than $CoCp_2$, along with the more dramatic reactivity upon reaction with stronger reductants such as $CoCp^*_2$, suggests that the slow equilibration between $CoCp_2$ and PbS QD surface states observed arises because the reduction potential of $CoCp_2$ is approximately isoenergetic with the reduction potential of a portion of the surface Pb^{2+} sites (Figure 3.27). This equilibration leads to gradual oleate ligand displacement over time. These Pb^{2+} surface sites are not energetically accessible by the weaker reductants employed. By comparison, more potent reductants increase the driving force for surface Pb^{2+} ion reduction leading to more rapid and complete surface charging, as well as conduction band population.

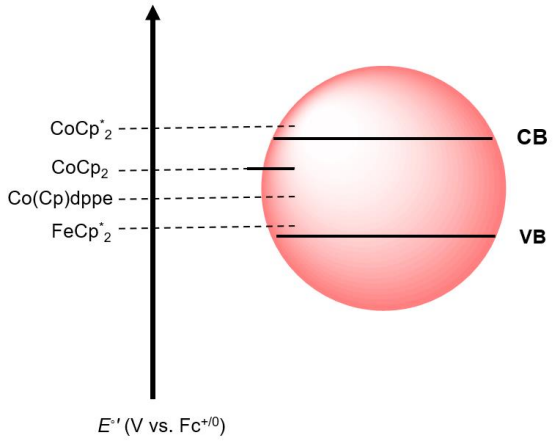

Figure 3.27 Depiction of the relative redox potentials of the redox-active probes used in this study versus band edge or surface-based electronic states in PbS QDs ranging in size from 2.6 to 5.1 nm.

While the driving force for electron transfer from a reductant may in theory be predicted by comparing the reduction potential of the reagent with the reduction potentials of the localized surface and CB edge states of QDs, precise measurement of the latter values is quite challenging in practice. As such, our conclusions are not trivial. Though reduction potential values for band edge states have been reported for thin films of QDs using techniques such as photoelectron emission spectroscopy and electrochemistry, these values inherently differ from those describing colloidal QDs due to differences in the nanocrystal

environment.[17,33,50] Additionally, the accuracy of reported values across all systems is questionable: variations in QD synthesis and purification methods, solvents and the influence of capping ligands via surface dipoles directly impact the absolute band edge positions.[51,52] As the reduction potentials of QD band edge and surface states are difficult to measure directly, the use of redox-active chemical probes spanning a wide range of reduction potentials therefore provides an indirect method to gauge the electronic state potentials based on the extent of reactivity observed by techniques such as UV-Vis-NIR absorbance or NMR spectroscopy.

3.3.5 Hypothesized Chalcogenide Defects may be Studied by Selective Probes

Following the above studies monitoring surface Pb^{2+} ion reduction by oleate ligand displacement, we sought to gain a more complete picture of other redox-active sites at PbS QD surfaces. The use of redox-active chemical probes can provide insight into sites that have been proposed experimentally and computationally.

Chalcogenide ions have been proposed as redox-active sites on the QD surface, though specific defect subpopulations can be quite challenging to probe experimentally.[7,24,29,53] In particular, oxidized S^{1-} species are expected to exist as stable disulfide dimers on as-synthesized QD surfaces.[24] To probe the presence of surface disulfides, studies were performed using a selective redox-active chemical probe. Tri-*n*-butylphosphine (Bu_3P) has been established to selectively reduce organic diselenides and disulfides.[24,54] Experiments in our lab confirm this reactivity for diphenyl disulfide, which is readily reduced to sulfates upon addition of Bu_3P in the presence of NaOH, yielding tri-*n*-butylphosphine oxide as a byproduct that may be monitored by $^{31}P\{^{1}H\}$ NMR spectroscopy (Figure 3.28).

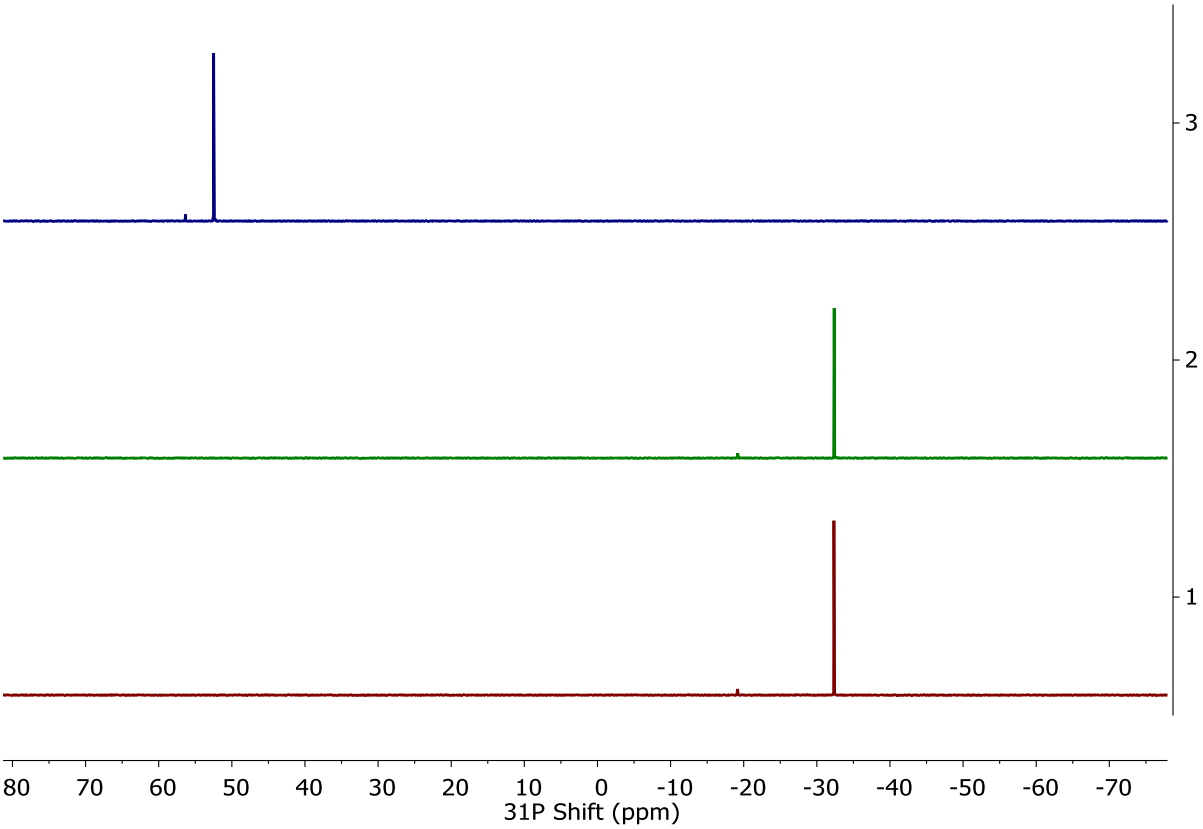

Figure 3.28 $^{31}P\{^{1}H\}$ NMR of 83 mM Bu_3P in THF (red), 83 mM Bu_3P with 2 equiv. NaOH in degassed water in THF (green), and 83 mM Bu_3P with 83 mM diphenyl disulfide and 2 equiv. NaOH in THF (blue).

Scheme 3.2 Reduction of Disulfide Moieties Using Tri-*n*-butylphosphine

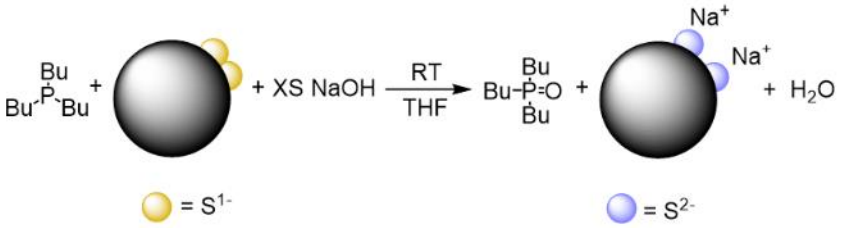

While reactions of Bu_3P with organic disulfides support the theory that disulfide dimers on QD surfaces may be reducible, to the best of our knowledge the presence of these chalcogenide dimers on individual QD surfaces has not yet been directly experimentally confirmed. To study this directly, PbS QDs were treated with Bu_3P in the presence of NaOH and monitored by $^{31}P\{^{1}H\}$ NMR spectroscopy for

evidence of Bu_3PO formation as a handle for disulfide reduction (Scheme 3.2). Notably, as demonstrated by a lack of broad features in the $^{31}P\{^1H\}$ NMR spectra, Bu_3P does not appear to bind to the PbS QD surface (Figure 3.29). Addition of approximately 1000 equiv. Bu_3P to solutions of PbS QDs in THF in the presence of 50 equiv. NaOH led to differing results for small (3.4 - 3.7 nm) versus large (4.7 – 5.1 nm) QD samples. Smaller QDs show very little reactivity; little to no Bu_3PO formation was observed even over several days (Figure 3.30). By comparison, in larger QDs, approximately 1% of the added Bu_3P (ca. 10 equiv./QD) was converted to Bu_3PO, indicating reactivity of the phosphine with surface disulfides (Figure 3.31). This size dependence may arise from the influence of morphology and surface stoichiometry on the relative population of these disulfide traps, where larger QDs may reveal disulfides on exposed (100) facets that are not present on smaller, octahedral nanocrystals. These results suggest that the (100) facets and (100)/(111) facet edges may be the most likely sites for disulfide defects to arise. Importantly, under the conditions employed we did not detect any reaction between Bu_3P and $Pb(oleate)_2$, confirming that the observed reactivity was due to surface sulfide species (Figure 3.32).

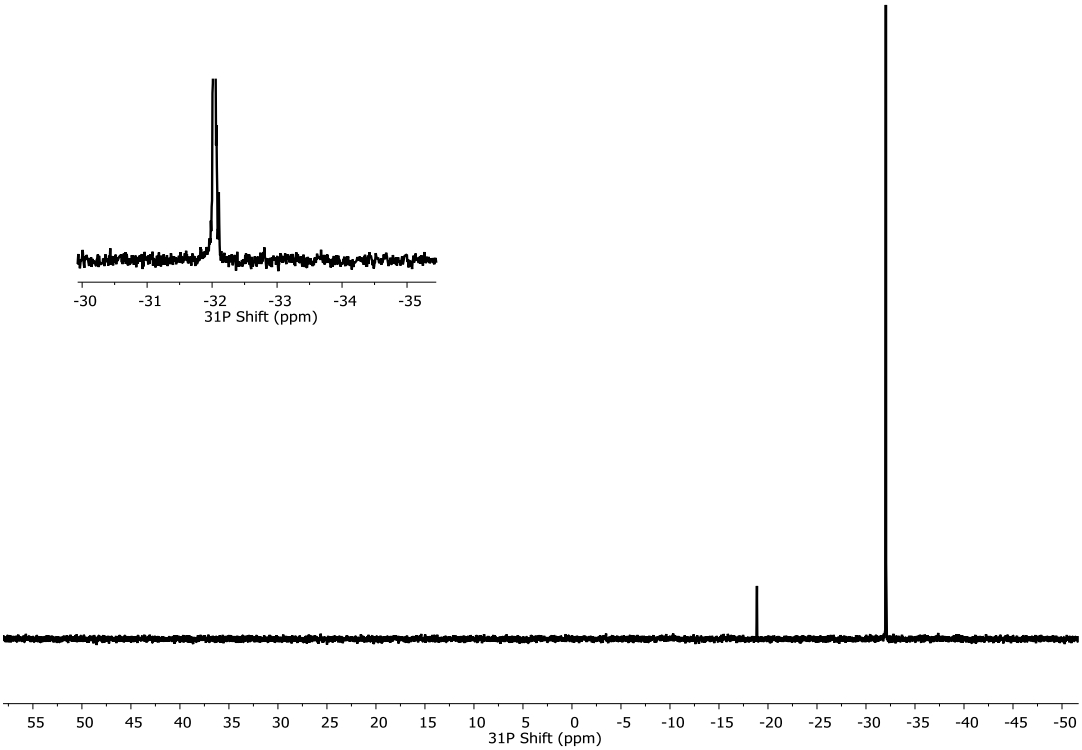

Figure 3.29 $^{31}P\{^{1}H\}$ NMR of 3.7 nm QD in THF (48 µM) with 1000 eq. Bu_3P added. Inset: Zoom-in of Bu_3P resonance at ca. −32 ppm. No significant broad features are present that would indicate binding of Bu_3P to the QD surface.

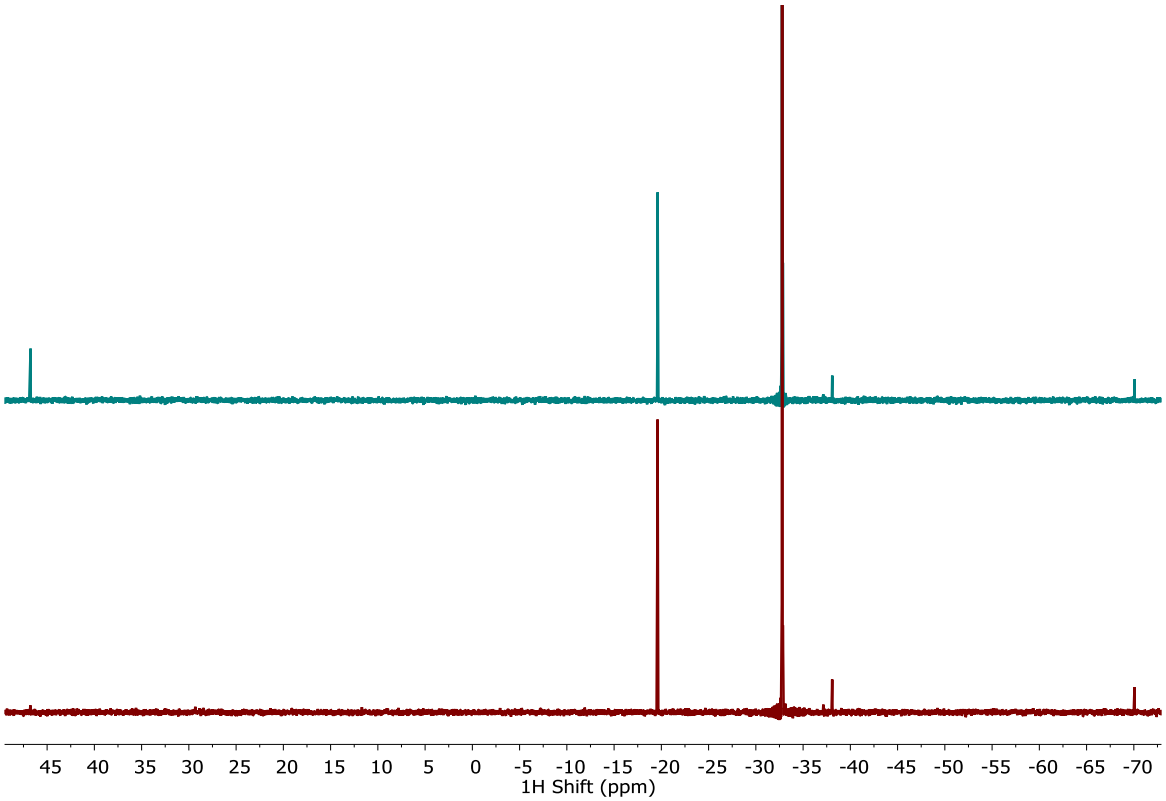

Figure 3.30 $^{31}P\{^{1}H\}$ NMR of 29.7 µM 3.4 nm PbS QD (red) and 21.9 µM 4.7 nm PbS QD (blue) in THF with 50 eq. NaOH in degassed deionized water with 1000 eq. Bu_3P added. NMR spectra collected on a 600 MHz NMR spectrometer.

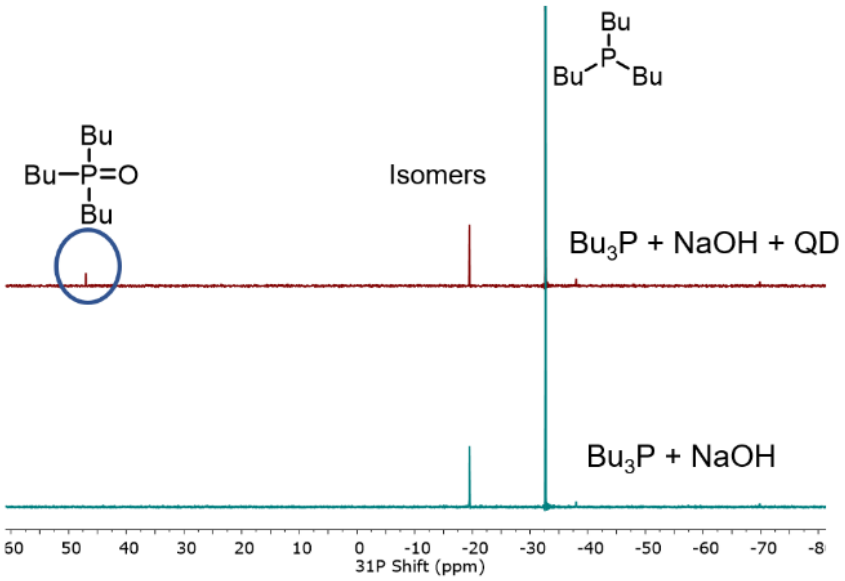

Figure 3.31 $^{31}P\{^{1}H\}$ NMR spectrum of (bottom) Bu_3P (28 mM) in THF with NaOH in degassed water. (top) 5.1 nm PbS QDs (29 µM) in THF with ~1000 equiv. Bu_3P and 50 equiv. NaOH in degassed water.

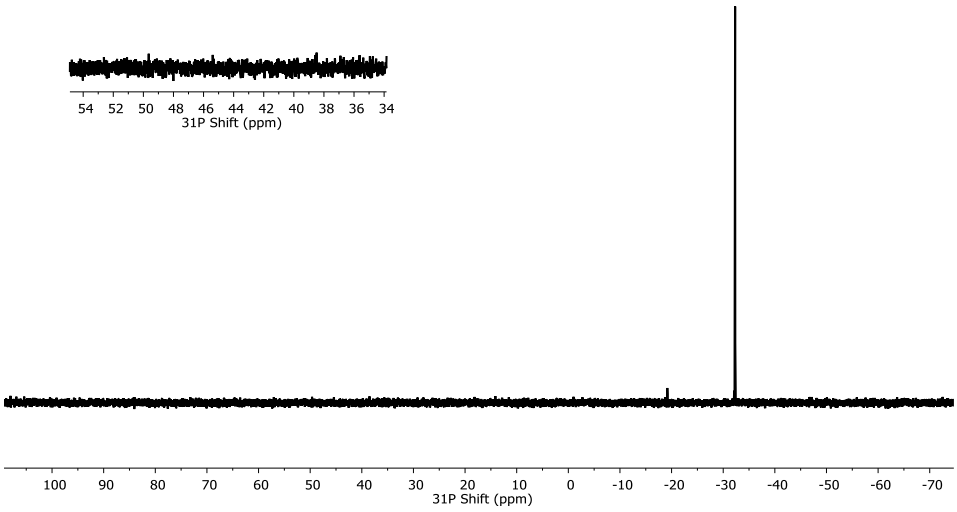

Figure 3.32 $^{31}P\{^{1}H\}$ NMR of 58 mM Bu_3P with 29 mM $Pb(oleate)_2$ in 2:1 Toluene: THF with 116 mM NaOH in degassed deionized water after mixing for 15 minutes. No major changes were observed after 3 days. Notably, there were problems with miscibility upon addition of NaOH in water to the solution of $Pb(oleate)_2$ and Bu_3P, and some $Pb(oleate)_2$ visibly precipitated out due to low solubility in water. NMR spectrum collected on a 500 MHz NMR spectrometer.

Lewis bases such as trialkylphosphines are known to displace Z-type ligands from QD surfaces at high concentrations; as such, it was important to rule out $Pb(oleate)_2$ displacement as a primary cause for the disulfide reactivity detected.[21,22,30] Specifically, we sought to determine whether the reactivity observed was caused by Bu_3P first displacing $Pb(oleate)_2$ to reveal underlying disulfide structures. ^1H NMR spectra show minimal change in bound versus free ligand populations (Figure 3.33 – Figure 3.34) of both 3.4 and 4.7 nm QDs with 1000 equiv. Bu_3P added, suggesting that this is not a dominant mechanism for the observed reactivity. Overall, the studies with a selective redox active probe, Bu_3P, provide compelling evidence for the existence and reactivity of surface disulfides on as-synthesized PbS QD surfaces. This work therefore serves as an example of using targeted experimental approaches to confirm or rule out the existence of hypothesized defect structures at QD surfaces.

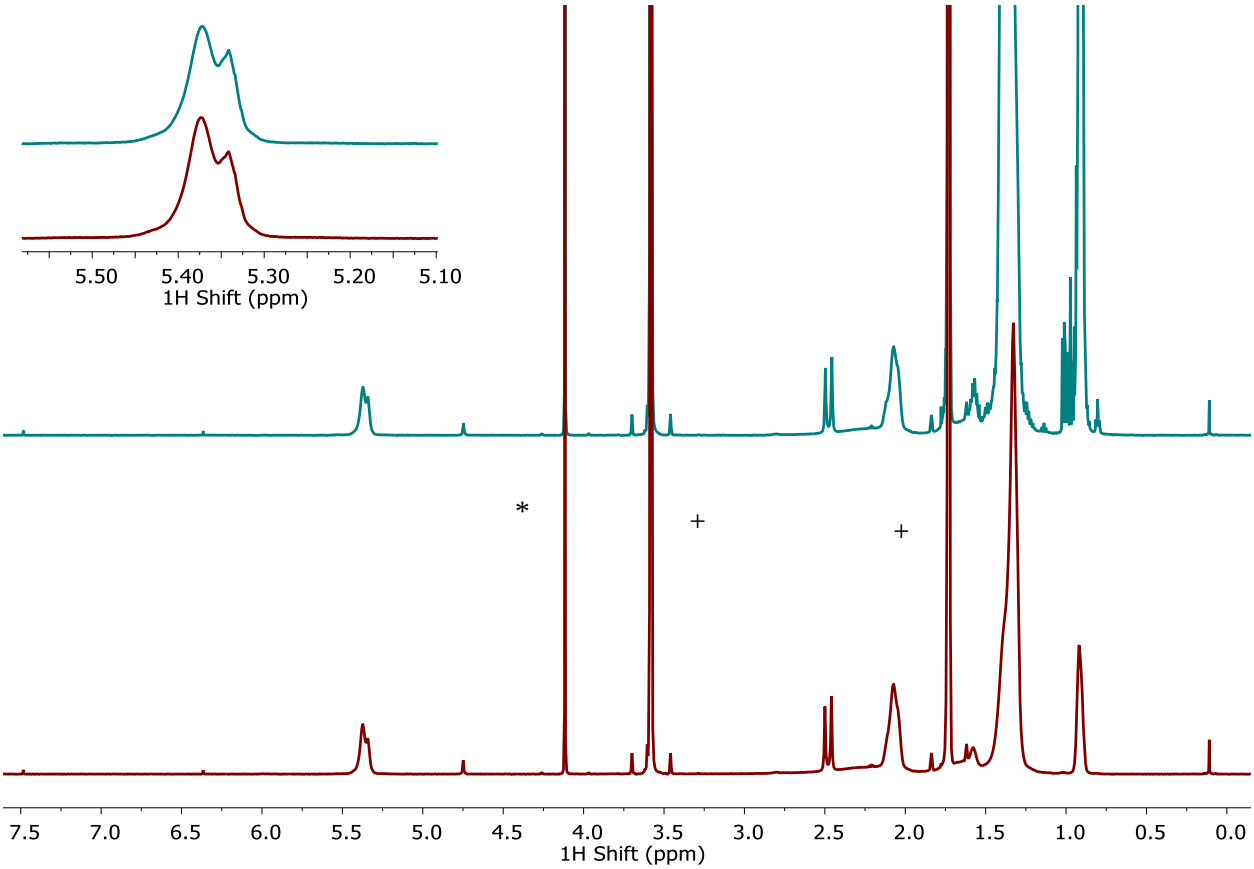

Figure 3.33 ^{1}H NMR of 48.5µM PbS QD (3.4 nm) in THF-d_8 without (red) and with (blue) 1000 eq. Bu_3P. Inset: Oleate alkene proton resonances show only minor difference in the ratio of bound/free ligand with and without Bu_3P. Approximately 20.8% free OA is detected in the QD only trace, and 21.6% free OA is detected with excess Bu_3P added. (*) denotes internal standard ferrocene and (+) denotes solvent residual. NMR spectra collected on 600 MHz NMR with cryoprobe utilizing a d1 delay of 30 seconds with 12 scans.

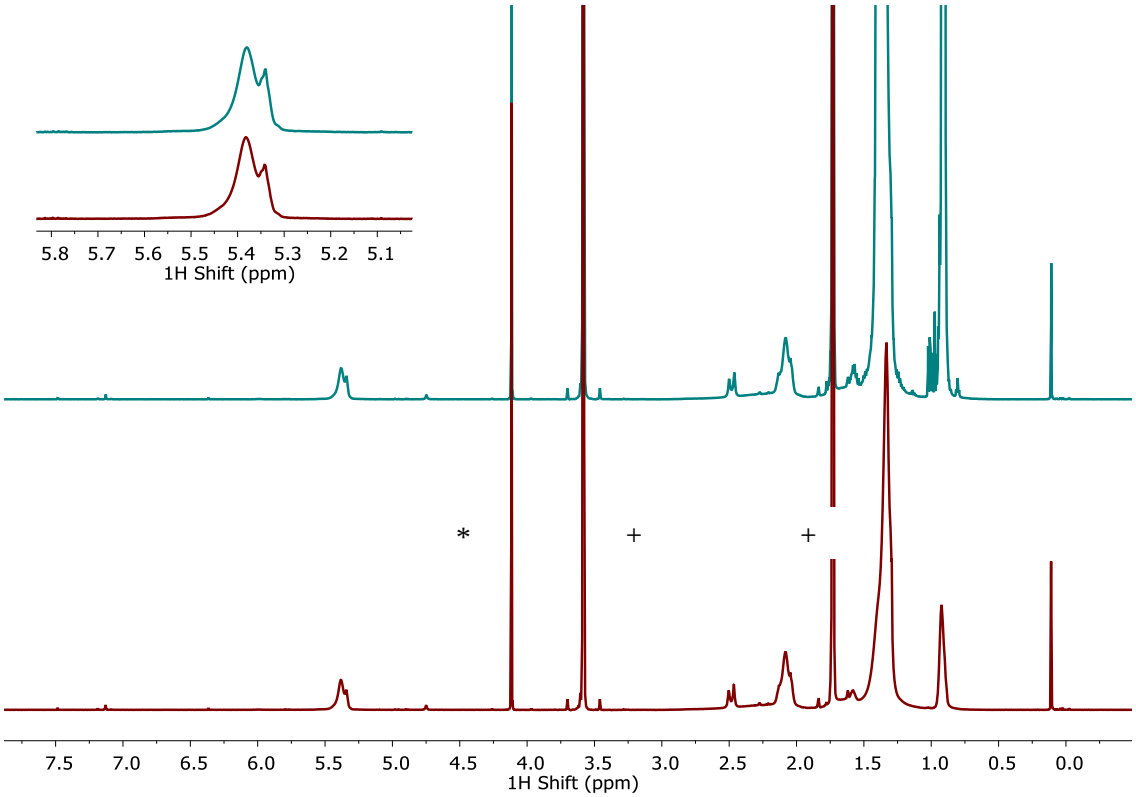

Figure 3.34 ^{1}H NMR of 48.5 µM PbS QD (4.7 nm) in THF-d_8 without (red) and with (blue) 1000 eq. Bu_3P. Inset: Oleate alkene proton resonances show only minor difference in the ratio of bound/free ligand with and without Bu_3P. Approximately 14.6% free OA is detected in the QD only trace, and 16.5% free OA is detected with excess Bu_3P added. (*) denotes internal standard ferrocene and (+) denotes solvent residual. NMR spectra collected on 600 MHz NMR with cryoprobe utilizing a d1 delay of 30 seconds with 12 scans.

3.3.6 Conclusions

In conclusion, through the use of a range of outer sphere reductants and selective redox reagents, we have gained an understanding of the native defects that exist on PbS QDs as well as those that are induced upon surface charging. Systematic investigations of the reactivity of the QD surfaces by NMR spectroscopy reveal oleate ligand displacement in response to reduction of surface Pb^{2+} ions. Comparison of the extent of ligand displacement across QD batches reveals a distinct size dependence, with larger QDs exhibiting a higher degree of ligand loss. This size-dependent surface reactivity correlates with recently proposed changes in PbS QD morphology with size.[22,30,31] Specifically, the emergence of new Pb^{2+} ion environments at (100) facets, and the edge sites between (100) and (111) facets, are proposed to

be the primary Pb species reduced leading to oleate displacement. Furthermore, we demonstrate that the strength of the reductant employed has a significant impact on the extent of surface charging and reactivity; stronger reducing agents result in a greater amount of overall ligand displacement, whereas weak reducing agents show minimal reactivity with the QDs. Finally, the reactivity of chalcogenide-based defects (disulfides) was explored using a selective trialkylphosphine reagent. Similar to reduction of Pb ions, disulfide reactivity displays a distinct size dependence with more reactivity observed for disulfide reduction in larger QDs.

Taken together, these studies suggest that there is a larger relative proportion of redox-active defect sites (both metal- and chalcogenide-based) present on larger PbS QDs. We argue that this size dependence is not simply because of increased surface area and total number of atoms in larger QDs; rather, changes in morphology correlated with increasing QD diameter leads to the formation of the redox-active defect sites probed herein. Overall, we present an example of using a powerful tool—chemical probes—in tandem with NMR spectroscopy to study the identity and reactivity of subpopulations of defect sites on QD surfaces.

Importantly, this work is a stepping stone toward establishing a detailed, molecular-level picture of QD surfaces by employing multiple complementary techniques and targeted reactions.[19] We hope that future works will build upon these findings to further understanding of the structural nature of defect sites and their reactivity with added charge. The QD field is now, more than ever, poised to do so through the recent emergence of new tools to study QD surface structure, including advanced multinuclear NMR spectroscopy methods (e.g., probing metal or chalcogen nuclei directly, or using dynamic nuclear polarization or cross-polarization magic-angle spinning enhancement methods, etc.)[55–61] and innovative computational tools to explore surface structure motifs.[6,7,28,62] Such an approach is critical to gaining a molecular-level understanding of QD surfaces, and reaching the full potential of QD-based systems.

REFERENCES

(1) Kovalenko, M. V; Manna, L.; Cabot, A.; Hens, Z.; Talapin, D. V; Kagan, C. R.; Klimov, V. I.; Rogach, A. L.; Reiss, P.; Milliron, D. J.; et al. Prospects of Nanoscience with Nanocrystals. *ACS Nano* **2015**, *9*, 1012–1057.

(2) Carey, G. H.; Abdelhady, A. L.; Ning, Z.; Thon, S. M.; Bakr, O. M.; Sargent, E. H. Colloidal Quantum Dot Solar Cells. *Chem. Rev.* **2015**, *115*, 12732–12763.

(3) Kershaw, S. V.; Jing, L.; Huang, X.; Gao, M.; Rogach, A. L. Materials aspects of semiconductor nanocrystals for pptoelectronic applications. *Mater. Horiz.* **2017**, *4*, 155–205.

(4) Kodaimati, M. S.; McClelland, K. P.; He, C.; Lian, S.; Jiang, Y.; Zhang, Z.; Weiss, E. A. Viewpoint: Challenges in Colloidal Photocatalysis and Some Strategies for Addressing Them. *Inorg. Chem.* **2018**, *57*, 3659–3670.

(5) McClelland, K. P.; Weiss, E. A. Selective Photocatalytic Oxidation of Benzyl Alcohol to Benzaldehyde or C–C Coupled Products by Visible-Light-Absorbing Quantum Dots. *ACS Appl. Energy Mater.* **2019**, *2*, 92–96.

(6) Giansante, C.; Infante, I. Surface Traps in Colloidal Quantum Dots: A Combined Experimental and Theoretical Perspective. *J. Phys. Chem. Lett.* **2017**, *8*, 5209–5215.

(7) Houtepen, A. J.; Hens, Z.; Owen, J. S.; Infante, I. On the Origin of Surface Traps in Colloidal II–VI Semiconductor Nanocrystals. *Chem. Mater.* **2017**, *29*, 752–761.

(8) Thomas, A.; Sandeep, K.; Somasundaran, S. M.; Thomas, K. G. How Trap States Affect Charge Carrier Dynamics of CdSe and InP Quantum Dots: Visualization through Complexation with Viologen. *ACS Energy Lett.* **2018**, *3*, 2368–2375.

(9) Brawand, N. P.; Goldey, M. B.; Vörös, M.; Galli, G. Defect States and Charge Transport in Quantum Dot Solids. *Chem. Mater.* **2017**, *29*, 1255–1262.

(10) Zou, H.; Dong, C.; Li, S.; Im, C.; Jin, M.; Yao, S.; Cui, T.; Tian, W.; Liu, Y.; Zhang, H. Effect of Surface Trap States on Photocatalytic Activity of Semiconductor Quantum Dots. *J. Phys. Chem. C* **2018**, *122*, 9312–9319.

(11) Kirkwood, N.; Monchen, J. O. V.; Crisp, R. W.; Grimaldi, G.; Bergstein, H. A. C.; du Fossé, I.; van der Stam, W.; Infante, I.; Houtepen, A. J. Finding and Fixing Traps in II–VI and III–V Colloidal Quantum Dots: The Importance of Z-Type Ligand Passivation. *J. Am. Chem. Soc.* **2018**, *140*, 15712–15723.

(12) van der Stam, W.; de Graaf, M.; Gudjonsdottir, S.; Geuchies, J. J.; Dijkema, J. J.; Kirkwood, N.; Evers, W. H.; Longo, A.; Houtepen, A. J. Tuning and Probing the Distribution of Cu^{+} and Cu^{2+} Trap States Responsible for Broad-Band Photoluminescence in $CuInS_2$ Nanocrystals. *ACS Nano* **2018**, *12*, 11244–11253.

(13) Veamatahau, A.; Jiang, B.; Seifert, T.; Makuta, S.; Latham, K.; Kanehara, M.; Teranishi, T.; Tachibana, Y. Origin of surface trap states in CdS quantum dots: relationship between size dependent photoluminescence and sulfur vacancy trap states. *Phys. Chem. Chem. Phys.* **2015**, *17*, 2850–2858.

(14) van der Stam, W.; du Fossé, I.; Grimaldi, G.; Monchen, J. O. V; Kirkwood, N.; Houtepen, A. J. Spectroelectrochemical Signatures of Surface Trap Passivation on CdTe Nanocrystals. *Chem. Mater.* **2018**, *30*, 8052–8061.

(15) Amelia, M.; Lincheneau, C.; Silvi, S.; Credi, A. Electrochemical properties of CdSe and CdTe quantum dots. *Chem. Soc. Rev.* **2012**, *41*, 5728 - 5743.

(16) Fedin, I.; Talapin, D. V. Probing the Surface of Colloidal Nanomaterials with Potentiometry *in Situ*. *J. Am. Chem. Soc.* **2014**, *136*, 11228–11231.

(17) Carroll, G. M.; Brozek, C. K.; Hartstein, K. H.; Tsui, E. Y.; Gamelin, D. R. Potentiometric Measurements of Semiconductor Nanocrystal Redox Potentials. *J. Am. Chem. Soc.* **2016**, *138*, 4310–4313.

(18) Chen, M.; Guyot-Sionnest, P. Reversible Electrochemistry of Mercury Chalcogenide Colloidal Quantum Dot Films. *ACS Nano* **2017**, *11*, 4165–4173.

(19) Hartley, C. L.; Kessler, M. L.; Dempsey, J. L. Molecular-Level Insight into Semiconductor Nanocrystal Surfaces. *J. Am. Chem. Soc.* **2021**, *143*, 1251–1266.

(20) Saniepay, M.; Mi, C.; Liu, Z.; Abel, E. P.; Beaulac, R. Insights into the Structural Complexity of Colloidal CdSe Nanocrystal Surfaces: Correlating the Efficiency of Nonradiative Excited-State Processes to Specific Defects. *J. Am. Chem. Soc.* **2018**, *140*, 1725–1736.

(21) Anderson, N. C.; Hendricks, M. P.; Choi, J. J.; Owen, J. S. Ligand Exchange and the Stoichiometry of Metal Chalcogenide Nanocrystals: Spectroscopic Observation of Facile Metal-Carboxylate Displacement and Binding. *J. Am. Chem. Soc.* **2013**, *135*, 18536–18548.

(22) Kessler, M. L.; Dempsey, J. L. Mapping the Topology of PbS Nanocrystals through Displacement Isotherms of Surface-Bound Metal Oleate Complexes. *Chem. Mater.* **2020**, *32*, 2561–2571.

(23) Hartley, C. L.; Dempsey, J. L. Electron-Promoted X-Type Ligand Displacement at CdSe Quantum Dot Surfaces. *Nano Lett.* **2019**, *19*, 1151–1157.

(24) Tsui, E. Y.; Hartstein, K. H.; Gamelin, D. R. Selenium Redox Reactivity on Colloidal CdSe Quantum Dot Surfaces. *J. Am. Chem. Soc.* **2016**, *138*, 11105–11108.

(25) Drijvers, E.; De Roo, J.; Martins, J. C.; Infante, I.; Hens, Z. Ligand Displacement Exposes Binding Site Heterogeneity on CdSe Nanocrystal Surfaces. *Chem. Mater.* **2018**, *30*, 1178–1186.

(26) Knowles, K. E.; Malicki, M.; Parameswaran, R.; Cass, L. C.; Weiss, E. A. Spontaneous Multielectron Transfer from the Surfaces of PbS Quantum Dots to Tetracyanoquinodimethane. *J. Am. Chem. Soc.* **2013**, *135*, 7264–7271.

(27) Pu, C.; Dai, X.; Shu, Y.; Zhu, M.; Deng, Y.; Jin, Y.; Peng, X. Electrochemically-stable ligands bridge the photoluminescence-electroluminescence gap of quantum dots. *Nat. Commun.* **2020**, *11*, 937.

(28) du Fossé, I.; ten Brinck, S.; Infante, I.; Houtepen, A. J. Role of Surface Reduction in the Formation of Traps in *n*-Doped II–VI Semiconductor Nanocrystals: How to Charge without Reducing the Surface. *Chem. Mater.* **2019**, *31*, 4575–4583.

(29) Voznyy, O.; Thon, S. M.; Ip, A. H.; Sargent, E. H. Dynamic Trap Formation and Elimination in Colloidal Quantum Dots. *J. Phys. Chem. Lett.* **2013**, *4*, 987–992.

(30) Choi, H.; Ko, J.-H.; Kim, Y.-H.; Jeong, S. Steric-Hindrance-Driven Shape Transition in PbS Quantum Dots: Understanding Size-Dependent Stability. *J. Am. Chem. Soc.* **2013**, *135*, 5278–5281.

(31) Beygi, H.; Sajjadi, S. A.; Babakhani, A.; Young, J. F.; van Veggel, F. C. J. M. Surface chemistry of as-synthesized and air-oxidized PbS quantum dots. *Appl. Surf. Sci.* **2018**, *457*, 1–10.

(32) Moreels, I.; Lambert, K.; Smeets, D.; De Muynck, D.; Nollet, T.; Martins, J. C.; Vanhaecke, F.; Vantomme, A.; Delerue, C.; Allan, G.; et al. Size-Dependent Optical Properties of Colloidal PbS Quantum Dots. *ACS Nano* **2009**, *3*, 3023–3030.

(33) Jasieniak, J.; Califano, M.; Watkins, S. E. Size-Dependent Valence and Conduction Band-Edge Energies of Semiconductor Nanocrystals. *ACS Nano* **2011**, *5*, 5888–5902.

(34) Connelly, N. G.; Geiger, W. E. Chemical Redox Agents for Organometallic Chemistry. *Chem. Rev.* **1996**, *96*, 877–910.

(35) Koh, Wk.; Koposov, A. Y.; Stewart, J. T.; Pal, B. N.; Robel, I.; Pietryga, J. M.; Klimov, V. I. Heavily doped *n*-type PbSe and PbS nanocrystals using ground-state charge transfer from cobaltocene. *Sci. Rep.* **2013**, *3*, 2004.

(36) Shim, M.; Guyot-Sionnest, P. n-type colloidal semiconductor nanocrystals. *Nature* **2000**, *407*, 981–983.

(37) Hens, Z.; Martins, J. C. A Solution NMR Toolbox for Characterizing the Surface Chemistry of Colloidal Nanocrystals. *Chem. Mater.* **2013**, *25*, 1211–1221.

(38) Kessler, M. L.; Starr, H. E.; Knauf, R. R.; Rountree, K. J.; Dempsey, J. L. Exchange equilibria of carboxylate-terminated ligands at PbS nanocrystal surfaces. *Phys. Chem. Chem. Phys.* **2018**, *20*, 23649–23655.

(39) Knauf, R. R.; Lennox, J. C.; Dempsey, J. L. Quantifying Ligand Exchange Reactions at CdSe Nanocrystal Surfaces. *Chem. Mater.* **2016**, *28*, 4762–4770.

(40) Zhao, J.; Holmes, M. A.; Osterloh, F. E. Quantum Confinement Controls Photocatalysis: A Free Energy Analysis for Photocatalytic Proton Reduction at CdSe Nanocrystals. *ACS Nano* **2013**, *7*, 4316–4325.

(41) Rajh, T.; Micic, O. I.; Lawless, D.; Serpone, N. Semiconductor Photophysics. 7. Photoluminescence and Picosecond Charge Carrier Dynamics in Cadmium Sulfide Quantum Dots Confined in a Silicate Glass. *J. Phys. Chem.* **1992**, *96*, 4633–4641.

(42) Shiragami, T.; Fukami, S.; Wada, Y.; Yanagida, S. Semiconductor Photocatalysis: Effect of Light Intensity on Nanoscale Cadmium Sulfide-Catalyzed Photolysis of Organic Substrates. *J. Phys. Chem.* **1993**, *97*, 12882–12887.

(43) Nedoluzhko, A. I.; Shumilin, I. A.; Nikandrov, V. V. Coupled Action of Cadmium Metal and Hydrogenase in Formate Photodecomposition Sensitized by CdS. *J. Phys. Chem.* **1996**, *100*, 17544–17550.

(44) Pagels, N.; Prosenc, M. H.; Heck, J. An *ansa*-Cobaltocene with a Naphthalene Handle: Synthesis and Spectroscopic and Structural Characterization. *Organometallics* **2011**, *30*, 1968–1974.

(45) Zherebetskyy, D.; Scheele, M.; Zhang, Y.; Bronstein, N.; Thompson, C.; Britt, D.; Salmeron, M.; Alivisatos, P.; Wang, L. Hydroxylation of the surface of PbS nanocrystals passivated with oleic acid. *Science* **2014**, *344*, 1380–1384.

(46) Hendricks, M. P.; Campos, M. P.; Cleveland, G. T.; Jen-La Plante, I.; Owen, J. S. A tunable library of substituted thiourea precursors to metal sulfide nanocrystals. *Science* **2015**, *348*, 1226–1230.

(47) Hines, M. A.; Scholes, G. D. Colloidal PbS Nanocrystals with Size-Tunable Near-Infrared Emission: Observation of Post-Synthesis Self-Narrowing of the Particle Size Distribution. *Adv. Mater.* **2003**, *15*, 1844–1849.

(48) Houtepen, A. J.; Vanmaekelbergh, D. Orbital Occupation in Electron-Charged CdSe Quantum-Dot Solids. *J. Phys. Chem. B* **2005**, *109*, 19634–19642.

(49) Elgrishi, N.; Kurtz, D. A.; Dempsey, J. L. Reaction Parameters Influencing Cobalt Hydride Formation Kinetics: Implications for Benchmarking H_2-Evolution Catalysts. *J. Am. Chem. Soc.* **2017**, *139*, 239–244.

(50) Brozek, C. K.; Hartstein, K. H.; Gamelin, D. R. Potentiometric Titrations for Measuring the Capacitance of Colloidal Photodoped ZnO Nanocrystals. *J. Am. Chem. Soc.* **2016**, *138*, 10605–10610.

(51) Brown, P. R.; Kim, D.; Lunt, R. R.; Zhao, N.; Bawendi, M. G.; Grossman, J. C.; Bulović, V. Energy Level Modification in Lead Sulfide Quantum Dot Thin Films through Ligand Exchange. *ACS Nano* **2014**, *8*, 5863–5872.

(52) Harris, R. D.; Bettis Homan, S.; Kodaimati, M.; He, C.; Nepomnyashchii, A. B.; Swenson, N. K.; Lian, S.; Calzada, R.; Weiss, E. A. Electronic Processes within Quantum Dot-Molecule Complexes. *Chem. Rev.* **2016**, *116*, 12865–12919.

(53) Tsui, E. Y.; Carroll, G. M.; Miller, B.; Marchioro, A.; Gamelin, D. R. Extremely Slow Spontaneous Electron Trapping in Photodoped *n*-Type CdSe Nanocrystals. *Chem. Mater.* **2017**, *29*, 3754–3762.

(54) Humphrey, R. E.; Potter, J. L. Reduction of Disulfides with Tributylphosphine. *Anal. Chem.* **1965**, *37*, 164–165.

(55) Aebli, M.; Piveteau, L.; Nazarenko, O.; Benin, B. M.; Krieg, F.; Verel, R.; Kovalenko, M. V. Lead-Halide Scalar Couplings in ^{207}Pb NMR of $APbX_3$ Perovskites (A = Cs, Methylammonium, Formamidinium; X = Cl, Br, I). *Sci. Rep.* **2020**, *10*, 8229.

(56) Piveteau, L.; Morad, V.; Kovalenko, M. V. Solid-State NMR and NQR Spectroscopy of Lead-Halide Perovskite Materials. *J. Am. Chem. Soc.* **2020**, *142*, 19413–19437.

(57) Chen, Y.; Smock, S. R.; Flintgruber, A. H.; Perras, F. A.; Brutchey, R. L.; Rossini, A. J. Surface Termination of $CsPbBr_3$ Perovskite Quantum Dots Determined by Solid-State NMR Spectroscopy. *J. Am. Chem. Soc.* **2020**, *142*, 6117–6127.

(58) Piveteau, L.; Ong, T.-C.; Walder, B. J.; Dirin, D. N.; Moscheni, D.; Schneider, B.; Bär, J.; Protesescu, L.; Masciocchi, N.; Guagliardi, A.; et al. Resolving the Core and the Surface of CdSe Quantum Dots and Nanoplatelets Using Dynamic Nuclear Polarization Enhanced PASS–PIETA NMR Spectroscopy. *ACS Cent. Sci.* **2018**, *4*, 1113–1125.

(59) Lee, D.; Wolska-Pietkiewicz, M.; Badoni, S.; Grala, A.; Lewiński, J.; De Paëpe, G. Disclosing Interfaces of ZnO Nanocrystals Using Dynamic Nuclear Polarization: Sol-Gel versus Organometallic Approach. *Angew. Chemie Int. Ed.* **2019**, *58*, 17163–17168.

(60) Zhang, J.; Zhang, H.; Cao, W.; Pang, Z.; Li, J.; Shu, Y.; Zhu, C.; Kong, X.; Wang, L.; Peng, X. Identification of Facet-Dependent Coordination Structures of Carboxylate Ligands on CdSe Nanocrystals. *J. Am. Chem. Soc.* **2019**, *141*, 15675–15683.

(61) Hanrahan, M. P.; Stein, J. L.; Park, N.; Cossairt, B. M.; Rossini, A. J. Elucidating the Location of Cd^{2+} in Post-synthetically Treated InP Quantum Dots Using Dynamic Nuclear Polarization ^{31}P and ^{113}Cd Solid-State NMR Spectroscopy. *J. Phys. Chem. C* **2021**, *125*, 2956–2965.

(62) Singh, S.; Tomar, R.; ten Brinck, S.; De Roo, J.; Geiregat, P.; Martins, J. C.; Infante, I.; Hens, Z. Colloidal CdSe Nanoplatelets, A Model for Surface Chemistry/Optoelectronic Property Relations in Semiconductor Nanocrystals. *J. Am. Chem. Soc.* **2018**, *140*, 13292–13300.

CHAPTER 4 : EFFECTS OF LIGAND SHELL COMPOSITION ON SURFACE REDUCTION IN PBS QUANTUM DOTS

This chapter was adapted with permission from *Hartley, C.L.; *Kessler, M.K.; Dones Lassalle, C.Y.; Camp, A.M.; Dempsey, J.L. Effects of Ligand Shell Composition on Surface Reduction in PbS Quantum Dots. *Submitted.*

4.1 Introduction

Semiconductor quantum dots (QDs) are a popular class of nanocrystals with applications in optoelectronic technologies ranging from commercial displays to p−n junction solar cells.[1–3] QDs have desirable characteristics for these applications including rapid interfacial charge transfer, high absorptivity, and incredible tunability accessed by varying QD size, material, or capping ligand.[2,4] This tunability of properties affords opportunities to optimize QDs for a given application via post-synthetic modification strategies, prior to incorporation into commercial devices.[1,2,5]

Perhaps the most common post-synthetic modification before use in devices is exchange of the native surface capping ligands with ligands that differ by their backbone or surface-binding head group (Scheme 4.1). As-synthesized metal chalcogenide QDs often possess long-chain alkyl-based ligands such as oleate, myristate, or *n*-octylphosphonate.[6] Though these ligands impart colloidal stability to the nanocrystals, their insulating nature inhibits electronic communication and charge transfer between QDs within a solid-state device.[5,7–9] Therefore, to improve conductivity in QD-based devices, these native capping ligands are frequently exchanged with ligands that have short or conjugated backbones and often contain strongly binding thiolate head groups, such as 3-mercaptopropionic acid or benzene dithiol.[10–14] Though ligand exchange methods are widely established, ligand-exchanged QDs are often not isolated from excess ligand and solvent. In studies where QDs are isolated post-exchange, characterization of bound ligand composition and of the QD surface is generally limited to qualitative observations of spectral handles in NMR or IR spectra corresponding to bound exchange ligands or loss of native ligands.

Despite the lack of comprehensive characterization of ligand-exchanged QDs, ligand exchange reactions on the QD surface are known to impact QD properties including colloidal stability, trap formation or passivation, absorptivity, and surface dipole moment, to name a few.[13,15–18] Without a complete picture of how the ligand composition of exchanged QDs affects physical and electronic properties, the ability to optimize devices relying upon these materials is limited.

Scheme 4.1 Structure of anionic X-type ligand bound to metal cation on QD surface[a]

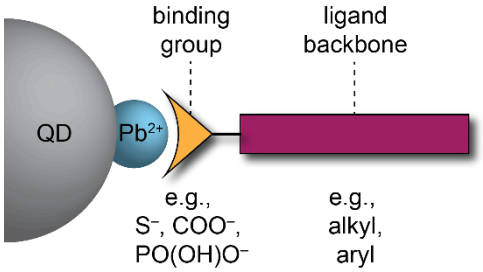

Scheme adapted from reference [17]

An added consideration when incorporating QDs into devices is the stability of the QD surface to added charge (e.g., from an electrode, external dopant, or QD−QD charge transfer). Recent work has demonstrated that upon adding charge to QDs via electrochemical, photochemical, and remote chemical doping (charging) processes, this excess added charge can reside in localized states on the QD surface.[19–22] When the charge is localized at some metal sites, X-type ligands are liberated for charge balance, as recently demonstrated in CdSe and PbS systems with native oleate ligands.[21,22] Yet while there have been a handful of recent experimental[19,21,22] and computational[23,24] studies of QD surface charging, ligand displacement is generally not well controlled or understood for QDs with different types of device-relevant capping ligands.

To achieve a more detailed understanding of QD surface modification methods with an eye toward improving QD-based devices, it is crucial to attain (i) rigorous characterization of exchanged QD properties and determination of extinction coefficients alongside direct comparisons with the native oleate-capped QD surface; and (ii) knowledge of how exchange ligands with common motifs impact the

extent of surface charging. PbS was selected as an ideal QD platform for these investigations because of its relevance to devices and widespread use in the literature.[3,25,26] We therefore isolated and characterized a series of partially ligand-exchanged PbS QDs (i.e., mixed-shell QDs) using three exchange ligands that differ by the ligand backbone or surface binding group. Each exchange ligand—an alkyl carboxylate, an aryl carboxylate, and an alkyl thiolate—possesses robust spectroscopic handles suitable for quantitative NMR analyses. The mixed-shell QDs are comprised of near-stoichiometric populations of the native oleate ligand and of the exchange ligand to enable direct assessment of the relative stability of each ligand toward surface charging within the same system. We then probed how each of these mixed-shell systems reacted to surface charging through comparative spectroscopic studies with added molecular reductants, discovering unique patterns of reactivity for each mixed-shell system. These observations provide valuable insight into the surface of the nanocrystals and how the surface is affected by ligand exchange and electronic charging.

4.2 Experimental

General Considerations. Toluene-d_8 was purchased from Cambridge Isotope Laboratories and freeze-pump-thawed to degas and then dried over activated 3 Å molecular sieves for at least 24 hours in a glovebox before use. PbO (99.999%), oleic acid (OA) (90%), 1-octadecene (ODE) (90%), *p*-toluic acid (98%), and 1,3,5-trimethoxybenzene (≥ 99%) were purchased from Sigma Aldrich and used as received. Bis(trimethylsilyl) sulfide ($(TMS)_2S$) (≥ 98%) was purchased from Sigma Aldrich and stored under N_2 in a glovebox. Cobaltocene ($CoCp_2$) was purchased from Sigma Aldrich and was purified by sublimation. Triethylamine (≥ 99.5%) was purchased from Sigma Aldrich and purified by distillation before use. Undec-10-enoic acid (UDA) (99%) was purchased from Acros Organics and was purified by distillation before use. Undec-10-ene-1-thiol (UDT) was synthesized as described previously,[27] freeze-pump-thawed to degas, and stored in a glovebox prior to use. Solvents used for purification of QDs and for UV−Vis absorbance studies were purchased from Fisher Scientific and VWR.

Synthesis and Purification of PbS QDs. Standard Schlenk line techniques were utilized to maintain an inert atmosphere during the synthesis of PbS QDs. PbS QDs ca. 3 nm in diameter were synthesized following previously reported procedures.[28,29] Lead(II) oxide (0.90 g, 4 mmol), oleic acid (2.54 mL, 8 mmol), and ODE (35 mL) were combined in a 100 mL three-neck round-bottom flask and stirred under vacuum at 100 °C for 2–3 h. The mixture was then heated to 120 °C to yield a clear and colorless solution. Simultaneously, $(TMS)_2S$ (0.42 mL, 2 mmol) and ODE (4 g) were combined in a 25 mL pear-shaped flask under inert atmosphere. The $(TMS)_2S$ mixture was injected rapidly into the $Pb(OA)_2$ solution at 120 °C. The reaction proceeded for 2.5 min at ca. 115 °C, during which time the solution turned dark brown. The reaction vessel was removed from the heating mantle and the QD solution was quenched by immersion first in a room temperature oil bath then an ice bath. 3 mL of the QD mixture were diluted with 1 mL toluene and then 8 mL of acetone were added to precipitate out the QDs. The mixture was then centrifuged at 9000 rpm for 10–15 min. After decanting the supernatant, the QDs were resuspended in 3 mL pentane and precipitated by addition of 4 mL MeOH and 4 mL acetone followed by centrifugation. Four more total precipitation–centrifugation cycles were carried out with alternating 2 mL pentane or toluene and 8 mL acetone. The PbS QDs were isolated from pentane by evaporation, yielding ca. 1.2 g of QDs. The QDs were stored as a solid in a nitrogen-filled glovebox.

QD Ligand Exchange Procedure. Each QD batch (oleate-PbS-1, -2, -3) was split into two portions; 60% of the batch was used in the ligand exchange procedures below, and 40% of each batch was used as for comparative studies with native oleate-capped PbS QDs. Purification of the exchanged QDs described below varied slightly based on what we found to result in pure and stable mixed-shell batches with each ligand system. In all cases, alcohol antisolvents were avoided to minimize ligand displacement from precipitation cycles.[30]

UDA/oleate-PbS QDs were obtained by addition of 200 equiv. UDA/QD to a ca. 300 µM solution of 3.2 nm PbS QDs with stirring in toluene at room temperature for 40 min. The UDA/oleate-PbS QDs were isolated from the reaction solution by two rounds of precipitation–centrifugation with a 1:5 ratio of

toluene:acetone. The UDA/oleate-PbS QDs were then suspended in pentane, dried under an N_2 stream and then stored in an N_2-filled glovebox.

Toluate/oleate-PbS QDs were obtained by stirring 600 equiv. triethylammonium *p*-toluate per QD with a 300 µM solution of 2.9 nm PbS QDs in toluene for 10 min. The QDs were isolated by two rounds of precipitation from 1:3 toluene:CH_3CN and centrifugation at 8500 rpm for 10 minutes. Toluate/oleate-PbS QDs were suspended in pentane, then the solvent removed under N_2 stream and vacuum before storage in an N_2-filled glovebox.

UDT/oleate-PbS QDs were obtained through reaction of 100 equiv. UDT/QD in a 300 µM solution of 3.1 nm PbS QDs in toluene for 30 min with stirring. The UDT/oleate-PbS QDs were isolated through six rounds of precipitation–centrifugation at ca. 8000 rpm as follows: 1:4 toluene:acetone; 1:2:2 toluene:acetone:CH_3CN; 1:4:7 DCM:acetone:CH_3CN; 1:9 toluene:acetone; 1:2:1 toluene:acetone:CH_3CN; and 1:7 toluene:acetone. The UDT/oleate-PbS QDs were dried from pentane under an N_2 stream then under vacuum and brought into an N_2-filled glovebox.

Absorbance Measurements. Absorbance measurements were recorded using Agilent Cary 60 and Cary 5000 (double-beam mode) UV−visible absorbance spectrophotometers. Nanocrystal concentrations were calculated from the absorbance at 400 nm using the ε_{400} value determined experimentally. For titration studies with added $CoCp_2$, the toluene QD stock solution was diluted to 2.5 µM and 3 mL were added to a custom-made quartz cuvette with a glass 14/20 joint adaptor top. The cuvette was equipped with a micro stir bar and sealed in the glovebox with a rubber septum secured with electrical tape and copper wire. A 15 mM solution of $CoCp_2$ in toluene was prepared and drawn up into a 500 µL gas-tight locking syringe. The charged syringe was then locked and the needle stuck into a rubber septum. After collecting a QD only (0 eq. $CoCp_2$) absorbance spectrum, the needle of the charged syringe was swiftly injected into the specialty cuvette and unlocked to add $CoCp_2$ to the QD solution incrementally with 50, 100, 250, 500, 750 and 1000 eq. $CoCp_2$. The syringe was locked between additions, and after adding the

reductant the solution in the cuvette was stirred vigorously for 30 seconds before collecting an absorbance spectrum.

Determination of Mixed-Shell QD Extinction Coefficients. A UV-Vis absorbance spectrum of a sample of PbS QDs was recorded in a 2 mm cuvette. The sample was carefully rinsed into a scintillation vial, dried under air stream, then heated in a box furnace at 450 °C for 30 min to pyrolyze the organics. The contents of the scintillation vial were digested for 4 hr in 0.5 mL HNO_3 (TraceMetal grade, Fisher Chemical). The sample was filtered through Whatman GF 6 glass filter paper with a pore size of <1 μm, rinsed into a 10 mL volumetric flask with 2% HNO_3 in Millipore water, and transferred to a 15 mL centrifuge tube. The sample was diluted by 250× to obtain a concentration of Pb within the confines of the calibration curve, targeting ca. 50 ppb Pb. ICP-MS was carried out on an Agilent 7500cx instrument operated in low resolution and tuned with a solution containing 100 ppb Li, Co, Y, Ce, and Ti. Calibration standards were prepared from appropriate dilutions of 100 ppm Pb in 0.5% HNO_3 (v/v) (Inorganic Ventures) with 2% HNO_3 (TraceMetal grade, Fisher Chemical) in 18.2 MΩ water. The Pb concentration obtained via ICP-MS was combined with the Pb:S ratio from XPS to yield the concentration of QDs in the UV-Vis sample (see **SI** for sample calculation). Beer's law was used to calculate the extinction coefficient at 400 nm (ε_{400}).

^{1}H NMR Spectroscopy Studies. NMR samples were prepared in a dry nitrogen-filled glovebox by measuring the concentration of PbS NC stock solutions via UV−Vis absorbance spectroscopy, diluting a calculated volume of stock solution with toluene-d_8 to obtain a concentration of 50 μM QDs, and adding 600 μL of this solution to a JYoung NMR tube to maintain an inert atmosphere during data collection. An internal standard solution of 1,3,5-trimethoxybenzene was prepared by dissolving ca. 13 mg in 1.5 mL of toluene-d_8, then 50 μL of this solution was added to each JYoung NMR tube. A 50 mM solution of $CoCp_2$ in toluene-d_8 was then prepared and aliquots of 0, 100, or 500 eq. per QD added to the JYoung NMR tubes. After $CoCp_2$ addition, the samples were allowed to equilibrate in the dark before collecting spectra

at intervals of 4, 24, 48, and 123 hours. Spectra were collected on a Bruker 600 MHz spectrometer with a 30 s d1 delay time and 8–12 scans. Additional parameters used in 2D NMR and relaxation studies (Table 4.1) are described further in the **Appendix C**.

Table 4.1 Delay time d1 check with toluate ligands. 600 MHz NMR, varied d1 delay time and used 12 scans for all. 46 µM QD in toluene-d_8 with 1,3,5-trimethoxybenzene as internal standard.

d1 delay time	bound toluate/QD	bound OA/QD	total toluate+OA ligands
30 sec	53	73	126
45 sec	50	73	123
60 sec	48	73	121
90 sec	53	74	127
120 sec	53	73	126
150 sec	54	73	128

X-ray Photoelectron Spectroscopy (XPS). Samples were prepared by depositing either liquid solutions onto Au-coated silicon wafers or solid powders onto freshly cut indium metal. The Au-coated silicon wafers were fabricated using a KJ Lesker sputter coater. Wafer pieces were sonicated in ethanol and dried under an air stream prior to dropcasting PbS QDs in pentane. XPS was performed using a Kratos Axis Ultra DLD X-ray photoelectron spectrometer with a monochromatic Al Kα X-ray source. Survey and high-resolution scans were obtained with pass energies of 80 and 20 eV, respectively. All spectra were corrected to the C 1s peak at 284.6 eV.

Transmission Electron Microscopy (TEM). Transmission electron microscopic images were recorded on a Thermo Scientific FEI Talos F200X S/TEM equipped with a 70 micron objective aperture, and at an accelerating voltage of 200 kV. Samples were prepared by filtering dilute solutions of nanocrystals in pentane through a 2 µm PTFE syringe filter and drop casting onto 400 mesh lacey carbon grids (Ted Pella, Inc.). Samples were dried overnight under vacuum at room temperature. Images were analyzed using *ImageJ* software.

4.3 Results and Discussion

4.3.1 Mixed-Ligand QD Preparation and Characterization.

Three batches of PbS QDs approximately 3 nm in diameter (2.9, 3.1, and 3.2 nm) were synthesized via the Hines and Scholes method and purified through precipitation−centrifugation cycles.[29,31] Approximate QD sizes were calculated from the empirical sizing curve reported by Moreels et al; these values are employed in tables and calculations below.[32] We find these sizes are smaller, though generally in good agreement with the average diameter determined from TEM image analysis (Figure 4.1 - Figure 4.3).[32] To systematically investigate the impacts of both ligand backbone (alkyl vs. aryl) and binding group (carboxylate vs. thiolate) on QD surface chemistry and reactivity upon charging the QDs with $CoCp_2$, we selected three exchange ligands. Sixty percent of each QD batch was reacted with either 200 equiv. undec-10-enoic acid (UDA), 600 equiv. triethylammonium *p*-toluate, or 100 equiv. undec-10-ene-1-thiol (UDT) (Scheme 4.2, see Experimental for details). The mixed-shell systems were obtained by stirring with exchange ligand for 10–40 minutes and purified via multiple precipitation–centrifugation cycles using polar, aprotic anti-solvents to precipitate the nonpolar QDs from solution. TEM imaging of the isolated QDs indicates that the size remained unchanged after the ligand exchange reaction (Figure 4.4 - Figure 4.6. The reaction stoichiometry was selected in order to obtain PbS QDs with mixed ligand shells comprised of a near 1:1 ratio of the native oleate ligands and the added ('exchange') ligand, herein referred to as mixed-shell QDs (see below for shell composition quantification). The 1:1 ratio of ligands in the mixed ligand shells maintains QD solubility in toluene and also provides approximately equal bound concentrations of each ligand to compare surface changes during charging studies (below). Portions of the unexchanged oleate-PbS QDs (named oleate-PbS-1, -2, and -3) were reserved to conduct comparative experiments in parallel with the mixed-shell systems.

Scheme 4.2 Exchange of Oleate Ligands for Comparative Studies

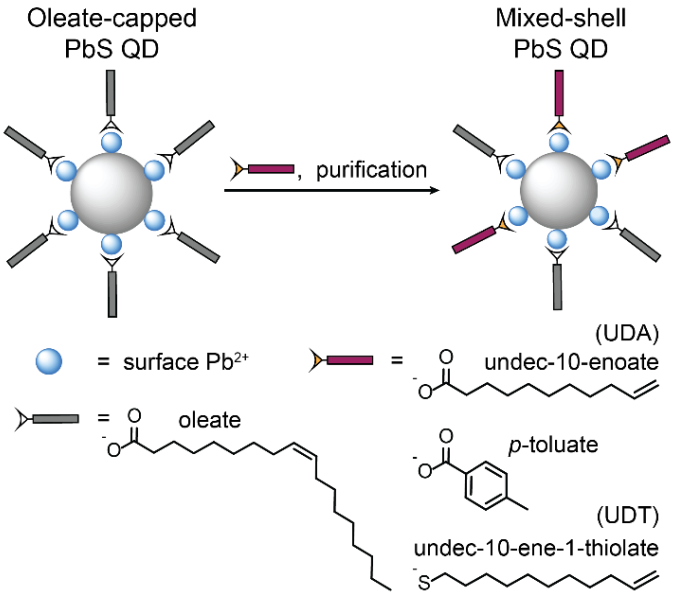

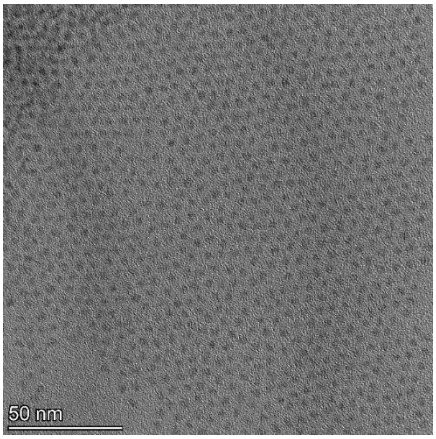

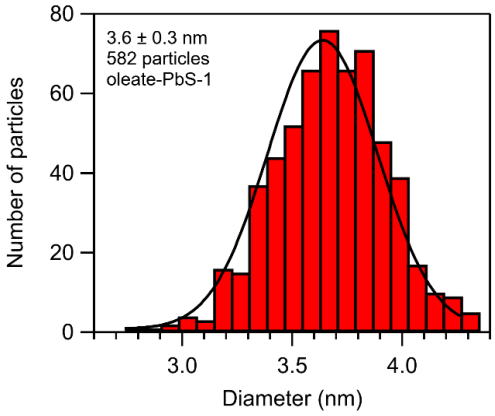

Figure 4.1 (*Left*) TEM image of as-synthesized oleate-PbS-1 used for comparison with System 1 (UDA/oleate-PbS QDs). (*Right*) Histogram constructed from analysis of the image in panel *a* using *ImageJ*. Average particle size is 3.6 ± 0.3 nm.

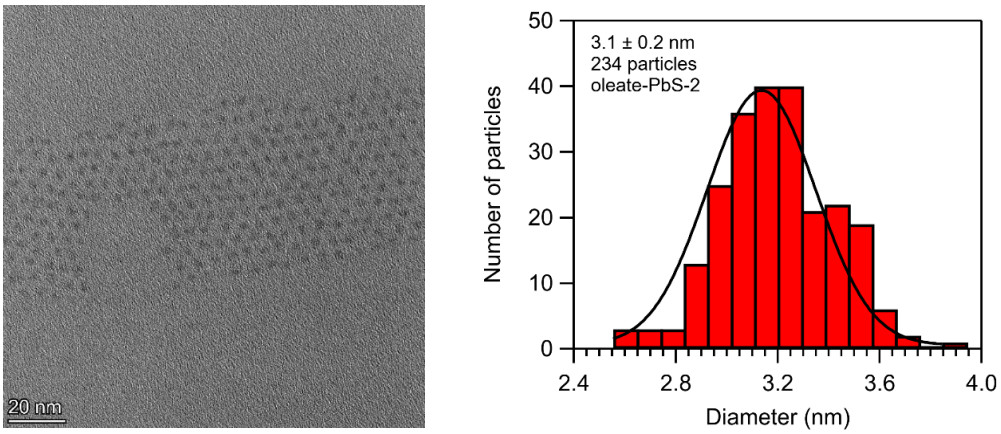

Figure 4.2 (*Left*) TEM image of as-synthesized oleate-PbS-2 used for comparison with System 2 (toluate/oleate-PbS QDs). (*Right*) Histogram constructed from analysis of the image in panel *a* using *ImageJ*. Average particle size is 3.1 ± 0.2 nm.

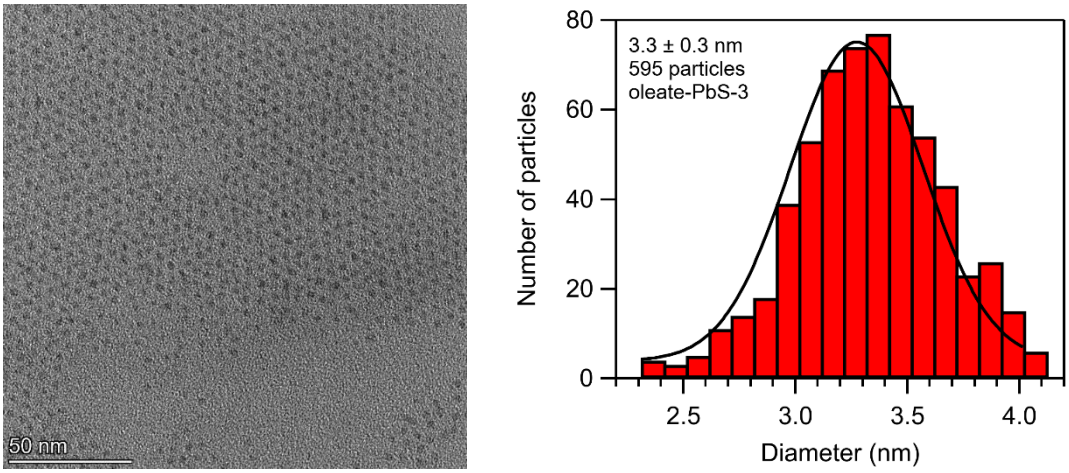

Figure 4.3 (*Left*) TEM image of as-synthesized oleate-PbS-3 used for comparison with System 3 (UDT/oleate-PbS QDs). (*Right*) Histogram constructed from analysis of the image in panel *a* using *ImageJ*. Average particle size is 3.3 ± 0.3 nm.

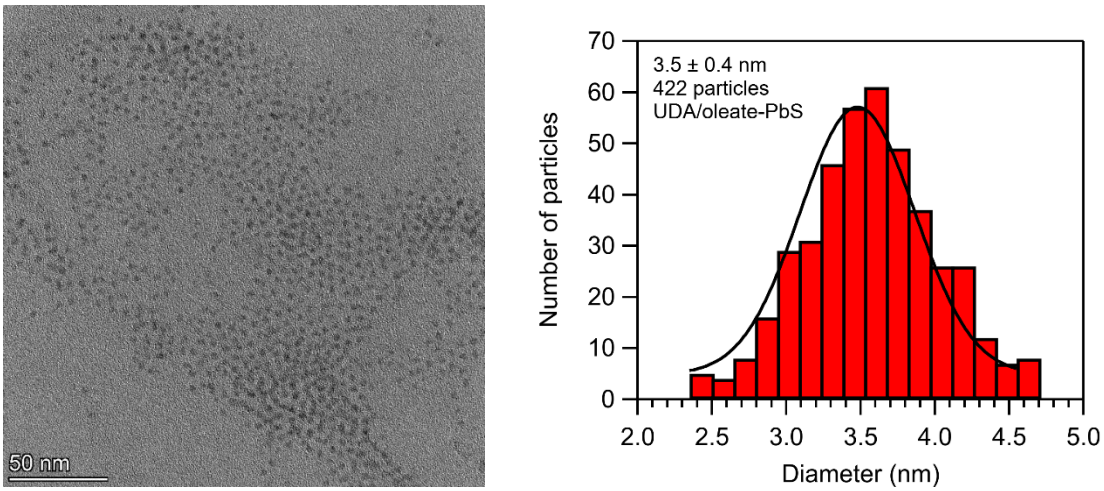

Figure 4.4 (*Left*) TEM image of exchanged and isolated UDA/oleate-PbS QDs (System 1). (*Right*) Histogram constructed from analysis of the image in panel *a* using *ImageJ*. Average particle size is 3.5 ± 0.4 nm.

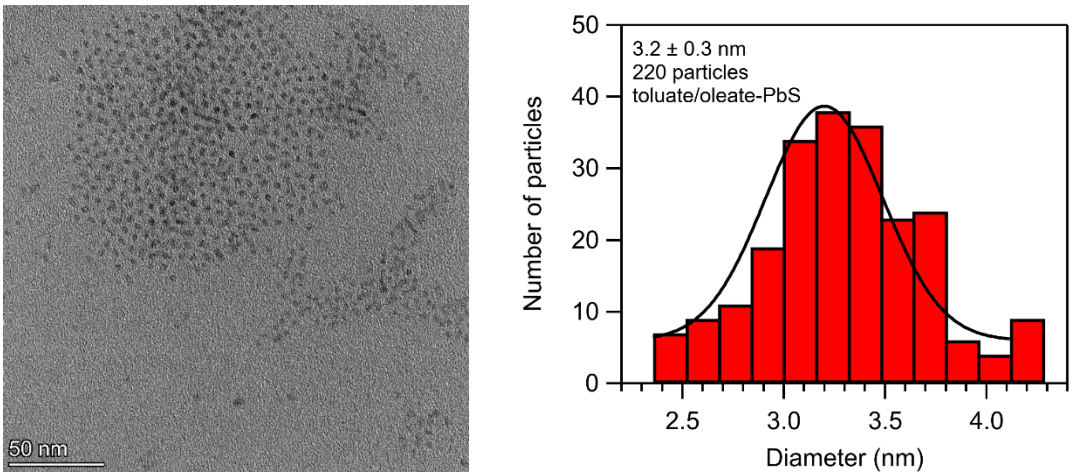

Figure 4.5 (*Left*) TEM image of exchanged and isolated toluate/oleate-PbS QDs (System 2). (*Right*) Histogram constructed from analysis of the image in panel *a* using *ImageJ*. Average particle size is 3.2 ± 0.3 nm.

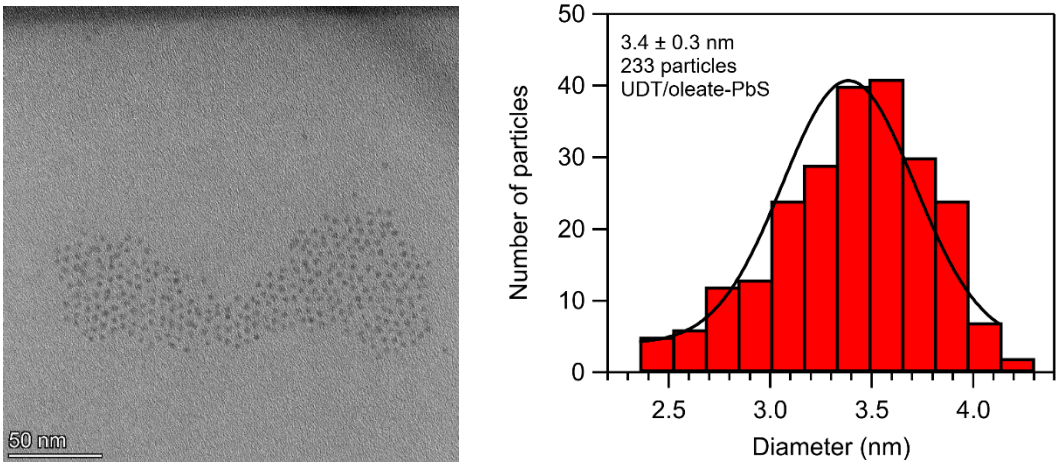

Figure 4.6 (*Left*) TEM image of exchanged and isolated UDT/oleate-PbS QDs (System 3). (*Right*) Histogram constructed from analysis of the image in panel *a* using *ImageJ*. Average particle size is 3.4 ± 0.3 nm.

The differences in reaction conditions to achieve each mixed-shell system—UDA/oleate-PbS, toluate/oleate-PbS, and UDT/oleate-PbS—demonstrate how equilibria dictate the extent of ligand exchange. In general, higher concentrations of carboxylic acid-terminated ligands are required to obtain mixed-shell QDs, whereas native oleate displacement occurs much more readily upon introduction of a thiol-terminated ligand; these differences reflect the equilibrium constants dictating the exchange process and the complexities of thiol reactivity.[27] Notably, the UDA ligand was introduced as the neutral carboxylic acid, whereas the *p*-toluate mixed-ligand QD was accessed through addition of the triethylammonium *p*-toluate salt.[16] Ligand exchange with UDA has been previously established as an X-type exchange mechanism on PbS QDs, wherein the acidic proton of the UDA carboxylic acid protonates a bound oleate ligand, liberating oleic acid.[29] Unlike UDA, the solubility of *p*-toluic acid in toluene is poor, rendering direct exchange ineffective. However, as previously demonstrated by Giansante et al., triethylammonium *p*-toluate undergoes exchange with native oleate ligands on PbS QDs.[16] The exchange proceeds through an X-type exchange mechanism akin to a salt metathesis that liberates triethylammonium oleate upon toluate binding. In contrast to carboxylic acid-terminated ligands, alkyl thiols have been established to undergo a variety of surface ligand reactions with oleate-capped QDs,

including X-type exchange,[27,33,34] L-type ligand binding (as a two-electron donor),[27,33,34] and L-type promoted Z-type ligand displacement (liberating a $Pb(oleate)_2$ ligand).[35,36] Investigations of these convoluted reaction mechanisms are underway in our lab.

After purification, the mixed-shell systems were characterized with ^{1}H NMR spectroscopy, which employs the alkene and aryl protons on the ligand backbones to probe the surface ligand composition. Distinct resonances for bound and free ligands in toluene-d_8 arise from aromatic solvent-induced shifting, an effect particularly useful for determining whether free ligand remains after purification or for observing free ligand liberated by chemical or redox probes.[37,38] The chemically inequivalent alkene protons of oleate are labeled **1 and 1′** in the chemical structure of Figure 4.7, though we note that these protons appear at the same resonance in ^{1}H NMR spectra. Clearly, oleate ligands are present in modest proportion in each mixed-ligand system, as evidenced by the diagnostic broad peak of bound oleate at ca. 5.65 ppm. The toluate/oleate-PbS spectrum shows that the oleate resonances (**1, 1′**) shift upfield by about 0.1 ppm. Additionally, the asymmetric peak observed in this sample likely indicates more heterogeneous broadening than the other systems (Figure 4.8).

The aryl protons of the toluate ligand appear at ca. 8.2 ppm and 7.1 ppm, though the broad peak at 7.1 ppm overlaps with the sharp signals of the toluene residual (Figure 4.9). Broad signals at ca. 6.0 ppm and 5.2 ppm in the UDA/oleate-PbS and UDT/oleate-PbS spectra are attributed to the terminal alkene protons of bound UDA and UDT ligands, respectively (Figure 4.10 - Figure 4.11). Notably, the UDT/oleate-PbS spectrum contains a second set of sharper peaks consistent with free UDT ligand near 5.8 ppm and 5.0 ppm. Despite a rigorous six-step purification protocol, 2D DOSY NMR experiments suggest that unbound UDT ligands persist, yet these ligands are strongly associated with the nanocrystal ligand shell (Figure 4.12). A possible dithiol species, which has a characteristic triplet at 2.53 ppm for the α-protons near the S–S group, comprises only ca. 5% of the total unbound UDT species (Figure 4.11). Thus, the exact nature (i.e., thiol vs. thiolate vs. dithiol) of this unbound UDT species is not known.

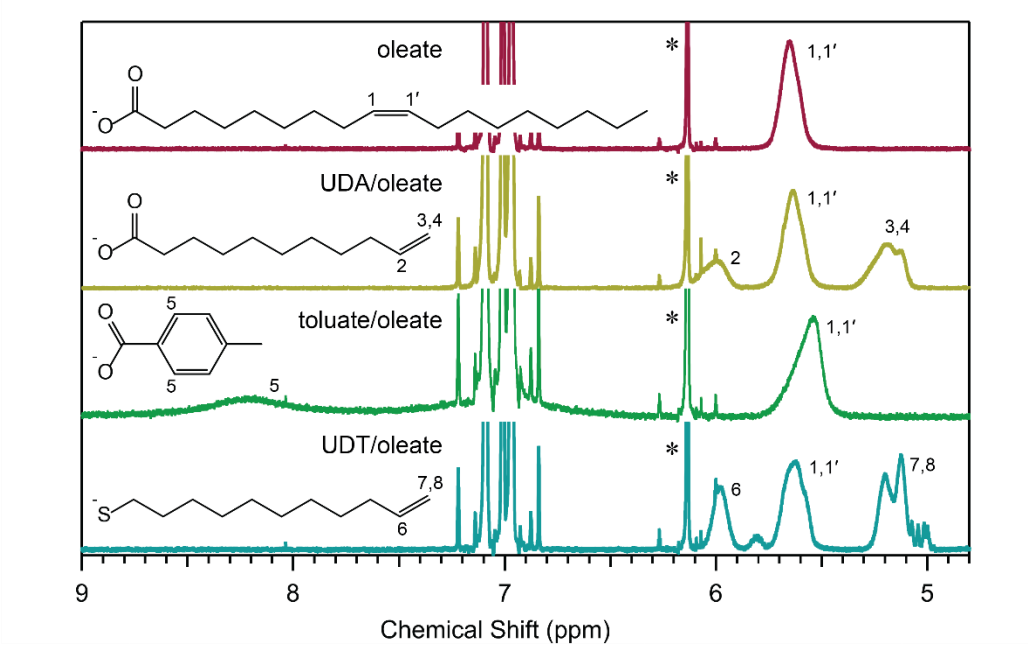

Figure 4.7 600 MHz ^{1}H NMR spectra of oleate-capped PbS (red), UDA/oleate-PbS (gold), toluate/oleate-PbS (green), and UDT/oleate-PbS (blue) QDs (all 46 µM) in toluene-d_8. The internal standard peak of 1,3,5-trimethoxybenzene is denoted by (*) and the solvent residual peaks are near 7.0 ppm.

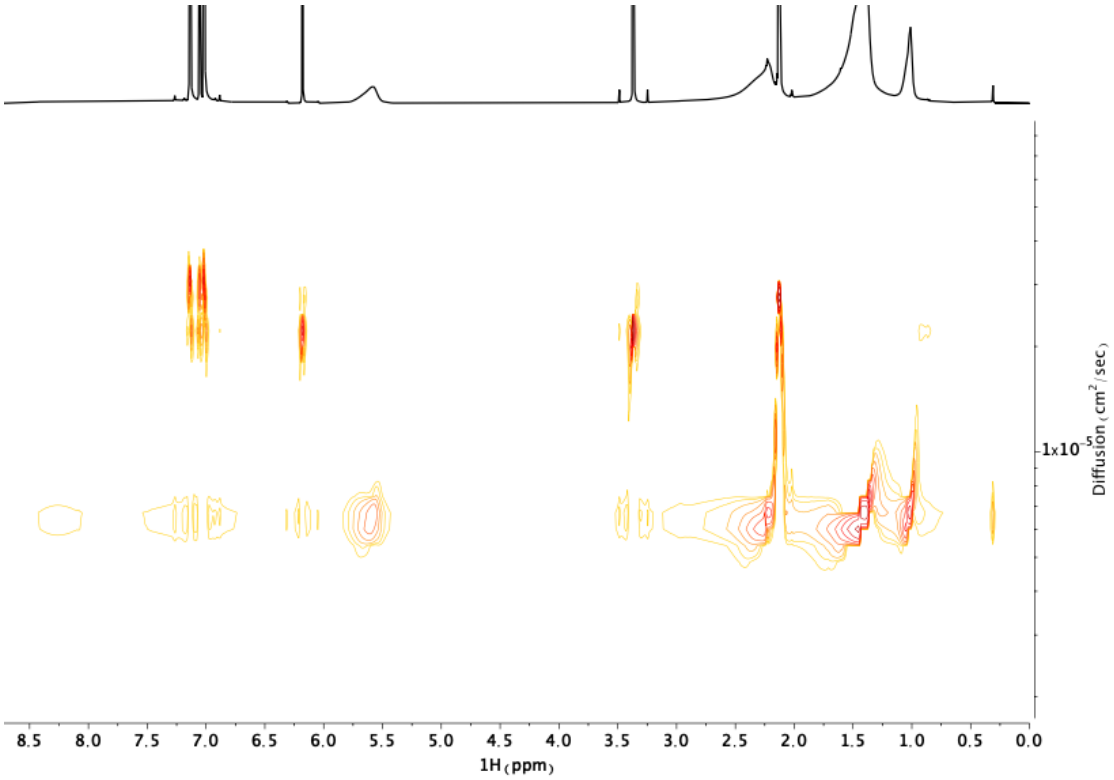

Figure 4.8 ^{1}H DOSY plot of the toluate/oleate-PbS QD system (150 μM in toluene-d_8). An optimized average 90° pulse length of 15.125 microseconds and a relaxation delay of 15 seconds were used for this experiment. A stebpgp1s pulse sequence was used to maximize signal to noise. A delta of 100 ms and a gradient pulse length (1100 msec) were used. An array of 1D spectra at 32 different gradient strengths with linear sampling were acquired and transformed using a Bayesian transformation in the MNOVA software suite (rf: 2, repetitions: 1). Analysis of the diffusion data reveals an estimated diffusion constant for the trimethoxybenzene internal standard of $2.2 \cdot 10^{-5}$ cm^2/sec. The toluate and oleate ligands show an estimated diffusion constant of $6.3 \cdot 10^{-6}$ cm^2/sec, indicating that all ligand resonances are broadened due to heterogeneous broadening and not due to a convolution of bound and free ligand. Additionally, the smaller diffusion constant for the ligand resonances relative to that of the internal standard indicates that they are bound to the QD surface.

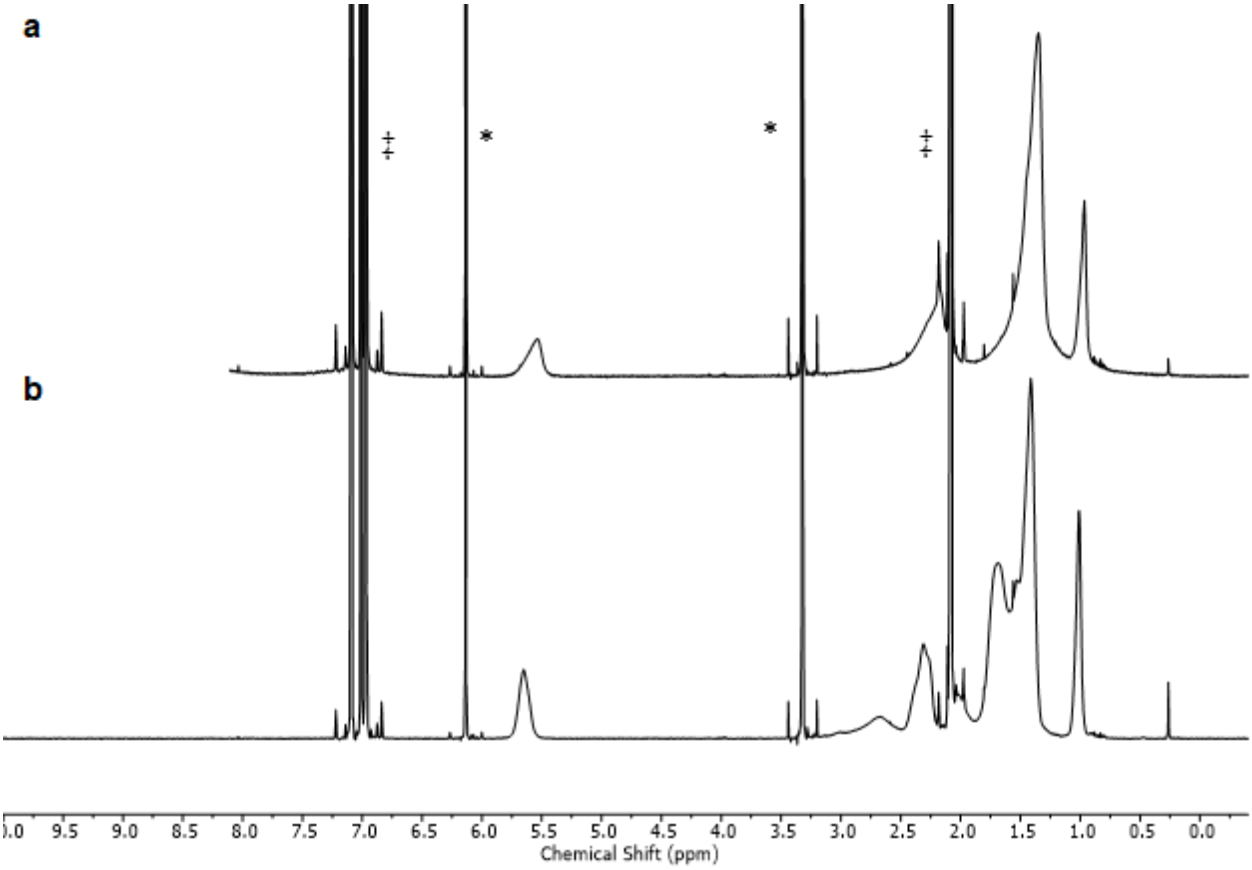

Figure 4.9 600 MHz ^{1}H NMR spectra in toluene-d_8 of a) toluate/oleate-PbS QDs and b) 2.9 nm oleate-PbS QDs. Sharp peaks denoted by ‡ are toluene solvent residuals, and peaks marked by * are protons within the internal standard 1,3,5-trimethoxybenzene.

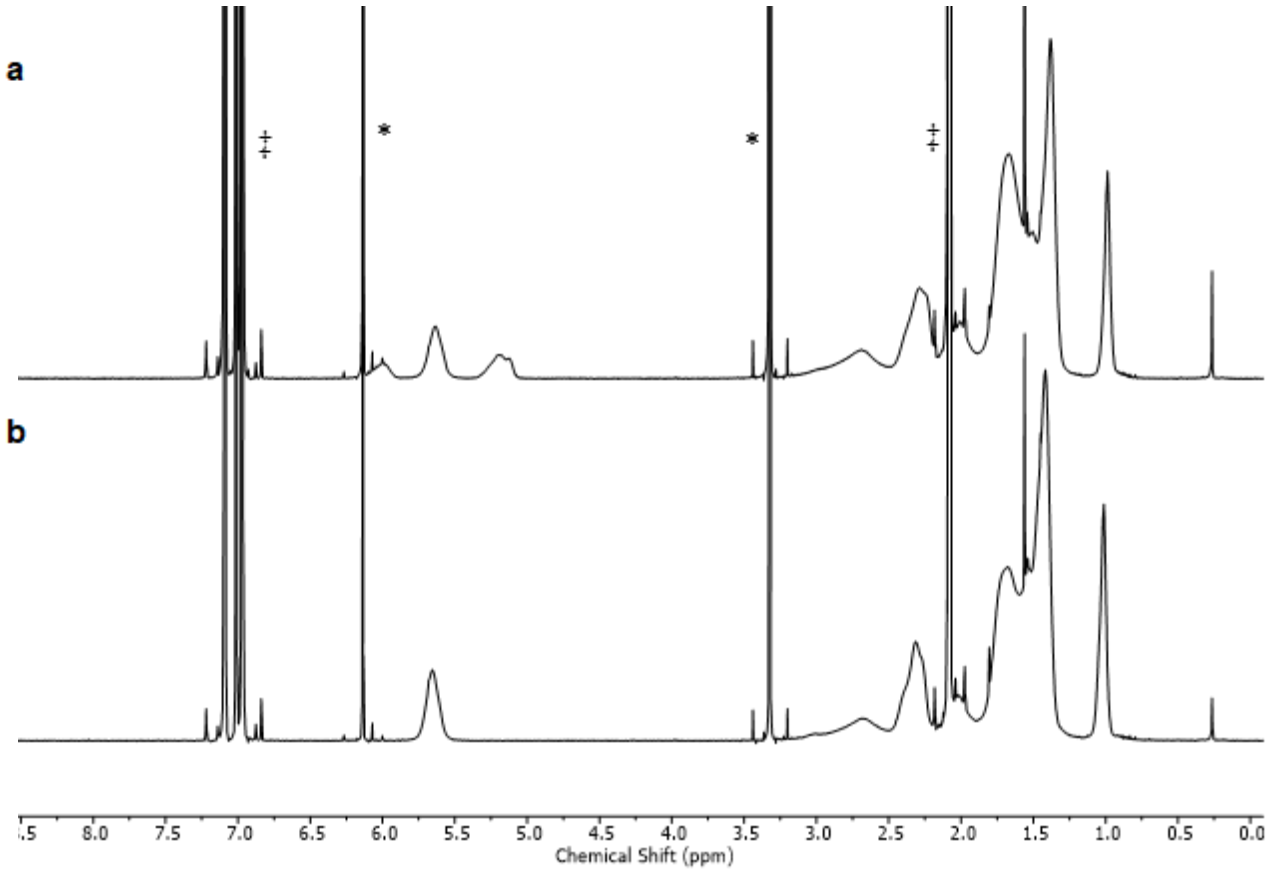

Figure 4.10 600 MHz ^{1}H NMR spectra in toluene-d_8 of a) UDA/oleate-PbS QDs and b) 3.1 nm oleate-PbS QDs. Sharp peaks denoted by ‡ are toluene solvent residuals, and peaks marked by * are protons within the internal standard 1,3,5-trimethoxybenzene. The impurity at 1.57 ppm is trace acetone.

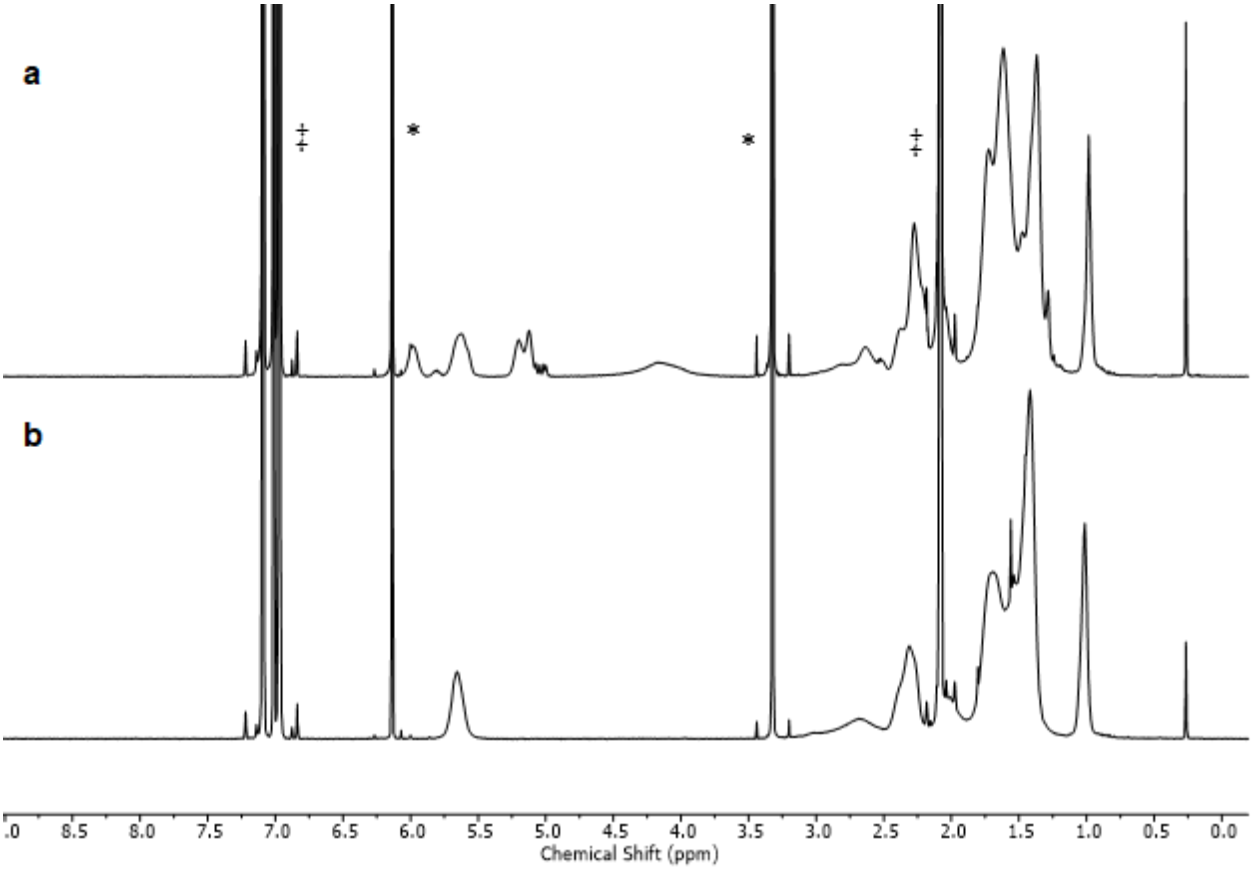

Figure 4.11 600 MHz ^{1}H NMR spectra in toluene-d_8 of a) UDT/oleate-PbS QDs and b) 3.1 nm oleate-PbS QDs. Sharp peaks denoted by ‡ are toluene solvent residuals, and peaks marked by * are protons within the internal standard 1,3,5-trimethoxybenzene. As noted, a triplet indicative of dithiol presence can be detected at 2.53 ppm for the protons closest to the S-S group. For the purified UDT/oleate-PbS QDs, the triplet integrates to ca. 0.3 dithiols per QD, about 5% of the total unbound UDT species.

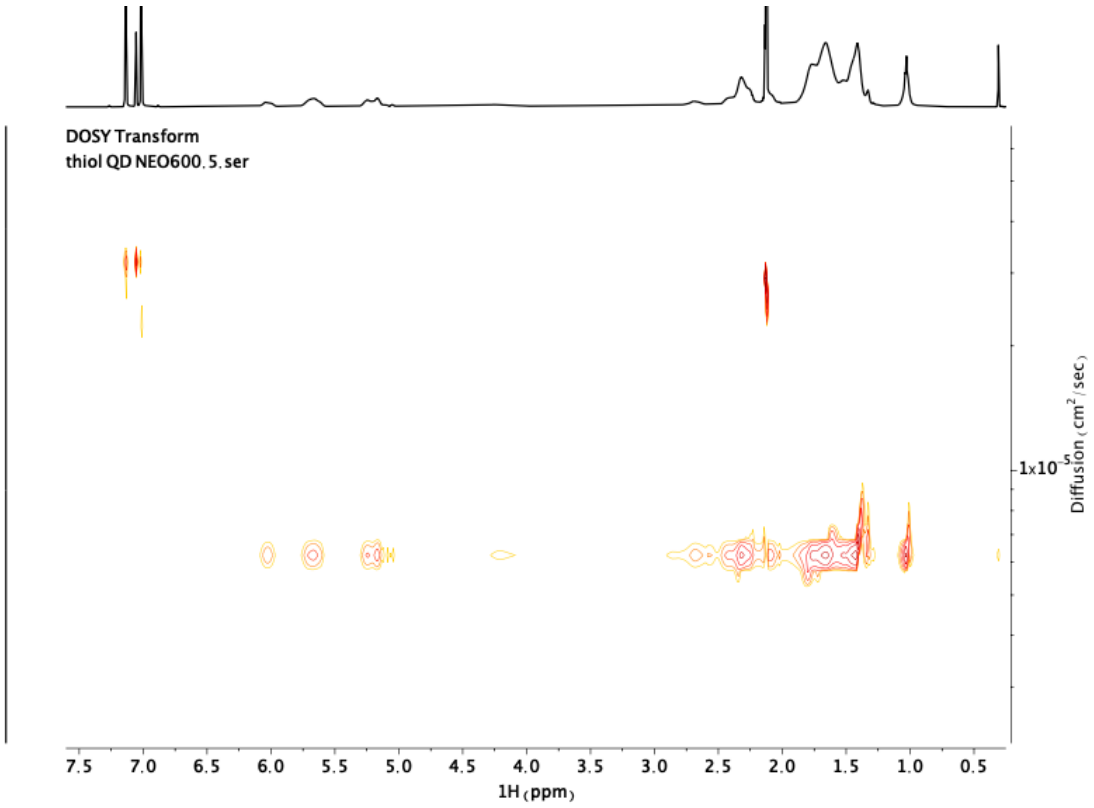

Figure 4.12 a) 2D DOSY plot of 150 μM UDT/oleate-PbS QDs in toluene-d_8. An average 90° pulse length was determined to be 10 microseconds for the sample, and a delay of 18 seconds was found to be sufficient for relaxation. Spectra were acquired with the stebpg1s pulse sequence to minimize relaxation effects. A delta of 100 ms and gradient pulse length of 1100 microseconds were used. An array of 16 gradient strengths with a linear sampling was chosen for this experiment. The array of protons was baseline corrected and fit using the three-parameter fitting function in MNOVA, indicating single exponential decay, and a Bayesian transformation (RF Factor: 2, Repetitions: 2) was applied to the array. b) Zoomed-in DOSY plot centered on the alkene region. All "bound" and "free" UDT alkene peaks diffuse together (approx. $6.3 \cdot 10^{-6}$ cm^2/s), indicating the "free" thiol species is strongly associated with the quantum dot. Additionally, the small diffusion constant for the ligand resonances indicates that they are bound to the QD surface.

While ^{1}H NMR spectroscopy is adept at characterizing the proton-rich ligand backbones, the binding group environments are more effectively probed by infrared spectroscopy (FTIR). The carboxylate O−C−O stretching frequencies at ca. 1400 cm^{-1} ($\nu_{symmetric}$) and 1530 cm^{-1} ($\nu_{asymmetric}$) in the oleate-PbS spectra (Figure 4.13**,** Figure 4.14) are consistent with a convolution of both chelating bidentate and bridging bidentate binding motifs and are in agreement with previous FTIR studies on oleate-capped PbS and CdSe QDs.[39,40] In the UDA/oleate-PbS spectrum, the appearance of a weak monosubstituted C=C stretch at 1641 cm^{-1} consistent with the terminal alkene of UDA confirms the formation of the

mixed-shell system, with the O−C−O stretching region remaining unchanged compared with the oleate-PbS QDs (Figure 4.13). The conjugated C=C stretching modes at 1607 cm^{-1} and 1586 cm^{-1} observed in the toluate/oleate-PbS spectrum support the exchange of native oleates for toluate ligands. In contrast with the UDA/oleate system, the carboxylate stretching region of toluate/oleate-PbS shifts to lower wavenumbers. We attribute this observation to the contribution of $\nu_{symmetric}$ and $\nu_{asymmetric}$ stretches of the bound toluate ligand to the overall O−C−O stretching region, which for free *p*-toluic acid are shifted to lower wavenumbers than those for free UDA (Figure 4.15). The FTIR spectrum of UDT/oleate-PbS QDs displays a C=C stretch at 1641 cm^{-1}, expected for the monosubstituted alkene of UDT (Figure 4.16). Furthermore, the addition of thiolate ligands appears to narrow the symmetric and asymmetric stretches of the $-COO^-$ group and shift them to slightly lower wavenumbers (Figure 4.13). These effects may be due to the significant decrease in total carboxylate ligand coverage in the UDT/oleate-PbS mixed-shell system.

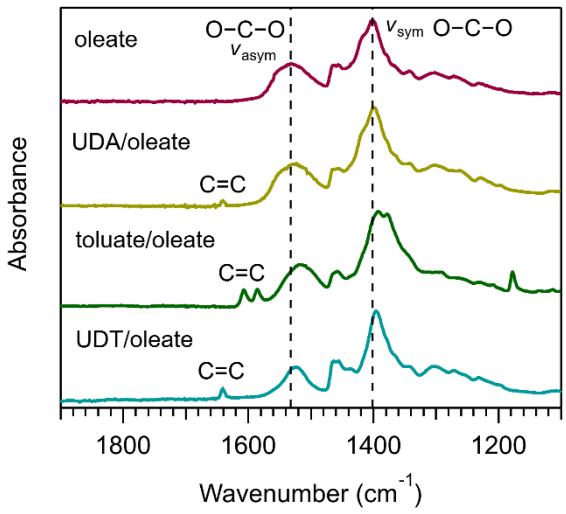

Figure 4.13 ATR-FTIR spectra of oleate-capped and mixed-shell PbS QDs showing the carboxylate stretching region; full spectra are provided in Figure 4.17. Dashed lines are provided to enable qualitative comparisons of how the peak positions observed in the oleate-PbS spectrum shift in the mixed-shell PbS spectra.

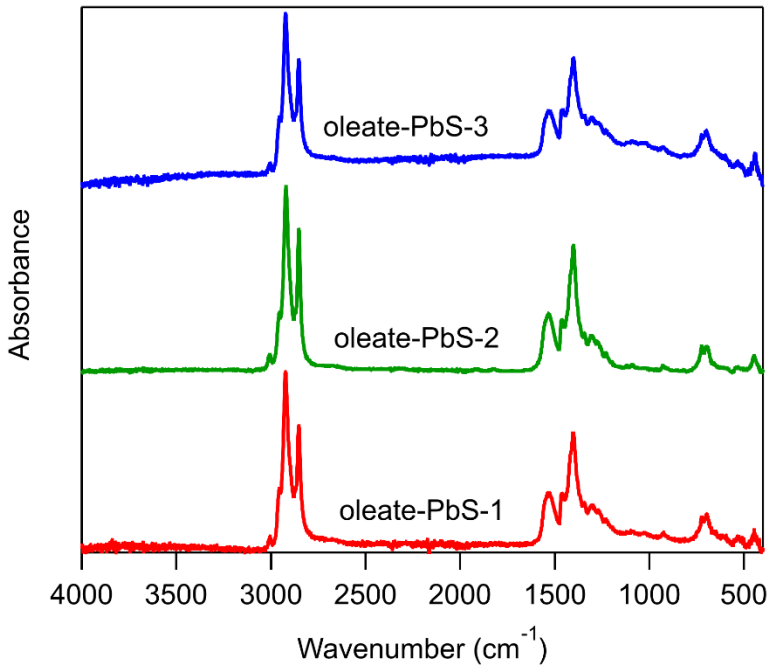

Figure 4.14 ATR-FTIR spectra of oleate-capped PbS QDs collected in absorbance mode. IR stretches are attributed to bound oleate ligands.

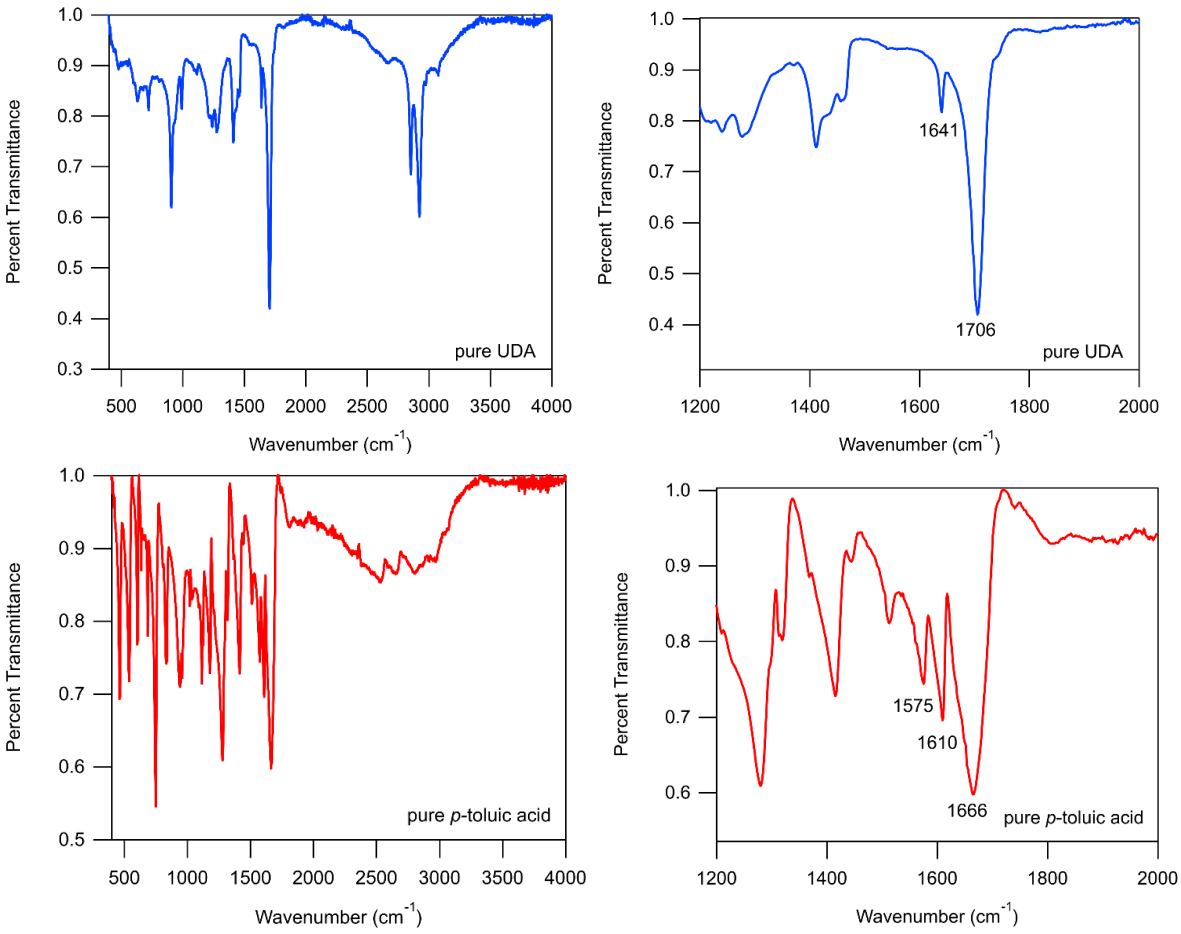

Figure 4.15 ATR-FTIR spectra of (*bottom*) *p*-toluic acid and (*top*) undec-10-enoic acid. Full spectra are provided on the left; zoomed-in spectra are shown on the right. The C=O stretch of *p*-toluic acid appears at 1666 cm^{-1}, and of UDA appears at 1706 cm^{-1}. The labeled aryl C=C peaks of *p*-toluic acid and alkene C=C peaks of UDA are mostly unchanged upon binding to the PbS QD.

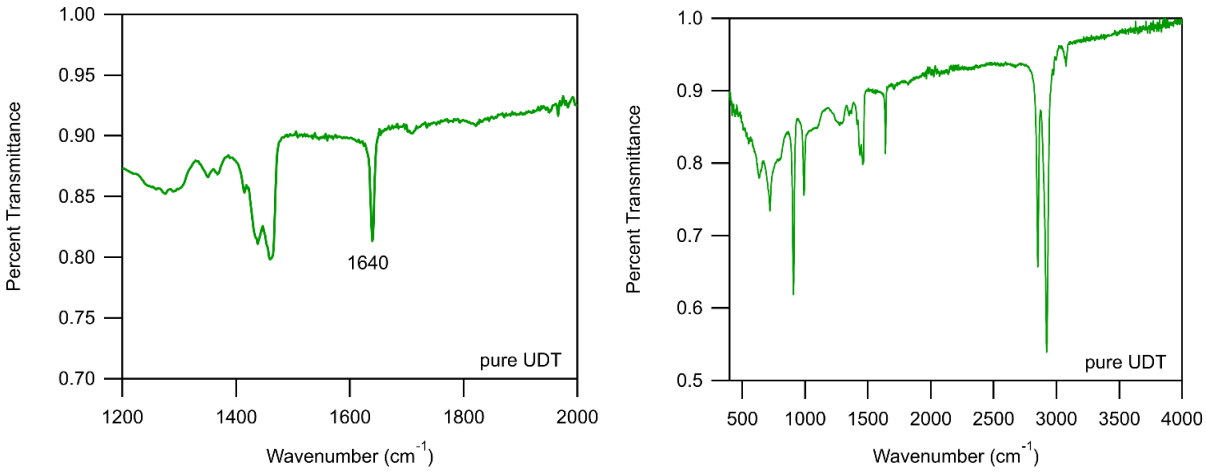

Figure 4.16 (*Left*) Full ATR-FTIR spectrum of undec-10-ene-1-thiol. (*Right*) Zoomed in spectrum of UDT, showing the C=C stretch at 1640 cm^{-1}, which appears unchanged in the spectrum of UDT/oleate-PbS QDs.

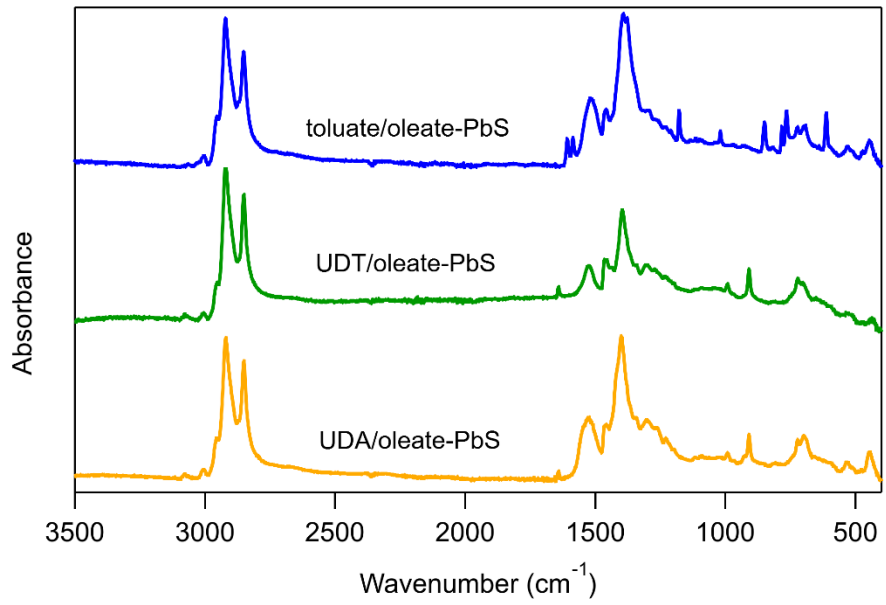

Figure 4.17 Full ATR-FTIR spectra for mixed-shell PbS QDs.

UV-Vis absorbance spectra of each oleate-only and mixed-shell QD sample were collected to evaluate how ligand exchange affects QD optical properties. The impact of nanocrystal surface chemistry on the excitonic absorption feature has been extensively discussed in the literature.[41,42] In the UDA/oleate-PbS absorbance spectrum, the λ_{max} remains fixed at the same wavelength as the oleate-PbS-1 spectrum, as anticipated for a mixed-shell QD comprised of two alkyl carboxylate ligands with similar electronic

structures (Figure 4.18). The toluate/oleate-PbS absorbance exhibits a 10 nm blue shift of the excitonic feature relative to the oleate-PbS-2 spectrum. This observation contrasts with the minor red shifting of the excitonic peak during *in situ* ligand exchange as previously demonstrated in the literature, yet a convolution of electronic and etching effects may contribute to the observed peak shifts in the post-exchanged sample spectrum.[16] Finally, the excitonic feature of the UDT/oleate-PbS system displays a 10 nm red shift relative to the oleate-PbS-3 spectrum, likely resulting from electronic contributions from the sulfur 3p orbitals of the thiolate ligand in the Pb−S bond to the overall electronic structure of the QD, particularly to the highest occupied orbitals comprising the valence band.[16,41]

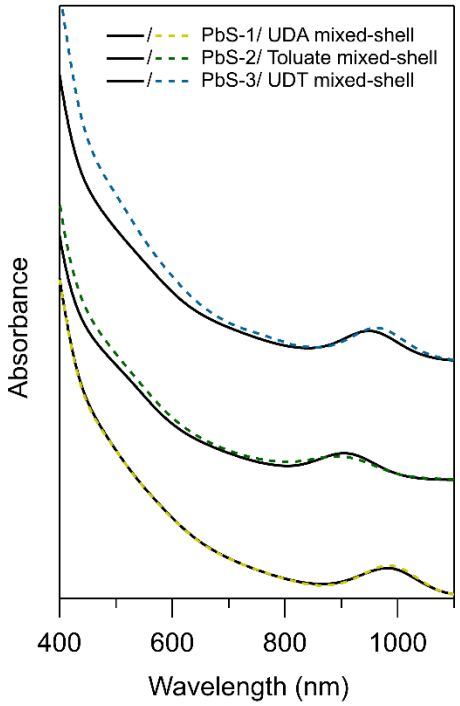

Figure 4.18 UV-Visible absorbance spectra of 2.5 µM oleate-PbS QDs and mixed-shell PbS QDs in toluene. Baselines are shifted arbitrarily to overlay; the QD samples display no detectable scatter.

4.3.2 Determination of Extinction Coefficients for Quantitative Analysis.

The absorbance spectra of our mixed-shell QDs in Figure 4.18 clearly demonstrate that the optical properties differ from the oleate-capped PbS QDs, with broadband absorbance enhancements and

excitonic peak shifts occurring in the toluate- and UDT-exchanged QD samples. While researchers often carry out *in situ* ligand exchange studies under the assumption that the concentration of QDs remains constant (i.e., precipitation of nanocrystals does not occur), the isolation of mixed-ligand shells after ligand exchange requires additional calculations to confirm QD concentrations. The widely cited 2009 study by Moreels et al. derived an empirical extinction coefficient at 400 nm for oleate-capped PbS QDs using Rutherford backscattering spectroscopy (RBS), UV-Vis absorption spectroscopy, and inductively coupled plasma mass spectrometry (ICP-MS).[32] More recently, Debellis et al. established empirical relationships to calculate the extinction coefficients of as-synthesized and ligand-exchanged PbS QDs with diameters of 2–7 nm using transmission electron microscopy (TEM), density functional theory (DFT), and ICP atomic emission spectroscopy.[43] However, such relationships may not translate perfectly across different ligand sets or apply at various extents of ligand exchange. We therefore slightly modified the experimental method of Moreels et al. to calculate the extinction coefficients of each oleate-PbS sample as well as the toluate/oleate, UDA/oleate, and UDT/oleate mixed-shell PbS samples studied herein (sample calculation provided in **Appendix C**).

Calculation of the extinction coefficient at 400 nm (ε_{400}) requires Beer's law,

Equation 4.1

$$A_{400} = \varepsilon_{400} bc$$

from which ε_{400} can be found if the absorbance value at 400 nm (A_{400}) and the concentration of QDs (c) are known (b is the path length of the cuvette, 0.2 cm). For each oleate-only and mixed-shell PbS sample, a UV-Vis absorbance spectrum was collected in benzene to determine the A_{400} value. Then, the QD concentration (c) in the cuvette was calculated using a combination of ICP-MS and XPS measurements to determine the total moles of Pb of the sample and the molar ratio of Pb ions per QD, respectively. To obtain the total moles of Pb in each UV-Vis sample, the QDs in the cuvette were completely transferred to a scintillation vial. The solvent was removed by evaporation and the remaining residue was pyrolyzed at 450 °C in a box furnace to decompose the organic oleate ligands and improve solubility of Pb^{2+} ions digested in concentrated HNO_3. Next, ICP-MS measurements of appropriately diluted samples of digested

QDs in ultrapure water yielded a concentration of Pb from which the total moles of Pb in each sample was found.

In order to convert the total Pb concentration from ICP-MS to a concentration of QDs, the molar ratio of Pb ions per QD was determined. We first estimated the total number of atoms (*N*) in an approximately spherical QD using Equation 2 (*d* = diameter of the QD in nm; *a* = lattice constant of bulk PbS, 0.5936 nm).

Equation 4.2

$$N = \frac{4\pi}{3}\left(\frac{d}{a}\right)^3$$

For the next step of the calculation, we employed XPS to determine the contributions of Pb and S to the total number of atoms in each QD (*N*). Integrations of Pb 4f and S 2p peaks in the XPS spectra yielded a Pb:S ratio for each sample, ranging from 1.7:1 to 2.1:1. (Figure 4.19, Table 4.2). These measurements fall within the range of Pb:S ratios previously reported for PbS QDs ca. 3 nm in diameter.[35,44–46] The Pb-rich QD composition implied by a greater than 1:1 Pb:S ratio also supports passivation of surface Pb^{2+} ions with anionic X-type ligands—a population of these PbX_2 moieties may be classified as Z-type ligands.[47] Notably, care was taken to obtain an accurate Pb:S ratio for the UDT/oleate-PbS QD sample which excluded the sulfur contribution from the thiolate ligands. The XPS spectrum displayed two doublets in the S 2p region which were deconvoluted and assigned to sulfur in the inorganic lattice versus sulfur in the UDT ligand (Figure 4.20). The assignment of sulfur in the UDT ligand was verified through XPS characterization of a lead dodecanethiolate species (Figure 4.21). The Pb:S ratio of each inorganic lattice was used to determine the relative stoichiometry of Pb and S ions per QD, and the absolute number of Pb and S ions per QD were calculated from the sum of Pb and S ions (*N*) obtained by Equation 4.2 (Table 4.3). Next, the total moles of Pb in each sample from ICP-MS was divided by the moles of Pb per QD from Equation 4.2 and XPS, therefore obtaining the concentration of QDs in the cuvette (*c*) using the initial volume of the UV-Vis sample. Finally, the A_{400} value and

calculated *c* value were utilized in Equation 4.1 to solve for the extinction coefficient at 400 nm (ε_{400}) (Table 4.4).

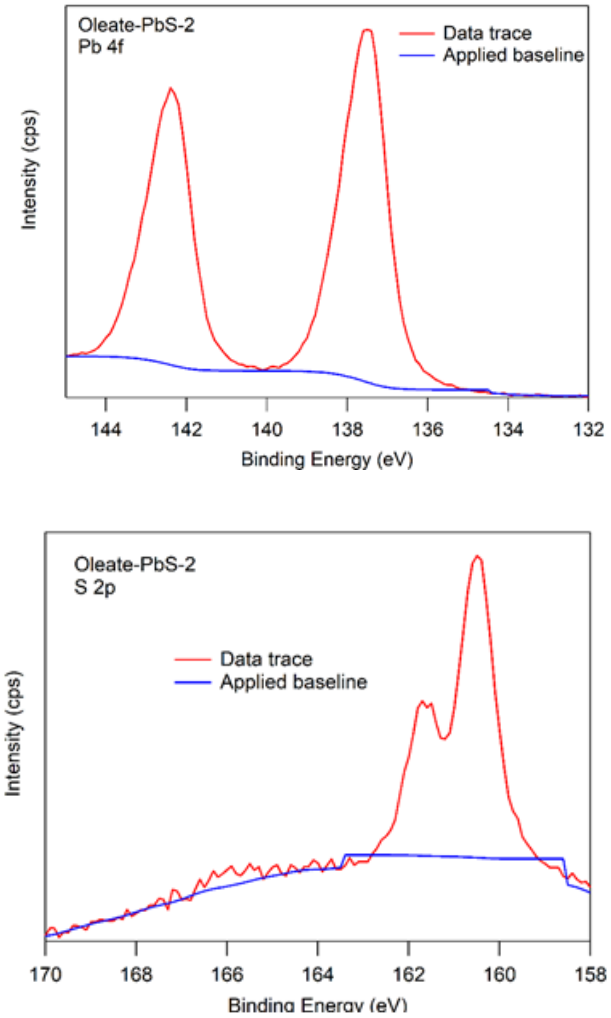

Figure 4.19 Representative XPS data of Pb 4f (*top*) and S 2p (*bottom*) regions for as-synthesized oleate-PbS-2 QDs.

Table 4.2 Pb:S ratios for oleate-PbS QDs and their corresponding mixed-shell PbS QDs. The Pb:S ratios were obtained from atomic concentrations of Pb and S determined by XPS. Two data points were obtained for two separate wafers by moving the wafer to examine a different spot on the surface.

		Pb:S ratios					
XPS Sample		**oleate-PbS-1**	**UDA/oleate-PbS[a]**	**oleate-PbS-2**	**toluate/oleate-PbS**	**oleate-PbS-3**	**UDT/oleate-PbS**
Wafer 1	**1**	2.06	1.82	2.21	1.91	1.89	1.74

	2	1.98	-	2.16	1.96	1.84	1.66
Wafer 2	**1**	1.88	1.83	2.01	1.88	1.79	1.72
	2	1.94	1.85	2.09	1.91	1.74	1.75
Average ± Std. Dev.		1.97 ± 0.08	1.83 ± 0.02	2.12 ± 0.09	1.92 ± 0.03	1.82 ± 0.06	1.72 ± 0.04

[a]Attempts to sample additional points on wafer 1 for UDA/oleate-PbS resulted in charging. Point 2 was therefore omitted.

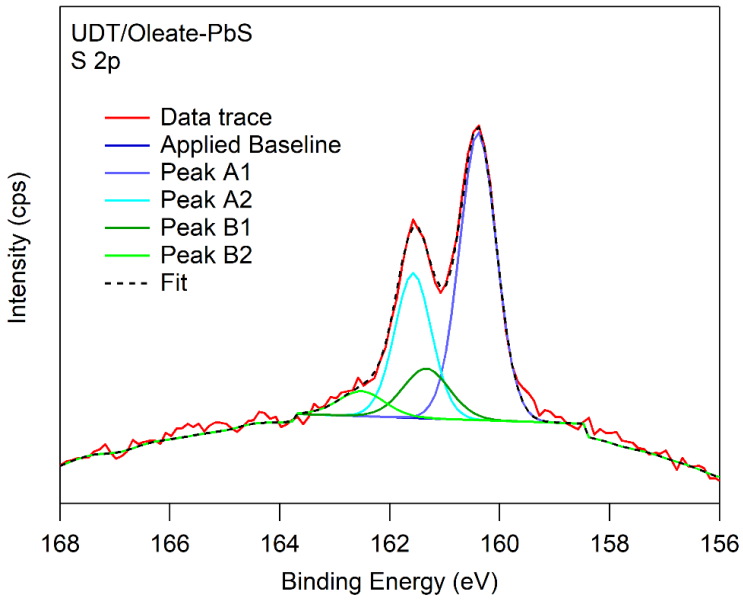

Figure 4.20 Representative S 2p region of XPS spectrum for UDT/oleate-PbS QDs. The doublet positioned at 160.4 eV (Peaks A1 and A2, 160.4 and 161.6 eV, respectively) is attributed to sulfur in the nanocrystalline PbS lattice while the doublet at 161.3 eV (Peaks B1 and B2, 161.3 and 162.5 eV, respectively) is attributed to Pb-bound thiolate ligands. A linear baseline was applied to the S 2p regions of 3.1 nm oleate-PbS and the exchanged UDT/oleate-PbS samples to standardize fitting parameters and enable comparison of Pb:S ratios for these samples. A dwell time of 10000 ms was used improve resolution of S 2p feature.

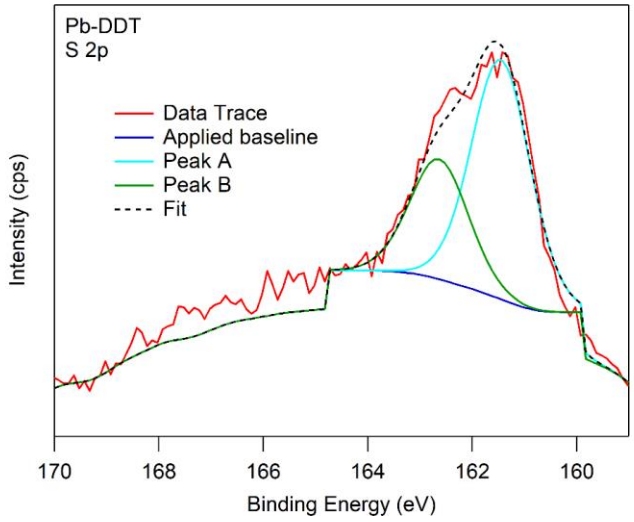

Figure 4.21 S 2p region of XPS spectrum for putative Pb-DDT complex. The spectrum is fit well by underlying features at 161.5 eV (Peak A) and 162.6 eV (Peak B). A dwell time of 10000 ms was used improve resolution of S 2p feature.

Table 4.3 Pb:S ratios from XPS, calculated total atoms per QD, and calculated Pb and S atoms per QD using the Pb:S ratios.

System	Sample	Average Pb:S ratio ± SD	Total Pb+S (*N*)[a]	Pb per QD	S per QD
1	Oleate-PbS-1	1.97 ± 0.08	681	451	230
	UDA/oleate-PbS	1.83 ± 0.02	681	441	240
2	Oleate-PbS-2	2.12 ± 0.09	493	335	158
	Toluate/oleate-PbS	1.92 ± 0.03	493	324	169
3	Oleate-PbS-3	1.82 ± 0.06	597	385	212
	UDT/oleate-PbS	1.72 ± 0.04	597	377	220

[a]Calculated per Equation 2

Table 4.4 Extinction coefficients obtained for the three batches of oleate-PbS QDs and different mixed-shell QDs compared with calculations from the empirical sizing curve established in the literature.

System	**Diameter[a] (nm)**	**Sample**	**Average ε_{400}[b] (M^{-1} cm^{-1})**	**Lit. ε_{400}[a] (M^{-1} cm^{-1})**
1	3.2	Oleate-PbS-1	$9.2 \cdot 10^5 \pm 4 \cdot 10^4$	$7.6 \cdot 10^5 \pm 0.3 \cdot 10^4$
		UDA/oleate-PbS	$9.2 \cdot 10^5 \pm 7 \cdot 10^4$	-
2	2.9	Oleate-PbS-2	$6.5 \cdot 10^5 \pm 3 \cdot 10^4$	$5.7 \cdot 10^5 \pm 0.2 \cdot 10^4$
		Toluate/oleate-PbS	$7.8 \cdot 10^5 \pm 3 \cdot 10^4$	-
3	3.1	Oleate-PbS-3	$7.6 \cdot 10^5 \pm 0.5 \cdot 10^4$	$6.9 \cdot 10^5 \pm 0.3 \cdot 10^4$
		UDT/oleate-PbS	$9.3 \cdot 10^5 \pm 0.4 \cdot 10^4$	-

[a]Diameter of QDs and literature extinction coefficient at 400 nm with error calculated via the method of Moreels et al.[32] [b] Average ε_{400} values and standard deviations are calculated using three samples.

Table 4.4 shows that the average ε_{400} values of oleate-PbS QDs increase with increasing diameter, as expected from previous studies.[32,43] In addition, data in Table 1 highlights that our experimental method yielded extinction coefficients of oleate-capped PbS in good agreement with those calculated by the method of Moreels et al. Comparison between the ε_{400} values of UDA/oleate-PbS and oleate-PbS-1 confirms that minor structural changes in the ligand backbone far from the binding group have little effect on the optical properties. However, comparison of the toluate/oleate-PbS system with oleate-PbS-2 reveals an increase in absorptivity which we attribute to electronic coupling between the electron-donating aryl group and the QD.[16,43,48] Similarly, the introduction of UDT to the ligand shell also results in a marked increase in the ε_{400} value for UDT/oleate-PbS. As UDT maintains an electronically similar ligand backbone to oleate (concluded from the UDA/oleate system), the difference arises from the exchange of carboxylates for thiolates. An increase in absorptivity with thiol-terminated ligands has been attributed to greater ligand–QD state mixing in the covalent surface bonding of thiolate-exchanged PbS QDs compared to carboxylate-capped QDs.[16,43,48] These observations are collectively consistent with *in*

situ ligand exchange experiments conducted on PbS QDs[16,43,48] as well as the UV-Vis absorbance spectra in Figure 4.18.

With empirical extinction coefficients in hand, quantitative characterization of the mixed-ligand QD surface is possible via NMR spectroscopy. Absolute ligand coverages are given in Table 4.5 and are summarized as UDA(39%)/oleate-PbS, toluate(44%)/oleate-PbS, and UDT(49%)/oleate-PbS. These shell ratios illustrate that the mixed-ligand systems studied here are comprised of slightly less than 50% exchange ligand and greater than 50% native oleate ligand. We found that the total ligand coverage of UDA/oleate-PbS QDs increased slightly compared with oleate-PbS-1. While slightly greater than 1:1 exchange ratios have been observed when reactivity beyond pure X-type exchange occurs, the contribution of non-X-type reactivity such as L-type binding is likely negligible for UDA.[29] We also observed that the total ligand coverage of toluate/oleate-PbS QDs decreased compared with oleate-PbS-2. The decrease in ligand coverage upon reaction with triethylammonium toluate is consistent with a slight etching of the QD surface supported by the minor blue shift observed in the UV-Vis spectrum (Figure 4.18). Lastly, the ligand coverage of UDT/oleate-PbS QDs did not significantly deviate from that of oleate-PbS-3. However, this 1:1 exchange ratio does not confirm pure X-type exchange, as simultaneous L-type binding alongside L-type promoted Z-type displacement may also give rise to near-1:1 exchange ratios.

Table 4.5 As-synthesized and ligand-exchanged PbS QD ligand coverages determined through integration of ligand peaks in the alkene region of ^{1}H NMR spectra. Error bars are the standard deviations of triplicate measurements.

System	**Diameter (nm)**	**Sample**	**Bound oleates/ QD**	**Bound exchange ligands/QD**	**Total bound ligands/QD**

1	3.2	Oleate-PbS-1	203 ± 1	-	203 ± 1
		UDA/oleate-PbS	135 ± 4	86 ± 0.3	221 ± 5
2	2.9	Oleate-PbS-2	151 ± 2	-	151 ± 2
		Toluate/oleate-PbS	74 ± 3	60 ± 6	135 ± 9
3	3.1	Oleate-PbS-3	175 ± 8	-	175 ± 8
		UDT/oleate-PbS	92 ± 3	88 ± 1	180 ± 4

4.3.3 Comparing Surface Charging of Mixed-Shell Batches with $CoCp_2$.

The reactivity of QD surfaces with excess charge via remote chemical doping (charging) has been recently demonstrated; displacement of native X-type oleate ligands in response to surface charging has been reported in CdSe and PbS QD systems (Scheme 4.3).[21,22] However, there have been no comparable studies as of yet investigating how this reactivity changes with non-oleate ligands. It is therefore of interest to compare the surface reactivity of the mixed-shell and oleate-capped PbS systems presented herein. In particular, studies of a short and conjugated ligand (toluate) and of a thiolate ligand (UDT) are expected to provide device-relevant insight as native oleate ligands are commonly exchanged for these ligand motifs prior to device incorporation.

Scheme 4.3 General mechanism of electron-promoted X-type ligand displacement induced upon metal chalcogenide (ME) QD surface charging

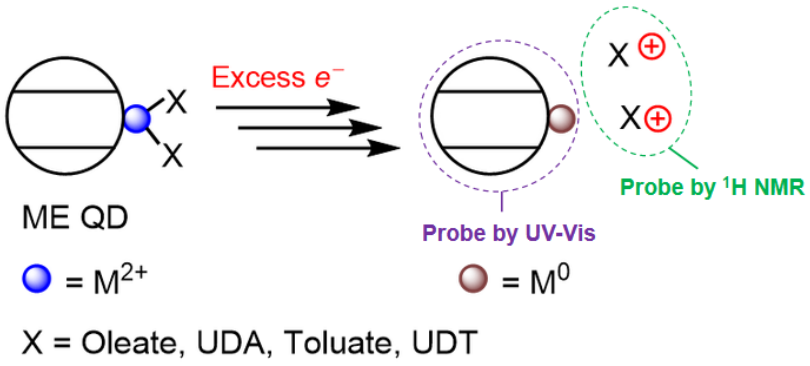

To probe the reactivity of the different mixed-shell systems upon surface charging, we performed systematic titrations by adding up to 500 eq. of the molecular reductant cobaltocene ($CoCp_2$, $E^{\circ\prime} = -1.3$ V vs. $Fc^{+/0}$) to the QDs, monitoring reactivity with ^{1}H NMR spectroscopy. Samples for NMR spectroscopy analysis were allowed to equilibrate for 4 hours prior to NMR measurements and then monitored over the course of several days (up to 123 hours). Samples were monitored over time in order to assess long-term QD stability in the presence of excess charge, and because of the previously identified slow equilibration between $CoCp_2$ and surface sites.[22] Complementary UV-Vis absorbance spectroscopy studies were also performed to gauge charging of surface versus band edge states; typically surface charging manifests as a minor red shift of the excitonic absorbance feature whereas band edge state charging is associated with a significant loss in excitonic absorbance.[21,22,49,50] The viability of this approach for investigating surface charging has been demonstrated previously.[21,22] Below we compare the reactivity observed for oleate-capped QDs and each mixed-shell system.

Oleate-PbS QDs. To establish the reactivity of the native oleate-capped PbS QDs with addition of excess charge, oleate-PbS-1, -2, and -3 were studied before and after addition of $CoCp_2$. The addition of excess $CoCp_2$ (100 or 500 eq.) leads to the loss of surface-bound oleate ligands yet maintains colloidal stability, consistent with previous reports (Figure 4.22a).[22] The loss of bound oleate ligands is quantified via NMR spectroscopy through the loss of integration of the broad resonance at 5.65 ppm, corresponding to the alkene protons on the surface-bound oleate ligands, relative to the internal standard 1,3,5-trimethoxybenzene. Concurrent with loss of the bound ligand feature, there is growth of a sharp resonance at 5.45 ppm that corresponds to the emergence of free (i.e., unbound) oleate ligand (Scheme 4.3). We also observe the emergence of a broad resonance at 6.2 ppm assigned as cyclopentadienyl protons of the oxidized cobaltocenium ($CoCp^+_2$), presumably charge balancing displaced oleate ligands as $[CoCp_2][oleate]$.[22]

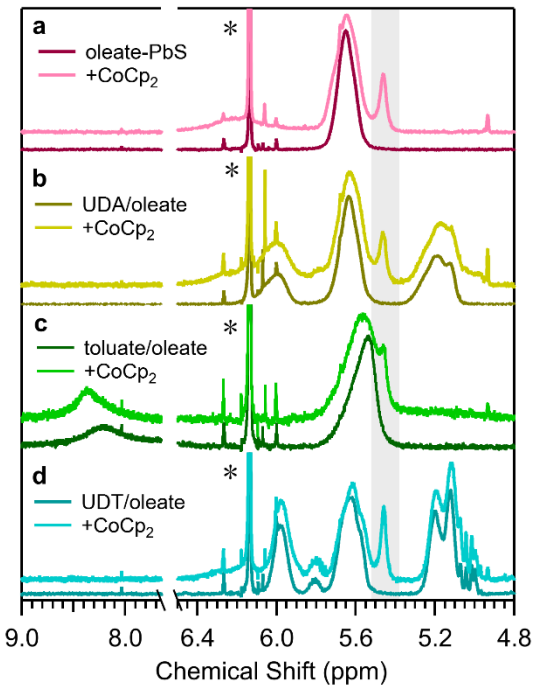

Figure 4.22 Stacked ^{1}H NMR spectra for QDs of each ligand system (46 µM) without and in the presence of 500 eq. $CoCp_2$ after 123 hours in toluene-d_8. The NMR region from 6.5 to 7.6 ppm was omitted to improve visual clarity by removing the significant solvent residual; full NMR spectra are in the **SI**. (*) indicates peak assignment to the internal standard 1,3,5-trimethoxybenzene. The light gray box highlights the free oleate ligand peak observed across all spectra.

Each of the oleate-PbS QD batches shows an increasing proportion of free oleate ligand with increasing equivalents of $CoCp_2$ added, as well as continued gradual oleate loss over time (Figure 4.23 - Figure 4.27). Quantification of the extent of oleate loss with 500 eq. $CoCp_2$ at the end of the study (123 hours) revealed 11.6 ± 5.1, 9.8 ± 2.3, and 14.7 ± 0.6% displacement of native oleate ligands from oleate-PbS-1, -2, and -3, respectively (Figure 4.28). We attribute the slight differences in the extent of oleate displacement among these native oleate-capped QDs to minor differences in QD size and batch-to-batch heterogeneities. These differences are consistent with previous studies of oleate-capped PbS QDs reacted with $CoCp_2$ that showed minor variations among similarly sized QD batches.[22] Finally, UV-Vis absorbance studies revealed a 2–4 nm red-shift of the excitonic absorbance feature, providing further evidence of surface charging with added $CoCp_2$ (Figure 4.29 - Figure 4.31).[22] Overall, the study of these oleate-capped PbS QDs provides a point of comparison for studies of the mixed-shell QD systems.

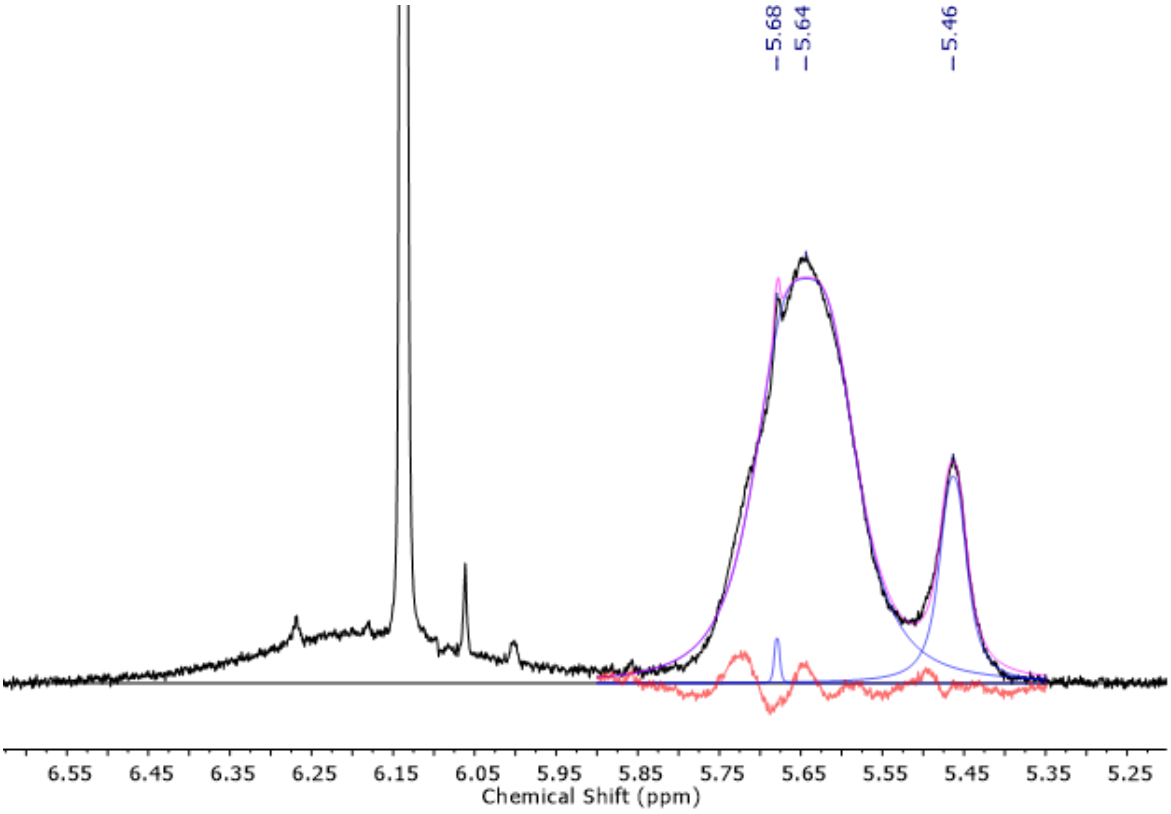

Figure 4.23 Multipeak fitting functions of the bound and free oleate ligands shown here for oleate-PbS-1 QD with 500 eq. $CoCp_2$ added after 123 hours. The original spectrum is shown in the black trace, the fits are shown as blue traces with the sum shown as a pink trace. Bound oleate was fit to a single peak situated at 5.64 ppm. Free oleate was fit to a single peak located at 5.46 ppm. The residual of the fit is shown in red. Peak at 5.68 is minor impurity.

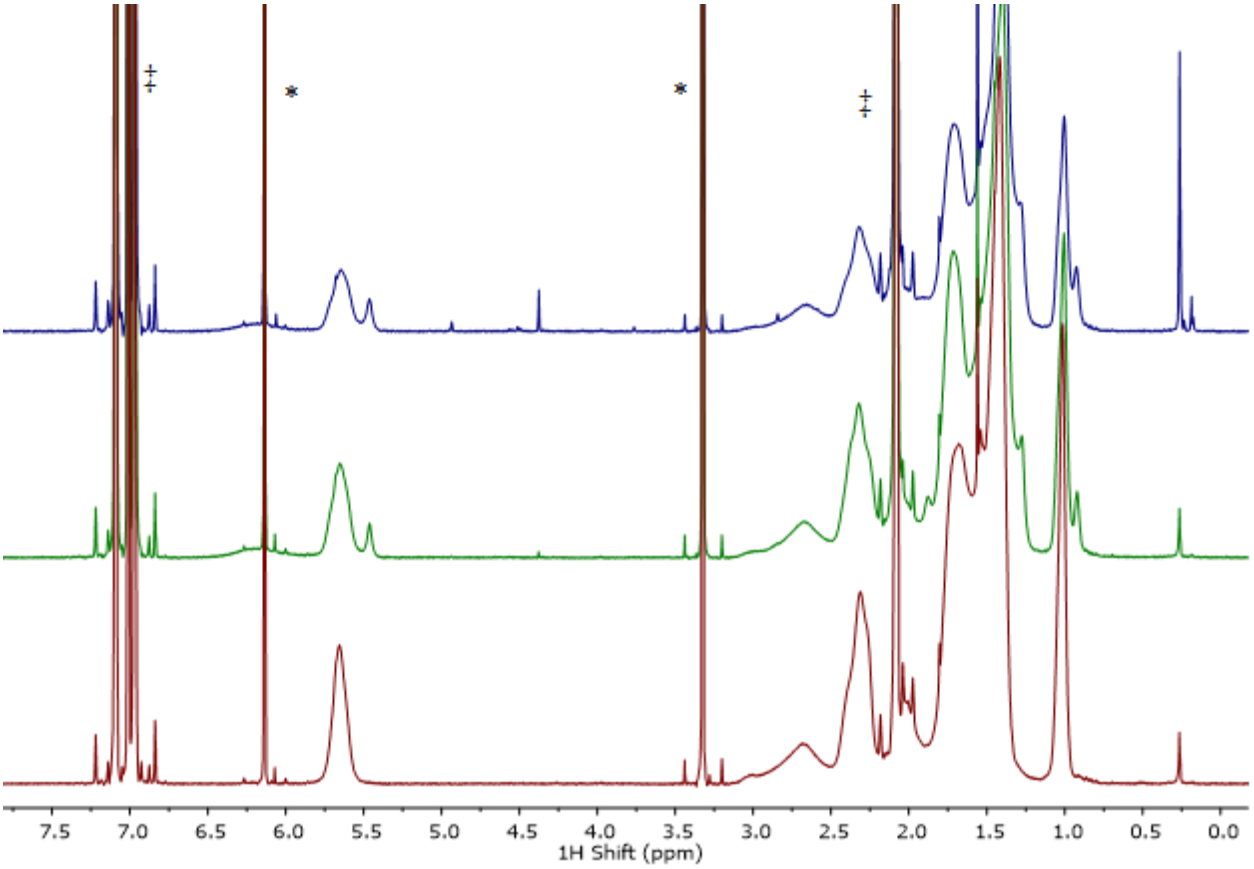

Figure 4.24 600 MHz ^{1}H NMR spectra in toluene-d_8 of oleate-PbS-1 QDs with 0 (red), 100 (green), and 500 (blue) eq $CoCp_2$ added after 123 hours. Peaks denoted by ‡ are toluene solvent residuals, and peaks marked by * are the internal standard 1,3,5-trimethoxybenzene.

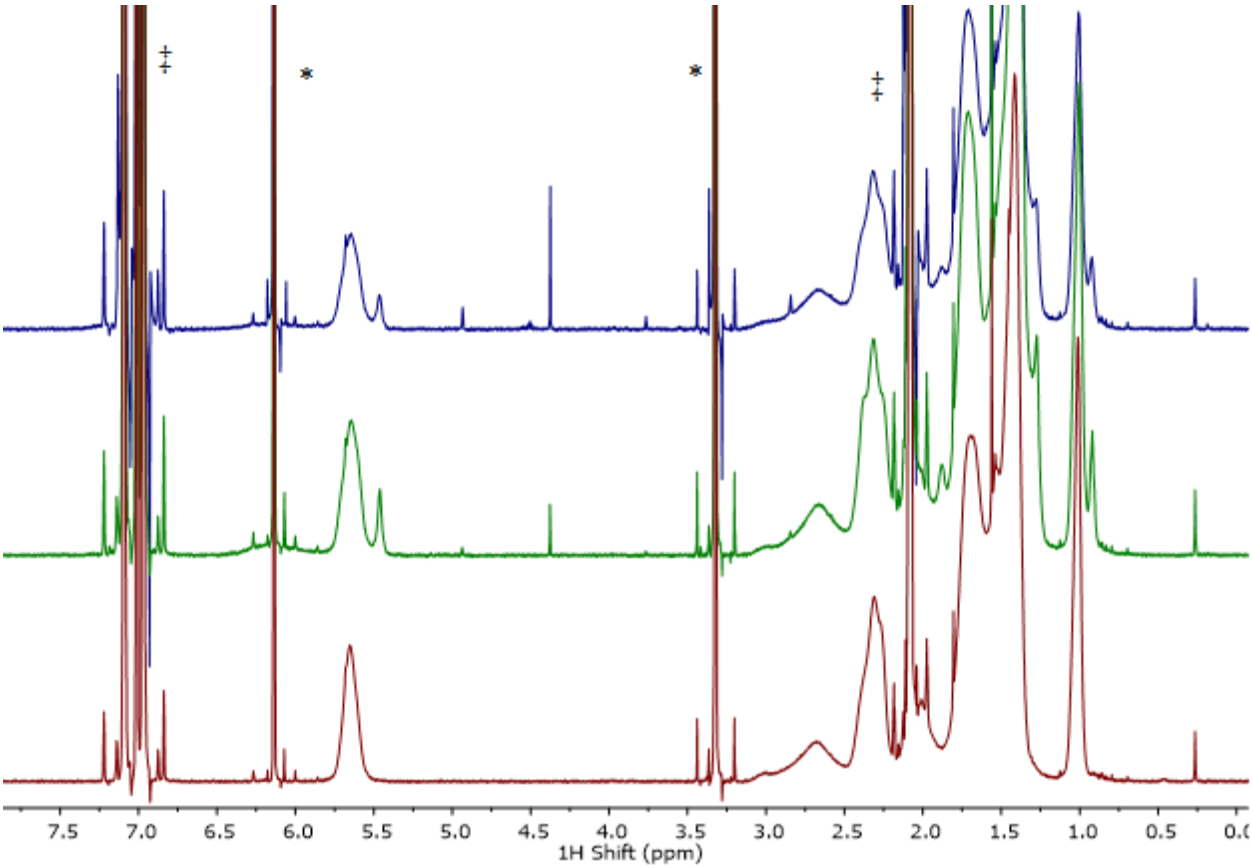

Figure 4.25 600 MHz ^{1}H NMR spectra in toluene-d_8 of oleate-PbS-2 QDs with 0 (red), 100 (green), and 500 (blue) eq $CoCp_2$ added after 123 hours. Peaks denoted by ‡ are toluene solvent residuals, and peaks marked by * are the internal standard 1,3,5-trimethoxybenzene.

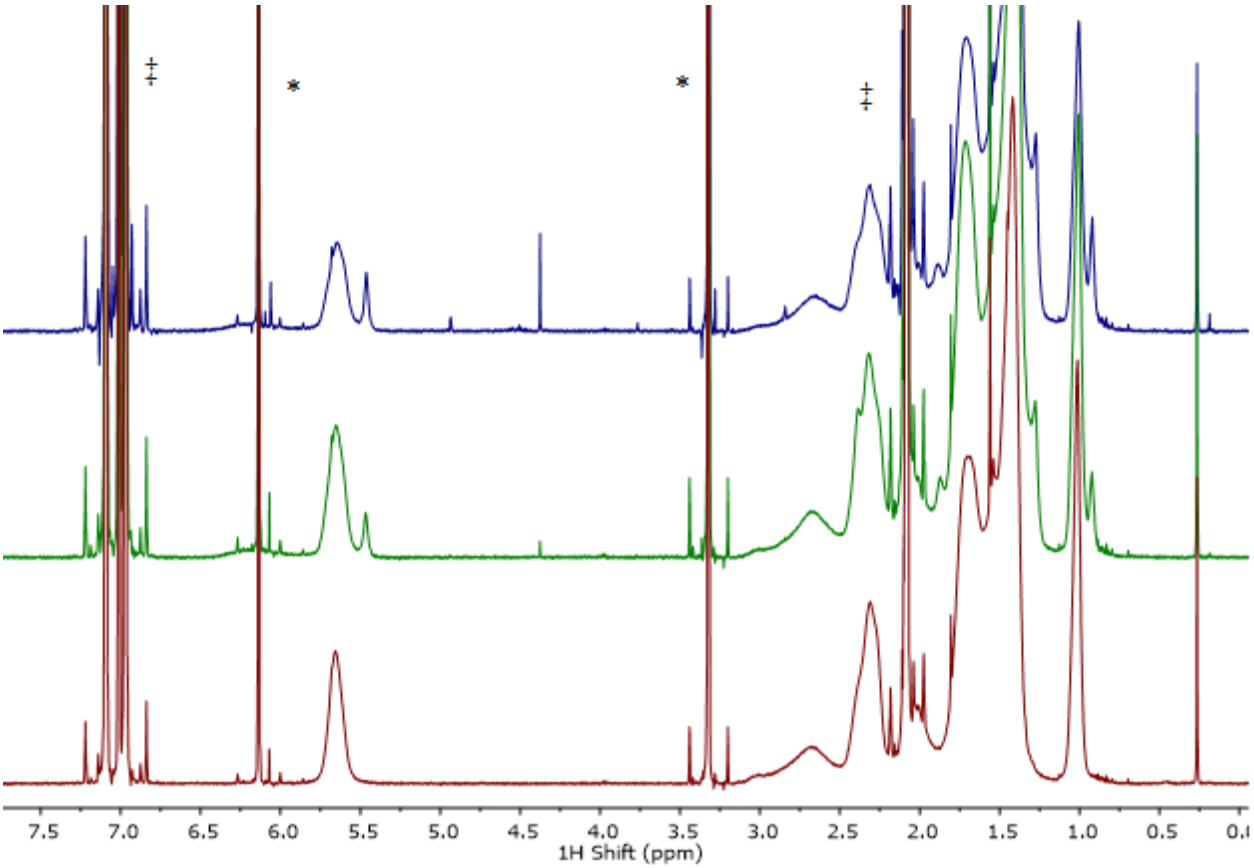

Figure 4.26 600 MHz ^{1}H NMR spectra in toluene-d_8 of oleate-PbS-3 QDs with 0 (red), 100 (green), and 500 (blue) eq $CoCp_2$ added after 123 hours. Peaks denoted by ‡ are toluene solvent residuals, and peaks marked by * are the internal standard 1,3,5-trimethoxybenzene.

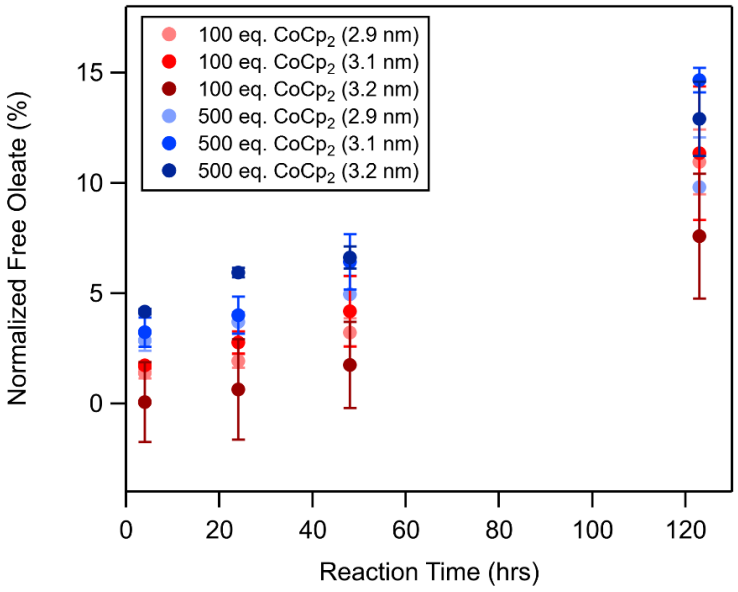

Figure 4.27 Quantification of oleate ligand displaced over time in native oleate-capped QD batches with 100 eq. $CoCp_2$ added (red) and 500 eq. $CoCp_2$ added (blue) (average values from triplicate runs ± standard deviation).

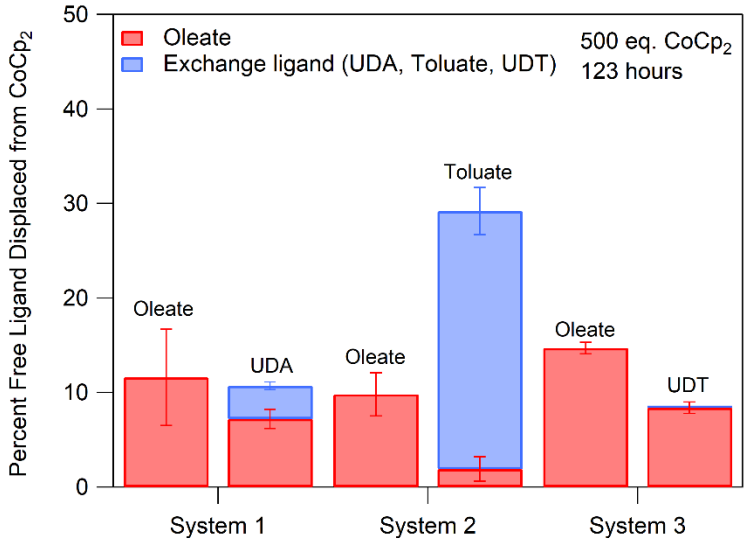

Figure 4.28 Quantitative ^1H NMR spectroscopy analysis of the reactivity of oleate-capped and mixed-shell QD systems with surface charging. Bar graph displays the percentage of initially bound ligand that is displaced upon addition of 500 eq. $CoCp_2$ after 123 hours. Data shown are the average values (± standard deviation in error bars) from running the experiments in triplicate.

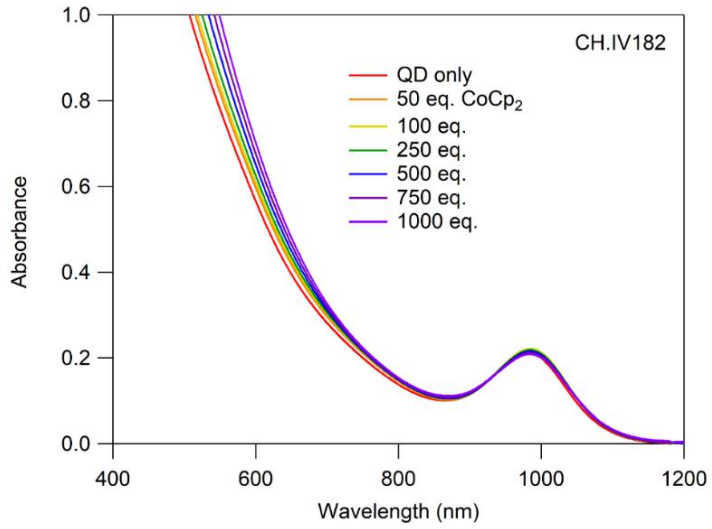

Figure 4.29 UV-Vis-NIR absorption spectrum of oleate-PbS-1 in toluene (2.5 µM) with added excess $CoCp_2$. We observe a 4 nm red shift with added $CoCp_2$.

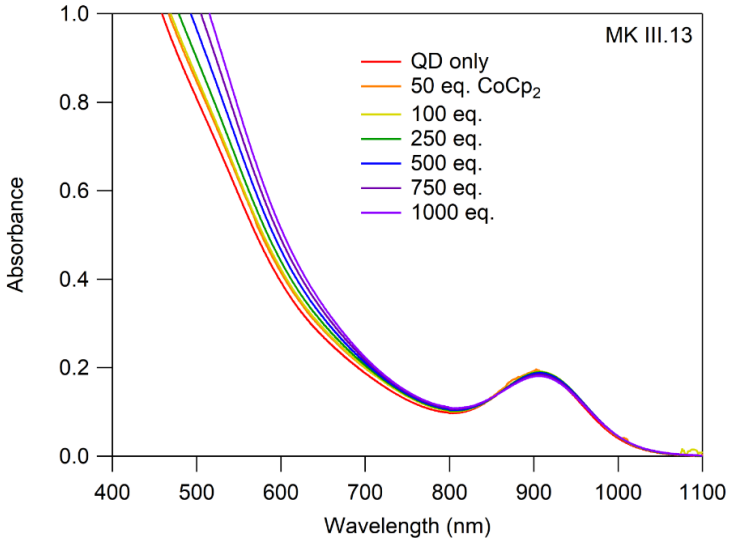

Figure 4.30 UV-Vis-NIR absorption spectrum of oleate-PbS-2 in toluene (2.5 µM) with added excess $CoCp_2$. We observe a 2 nm red shift with added $CoCp_2$.

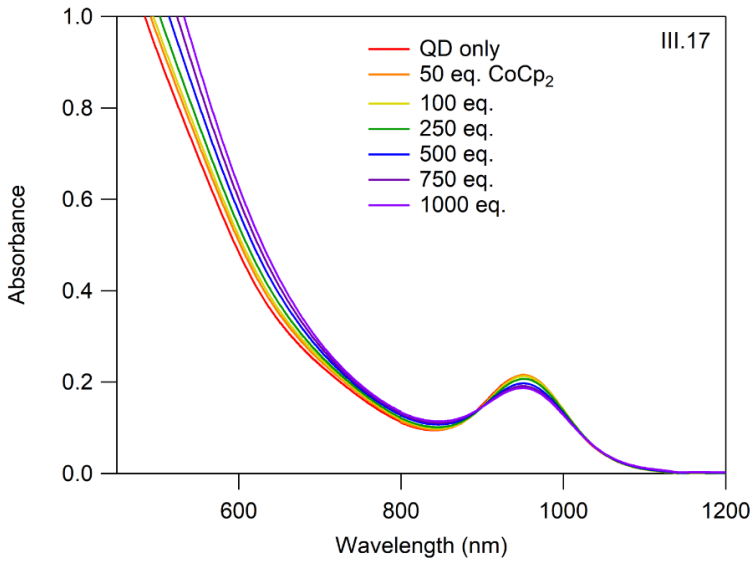

Figure 4.31 UV-Vis-NIR absorption spectrum of oleate-PbS-3 in toluene (2.5 µM) with added excess $CoCp_2$. We observe a 2 nm red shift and minor loss of absorbance with added $CoCp_2$.

System 1 – UDA/oleate-PbS. The effect of added $CoCp_2$ on the UDA/oleate-PbS mixed-shell system was studied as described above to compare with the reactivity of oleate-PbS-1. Because UDA and oleate are both structurally similar long-chain alkyl carboxylates, we anticipated that the UDA/oleate system would show comparable reactivity to oleate-PbS-1. In comparing the degree of ligand displacement induced with added $CoCp_2$, we find that this is indeed the case. Similar to oleate-PbS-1, the UDA/oleate-PbS system displays gradual displacement of both oleate and UDA ligands with an increasing excess of $CoCp_2$ added (Figure 4.22b) as quantified by fitting the distinct bound and free ligand NMR resonances (Figure 4.32). The QDs appear to be stable even in the presence of excess charge and continue to show gradual ligand loss over time (Figure 4.33 - Figure 4.34). After 123 hours in the presence of 500 eq. $CoCp_2$, we observe a total ligand loss of 10.7 ± 0.9 % (7.2% from oleate and 3.5% from UDA) (Figure 4.28) wherein both displaced oleate and UDA appear to be lost concurrently. Complementary UV-Vis absorbance studies of the UDA/oleate-PbS QDs with added $CoCp_2$ show a minor red shift (2 nm) and slight loss in the excitonic absorbance (Figure 4.35). The changes seen in the absorbance spectra upon adding $CoCp_2$ qualitatively agree with those of the oleate-PbS-1 QDs,

suggesting that there is not a significant change in the electronic structure or surface dipole of the QDs upon exchange with UDA ligands.

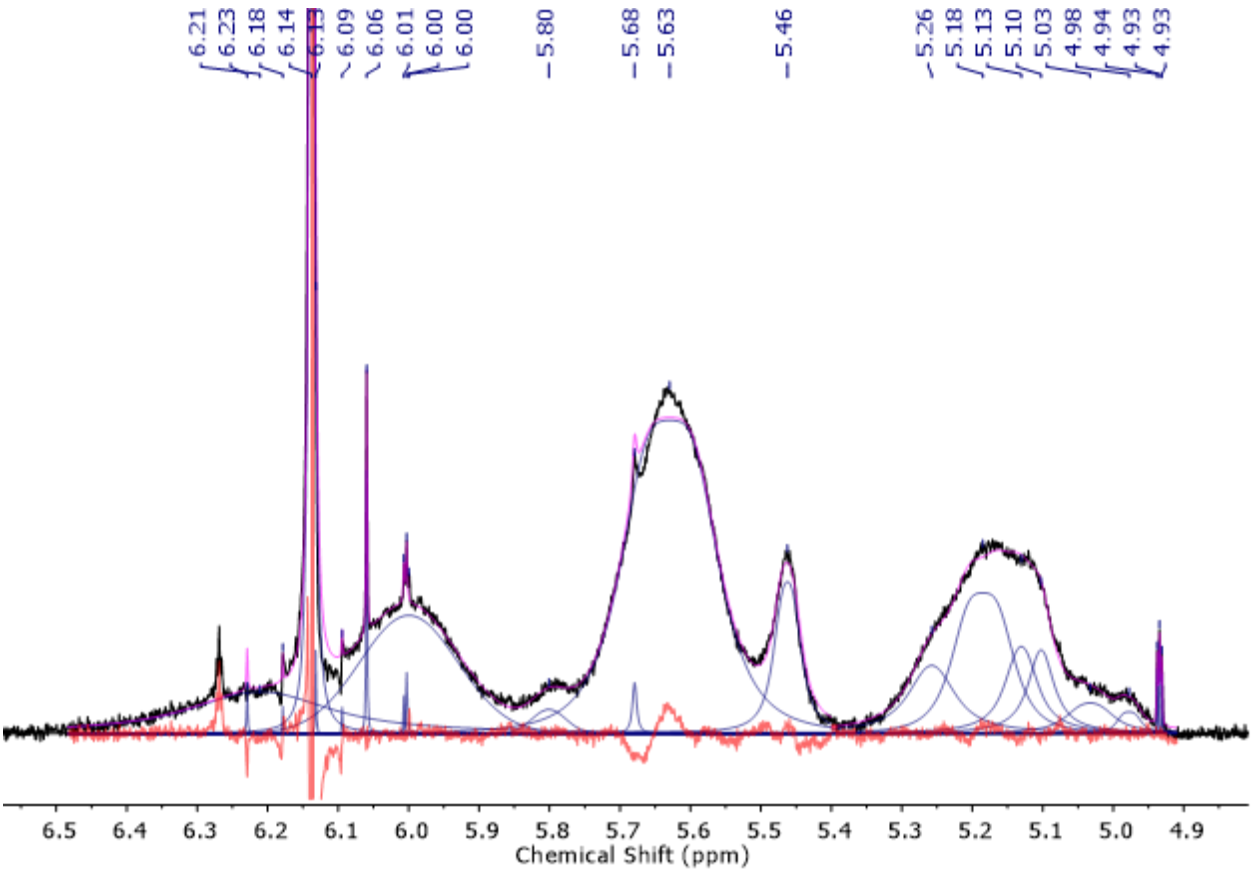

Figure 4.32 Multipeak fitting functions of the bound and free ligands shown here for UDA/oleate-PbS QD with 500 eq. $CoCp_2$ added after 123 hours. The original spectrum is shown in the black trace, the fits are shown as blue traces with the sum shown as a pink trace. Bound oleate was fit to a single peak located at 5.63 ppm and free oleate was fit to a single peak at 5.46 ppm. Bound UDA was calculated by averaging the broad peak at 6.00 ppm (alkene CH, 1H) and the four peaks between 5.26 and 5.10 ppm (alkene CH_2, 2H), normalized to the same number of protons. Free UDA was calculated by averaging the broad peak at 5.80 ppm (1H) and the two peaks at 5.03 and 4.98 ppm (2H), normalized to the same number of protons. The residual of the fit is shown in red. Peaks at 5.68 ppm and the triplet at 4.93 ppm are minor impurities.

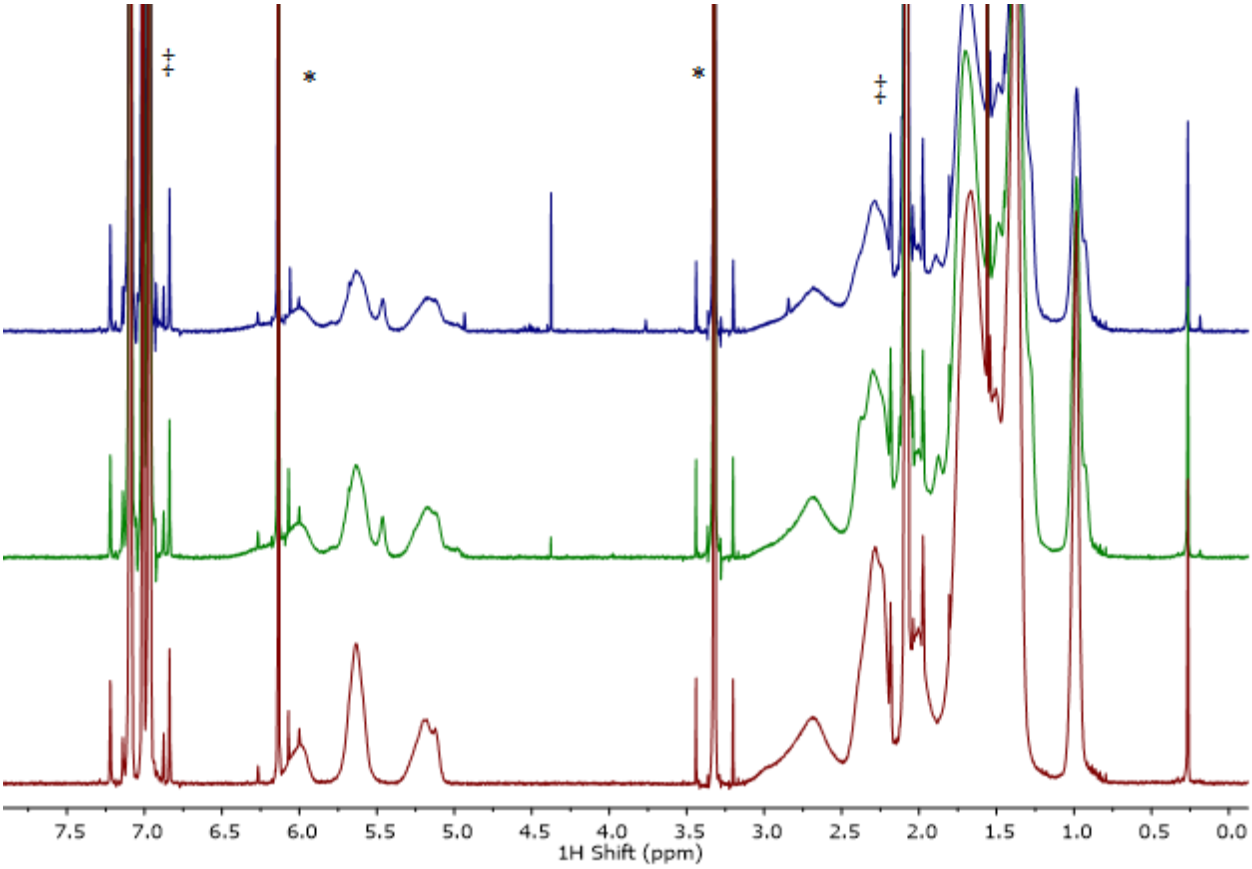

Figure 4.33 600 MHz ^{1}H NMR spectra in toluene-d_8 of UDA/oleate-PbS QDs with 0 (red), 100 (green), and 500 (blue) eq $CoCp_2$ added after 123 hours. Peaks denoted by ‡ are toluene solvent residuals, and peaks marked by * are the internal standard 1,3,5-trimethoxybenzene.

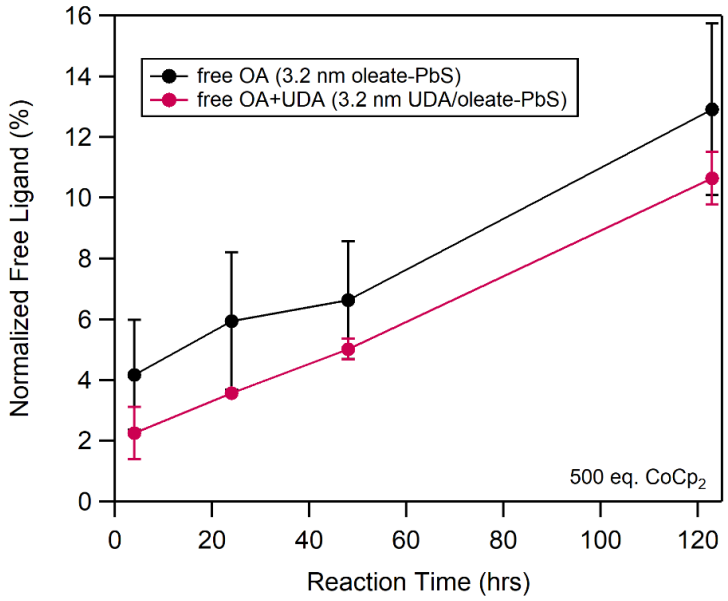

Figure 4.34 Quantification of ligand displaced in oleate-PbS-1 (black) and UDA/oleate-PbS (pink) batches with 500 eq $CoCp_2$ added over time (average values from triplicate runs ± standard deviation). Lines connecting data points are a guide to the eye.

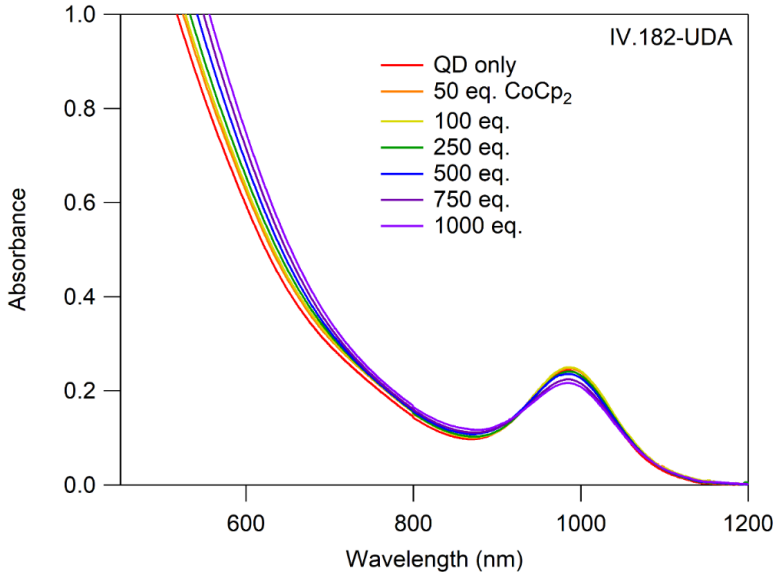

Figure 4.35 UV-Vis-NIR absorption spectrum of UDA/oleate-PbS in toluene (2.5 µM) with added excess $CoCp_2$. We observe a 2 nm red shift and minor loss of absorbance with added $CoCp_2$.

The very comparable response to added $CoCp_2$ between the UDA/oleate-PbS (10.7 ± 0.9% ligand loss) and oleate-PbS-1 QDs (11.6 ± 5.1% ligand loss) agrees well with our predictions of similar

reactivity for two long-chain alkyl carboxylates such as UDA and oleate. However, there is a slight difference in the relative proportions of oleate versus UDA displaced from the surface. Less UDA is displaced relative to the amount of initially bound UDA (8.7 ± 0.83% UDA displaced of total UDA bound) compared with oleate displaced relative to the starting amount of bound oleate (11.9 ± 1.8% oleate displaced of total oleate bound) (Figure 4.36). The observed X-type displacement may be convoluted by differences in relative subpopulations of exchanged UDA that have different binding modes or that bind to different facets compared with native oleate, but overall demonstrates similar reactivity of surface-bound UDA and oleate. These results demonstrate that long-chain alkyl carboxylates are prone to undergo an electron-promoted dissociation mechanism from PbS surfaces.

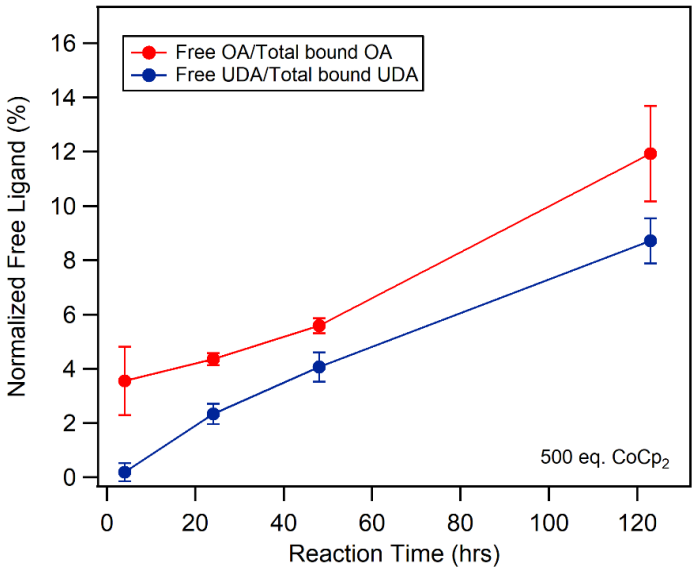

Figure 4.36 Quantification of the amount of displaced oleate (red, normalized to the starting amount of bound oleate) versus displaced UDA (blue, normalized to the starting amount of bound UDA) in UDA/oleate-PbS with 500 eq $CoCp_2$ added over time (average values from triplicate runs ± standard deviation). Lines connecting data points are a guide to the eye.

System 2 – Toluate/oleate-PbS. Having established that alkyl carboxylate ligands such as oleate and UDA show similar surface reactivity with added charge, we next sought to examine the effect of varying the ligand backbone while maintaining the carboxylate binding group. To do so, we studied PbS

QDs with a mixed-shell composition of toluate and oleate ligands (toluate/oleate-PbS). ^{1}H NMR spectra indicate toluate and oleate ligands are displaced over time with added $CoCp_2$ (Figure 4.22c, Figure 4.37 - Figure 4.39). However, significant differences arise in both the NMR and UV-Vis absorbance spectra of the toluate/oleate-PbS QDs compared with the oleate- and UDA/oleate-PbS systems discussed above. Analysis and interpretation of these spectral differences were critical toward our aim of quantitatively assessing the reactivity of toluate/oleate-PbS QDs with excess charge.

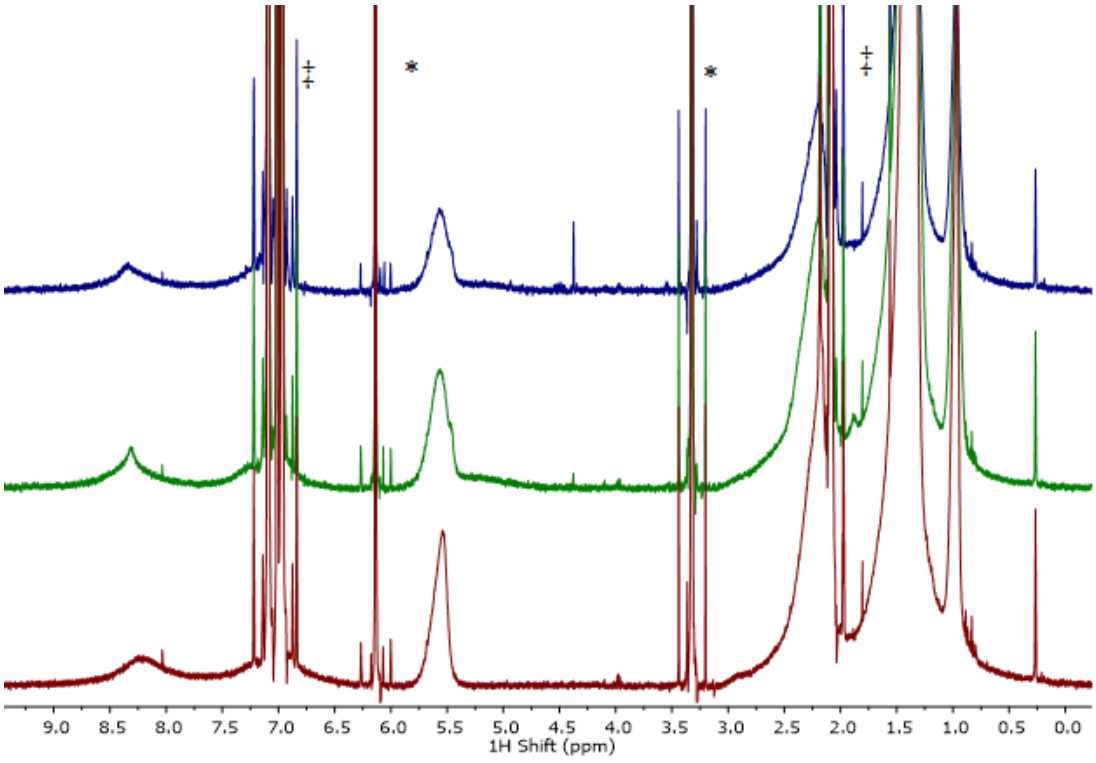

Figure 4.37 600 MHz ^{1}H NMR spectra in toluene-d_8 of toluate/oleate-PbS QDs with 0 (red), 100 (green), and 500 (blue) eq $CoCp_2$ added after 123 hours. Peaks denoted by ‡ are toluene solvent residuals, and peaks marked by * are the internal standard 1,3,5-trimethoxybenzene.

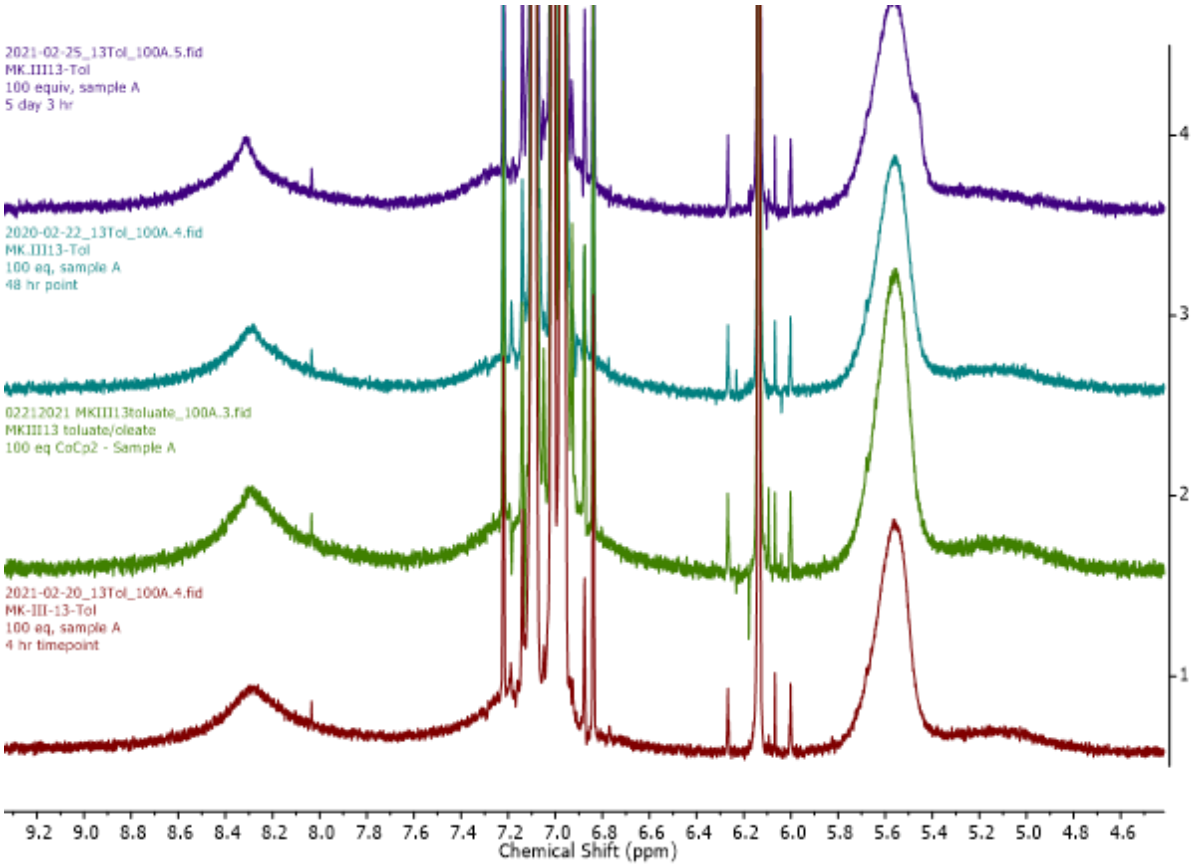

Figure 4.38 Toluate/oleate-PbS QDs in toluene-d_8 with 100 eq. $CoCp_2$ added at 4 hours (red), 24 hours (green), 48 hours (blue) and 123 hours (purple). Over time the sharp free toluate peak at 8.3 ppm shifts downfield.

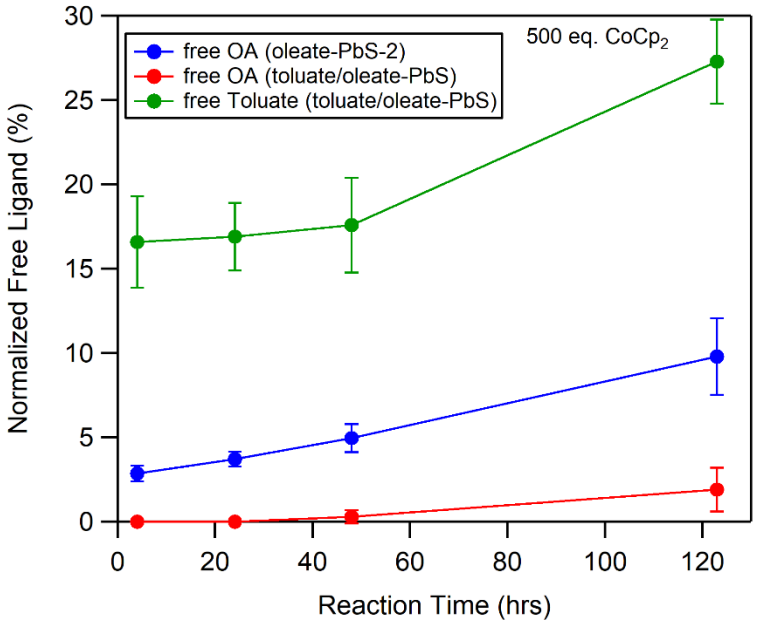

Figure 4.39 Quantification of free ligand in oleate-PbS-2 (blue) and free toluate (green) and free oleate (red) in toluate/oleate-PbS batches over time with 500 eq $CoCp_2$ added (average values from triplicate runs ± standard deviation). Lines connecting data points are a guide to the eye.

First, qualitative observations from the NMR spectra of the toluate/oleate-PbS QDs in the presence of $CoCp_2$ indicate markedly different reactivity for this system. Specifically, we observe an upfield shift of the broad peak assigned to $CoCp^+_2$; this resonance appears at ca. 5.2 ppm in the toluate/oleate-PbS system, compared with 6.2 ppm in the oleate-PbS QDs. The upfield shift of the $CoCp^+_2$ peak may be a result of ring current effects upon ion pairing with displaced toluate anions.[51] Furthermore, upon addition of reductant, the toluate resonance at 8.2 ppm narrows and shifts 0.1 ppm downfield (Figure 4.22c). As described below, we interpret the narrowing and downfield shift observed in the toluate ligand resonance as indicative of toluate displacement.

UV-Vis absorbance spectroscopy studies also show qualitative distinctions between the toluate/oleate-PbS QDs and the other QD systems. With added reductant, a 10 nm red shift is observed (Figure 4.40). This dramatic optical response is suggestive of a Stark effect or Coulombic repulsion from an induced electric field at the QD surface caused by localized charges. Taken together, the NMR and UV-Vis absorbance spectra indicate that the toluate/oleate-PbS QDs experience a greater degree of

surface charging than oleate- and UDA/oleate-PbS QDs. Consistent with this observation, the toluate/oleate-PbS system is not stable over long timescales with excess $CoCp_2$; after 24 hours traces of a fine black precipitate were observed in samples containing reductant. This is perhaps due to increased polarization of the surface upon charging, consistent with the application of short, conjugated ligands to improve conductivity in QD-based devices.[5]

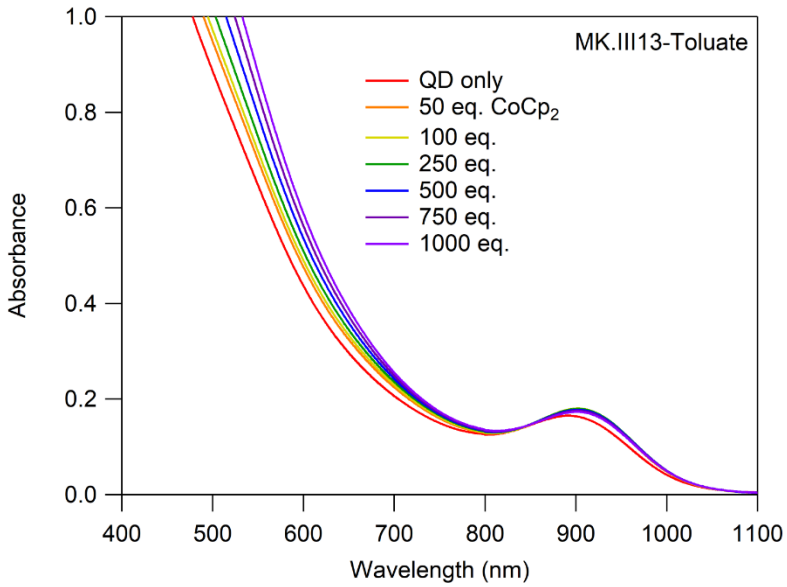

Figure 4.40 UV-Vis-NIR absorption spectrum of toluate/oleate-PbS in toluene (2.5 µM) with added excess $CoCp_2$. We observe a 10 nm red shift with added $CoCp_2$.

As shown in Figure 4.22c, the aryl feature of the toluate ligand narrows and shifts downfield when reductant is added to toluate/oleate-PbS QDs. This is in contrast with the appearance of two distinct resonances upon adding reductant to the oleate- and UDA/oleate-PbS QDs corresponding to bound and free alkyl ligands (Figure 4.22). In the case of the toluate/oleate-PbS QDs, however, control studies adding excess triethylammonium toluate ligand reveal that the presence of free ligand in this system indeed results in a single shifted and narrowed aryl resonance rather than two distinct sets of ligand peaks (Figure 4.41). In light of the lack of two separate, easily resolvable features, typical peak fitting methods to obtain values of bound and free toluate ligand are less accessible.

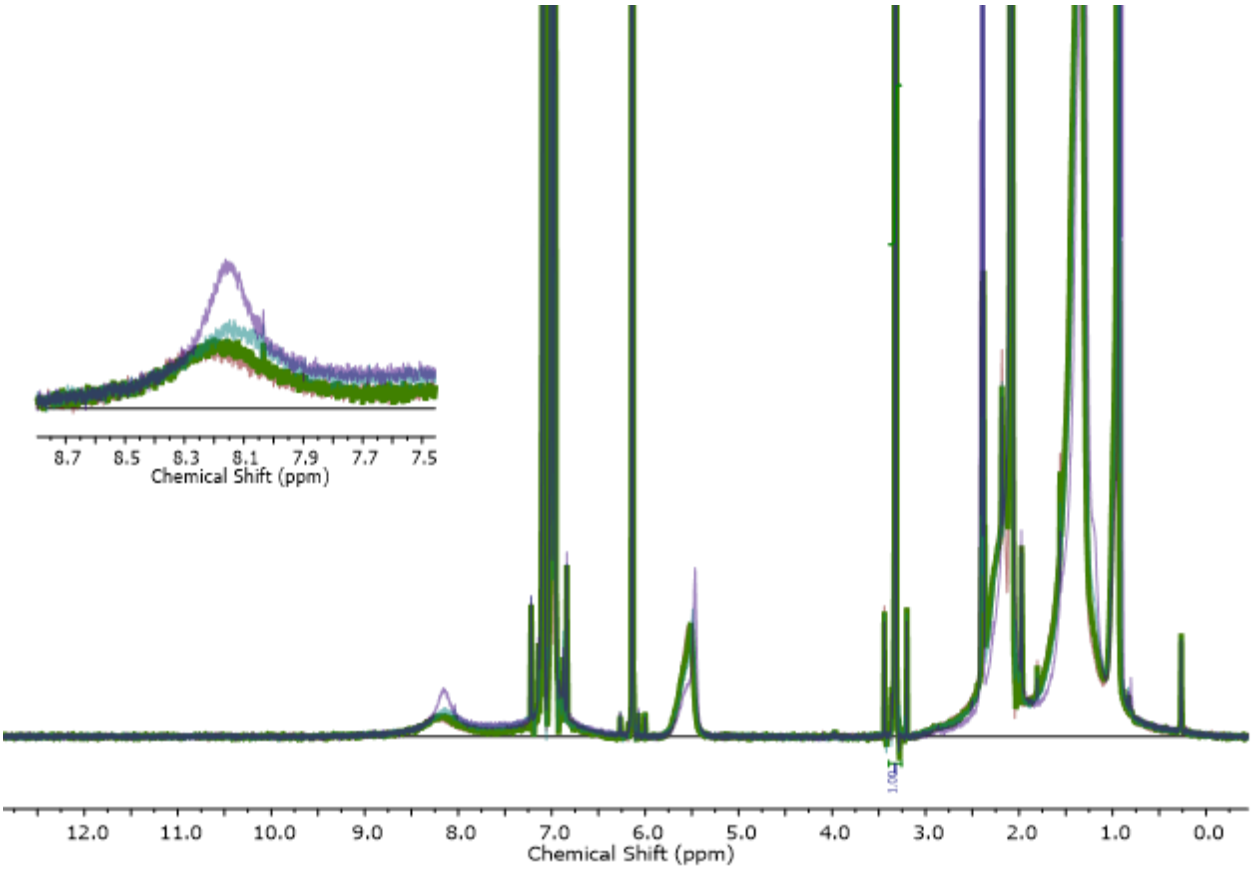

Figure 4.41 Toluate/oleate-PbS in toluene-d_8 with added $TEAH^+$-Toluate ligand showing sharpening and shift up field with added free ligand: 0 eq. $TEAH^+$-Toluate (green), 5 eq. $TEAH^+$-Toluate (red), 15 eq. TEAH+-Toluate (blue), 40 eq. $TEAH^+$-Toluate (purple). Inset: Zoom-in of toluate ligand peak.

To first determine if the narrowing and downfield shift observed in Figure 4.22b indicates dissociated toluate ligand in response to added $CoCp_2$, a sample of toluate/oleate-PbS QDs reduced with $CoCp_2$ was precipitated from solution using acetonitrile and acetone antisolvents. The antisolvent supernatant, anticipated to contain cobaltocenium toluate if added charge displaces the toluate ligands, was analyzed by ^1H NMR spectroscopy. Indeed, free toluate ligand was detected in the supernatant (Figure 4.42 - Figure 4.46). This finding provided confidence that the sharpening and downfield shift of the toluate NMR resonance with added $CoCp_2$ is indicative of toluate displacement from the surface. Interestingly, the displacement of free ligand in this system leads to a downfield shift of the toluate NMR

resonance; this is in contrast with typical observations of free ligand appearing upfield of bound ligand resonances.[37] We anticipate that the observed downfield shift is caused by significant electronic interactions of freed ligand with excess charge localized at the QD surface, consistent with our finding of significant surface charging from UV-Vis absorbance studies. We therefore fit the aryl resonance consistently to two overlapping features. The resonance fixed at 8.2 ppm was assigned to bound toluate and the peak allowed to float between 8.3–8.4 ppm was assigned to free toluate (Figure 4.47).

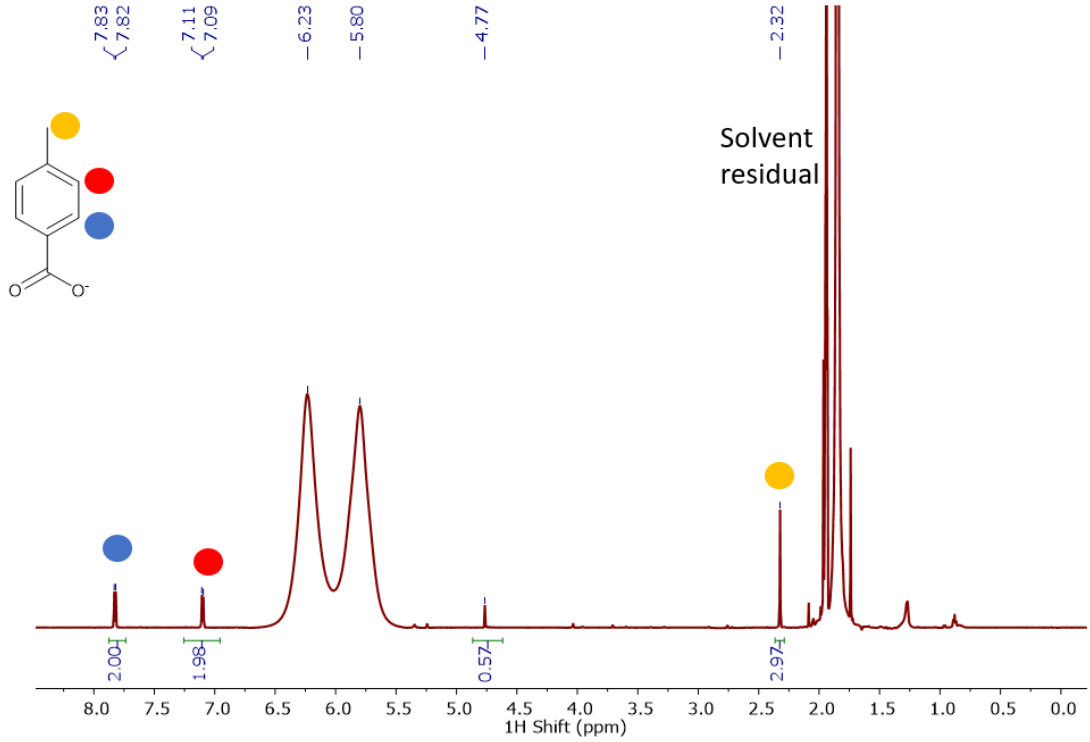

Figure 4.42 ^{1}H NMR of supernatant from isolating free toluate ligand from reduced QDs through precipitation in acetonitrile-d_3. Paramagnetic cobaltocene was detected at ca. −44 ppm. The peaks attributed to free toluate compare well with that of [TEAH^{+}][toluate] (Figure 4.46).

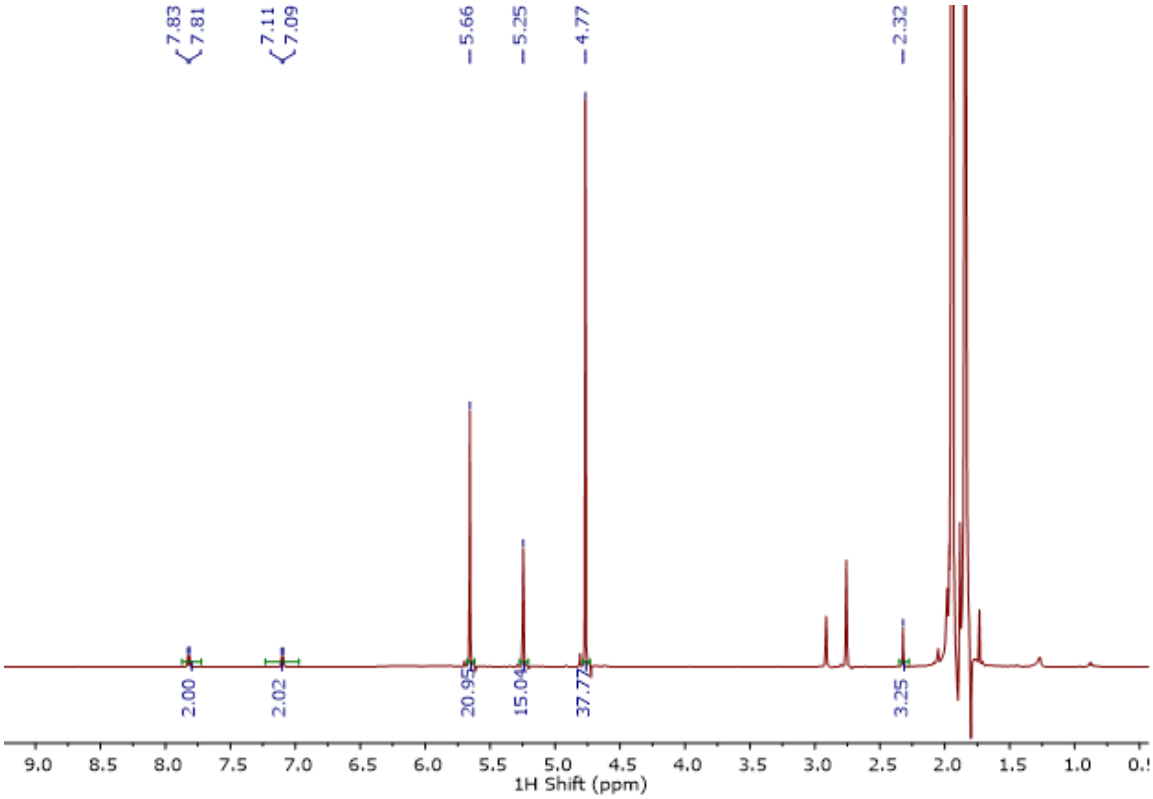

Figure 4.43 ^{1}H NMR of supernatant from isolating free toluate ligand from reduced QDs through precipitation in acetonitrile-d_3 upon oxidation with air, showing the sharpening of the $CoCp_2^+$ resonance present in excess due to oxidation of paramagnetic $CoCp_2$ in the sample, and paramagnetic impurities.

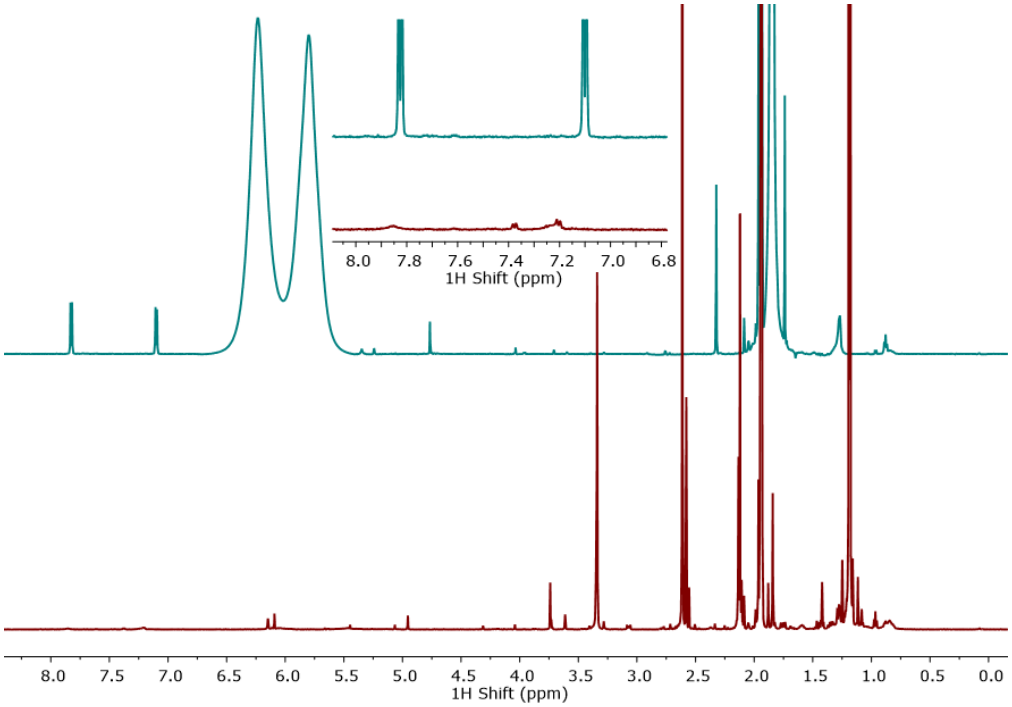

Figure 4.44 Stacked ^{1}H NMR spectra of (bottom) supernatant from precipitation of toluate/oleate-PbS QDs with acetonitrile and acetone antisolvents, and (top) supernatant from precipitation of toluate/oleate-PbS reacted with $CoCp_2$. Both NMR samples are in acetonitrile-d_3 and were run on a 600 MHz NMR spectrometer. Inset shows a zoom-in of the aryl region showing no free toluate ligand present in the control sample.

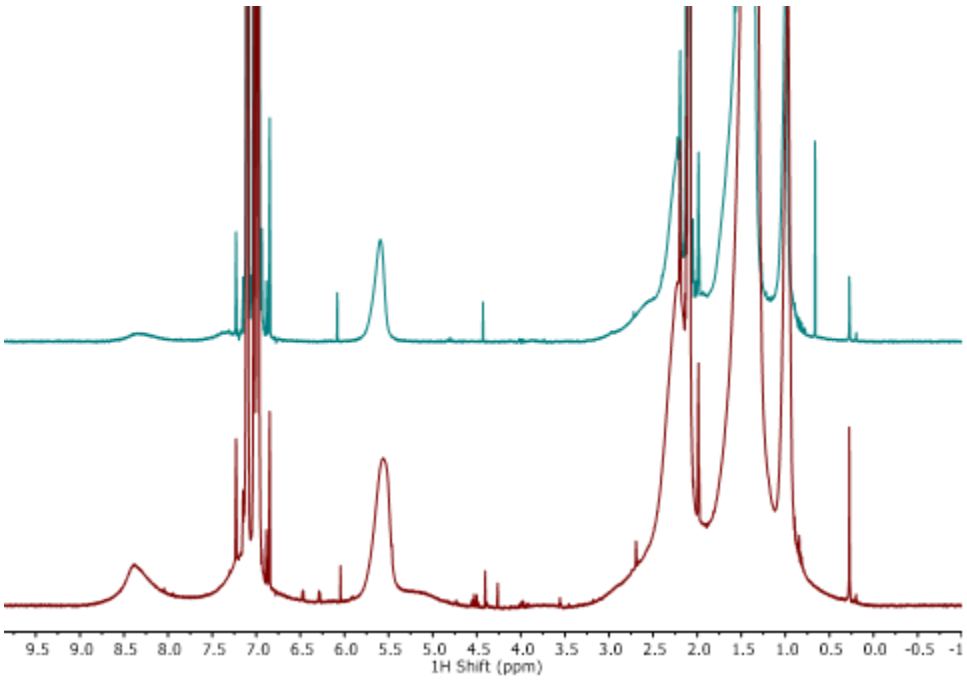

Figure 4.45 ^{1}H NMR of QD mixture before (bottom) and after (top) precipitation in toluene-d_8.

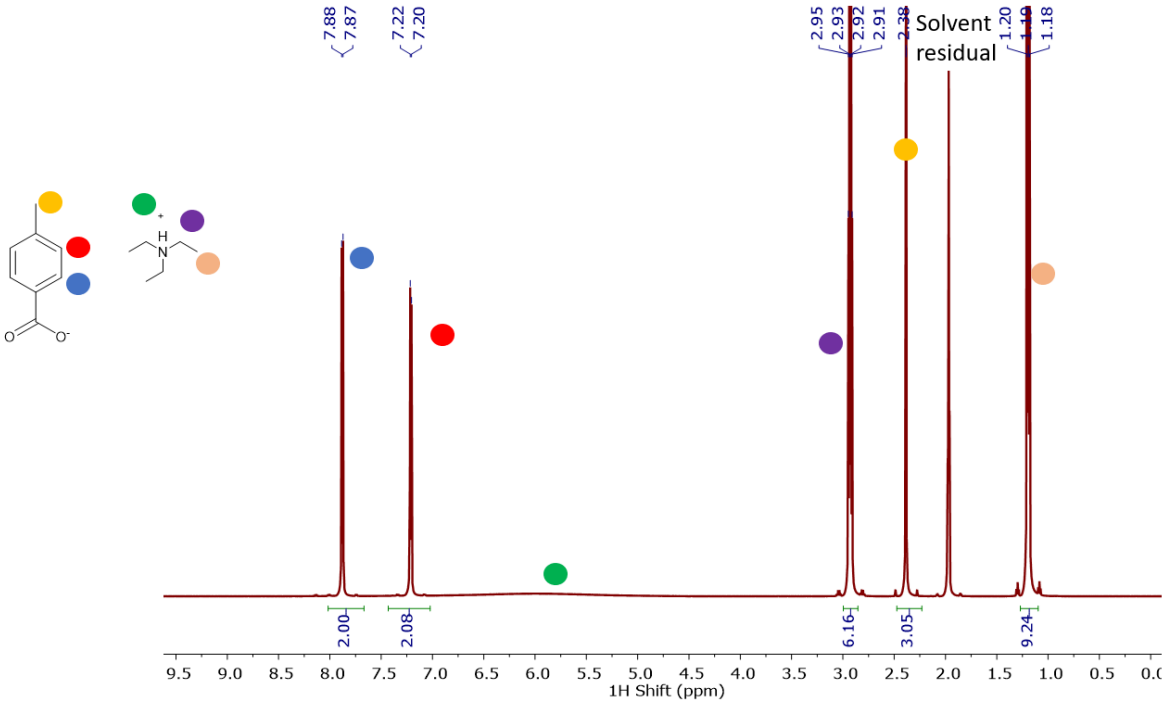

Figure 4.46 ^{1}H NMR of triethylammonium *p*-toluate in acetonitrile-d_3.

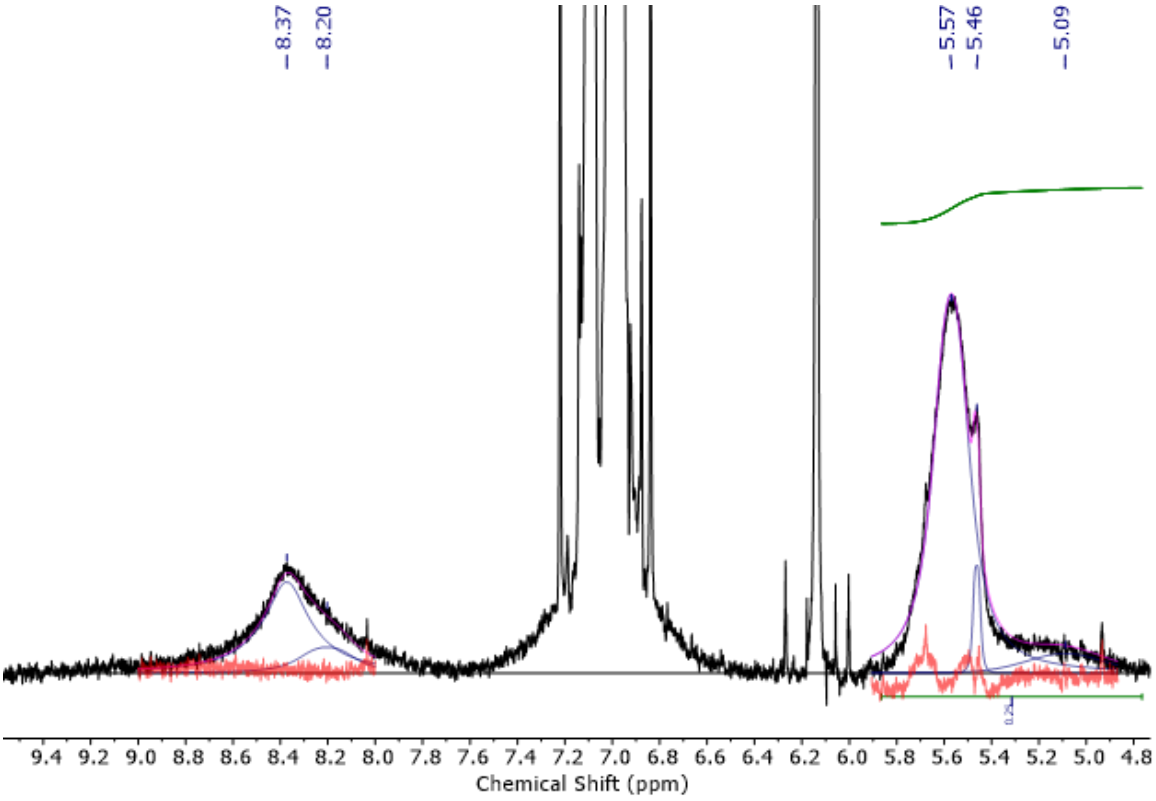

Figure 4.47 Multipeak fitting functions of the bound and free ligands shown here for toluate/oleate-PbS QD with 500 eq. $CoCp_2$ added after 123 hours. The original spectrum is shown in the black trace, the fits are shown as blue traces with the sum shown as a pink trace. The residual of the fit is shown in red. Bound oleate was calculated through subtraction of the broad $CoCp^+_2$ resonance at 5.1 ppm and the sharp free oleate resonance at 5.46 ppm from the total integration of the region between 5.9 and 4.8 ppm (shown by green bar). Due to the asymmetry of the bound oleate peak, we found this method gave the most consistent total oleate integration over time and across samples. Bound toluate was fixed 8.2 ppm, consistent with the peak shift of toluate/oleate-PbS QDs in the absence of $CoCp_2$. The free toluate feature was allowed to float, and was fit to a sharper feature at 8.37 ppm.

Careful fitting of ^{1}H NMR spectra reveal that, unlike in the UDA/oleate-PbS mixed-ligand system, there appears to be a significant preference for loss of the exchange ligand (toluate) over native oleate ligands (Figure 4.28). Interestingly, unlike the oleate-PbS and UDA/oleate-PbS QDs that show gradual ligand loss over a period of days, the toluate/oleate-PbS QDs show a significant amount of toluate loss (ca. 10-15%) within the first 4 hours of reactivity with added reductant (Figure 4.39). This more expeditious and dramatic ligand dissociation in the toluate/oleate-PbS system suggests that these QDs reach equilibrium with excess $CoCp_2$ more rapidly than the long-chain alkyl carboxylate-capped QDs.

Quantification of toluate and oleate loss by ^{1}H NMR spectroscopy indicate that 29% of initially bound ligand (27% from toluate loss and 2% oleate loss) is displaced upon reaction with $CoCp_2$, with added charge preferentially promoting displacement of toluate over oleate. The preference for toluate displacement may be rationalized by considering differences in the binding strength of the toluate versus oleate ligands at PbS QD surfaces. Based on relative Lewis basicity, the toluate ligands are expected to be less effective donors to Lewis acidic Pb^{2+} surface ions compared with the more basic oleate; this is reflected in the large difference in pK_a of the conjugate acid of toluate (pK_a ~4) compared with oleate (pK_a ~9.85).[52,53] This difference in basicity of each ligand is anticipated to weaken the bond stabilization of the toluate ligands to surface Pb^{2+} relative to that of the oleate ligands, which could lead to preferential cleavage of the toluate–Pb bond upon Pb^{2+} ion reduction by $CoCp_2$. In other words, because the toluate ligands are less donating, the toluate-bound Pb^{2+} ions are expected to be more electron-poor than oleate-bound Pb^{2+} ions. We anticipate that this would result in the toluate-bound Pb ions being more readily reduced than oleate-bound Pb ions and thus being a more thermodynamically favored state to trap charge. This may in part explain both the preference for toluate dissociation over oleate dissociation as well as the minimal amount of oleate loss overall compared with the oleate-PbS and UDA/oleate mixed-shell QDs.

Finally, the overall ligand displacement of toluate/oleate-PbS QDs is substantially higher compared with the oleate- and UDA/oleate-PbS QDs; as noted, after 123 hours in the presence of 500 eq. $CoCp_2$, we observe a loss of 29% of the total initially bound ligands (Figure 4.28) compared to only ca. 10–15% ligand loss in the oleate-PbS and UDA/oleate-PbS QDs. We interpret this as an indicator of the relative energetics of oleate- vs. UDA- vs. toluate-bound Pb^{2+} states. Consistent with the preferential displacement of toluate over oleate described above, the greater degree of ligand displacement in the toluate/oleate-PbS QDs may result from the toluate-bound Pb^{2+} ions being lower in energy than the oleate-bound Pb^{2+} species or other spectroscopically silent surface states that may accept excess charge (i.e., disulfide defects).[22] A lower relative energy of the toluate-bound Pb^{2+} ions would result in more electron trapping at these surface sites, consistent with higher degrees of ligand displacement. While subjectivity may be inherent to multipeak NMR fitting of the overlapping toluate aryl resonances, within

two extreme bounds of fitting we estimate an error of 5% in our reported fits. Within the range of 20–30%, however, the toluate/oleate-PbS QDs lose measurably more bound ligand than the other systems explored herein.

In sum, the toluate/oleate-PbS system demonstrates that changing the surface capping ligand backbone from a long alkyl chain to a short, conjugated moiety can dramatically affect reactivity of the QD surface with charging. We propose that the observed preference for toluate loss over native oleate displacement results from differences in electron donation from the ligand to the surface Pb^{2+} ion, and therefore different energetics for the electron trap states localized at toluate–Pb and oleate–Pb sites. The greater propensity for toluate dissociation over oleate with added reductant may contribute to the diminished stability of the toluate/oleate-PbS system.

System 3 – UDT/oleate-PbS. To probe the impact of changing the ligand binding group on QD surface reactivity with added charge, we studied the UDT/oleate-PbS QDs upon addition of excess $CoCp_2$. The UDT ligand conveniently allows us to isolate differences in reactivity that are induced solely by the thiolate versus carboxylate ligand binding groups; the structurally identical ligand backbones of UDT and UDA ensure that any differences observed in reactivity between UDT/oleate-PbS and UDA/oleate-PbS QDs with added $CoCp_2$ are due to the difference in binding group. As discussed above, samples of UDT/oleate-PbS QDs contained a small fraction of unbound UDT and a minor amount of disulfide that we were unable to remove even with multiple post-exchange purification steps. However, we did not detect any reaction between the free thiol and disulfide with added $CoCp_2$—NMR titrations show a minor increase in the amount of disulfide present over time rather than reduction of the disulfide bond to form $[CoCp^+_2][RS^-]$. Similar to oleate-PbS-3 and the mixed-shell systems discussed above, and quantified by NMR fitting (Figure 4.48), addition of excess $CoCp_2$ results in a gradual displacement of initially bound ligands that increases over time and with the amount of $CoCp_2$ added (Figure 4.22d - Figure 4.49 - Figure 4.50). Specifically, after 123 hours with 500 eq. $CoCp_2$ added, 8.4 ± 0.6% of the total ligand was displaced (Figure 4.28). Interestingly, the displaced ligands were exclusively oleates,

appearing as a sharp peak at 5.45 ppm in Figure 4.22d; no increase in the free UDT ligand resonances were observed over time. The reactivity of UDT/oleate-PbS with $CoCp_2$ was also assessed by UV-Vis absorbance spectroscopy (Figure 4.51). The spectra of the UDT/oleate-PbS QD system shows a minor red shift (1 nm) upon addition of $CoCp_2$—similar to that observed with oleate-PbS-3 and consistent with surface charging.

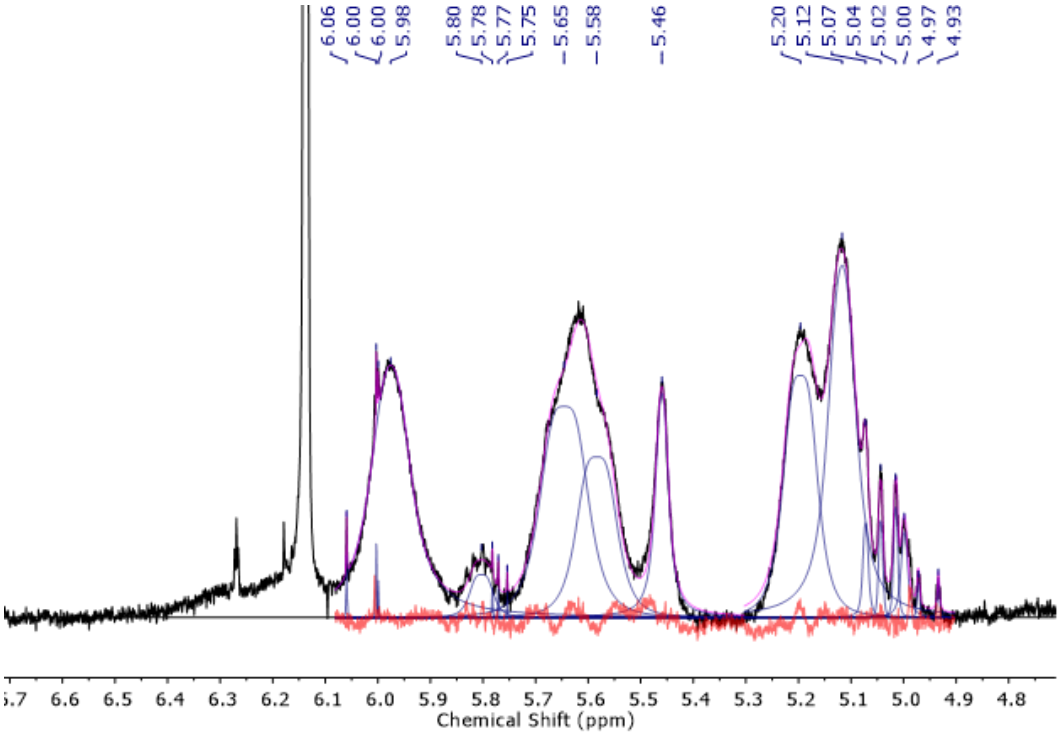

Figure 4.48 Multipeak fitting functions of the bound and free ligands shown here for UDT/oleate-PbS QD with 500 eq. $CoCp_2$ added after 123 hours. The original spectrum is shown in the black trace, the fits are shown as blue traces with the sum shown as a pink trace. Bound oleate was fit to two peaks located at 5.65 and 5.58 ppm and free oleate was fit to a single peak at 5.46 ppm. Bound UDT was calculated by averaging the broad peak at 5.98 ppm (alkene CH, 1H) and the two peaks at 5.20 and 5.12 ppm (alkene CH_2, 2H), normalized to the same number of protons. Free UDT was calculated by averaging the broad peak at 5.80 ppm (1H) and the four peaks between 5.07 and 4.97 ppm (2H), normalized to the same number of protons. The residual of the fit is shown in red. Peaks at 6.06 ppm and the triplet at 4.93 ppm are minor impurities.

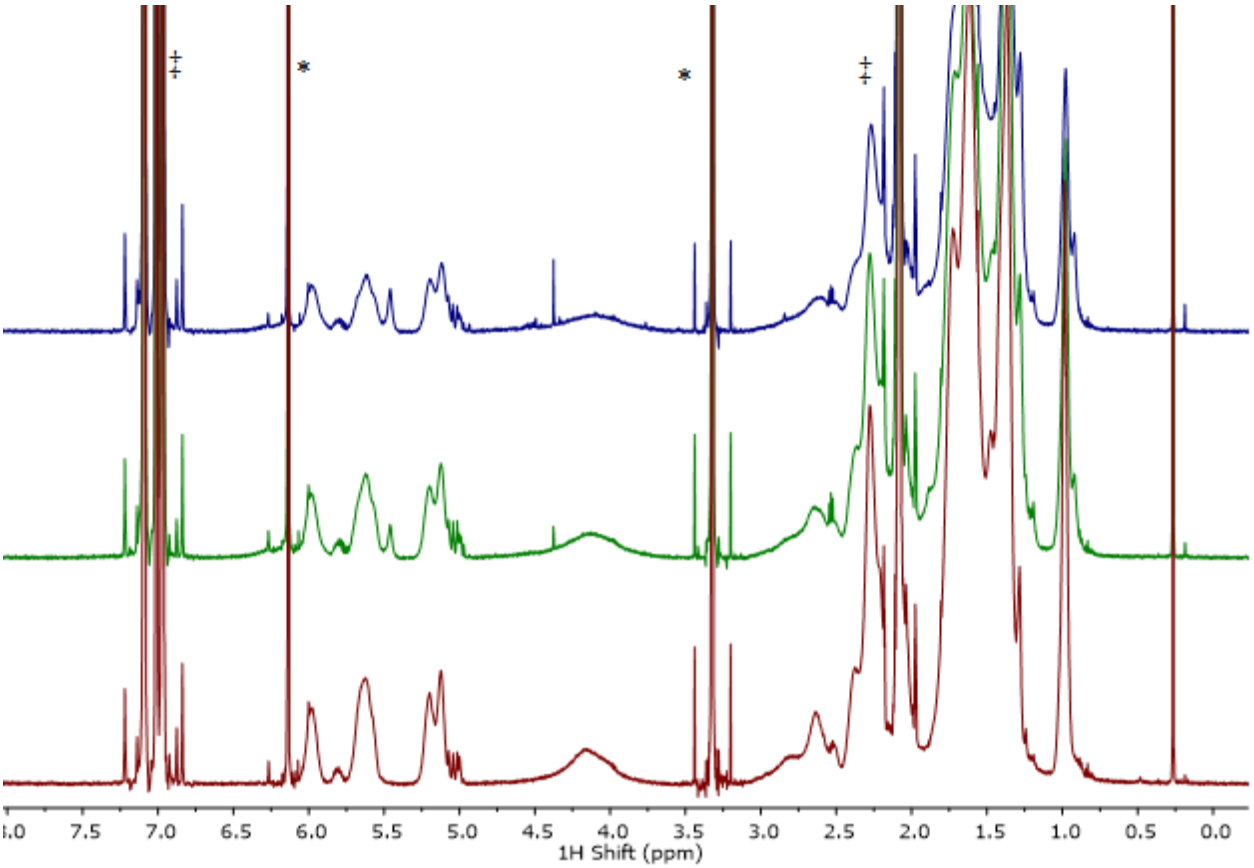

Figure 4.49 600 MHz ^{1}H NMR spectra in toluene-d_8 of UDT/oleate-PbS QDs with 0 (red), 100 (green), and 500 (blue) eq $CoCp_2$ added after 123 hours. Peaks denoted by ‡ are toluene solvent residuals, and peaks marked by * are the internal standard 1,3,5-trimethoxybenzene.

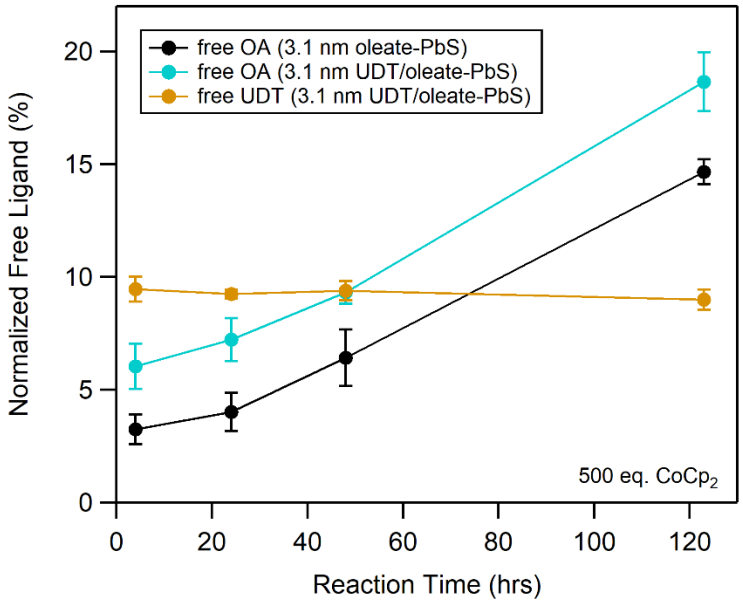

Figure 4.50 Quantification of free ligand in oleate-PbS-3 (black) and UDT/oleate-PbS (yellow, blue) batches with 500 eq $CoCp_2$ added over time (average values from triplicate runs ± standard deviation). Importantly, the amount of free UDT at time = 0 remains consistent throughout the titration. Lines connecting data points are a guide to the eye.

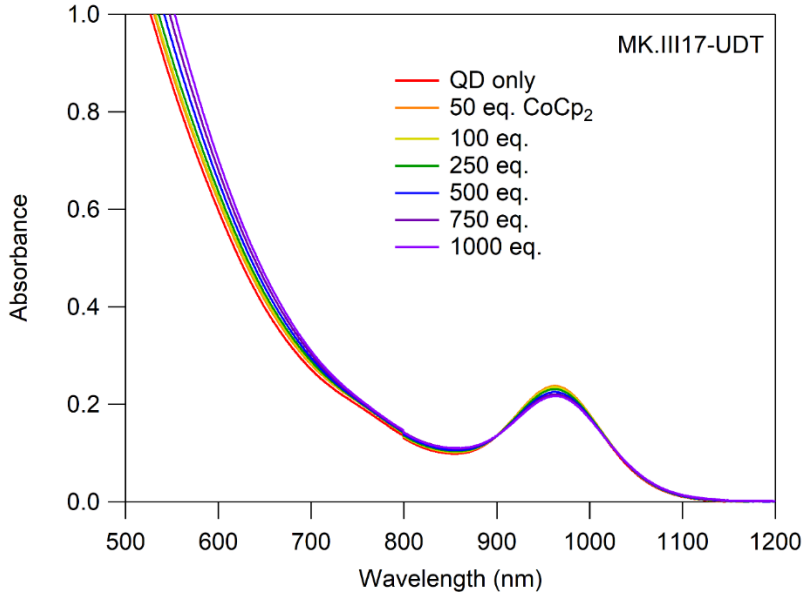

Figure 4.51 UV-Vis-NIR absorption spectrum of UDT/oleate-PbS in toluene (2.5 µM) with added excess $CoCp_2$. We observe a 1 nm red shift and minor loss of absorbance with added $CoCp_2$.

The observation that UDT is not lost from the surface upon addition of $CoCp_2$ indicates that the change in binding functional group from a carboxylate to a thiolate results in a distinct change in reactivity compared with the oleate- and UDA/oleate-PbS systems. This distinct reactivity may arise from differences in ligand binding mode between the UDT/oleate-PbS and oleate-PbS-3 QDs. A mixture of X-type thiolate and L-type thiol binding may comprise the bound UDT at the QD surface, as thiols are known to be able to bind in both modes.[33,34] Our data show that the ligand coverages of oleate-PbS-3 and UDT/oleate-PbS remain the same within error (Table 4.5), which may support X-type thiolate binding at the surface. Raman analysis of the UDT/oleate-PbS QDs in an effort to identify S–H thiol stretches was inconclusive due to significant background signal (Figure 4.52); thus, we cannot definitively rule out the possibility of bound L-type UDT (RSH). While anionic X-type UDT (RS^-) could potentially be displaced with surface charging in order to maintain charge balance, L-type ligands are not anticipated to be displaced via an electron-promoted mechanism.[21,24] Notably, the presence of X-type versus L-type binding of UDT is not readily distinguished by NMR spectroscopy, and the complexity of UDT binding modes remains to be elucidated through further studies.

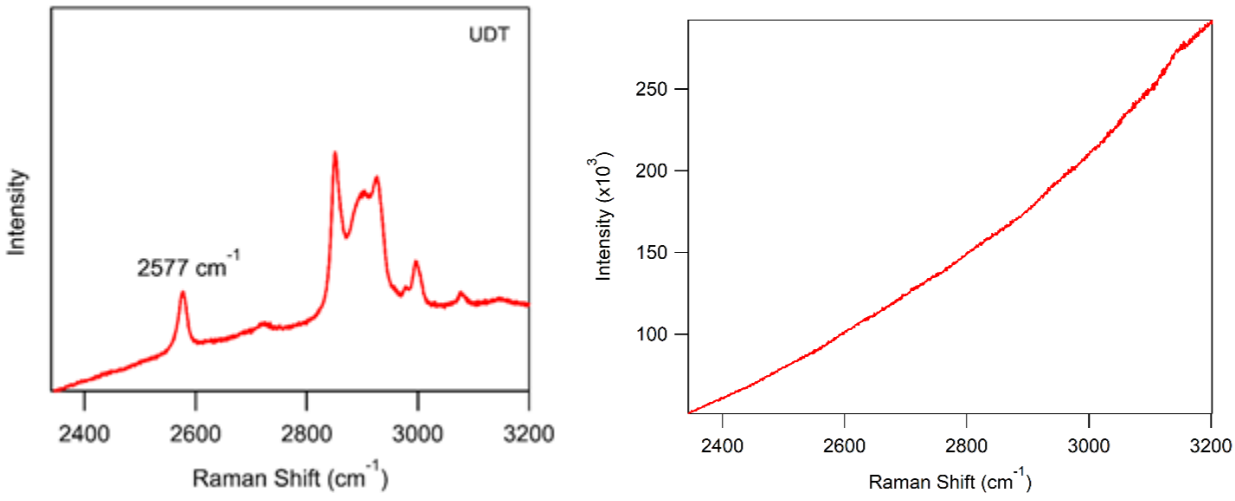

Figure 4.52 (*left*) The Raman band at 2577 cm^{-1} is attributed to the S–H vibration of undec-10-ene-1-thiol (UDT). (*right*) Raman measurements of UDT/oleate-PbS QDs did not show evidence of this S–H stretch.

A second explanation for the observed preference for oleate over UDT displacement upon charging is based on differences in the relative binding strengths of each ligand. Thiolates have been established to bind tightly to CdSe and PbS QDs.[5,27] The greater binding strength of thiolates compared with carboxylate ligands has been rationalized in several ways.[5,27,54,55] The more favorable binding of soft thiolate ligands with soft Lewis acids such as Cd^{2+} or Pb^{2+} compared with hard carboxylate ligands is well explained by hard-soft acid-base theory. Additionally, the slightly higher bond dissociation energy of Pb–S bonds (398 kJ/mol) compared with Pb–O bonds (382 kJ/mol) is in agreement with an enhanced binding strength of thiolates.[56] A similar argument may be made using the relative basicity of alkyl thiolates versus alkyl carboxylates. Thiols such as dodecanethiol have predicted pK_a values of ~10.5 whereas oleic acid has a reported pK_a of ~9.85.[52,53] The slightly higher pK_a of the thiol reflects greater Lewis basicity of UDT and is consistent with its binding of Pb^{2+} surface ions more tightly than oleate ligands bind Pb^{2+} ions.[52]

Clearly, the impact of a binding ligand with significant electronic contributions from the ligand backbone or binding group may impact the energetics of the Pb–X surface state. We found that toluate-Pb states are thermodynamically more favorable to reduce than oleate-Pb states; conversely, we infer from our ^{1}H NMR spectroscopy data that thiolate-Pb states are less favorable to reduce in the presence of $CoCp_2$. In addition, oleate dissociation from UDT/oleate-PbS is noticeably lower (8.4 ± 0.6% total oleate loss) than oleate loss from oleate-PbS-3 (14.7 ± 0.6% total oleate loss). This suggests that the presence of bound thiolate ligands may perturb the energies of the oleate-Pb^{2+} ions in the mixed thiolate/carboxylate system. Alternatively, excess charge from $CoCp_2$ may localize in spectroscopically silent states more readily on the UDT/oleate-PbS QDs, contributing to the lesser extent of oleate loss. Overall, the comparison of the UDT/oleate-PbS system with the native oleate-capped QDs suggests that thiolate ligands are more strongly bound to surface Pb^{2+} sites than native oleate ligands and that thiolate-capped

QDs may be more resilient to displacement and defect formation caused by surface charging. Importantly, although UDT and UDA have identical long-chain alkyl backbones, the surface binding group of each ligand (thiolate versus carboxylate) clearly influences the stability of surface Pb^{2+} ions toward reduction.

4.4 Conclusions

Mixed-shell PbS QDs were prepared from oleate-capped PbS QDs using exchange ligands with prominent ^{1}H NMR spectroscopic handles to quantify bound and free ligand populations in the post-exchanged systems and upon charging with $CoCp_2$. Investigations of the surface electronic structure of the mixed-shell systems through UV-Vis absorbance and IR spectroscopies showed evidence that broadband absorption across the UV-Visible range is indeed enhanced by the addition of device-relevant ligand functionalities, including thiolate binding groups and conjugated aryl backbones. A method combining ICP-MS, UV-Vis, and XPS was also developed to obtain extinction coefficients for mixed-ligand systems, a necessary step toward quantifying the reactivity of post-exchanged QDs with $CoCp_2$. Charging of the UDA/oleate, toluate/oleate, and UDT/oleate-PbS QD systems with $CoCp_2$ demonstrated that X-type carboxylate ligands with aryl backbones are most likely to be displaced in the presence of excess electrons, followed by alkyl carboxylates, and finally thiolates. We attribute these observations in large part to differences in ligand binding strength and pK_a values of the ligand conjugate acids. Additionally, the differing degrees of ligand displacement may serve as a reporter on the relative energetics of the resulting Pb–X surface state.

In sum, this chapter demonstrated that the extent of ligand exchange in colloidal QD solutions can be exploited to attain mixed-shell compositions with near stoichiometric populations of two distinct ligands. Together, these systems enabled extensive comparisons to study the properties of nanocrystals, in both the presence and absence of excess reductant. Our work suggests that devices employing exchange ligands with short, conjugated backbones or with low binding affinities may degrade over time in electron-rich environments, yet strongly bound groups such as thiolates appear robust under such conditions. While it is important to recognize the limitations of translating our observations in colloidal

samples directly to solid state devices, this work provides meaningful insight into QD surface chemistry, ligand exchange, and redox reactivity.

REFERENCES

(1) Kovalenko, M. V.; Manna, L.; Cabot, A.; Hens, Z.; Talapin, D. V.; Kagan, C. R.; Klimov, V. I.; Rogach, A. L.; Reiss, P.; Milliron, D. J.; et al. Prospects of Nanoscience with Nanocrystals. *ACS Nano* **2015**, *9*, 1012–1057.

(2) Talapin, D. V.; Lee, J.-S.; Kovalenko, M. V.; Shevchenko, E. V. Prospects of Colloidal Nanocrystals for Electronic and Optoelectronic Applications. *Chem. Rev.* **2010**, *110*, 389–458.

(3) Carey, G. H.; Abdelhady, A. L.; Ning, Z.; Thon, S. M.; Bakr, O. M.; Sargent, E. H. Colloidal Quantum Dot Solar Cells. *Chem. Rev.* **2015**, *115*, 12732–12763.

(4) Kershaw, S. V.; Jing, L.; Huang, X.; Gao, M.; Rogach, A. L. Materials aspects of semiconductor nanocrystals for optoelectronic applications. *Mater. Horiz.* **2017**, *4*, 155–205.

(5) Boles, M. A.; Ling, D.; Hyeon, T.; Talapin, D. V. The surface science of nanocrystals. *Nat. Mater.* **2016**, *15*, 364–364.

(6) Peterson, M. D.; Cass, L. C.; Harris, R. D.; Edme, K.; Sung, K.; Weiss, E. A. The Role of Ligands in Determining the Exciton Relaxation Dynamics in Semiconductor Quantum Dots. *Annu. Rev. Phys. Chem.* **2014**, *65*, 317–339.

(7) Soreni-Harari, M.; Yaacobi-Gross, N.; Steiner, D.; Aharoni, A.; Banin, U.; Millo, O.; Tessler, N. Tuning Energetic Levels in Nanocrystal Quantum Dots through Surface Manipulations. *Nano Lett.* **2008**, *8*, 678–684.

(8) Gao, Y.; Aerts, M.; Sandeep, C. S. S.; Talgorn, E.; Savenije, T. J.; Kinge, S.; Siebbeles, L. D. A.; Houtepen, A. J. Photoconductivity of PbSe Quantum-Dot Solids: Dependence on Ligand Anchor Group and Length. *ACS Nano* **2012**, *6*, 9606–9614.

(9) Oh, S. J.; Wang, Z.; Berry, N. E.; Choi, J.-H.; Zhao, T.; Gaulding, E. A.; Paik, T.; Lai, Y.; Murray, C. B.; Kagan, C. R. Engineering Charge Injection and Charge Transport for High Performance PbSe Nanocrystal Thin Film Devices and Circuits. *Nano Lett.* **2014**, *14*, 6210–6216.

(10) Reinhart, C. C.; Johansson, E. Colloidally Prepared 3-Mercaptopropionic Acid Capped Lead Sulfide Quantum Dots. *Chem. Mater.* **2015**, *27*, 7313–7320.

(11) Chang, J.; Ogomi, Y.; Ding, C.; Zhang, Y. H.; Toyoda, T.; Hayase, S.; Katayama, K.; Shen, Q. Ligand-dependent exciton dynamics and photovoltaic properties of PbS quantum dot heterojunction solar cells. *Phys. Chem. Chem. Phys.* **2017**, *19*, 6358–6367.

(12) Xu, F.; Gerlein, L. F.; Ma, X.; Haughn, C. R.; Doty, M. F.; Cloutier, S. G. Impact of Different Surface Ligands on the Optical Properties of PbS Quantum Dot Solids. *Materials.* **2015**, *8*, 1858–1870.

(13) Brown, P. R.; Kim, D.; Lunt, R. R.; Zhao, N.; Bawendi, M. G.; Grossman, J. C.; Bulović, V. Energy Level Modification in Lead Sulfide Quantum Dot Thin Films through Ligand Exchange. *ACS Nano* **2014**, *8*, 5863–5872.

(14) Chen, J.; Zheng, S.; Jia, D.; Liu, W.; Andruszkiewicz, A.; Qin, C.; Yu, M.; Liu, J.; Johansson, E. M. J.; Zhang, X. Regulating Thiol Ligands of p-Type Colloidal Quantum Dots for Efficient Infrared Solar Cells. *ACS Energy Lett.* **2021**, *6*, 1970–1979.

(15) Giansante, C.; Carbone, L.; Giannini, C.; Altamura, D.; Ameer, Z.; Maruccio, G.; Loiudice, A.; Belviso, M. R.; Cozzoli, P. D.; Rizzo, A.; et al. Colloidal Arenethiolate-Capped PbS Quantum Dots: Optoelectronic Properties, Self-Assembly, and Application in Solution-Cast Photovoltaics. *J. Phys. Chem. C* **2013**, *117*, 13305–13317.

(16) Giansante, C.; Infante, I.; Fabiano, E.; Grisorio, R.; Suranna, G. P.; Gigli, G. "Darker-than-Black" PbS Quantum Dots: Enhancing Optical Absorption of Colloidal Semiconductor Nanocrystals via Short Conjugated Ligands. *J. Am. Chem. Soc.* **2015**, *137*, 1875–1886.

(17) Giansante, C. Library Design of Ligands at the Surface of Colloidal Nanocrystals. *Acc. Chem. Res.* **2020**, *53*, 1458–1467.

(18) Harris, R. D.; Bettis Homan, S.; Kodaimati, M.; He, C.; Nepomnyashchii, A. B.; Swenson, N. K.; Lian, S.; Calzada, R.; Weiss, E. A. Electronic Processes within Quantum Dot-Molecule Complexes. *Chem. Rev.* **2016**, *116*, 12865–12919.

(19) Tsui, E. Y.; Hartstein, K. H.; Gamelin, D. R. Selenium Redox Reactivity on Colloidal CdSe Quantum Dot Surfaces. *J. Am. Chem. Soc.* **2016**, *138*, 11105–11108.

(20) Pu, C.; Dai, X.; Shu, Y.; Zhu, M.; Deng, Y.; Jin, Y.; Peng, X. Electrochemically-stable ligands bridge the photoluminescence-electroluminescence gap of quantum dots. *Nat. Commun.* **2020**, *11*, 937.

(21) Hartley, C. L.; Dempsey, J. L. Electron-Promoted X-Type Ligand Displacement at CdSe Quantum Dot Surfaces. *Nano Lett.* **2019**, *19*, 1151–1157.

(22) Hartley, C. L.; Dempsey, J. L. Revealing the Molecular Identity of Defect Sites on PbS Quantum Dot Surfaces with Redox-Active Chemical Probes. *Chem. Mater.* **2021**, *33*, 2655–2665.

(23) Voznyy, O.; Thon, S. M.; Ip, A. H.; Sargent, E. H. Dynamic Trap Formation and Elimination in Colloidal Quantum Dots. *J. Phys. Chem. Lett.* **2013**, *4*, 987–992.

(24) du Fossé, I.; ten Brinck, S.; Infante, I.; Houtepen, A. J. Role of Surface Reduction in the Formation of Traps in *n*-Doped II–VI Semiconductor Nanocrystals: How to Charge without Reducing the Surface. *Chem. Mater.* **2019**, *31*, 4575–4583.

(25) Lu, H.; Carroll, G. M.; Neale, N. R.; Beard, M. C. Infrared Quantum Dots: Progress, Challenges, and Opportunities. *ACS Nano*. **2019**, *13*, 939–953.

(26) Kahmann, S.; Loi, M. A. Trap states in lead chalcogenide colloidal quantum dots—origin, impact, and remedies. *Appl. Phys. Rev.* **2020**, *7*, 041305.

(27) Knauf, R. R.; Lennox, J. C.; Dempsey, J. L. Quantifying Ligand Exchange Reactions at CdSe Nanocrystal Surfaces. *Chem. Mater.* **2016**, *28*, 4762–4770.

(28) Hines, M. A.; Scholes, G. D. Colloidal PbS Nanocrystals with Size-Tunable Near-Infrared Emission: Observation of Post-Synthesis Self-Narrowing of the Particle Size Distribution. *Adv. Mater.* **2003**, *15*, 1844–1849.

(29) Kessler, M. L.; Starr, H. E.; Knauf, R. R.; Rountree, K. J.; Dempsey, J. L. Exchange equilibria of carboxylate-terminated ligands at PbS nanocrystal surfaces. *Phys. Chem. Chem. Phys.* **2018**, *20*, 23649–23655.

(30) Hassinen, A.; Moreels, I.; De Nolf, K.; Smet, P. F.; Martins, J. C.; Hens, Z. Short-Chain Alcohols Strip X-Type Ligands and Quench the Luminescence of PbSe and CdSe Quantum Dots, Acetonitrile Does Not. *J. Am. Chem. Soc.* **2012**, *134*, 20705–20712.

(31) Kessler, M. L.; Dempsey, J. L. Mapping the Topology of PbS Nanocrystals through Displacement Isotherms of Surface-Bound Metal Oleate Complexes. *Chem. Mater.* **2020**, *32*, 2561–2571.

(32) Moreels, I.; Lambert, K.; Smeets, D.; De Muynck, D.; Nollet, T.; Martins, J. C.; Vanhaecke, F.; Vantomme, A.; Delerue, C.; Allan, G.; et al. Size-Dependent Optical Properties of Colloidal PbS Quantum Dots. *ACS Nano* **2009**, *3*, 3023–3030.

(33) Yao, Y.; Buhro, W. E. Thiol Versus Thiolate Ligation on Cadmium Selenide Quantum Belts. *Chem. Mater.* **2020**, *32*, 205–214.

(34) Lystrom, L.; Roberts, A.; Dandu, N.; Kilina, S. Surface-Induced Deprotonation of Thiol Ligands Impacts the Optical Response of CdS Quantum Dots. *Chem. Mater.* **2021**, *33*, 892–901.

(35) Shestha, A.; Yin, Y.; Andersson, G. G.; Spooner, N. A.; Qiao, S.; Dai, S. Versatile PbS Quantum Dot Ligand Exchange Systems in the Presence of Pb-Thiolates. *Small* **2017**, *13*, 1602956.

(36) Weinberg, D. J.; He, C.; Weiss, E. A. Control of the Redox Activity of Quantum Dots through Introduction of Fluoroalkanethiolates into Their Ligand Shells. *J. Am. Chem. Soc.* **2016**, *138*, 2319–2326.

(37) De Roo, J.; Yazdani, N.; Drijvers, E.; Lauria, A.; Maes, J.; Owen, J. S.; Van Driessche, I.; Niederberger, M.; Wood, V.; Martins, J. C.; et al. Probing Solvent–Ligand Interactions in Colloidal Nanocrystals by the NMR Line Broadening. *Chem. Mater.* **2018**, *30*, 5485–5492.

(38) Hartley, C. L.; Kessler, M. L.; Dempsey, J. L. Molecular-Level Insight into Semiconductor Nanocrystal Surfaces. *J. Am. Chem. Soc.* **2021**, *143*, 1251–1266.

(39) Cass, L. C.; Malicki, M.; Weiss, E. A. The Chemical Environments of Oleate Species within Samples of Oleate-Coated PbS Quantum Dots. *Anal. Chem.* **2013**, *85*, 6974–6979.

(40) Zhang, J.; Zhang, H.; Cao, W.; Pang, Z.; Li, J.; Shu, Y.; Zhu, C.; Kong, X.; Wang, L.; Peng, X. Identification of Facet-Dependent Coordination Structures of Carboxylate Ligands on CdSe Nanocrystals. *J. Am. Chem. Soc.* **2019**, *141*, 15675–15683.

(41) Giansante, C. Surface Chemistry Control of Colloidal Quantum Dot Band Gap. *J. Phys. Chem. C* **2018**, *122*, 18110–18116.

(42) Krause, M. M.; Kambhampati, P. Linking surface chemistry to optical properties of semiconductor nanocrystals. *Phys. Chem. Chem. Phys.* **2015**, *17*, 18882–18894.

(43) Debellis, D.; Gigli, G.; ten Brinck, S.; Infante, I.; Giansante, C. Quantum-Confined and Enhanced Optical Absorption of Colloidal PbS Quantum Dots at Wavelengths with Expected Bulk Behavior. *Nano Lett.* **2017**, *17*, 1248–1254.

(44) Choi, H.; Ko, J.-H.; Kim, Y.-H.; Jeong, S. Steric-Hindrance-Driven Shape Transition in PbS Quantum Dots: Understanding Size-Dependent Stability. *J. Am. Chem. Soc.* **2013**, *135*, 5278–5281.

(45) Kroupa, D. M.; Vörös, M.; Brawand, N. P.; McNichols, B. W.; Miller, E. M.; Gu, J.; Nozik, A. J.; Sellinger, A.; Galli, G.; Beard, M. C. Tuning Colloidal Quantum Dot Band Edge Positions through Solution-Phase Surface Chemistry Modification. *Nat. Commun.* **2017**, *8*, 2–9.

(46) Hou, B.; Cho, Y.; Kim, B. S.; Hong, J.; Park, J. B.; Ahn, S. J.; Sohn, J. I.; Cha, S.; Kim, J. M. Highly Monodispersed PbS Quantum Dots for Outstanding Cascaded-Junction Solar Cells. *ACS Energy Lett.* **2016**, *1*, 834–839.

(47) Anderson, N. C.; Hendricks, M. P.; Choi, J. J.; Owen, J. S. Ligand Exchange and the Stoichiometry of Metal Chalcogenide Nanocrystals: Spectroscopic Observation of Facile Metal-Carboxylate Displacement and Binding. *J. Am. Chem. Soc.* **2013**, *135*, 18536–18548.

(48) Kroupa, D. M.; Vörös, M.; Brawand, N. P.; Bronstein, N.; McNichols, B. W.; Castaneda, C. V; Nozik, A. J.; Sellinger, A.; Galli, G.; Beard, M. C. Optical Absorbance Enhancement in PbS QD/Cinnamate Ligand Complexes. *J. Phys. Chem. Lett.* **2018**, *9*, 3425–3433.

(49) Shim, M.; Guyot-Sionnest, P. n-type colloidal semiconductor nanocrystals. *Nature* **2000**, *407*, 981–983.

(50) Koh, W.; Koposov, A. Y.; Stewart, J. T.; Pal, B. N.; Robel, I.; Pietryga, J. M.; Klimov, V. I. Heavily Doped *n*-Type PbSe and PbS Nanocrystals Using Ground-State Charge Transfer from Cobaltocene. *Sci. Rep.* **2013**, *3*, 2004.

(51) Cox, R. .; Terry, H. . Lithium-7 NMR studies of aromatic ion pairs. *J. Magn. Reson.* **1974**, *14*, 317–322.

(52) Bronstein, N. D.; Martinez, M. S.; Kroupa, D. M.; Vörös, M.; Lu, H.; Brawand, N. P.; Nozik, A. J.; Sellinger, A.; Galli, G.; Beard, M. C. Designing Janus Ligand Shells on PbS Quantum Dots Using Ligand–Ligand Cooperativity. *ACS Nano* **2019**, *13*, 3839–3846.

(53) Kanicky, J. R.; Shah, D. O. Effect of Degree, Type, and Position of Unsaturation on the pK_a of Long-Chain Fatty Acids. *J. Colloid Interface Sci.* **2002**, *256*, 201–207.

(54) Zhao, X.; Gorelikov, I.; Musikhin, S.; Cauchi, S.; Sukhovatkin, V.; Sargent, E. H.; Kumacheva, E. Synthesis and Optical Properties of Thiol-Stabilized PbS Nanocrystals. *Langmuir* **2005**, *21*, 1086–1090.

(55) Nag, A.; Kovalenko, M. V.; Lee, J.-S.; Liu, W.; Spokoyny, B.; Talapin, D. V. Metal-Free Inorganic Ligands for Colloidal Nanocrystals: S^{2-}, HS^-, Se^{2-}, HSe^-, Te^{2-}, HTe^-, TeS_3^{2-}, OH^-, and NH_2^- as Surface Ligands. *J. Am. Chem. Soc.* **2011**, *133*, 10612–10620.

(56) Luo, Y. R. *Comprehensive Handbook of Chemical Bond Energies*; CRC Press: Boca Raton, FL, 2007.

CHAPTER 5 : DEVELOPMENT OF QUANTUM DOT-BASED SYSTEMS TO PROBE CHARGE TRANSFER IN THE MARCUS INVERTED REGION

5.1 Introduction

Photoinduced charge transfer in systems involving quantum dots (QDs) is of great interest due to the widespread use of these nanoscale materials in light-driven devices such as solar cells and systems for photocatalysis. Studying the photochemical and photophysical behavior of QDs in detail, however, is not trivial. For instance, due to their large surface area to volume ratio QD photochemistry is frequently affected by non-radiative recombination sites (i.e., trap states) at the surface. Additionally, quantum confinement of QDs in all three dimensions leads to a strong degree of coupling of the dynamics of charge carriers (electron and hole) in an exciton pair which can affect photophysical behavior compared with bulk semiconductors.[1] As such, better understanding charge transfer mechanisms from photoexcited QDs has been a major area of study over the last several decades. In an effort to accurately model charge transfer mechanisms, one model that has commonly been considered is semiclassical Marcus theory. In non-adiabatic semiclassical Marcus theory, the rate of electron transfer (k_{ET}) is described by the expression:

Equation 5.1

$$k_{ET} = \frac{2\pi}{\hbar}|H_{DA}|^2 \frac{1}{\sqrt{4\pi\lambda k_B T}} e^{\left(\frac{-(\lambda+\Delta G°)^2}{4\lambda k_B T}\right)}$$

where the key experimental parameters include reorganization energy (λ), electronic coupling of the donor-acceptor (D-A) states reflected by the coupling constant (H_{DA}), and the free energy change of electron transfer ($\Delta G°$).[1,2] Other parameters considered are the temperature (T) and Boltzmann constant (k_B). In this model, reactants and products of a charge transfer reaction can be drawn as potential energy

surfaces (Figure 1). Consequently, depending on the aforementioned parameters and the resulting overlap of the D-A reactant and product states, there are three possible electron transfer (ET) regimes: normal, activationless, and inverted (Figure 5.1). Importantly, this relationship between driving force and the electron transfer rate is based upon a two-state model best modeled by the case of a molecular donor and acceptor.[1]

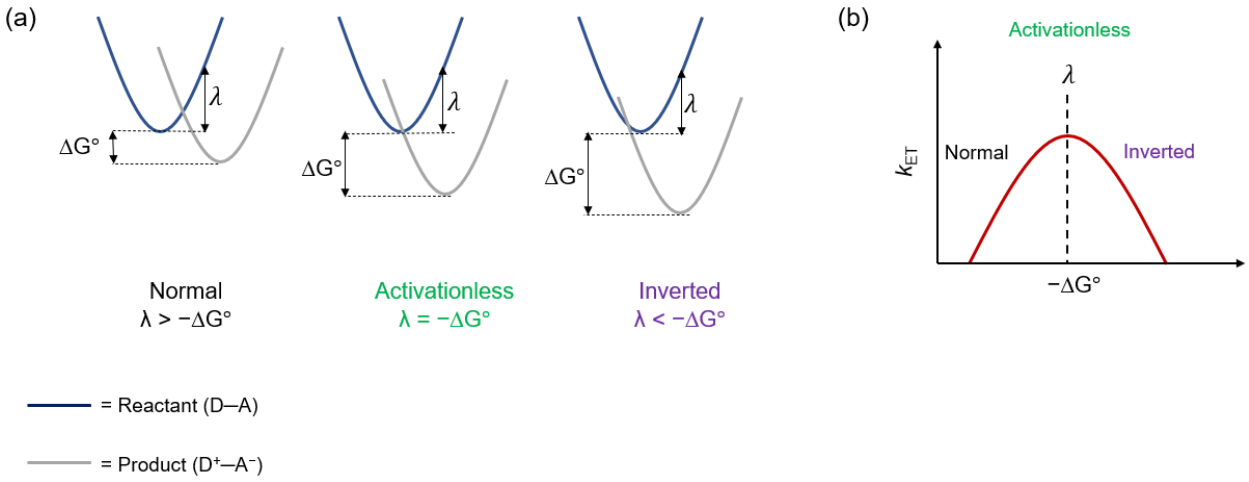

Figure 5.1 (a) Potential energy surfaces of reactant and product states showing overlap and free energy change ($\Delta G°$) and reorganization energy (λ) for the normal, activationless and inverted regimes. Vibrational states are omitted for clarity.; (b) Plot demonstrating the anticipated relationship between rate of electron transfer (k_{ET}) and driving force ($-\Delta G°$) and the correlated normal, activationless and normal regimes. Figures adapted from Reference [2].

Indeed, empirical adjustments to the two-state Marcus theory equation, such as the Marcus-Gerischer equation, have been derived for better predicting the relationship between charge transfer rate and driving force for charge transfer to semiconductor materials that possess a continuum of possible acceptor states.[1,3,4] In the Marcus-Gerischer equation, for example, the rate of charge transfer is determined by integrating over all possible acceptor state potentials, allowing for a model that better explains experimental observations with semiconductor materials than the two-state Marcus model. It is not obvious, though, how modeling of charge transfer dynamics may be affected in the case of charge transfer *from* a material such as a QD to an acceptor with a discrete electronic state (i.e., a molecular

acceptor, either freely diffusing or covalently linked to the QD). QDs have both a continuum of states at as well as discrete band edge states arising from quantum confinement (Figure 5.2). In the case where an electron or hole is transferred from a discrete band edge state in the QD in charge transfer from a photoexcited QD (QD*), it could be envisioned that this process might be well-modeled by the two-state nonadiabatic Marcus equation. However, multiple research groups have reported that semiclassical two-state Marcus theory does not adequately describe photoinduced ET or hole transfer (HT) from QD* to molecular acceptors.[3,5–7] Specifically, the major discrepancy with Marcus theory is that in the cases of photoinduced charge transfer with QDs, no inverted region is observed.

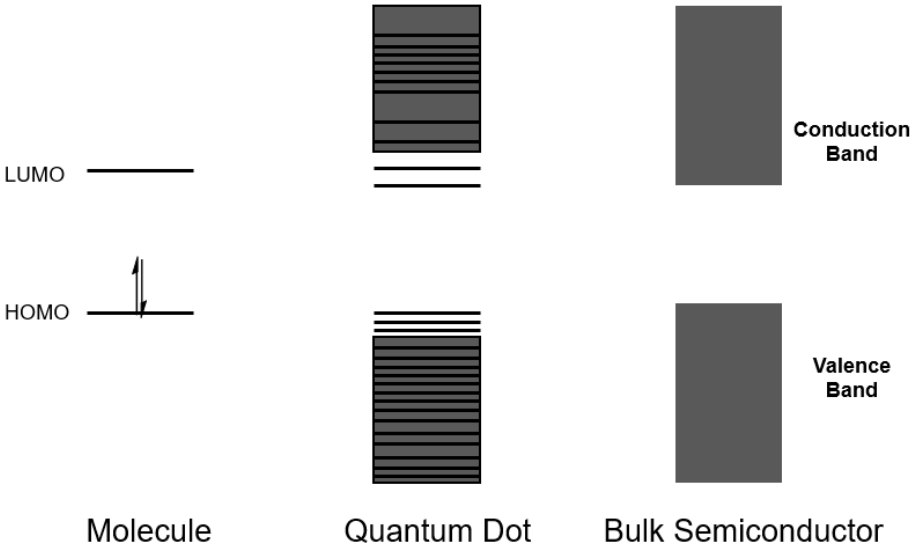

Figure 5.2 Electronic structure of a molecule compared with a quantum dot or a bulk semiconductor material.

For example, Zhu et al. reported in 2014 the study of photoinduced ET from CdE (E = S, Se, Te) QDs to three molecular acceptors with varying driving force (−ΔG°) for ET: anthraquinone, methyl viologen, and methylene blue ($E^{\circ\prime}$ = −4.0, −4.3, and −4.7 V vs. vacuum, respectively).[8] Using a combination of steady-state and time-resolved spectroscopic techniques Zhu et al. demonstrated that rather than the rate of ET decreasing at higher driving forces, as predicted by conventional Marcus theory in the inverted regime, the rate of ET appeared to plateau in all systems for a range of reorganization

energy values. Similarly, Olshansky et al. probed photoinduced hole transfer (HT) to study how the rate of HT varied with driving force.[6,9] Within their system, interfacial HT from a photoexcited CdSe/CdS core/shell QD to covalently bound functionalized ferrocene hole acceptor molecules was monitored. Similar to Zhu et al., a plateau of the rate of hole transfer with increased driving force was observed rather than the realization of the Marcus inverted region.

In these works, the lack of observation of a Marcus inverted region with increasing driving force were rationalized by invoking an Auger-assisted mechanism.[5,6] In an Auger-assisted ET mechanism, movement of the exciton electron and hole have coupled dynamics due to quantum confinement experienced in QDs. A proposed result is that transfer of an excitonic electron or hole in a photoexcited QD will lead to a simultaneous promotion of the other carrier into higher energy states.[1] This coupling of electron and hole motion is enabled by the coupled dynamics in a quantum confined system; such coupling is generally absent in molecular species. For example, in the case of photoinduced ET monitored by Zhu et al., it was proposed that ET from the conduction band (CB) edge state to the molecular acceptor occurs simultaneously with balance band (VB) hole promotion to a higher energy VB state (Figure 5.3). Therefore, the energy of the end product state (QD^{+}-A^{-}) varies based on the VB state the hole is promoted into, resulting in a "manifold" of possible product states.[5] This leads to the rate of ET being effectively independent of driving force (where driving force is defined by a non-Auger assisted ET process) and diminishes the chance of observing an inverted region (Figure 5.3).

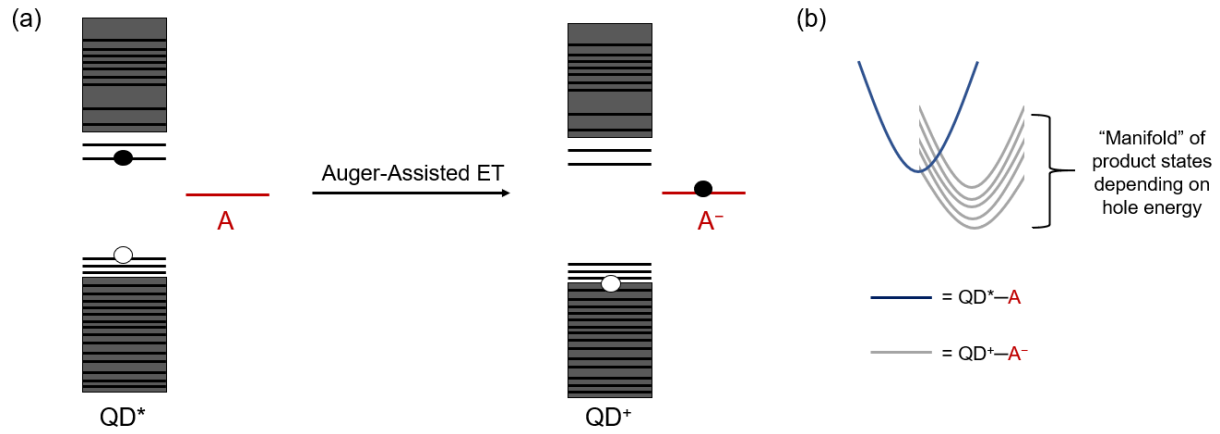

Figure 5.3 (a) Auger-assisted ET from a photoexcited QD (QD*) to a generic molecular acceptor (A). Due to coupling of the electron and hole in QDs, energy is conserved upon ET by promotion of the valence band hole to a higher energy state. (b) Depiction of reactant and manifold of product states resulting from variable hole energies as a result of the Auger-assisted ET mechanism; the manifold of product states leads to avoidance of the Marcus inverted regime. Figures adapted from Reference 1.

Our Approach

In this chapter, we seek to determine whether there are circumstances under which the Marcus inverted region can be observed for ET from QDs to molecular species by circumventing the Auger-assisted pathway in that specific charge transfer step. The goal is to design a system that effectively decouples the excitonic carriers that leads to Auger-assisted ET, one in which rapid valence band hole filling is followed by interfacial ET of the CB electron to a molecular acceptor (Figure 5.4). Notably, it has been established by Olshansky and others that the Auger-assisted mechanism applies to charge transfer of both the electron and hole;[6,7] in other words, step 1 (hole filling by a molecular donor) may result in excitation of the CB electron into a higher energy state via an Auger-assisted mechanism. This can be probed within our system via ultrafast spectroscopy measurements by monitoring for CB intraband transitions that would indicate the generation of hot electrons.[10] Importantly, cooling of "hot electrons" to band edge states from higher energy states is reported to be on sub-picosecond timescales in CdE QDs, so we anticipate that the electron would cool down to the band edge state prior to ET to the acceptor molecule.[3] Regardless, using transient absorption spectroscopy it will be possible to confirm these reports, or determine the population of QDs that participate in hot carrier transfer should that occur in our system.

Step 2 (electron transfer to a molecular acceptor) could then proceed by ET from the QD band edge state to the acceptor. By eliminating the valence band hole prior to ET and then monitoring step 2, we hypothesize that the CB electron will act as an independent charge carrier and ET will therefore be well modeled by semiclassical two-state Marcus theory. The work presented here are approaches towards identifying compatible QD materials and molecular reagents needed to realize such a system.

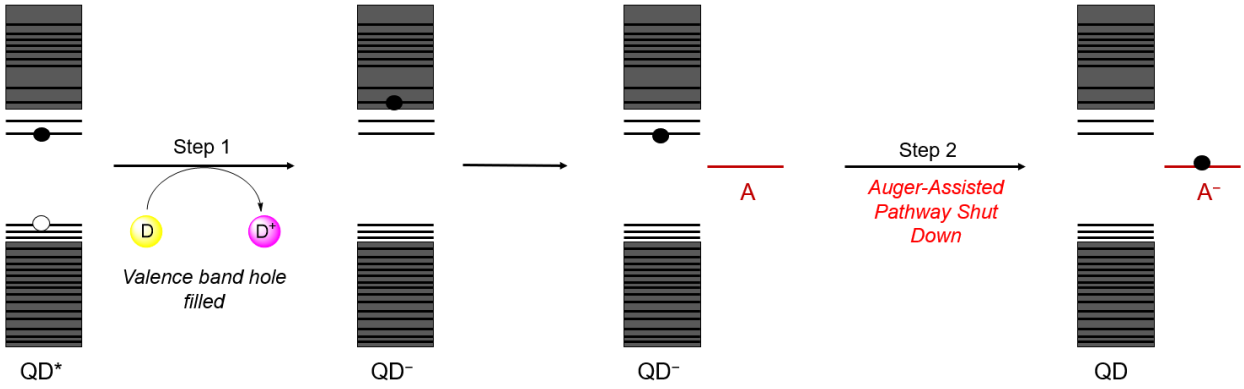

Figure 5.4 Proposed system for shutting down the Auger-assisted mechanism by quenching the valence band hole with a molecular donor (D) to form QD^- prior to electron transfer to a generic molecular acceptor (A).

Two system designs are presented: in system 1 (Figure 5.5a), CdE (E = Se, S) QDs are combined with a single freely diffusing redox-active molecular partner that can serve both as a donor (D) and an acceptor in its oxidized form (D^+). A variety of potential redox-active molecular partners are presented and tested for compatibility with the QDs. Within this system design, our intent was to track charge transfer steps and rates using time-resolved spectroscopy and monitoring the optical handles of the neutral or charged QD and/or the neutral or oxidized molecular partner. Due to experimental limitations in system 1 (vida infra), another approach (system 2) was later explored.

In system 2 (Figure 5.5b), a wider band gap material of QDs (ZnO) is employed with a molecular donor (D) that irreversibly fills the VB hole to generate QDs with an excess CB electron (QD^-). Several possible targets for molecular donors are presented and discussed. Once QD^- is generated, ET to a distinct molecular acceptor (A) will be monitored by optical absorbance handles of A^- or regeneration of the

neutral QD. By varying the QD size (i.e., band edge potentials) and reduction potential of the molecular acceptor, it will then be possible to monitor changes in the rate of ET with driving force for comparing with Marcus theory predictions. Future work will utilize ultrafast spectroscopy measurements to probe whether the Marcus inverted regime can indeed be observed if the VB hole is removed prior to ET to a molecular acceptor.

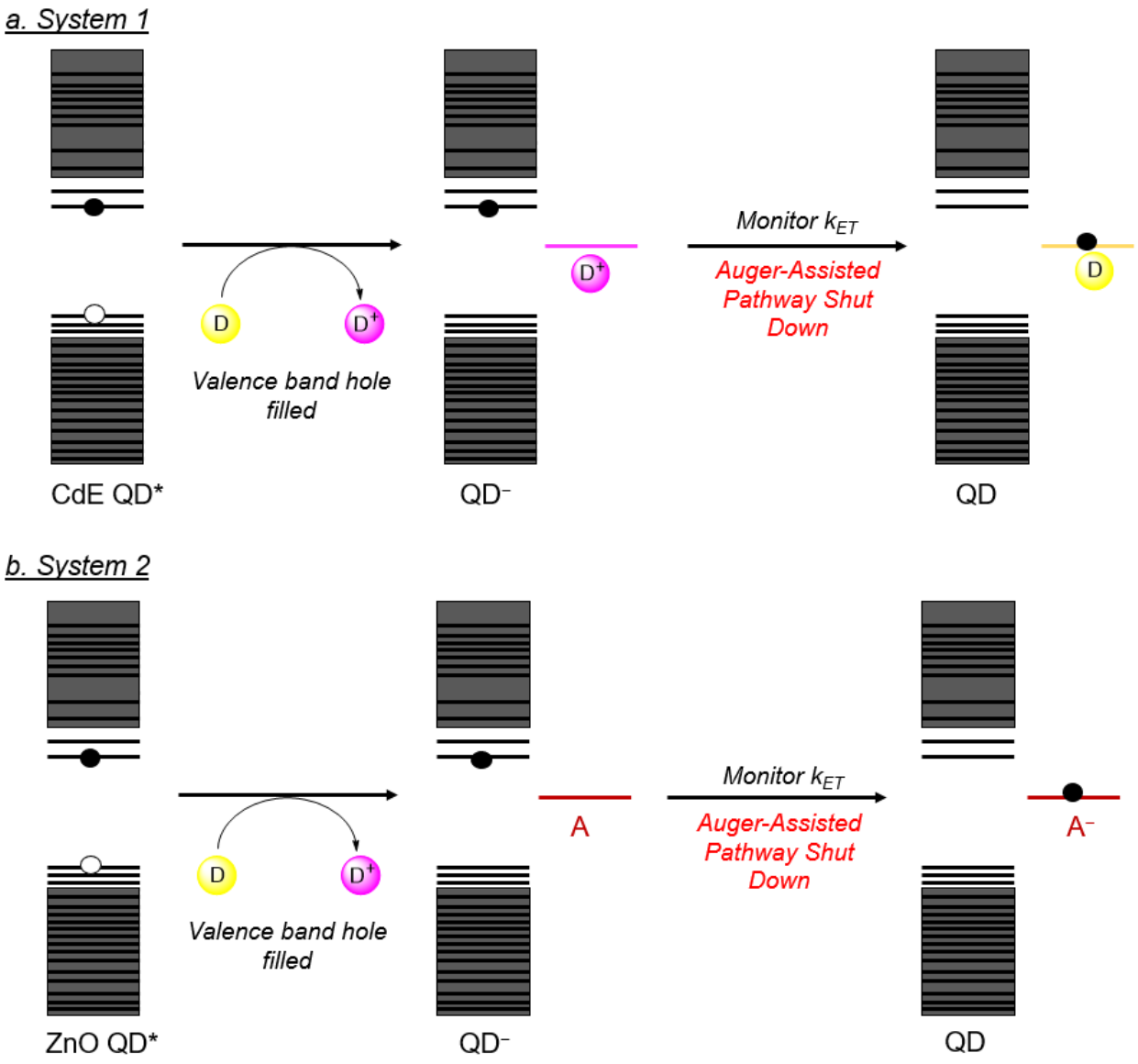

Figure 5.5 System designs for probing the Marcus inverted region with ET from QDs to a molecular acceptor: (a) System 1 utilizes CdE QDs with a single redox-active molecular partner (D), and (b) System 2 employs ZnO QDs with separate molecular donor (D) and acceptor (A) molecules.

5.2 Results and Discussion

5.2.1 System 1.

We first sought to prepare a system with QDs and a redox-active molecule that could serve either as a reductant (donor, D) to fill the VB hole upon QD excitation, or to be both a VB hole donor and CB electron acceptor in its oxidized form (D^+). We predicted that re-formation of D (or the neutral QD) could be monitored by optical spectroscopy upon ET from the QD^- CB electron to D^+ to regenerate the neutral QD (Scheme 5.1). Initial candidates were screened with the intent of using a single molecular donor and acceptor (D^+).

Scheme 5.1 Proposed design of System 1 for investigating photoinduced charge transfer with QDs and molecular redox agent that can act as a donor (D) and/or acceptor in its oxidized form (D^+)

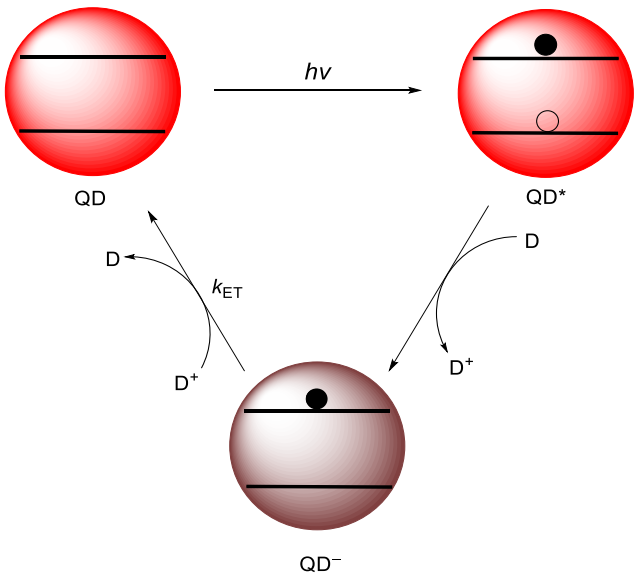

Exploratory studies were performed to test compatibility between QD material and hole quencher (reductant) candidates. Small oleate-capped CdSe QDs (2.3 – 3.1 nm in diameter) were first studied as a target material for this system. CdSe QDs were selected because of their widespread use in the literature

and in photoinduced ET studies specifically.[6,8,11] A range of outer-sphere reductants were evaluated for this system.

Bis(benzene) chromium ($Cr(C_6H_6)_2$).

To begin the compatibility studies of redox-active molecular reagents and CdSe QDs, $Cr(C_6H_6)_2$ was selected as a candidate due to its moderately reducing reduction potential ($E°' = -1.2$ V vs $Fc^{+/0}$) and anticipated lack of undesired side reactivity. To first screen for ground-state reactivity, UV-Vis absorption spectra were measured of the QDs in the presence of an increasing excess of $Cr(C_6H_6)_2$ (Figure 5.6). The lack of spectral changes upon addition of up to 80 eq. $Cr(C_6H_6)_2$ indicate that neither ground-state CB charging nor significant surface etching occur with this reagent.

Both steady-state and time-resolved emission spectra of the CdSe QDs in the presence of excess $Cr(C_6H_6)_2$ were then measured to observe whether VB hole quenching (as evidenced by emission loss) occurs upon photoexcitation of the QDs. Interestingly, emission quenching is observed in both steady-state and time-resolved spectra (Figure 5.7). However, the upward curvature and distinct slopes of the steady-state and time-resolved lifetime quenching suggest combined static and dynamic quenching, perhaps through a quenching sphere of action mechanism. This hypothesized combined static and dynamic quenching complicates analysis of photoinduced ET in this system. Additionally, the lack of strong spectral handles of either the neutral or oxidized forms of $Cr(C_6H_6)_2$ limit its utility for time-resolved optical studies.

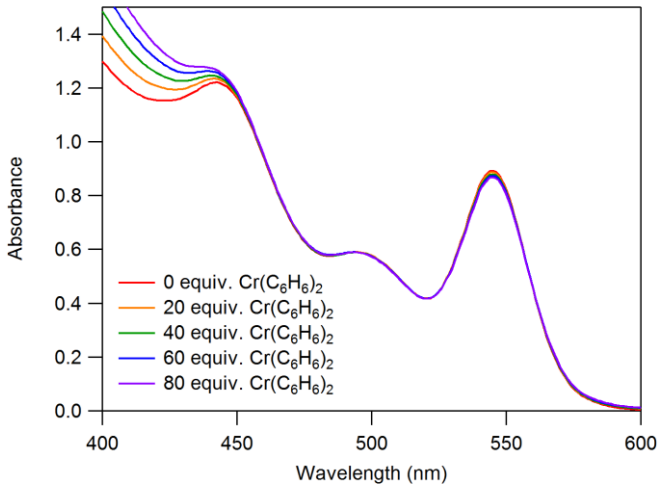

Figure 5.6 UV-Vis absorption spectra of CdSe QDs (3.1 nm, 4.9 µM) with addition of excess $Cr(C_6H_6)_2$ in tetrahydrofuran.

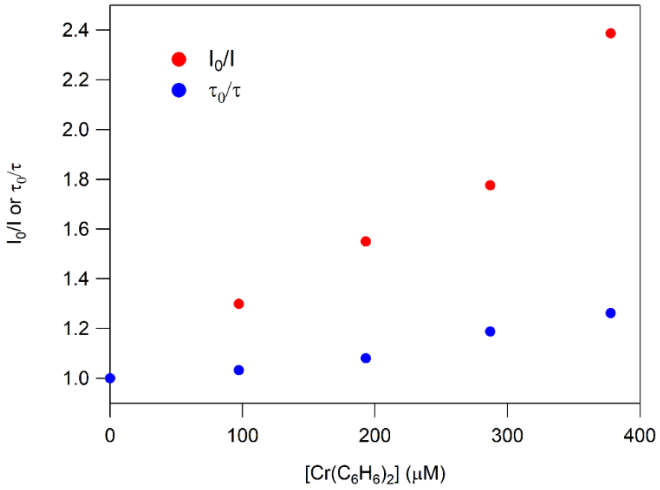

Figure 5.7 Stern-Volmer analysis of steady-state PL and lifetime quenching of CdSe QDs (3.1 nm, 4.9 µM) upon addition of $Cr(C_6H_6)_2$ in tetrahydrofuran. Steady-state emission measurements used an excitation wavelength of 545 nm. Emission lifetime was measured by TCSPC with a 485 nm LED excitation source. A detection wavelength was 560 nm was selected for lifetime studies.

Decamethylferrocene ($FeCp^*_2$).

A milder molecular reductant, $FeCp^*_2$ ($E^{o\prime}$ = −0.48 V vs $Fc^{+/0}$) was next explored as a potential VB hole quencher of photoexcited CdSe QDs. UV-Vis absorption spectra confirm no ground-state reactivity between the $FeCp^*_2$ and the QDs (Figure 5.8). Steady-state (Figure 5.9) and time-resolved

(Figure 5.10) emission spectra of CdSe QDs revealed almost no change in the presence of excess $FeCp^*_2$. The lack of observed quenching indicates that valence band hole quenching by $FeCp^*_2$ may not be favorable with CdSe QDs. Consequently, stronger hole quencher reagents were next explored.

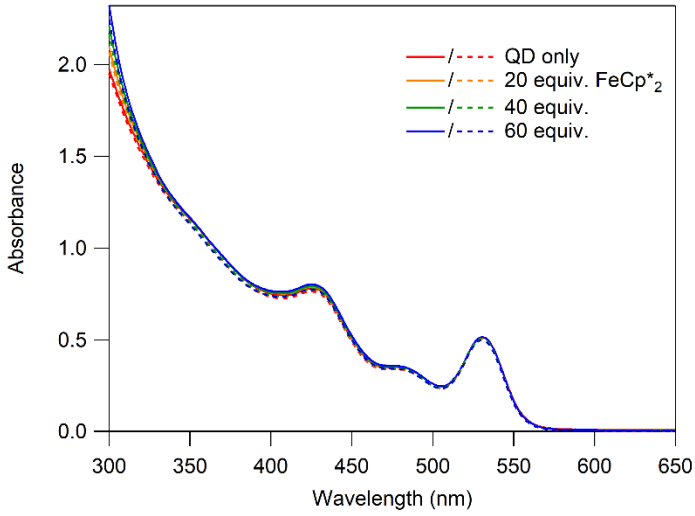

Figure 5.8 Absorbance spectra of CdSe QDs (2.8 nm, 3 µM) with addition of excess $FeCp^*_2$ in toluene. Solid/dotted lines indicate before/after photoluminescence measurements to gauge photostability.

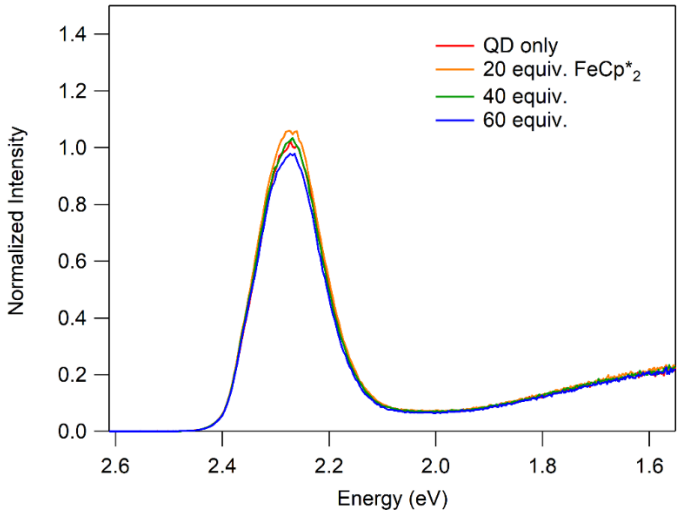

Figure 5.9 Emission spectra of CdSe QDs (2.8 nm, 3 µM) with addition of excess $FeCp^*_2$ in toluene. An excitation wavelength of 531 nm was used with a 515 nm long-pass filter.

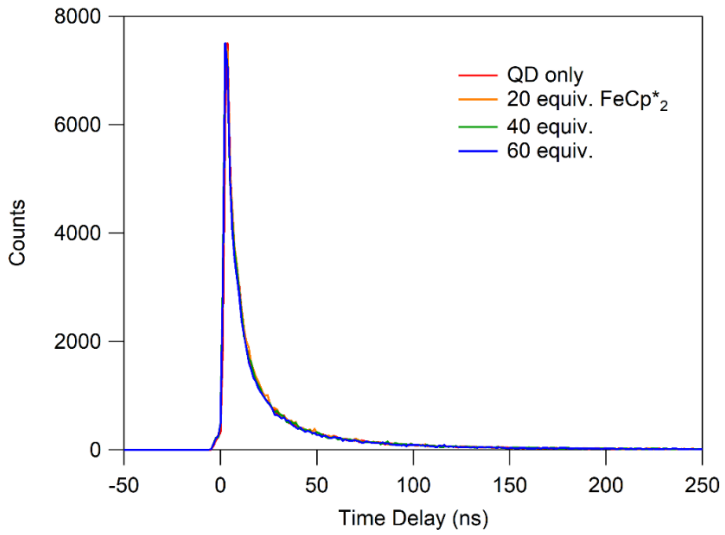

Figure 5.10 Time-resolved emission spectra of CdSe QDs (2.8 nm, 3 µM) with addition of excess $FeCp^*_2$ in toluene. A 485 nm LED excitation source was used with a 515 nm long-pass filter, 4096 channels, and 50 µs pulse going to 7500 counts. A detection wavelength of 545 nm was selected.

Cobaltocene ($CoCp_2$).

A more potent reducing agent, $CoCp_2$ ($E^{o\prime}$= −1.3 V vs $Fc^{+/0}$), was next probed for reactivity with CdSe QDs. UV-Vis absorption spectra reveal no significant changes upon addition of excess $CoCp_2$ to CdSe QDs, with only an increase in absorption due to added $CoCp_2$ that overlaps with the shoulder of QD absorbance (Figure 5.11). Emission spectra of the QDs (Figure 5.12– Figure 5.13) reveal a suppression of emission, indicating effective quenching of the VB hole by $CoCp_2$ upon QD photoexcitation. Although $CoCp_2$ successfully engages in photoinduced ET with CdSe QDs, this particular reagent was ultimately abandoned because of significant optical overlap of $CoCp_2$ and $CoCp_2^+$ with the CdSe QD absorbance features. However, these studies illustrated the viability of a moderately reducing reagent for photoinduced ET studies with CdSe QDs.

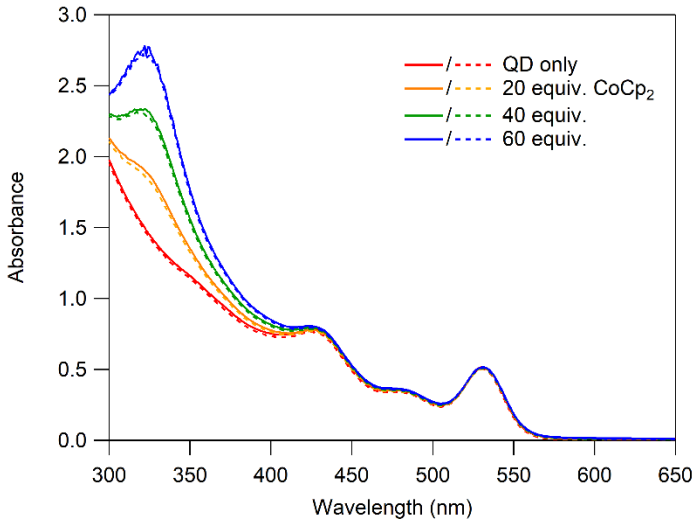

Figure 5.11 Absorbance spectra of CdSe QDs (2.8 nm, 3 µM) with addition of excess $CoCp_2$ in toluene. Solid/dotted lines indicate before/after photoluminescence measurements to gauge photostability.

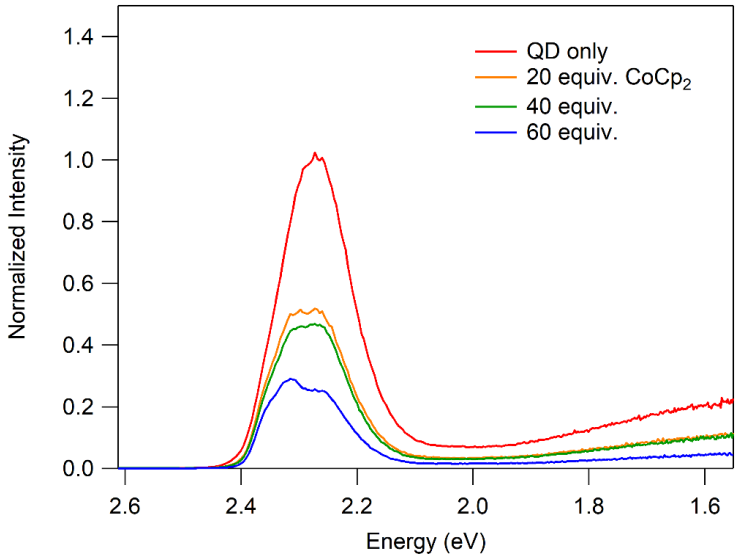

Figure 5.12 Emission spectra of CdSe QDs (2.8 nm, 3 µM) with addition of excess $CoCp_2$ in toluene. An excitation wavelength of 531 nm was used with a 515 nm long-pass filter. As emission from the QDs decreases, there are two apparent features due to solvent scatter overlapping with the emission feature.

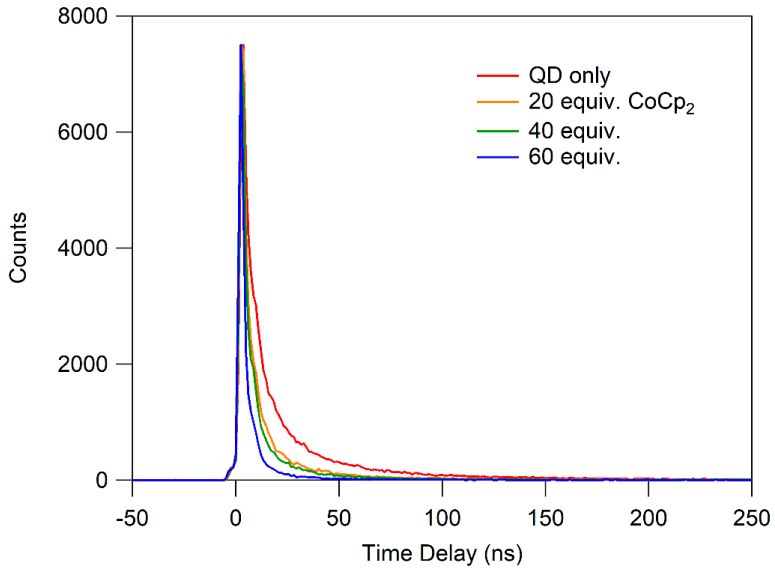

Figure 5.13 Time-resolved emission spectra of CdSe QDs (2.8 nm, 3 µM) with addition of excess $CoCp_2$ in toluene. A 485 nm LED excitation source was used with a 515 nm long-pass filter, 4096 channels, and 50 µs pulse going to 7500 counts. A detection wavelength of 545 nm was selected.

1,2-bis(diphenylphosphino)ethane cyclopentadienyl cobalt (I) (CoCp(dppe)).

Next, a moderate reducing Co reagent, CoCp(dppe), was studied for compatibility with CdSe QDs. No significant ground state reactivity is observed by UV-Vis absorbance spectroscopy (Figure 5.14). While some emission quenching is observed (Figure 5.15 – Figure 5.16), the complete overlap of absorbance of the CoCp(dppe) with the CdSe absorbance features (Figure 5.14) is undesirable for use in photoinduced ET studies as it makes it difficult to monitor changes in the optical handles of either the CoCp(dppe) or CdSe reagents upon reduction or oxidation.

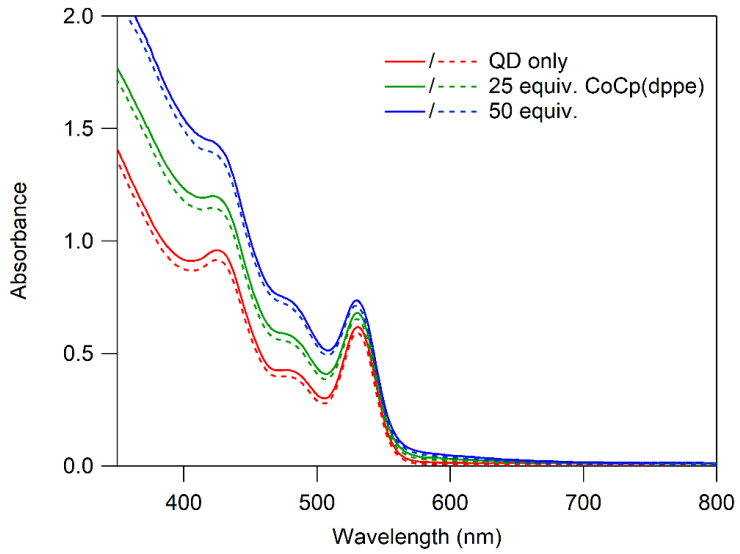

Figure 5.14 UV-Vis absorption spectra of CdSe QDs (2.8 nm, 3.6 µM) with addition of excess CoCp(dppe) in toluene. Dashed lines indicate after PL experiment/irradiation to check for photodegradation.

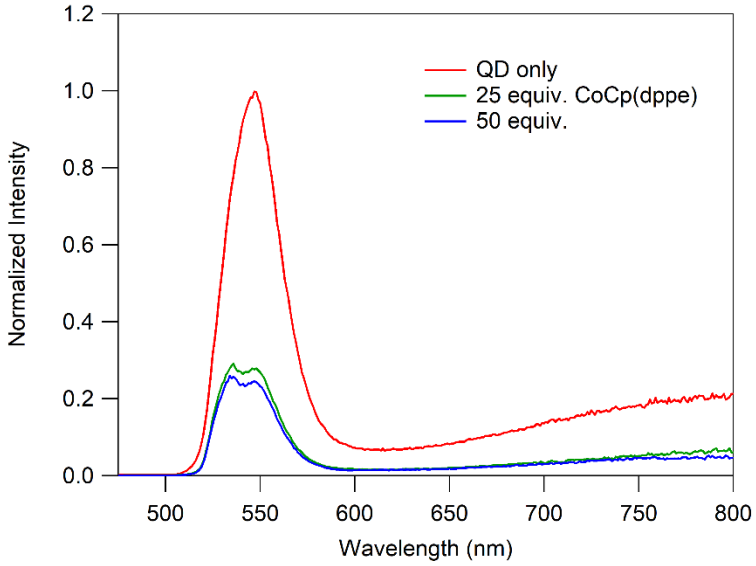

Figure 5.15 Emission spectra of CdSe QDs (2.8 nm, 3.6 µM) with addition of excess CoCp(dppe) in toluene. An excitation wavelength of 531 nm was used with a 515 nm long-pass filter. As emission from the QDs decreases, there are two apparent features due to solvent scatter overlapping with the emission feature.

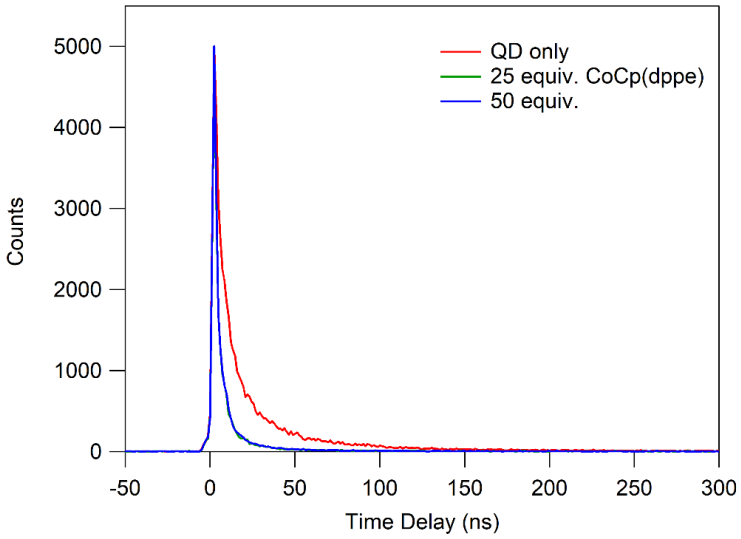

Figure 5.16 Time-resolved emission spectra of CdSe QDs (2.8 nm, 3.6 µM) with addition of excess CoCp(dppe) in toluene. A 485 nm LED excitation source was used with a 515 nm long-pass filter, 4096 channels, and 5000 counts. A detection wavelength of 545 nm was selected.

1,2-bis(diphenylphosphino)benzene cyclopentadienyl cobalt (I) (CoCp(dppbz)).

In order to try and circumvent the overlap of absorbance handles limiting the use of CoCp(dppe), an analogous complex with a benzene ring incorporated into the diphosphine ligand, CoCp(dppbz), was prepared. The purified and isolated complex showed a red-shifted absorbance compared with CoCp(dppe) (Figure 5.17). This red-shifted absorbance was expected to be advantageous when used with small CdSe QDs because of decreased overlap with QD absorption features, making it easier to monitor oxidation of the reductant via optical signatures.

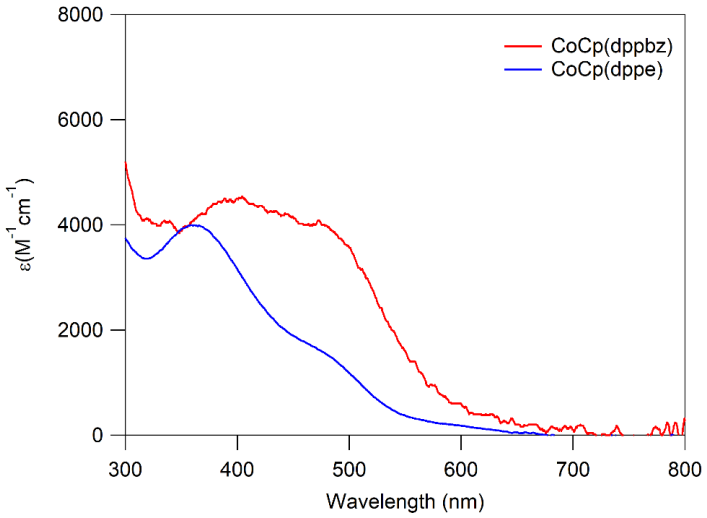

Figure 5.17 UV-Vis absorption spectrum comparing the molar absorptivity of CoCp(dppbz) with CoCp(dppe) in benzene.

The CoCp(dppbz) complex was then titrated into a sample of CdSe QDs to assess whether it can fill the valence band hole of photoexcited QDs. The QDs did not show any ground state reactivity with the CoCp(dppbz) as the UV-Vis absorption spectra simply showed an overlay of the absorbance of the QDs and the complex (Figure 5.18). Reactivity upon irradiating the QDs was assessed by both steady-state and time-resolved emission spectroscopy and summarized in Figure 5.19. Surprisingly, the added CoCp(dppbz) led to no change in the emission lifetime of the CdSe QDs even though significant quenching of the stead-state emission was observed. This suggests a more complex interfacial ET mechanism or static quenching component, which was ultimately undesirable for this project.

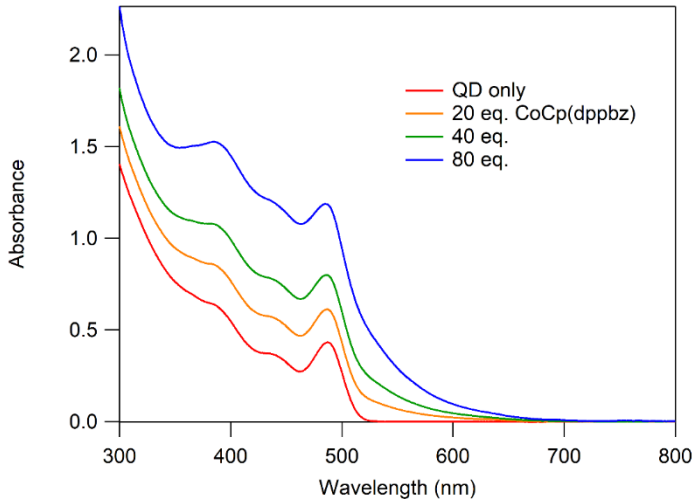

Figure 5.18 UV-Vis absorption spectra of CdSe QDs (2.3 nm, 2.7 µM) with added CoCp(dppbz) in 0.1 M $[Bu_4N][BF_4]$ in 10:1 toluene:acetonitrile.

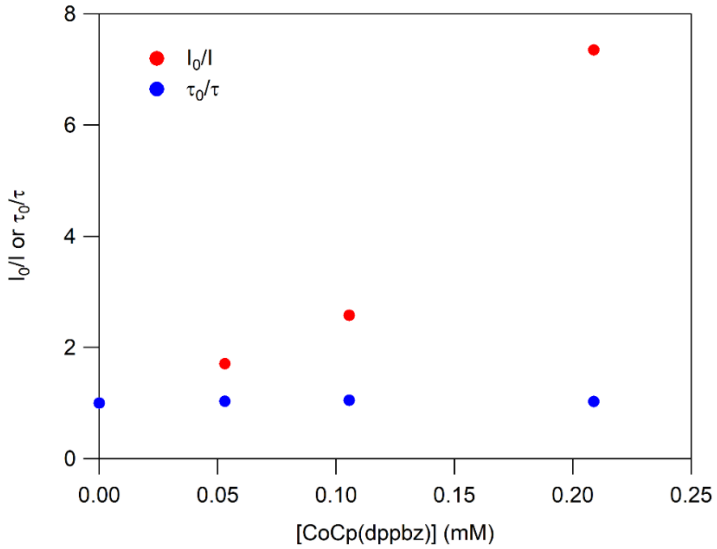

Figure 5.19 Stern-Volmer plot of CoCp(dppbz) with CdSe QD (2.3 nm, 2.7 µM) in 0.1 M $[Bu_4N][BF_4]$ in 10:1 toluene:acetonitrile. For SS-PL used excitation wavelength of 488 nm with 495 nm long-pass filter. A 485 nm LED excitation source was used to collect lifetime data with 4096 channels, 2 µs pulse, and 5000 counts. A detection wavelength was 507 nm was selected for emission lifetime measurements.

After evaluating the first set of reductants with CdSe QDs, we next turned our attention to studying a wider band gap QD material that would more easily have its VB hole filled by mild reducing reagents and likely have less absorbance feature overlap with molecular partners that absorb in the visible

range: cadmium sulfide (CdS).[8] Therefore, the next QD material investigated was small oleate-capped CdS QDs (3.6 nm diameter).

Decamethylferrocene ($FeCp^*_2$).

The reactivity of $FeCp^*_2$ with CdS QDs was first assessed by UV-Vis absorbance spectroscopy and showed no change in the optical handles of the QDs with up to 80 eq. $FeCp^*_2$ added **(**Figure 5.20). Surprisingly, no quenching was observed in steady-state (Figure 5.21) or time-resolved (Figure 5.22**)** emission spectroscopy, indicating that perhaps the VB edge potentials and reduction potential of the $FeCp^*_2$ are not favorably aligned to reduce the photogenerated VB hole. It has also been shown that charge transfer can be better achieved between QDs and ferrocene derivatives by covalently anchoring the molecules to the QD surface (e.g., via a carboxylic acid, thiol or amino linker) due to improved orbital overlap (coupling).[6,12] This approach could be taken in future works to increase the likelihood of interfacial charge transfer with ferrocene-derived hole quenchers; however, it is important to keep in mind that the rate of back electron transfer will also likely increase with covalently anchored donors.

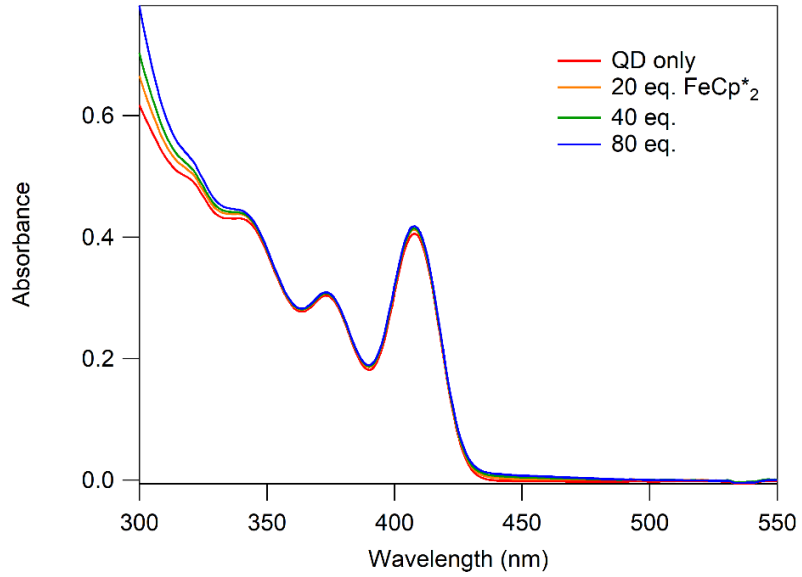

Figure 5.20 UV-Vis absorption spectra of CdS QDs (3.6 nm, 1 µM) with addition of excess $FeCp^*_2$ in 0.05 M $[Bu_4N][BF_4]$ in 10:1 toluene:acetonitrile.

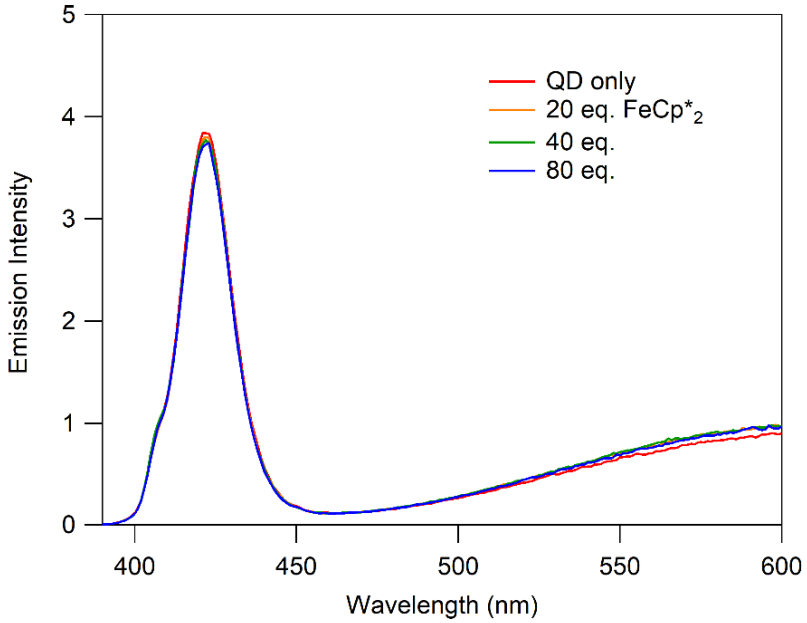

Figure 5.21 Emission spectra of CdS QDs (3.6 nm, 1 µM) with addition of excess $FeCp^*_2$ in 0.05 M $[Bu_4N][BF_4]$ in 10:1 toluene:acetonitrile. An excitation wavelength of 407 nm was used.

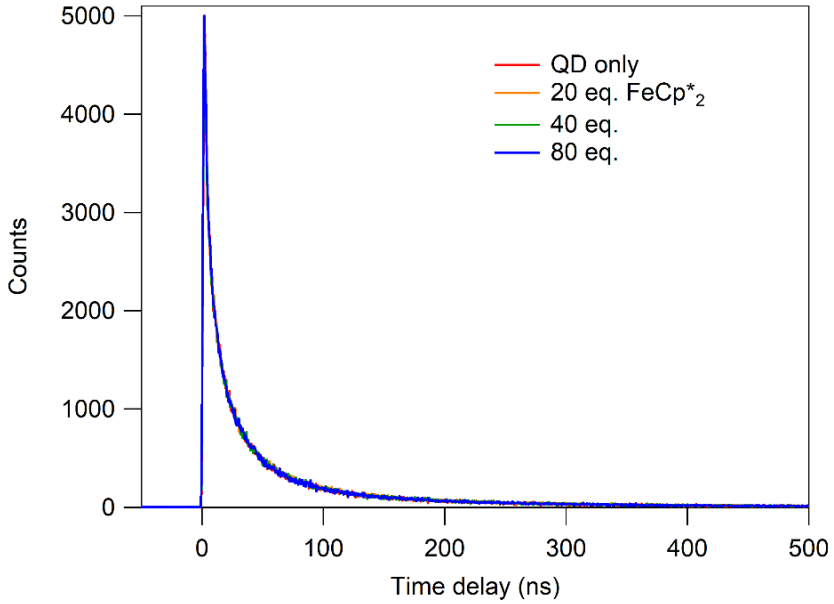

Figure 5.22 Time-resolved emission spectra of CdS QDs (3.6 nm, 1 µM) with addition of excess $FeCp^*_2$ in 0.05 M $[Bu_4N][BF_4]$ in 10:1 toluene:acetonitrile. An excitation wavelength of 369 nm was used with TCSPC setup using a 2 µs pulse, 4096 channels and 5000 counts. A detection wavelength of 422 nm was selected for TCSPC measurements.

Tris(bipyridine) chromium (II) ($Cr(bpy)_3^{2+}$).

To move to a slightly stronger but still mild reducing agent, we next targeted $Cr(bpy)_3^{2+}$. This complex is a deep purple color and turns yellow upon oxidation, resulting in strong optical handles that may be monitored for evidence of charge transfer with QDs (Figure 5.23).[13] In the photoinduced ET studies below, the BArF salt analogue of $Cr(bpy)_3^{2+}$ was used to improve solubility in nonpolar solvents.

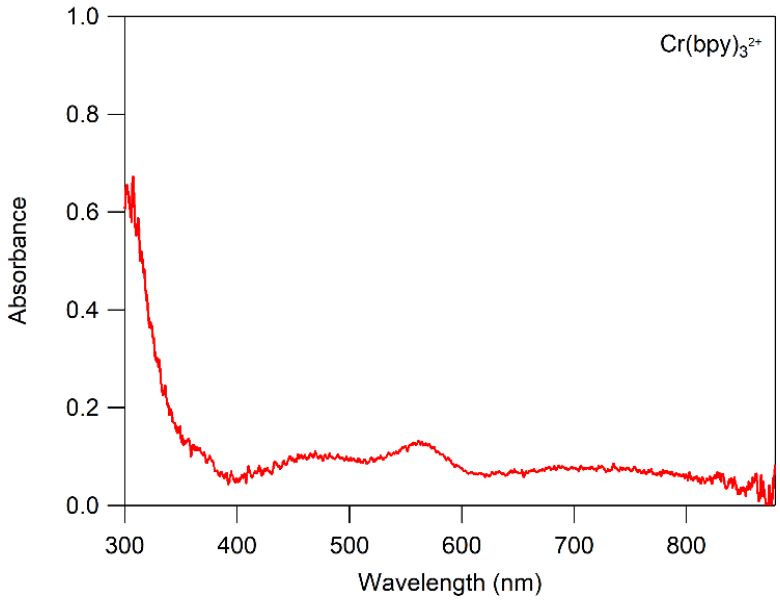

Figure 5.23 UV-Vis absorption spectrum of $[Cr(bpy)_3][BF_4]_2$ in acetonitrile.

UV-Vis absorption spectra of CdS QDs in the presence of excess $Cr(bpy)_3^{2+}$ reflect a clean overlay of the spectral handles of each individual species, indicating no ground-state reactivity (Figure 5.24). While the steady-state emission shows significant quenching in the presence of $Cr(bpy)_3^{2+}$ (Figure 5.25), the time-resolved emission data show a surprising lack of change in lifetime (Figure 5.26). This discrepancy suggests that the emission quenching of the CdS QDs occurs by a static quenching mechanism. Overall, this is unfavorable for studying photoinduced ET because it may lead to geminate recombination of charges before cage escape, limiting our ability to measure CT rates.

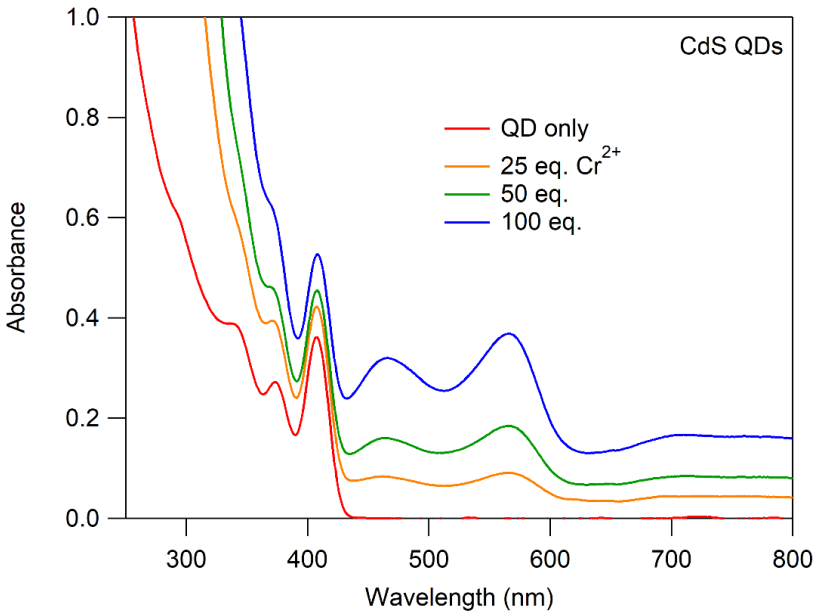

Figure 5.24 UV-Vis absorption spectra of CdS QDs (3.6 nm, 1 µM) with addition of excess $Cr(bpy)_3^{2+}$ in 0.1 M $[Bu_4N][PF_6]$ in dichloromethane.

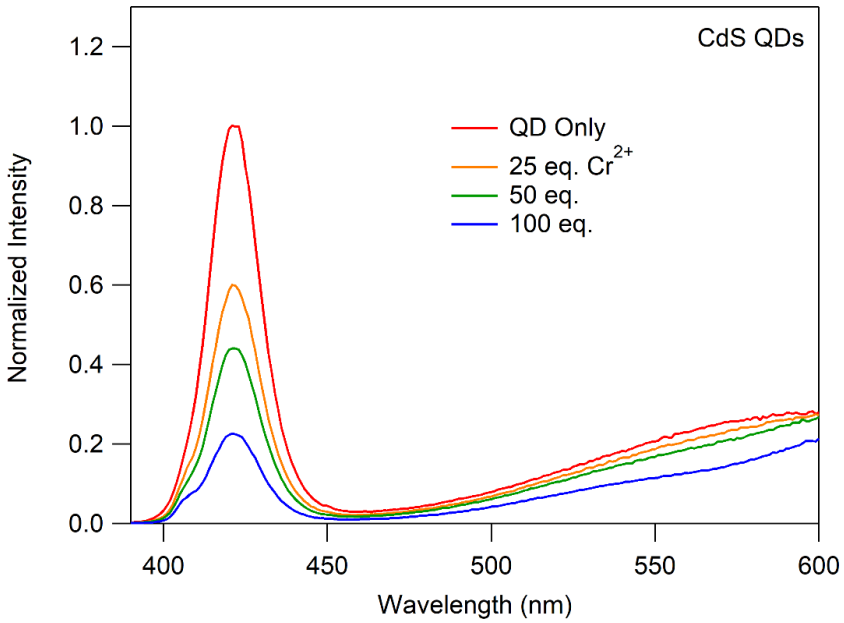

Figure 5.25 Emission spectra of CdS QDs (3.6 nm, 1 µM) with addition of excess $Cr(bpy)_3^{2+}$ in 0.1 M $[Bu_4N][PF_6]$ in dichloromethane. An excitation wavelength of 407 nm was used.

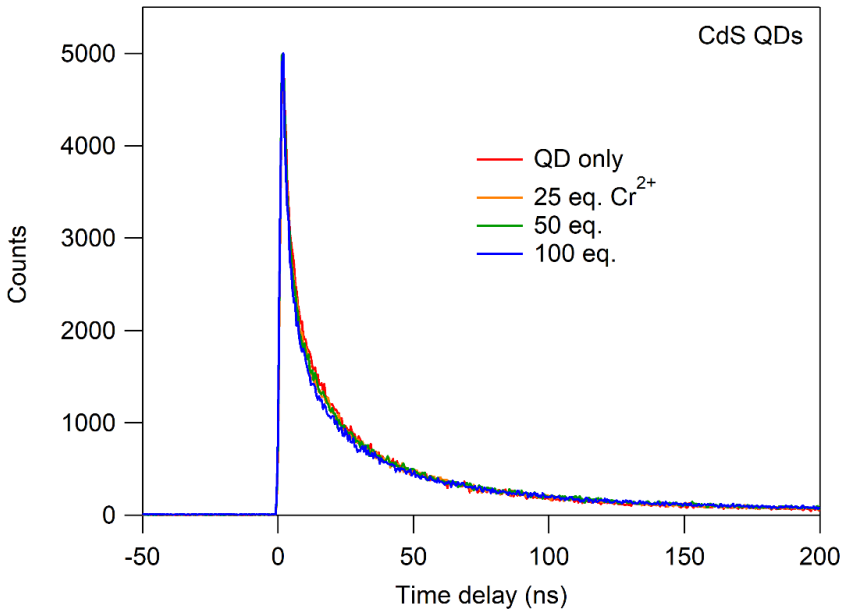

Figure 5.26 Time-resolved emission spectra of CdS QDs (3.6 nm, 1 µM) with addition of excess $Cr(bpy)_3^{2+}$ in 0.1 M $[Bu_4N][PF_6]$ in dichloromethane. An excitation wavelength of 369 nm was used with TCSPC with 2 µs pulse, 4096 channels, and 5000 counts. A detection wavelength of 422 nm was selected for TCSPC measurements.

Overall, these preliminary studies identified several inherent challenges with the design of system 1. Namely, difficulties with identifying compatible molecular donors arose from difficulty in identifying reagents that 1) do not have optical handles that overlap with CdSe QD absorbance or emission features; 2) do not engage in a static quenching mechanism or limit cage escape of charged species; and 3) limit recombination pathways via reversible CT with the QD to enable observation of charged species in solution. The results described above are summarized in Table 5.1.

Table 5.1 Reagents assessed in System 1 design and outcomes of studies

QD Material (diameter)	Molecular Redox Agent	$E^{\circ\prime}$ (V vs. $Fc^{+/0}$) of Molecular Redox Agent	Limitations of System Components	Reduction Potential Source
CdSe (2.8 nm)	$CoCp_2$	−1.33	Optical handles overlap substantially with QD absorbance and cannot distinguish; $CoCp_2^+$ absorbance feature at ca. 330 nm too blue to probe by time-resolved spectroscopy	[14]
CdSe (3.1 nm)	$Cr(C_6H_6)_2$	−1.22	Lack of color difference between Cr^0 and Cr^+ species limits success of this system	Measured by cyclic voltammetry
CdSe (2.8 nm)	CoCp(dppe)	−0.93	Optical handles overlap substantially with QD absorbance and cannot distinguish	[15]
CdSe (2.3 nm)	CoCp(dppbz)	Not determined	Static quenching observed, suggesting possible interaction with QD surface	-
CdSe (2.8 nm)	$FeCp^*_2$	−0.48	No emission quenching observed	[14]
CdS (3.6 nm)	$Cr(bpy)_3^{2+}$	−0.63	Static quenching observed, suggesting possible interaction with QD surface	Measured by cyclic voltammetry by labmate Dr. Chris Lennox
CdS (3.6 nm)	$FeCp^*_2$	−0.48	No emission quenching observed	[14]

5.2.2 System 2.

Given the challenges in identifying compatible system components for a strategy based on System 1, we revised the design criteria and developed a new plan for probing the Marcus Inverted Region in QD charge transfer. First, we sought to design a system in which VB hole quenching would be faster than interfacial ET and, if possible, irreversible in order to limit charge recombination. Second, we need a system in which we can differentiate clearly between the QD and molecular reagent optical handles. Third, it is critical to have firmly established photochemistry (or lack thereof) between different system components. The proposed system design to meet these criteria is depicted in Scheme 5.2.

Scheme 5.2 System to generate QD^- by first photoexciting the QD, then using some sacrificial donor (D) and monitoring k_{ET} to some acceptor molecule, shown here as methyl viologen (MV^{2+}).

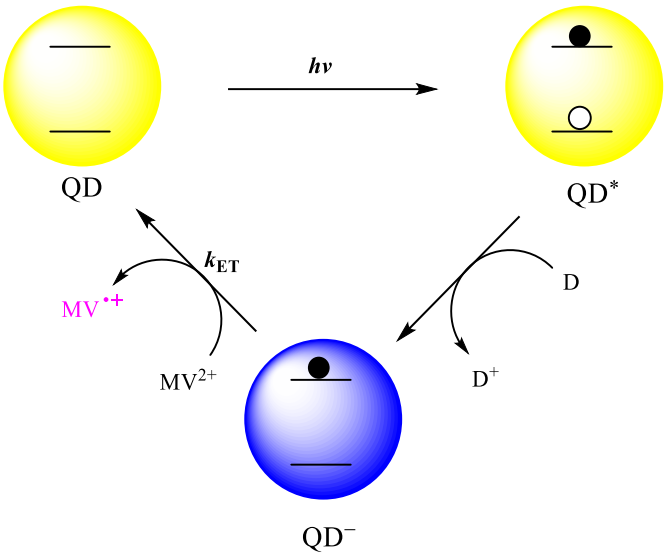

In this revised system, ZnO was pursued as the QD material. ZnO was selected because it is a wide band gap material; as ZnO absorbs in the UV it is unlikely to overlap with spectral handles of molecular acceptors in the visible range. Furthermore, ZnO QDs have been shown to be prone to the Auger-assisted mechanism in photoinduced charge transfer systems.[7] Conveniently, a wide range of molecular reagents have been reported to irreversibly fill the VB holes of photoexcited ZnO nanocrystals and were considered for use in this system. These are summarized in Table 5.2.

Table 5.2 Hole quenchers considered for System 2

Hole Quencher	Notes	Reference
Ethanol	Established to quench VB hole within 15 ps, well studied across many systems and ZnO particle sizes	[16–18]
Lithium triethylborohydride	Established to quench VB hole very effectively in ZnO, but reportedly forms Zn^0 and may degrade QDs with this undesirable side chemistry	[18]
Amines	Widely used sacrificial electron donors. However, amines are known to strip Z-type ligands and etch QDs. While these could be effective hole quenchers, this side reactivity should be avoided if possible	[19]
Mercaptopropionic acid ligand	Harder to control the amount of hole quencher present if the hole quencher is the ligand; More widely used in CdE (E = Se, S) QDs	[8,20]

In considering viable molecular acceptor candidates, methyl viologen (MV^{2+}, $E^{\circ\prime} = -0.82$ V vs. $Fc^{+/0}$) was attractive due to its strong optical handles in the visible region upon accepting an electron to form $MV^{\cdot+}$.[21] By varying similarly structured acceptor molecules of varying reduction potentials such as benzyl viologen ($E^{\circ\prime} = -0.74$ V vs. $Fc^{+/0}$) or *N*,*N*'-propylene-1,10-phenanthrolinium ($E^{\circ\prime} = -0.51$ V vs. $Fc^{+/0}$), we may be able to more easily compare rates of ET and driving force between systems.[20,22,23] Additionally, MV^{2+} has been shown to be a compatible electron acceptor from photoexcited small ZnO QDs (radius = 1.7 – 2.65 nm).[24] If preliminary studies with MV^{2+} are not successful, benzoquinones are another class of molecular acceptors that could be similarly promising for this system.[25]

Towards this end, ZnO nanoparticles of approximately 3.4 nm diameter were synthesized and capped with dodecylamine ligands using a modified literature procedure (see **Experimental Section**). Nanoparticle diameter was determined by established empirical relationships between absorbance spectrum and particle size.[26] The ZnO QDs display an absorbance feature at 328 nm and a strong emission feature at 552 nm (Figure 5.27). Emission in the visible and a large Stokes shift is common in ZnO QDs and indicative of trap emission via recombination of the CB electron with a surface-trapped hole.[16] The radiative lifetime of the visible PL was determined to be a biexponential function with components of approximately 890 ns and 30 ns, in reasonable agreement with previously reported systems (Figure 5.28).[16]

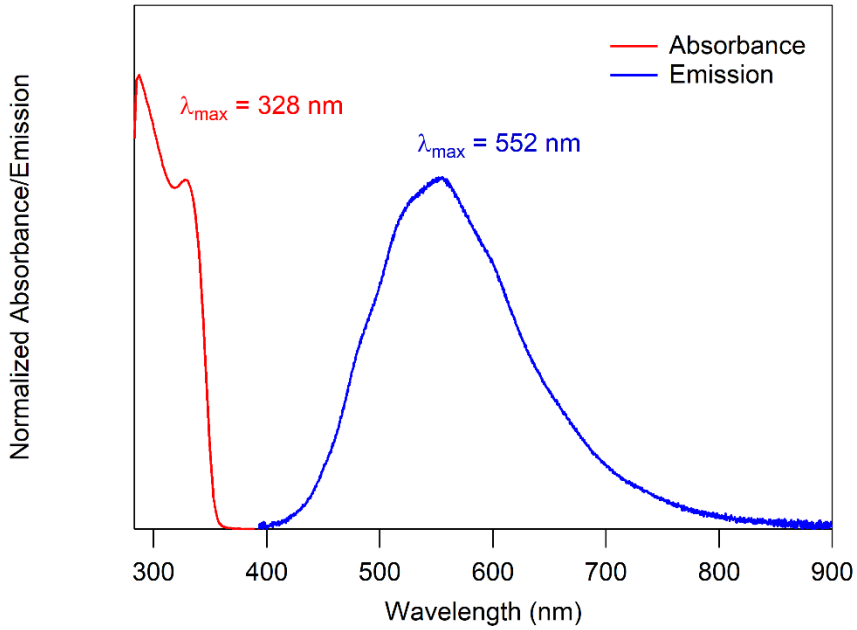

Figure 5.27 Normalized absorbance and emission spectra of 5 µM ZnO nanocrystals in toluene. Steady-state emission data collected using an LED excitation wavelength of 365 nm.

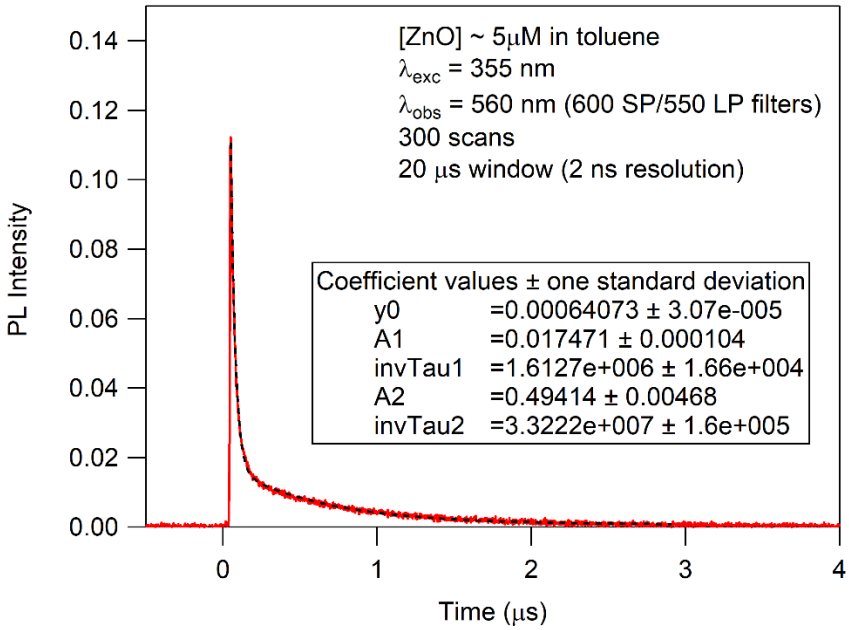

Figure 5.28 Time-resolved photoluminescence data of 5 µM ZnO nanocrystals in toluene. Data was collected using an excitation wavelength of 355 nm. A detection wavelength of 560 nm was employed.

Preliminary studies were conducted with ZnO NCs and ethanol, to confirm valence band hole filling upon photoexcitation of the NCs and establish how long it takes to generate QD^- using our setup. For these studies, a ca. 2 µM solution of ZnO NCs was prepared in a nitrogen-filled glovebox in 1:1 THF:toluene and an excess of ethanol (0.8 – 1.4 M) of ethanol added into a sealed gas-tight Kontes-adapted cuvette. Outside of the glovebox, the sample was irradiated with UV light and changes in the NC absorbance and emission spectra tracked over the course of several hours. Consistent with literature reports that employ irradiation times of 45 min to 4 hours,[16,18] after approximately 1 hour we observe a significant bleach of the excitonic absorption feature (Figure 5.29). The absorbance bleach appears to be complete after an hour as there are no major changes even with two more hours of irradiation. Concurrently, a loss of visible trap-related emission is observed (Figure 5.30). These optical changes are consistent with formation of photodoped QD^-; upon accumulation of electrons in the band edge state, the probability of excitation into that already filled state is lowered, resulting in the bleach of the excitonic absorbance feature.[18] Similarly, visible photoluminescence is quenched due to available nonradiative Auger recombination pathways with excess conduction band electrons present.[16]

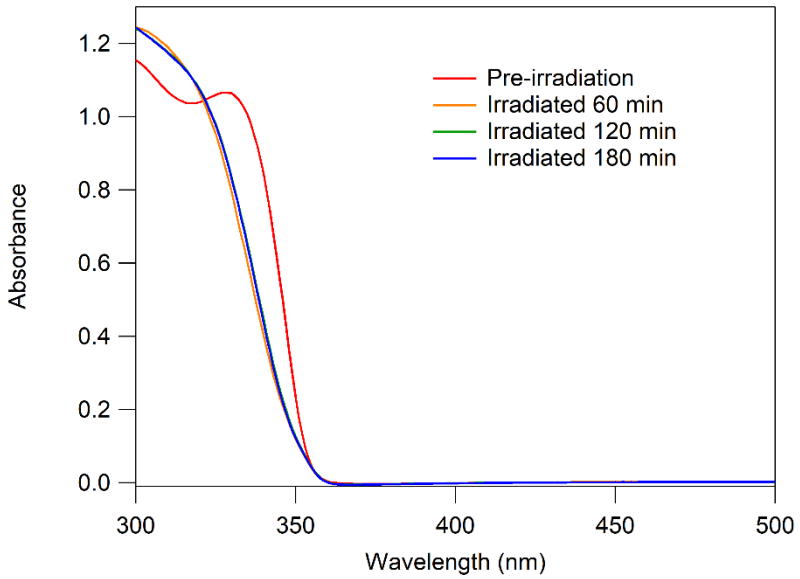

Figure 5.29 UV-Vis absorbance spectra of ZnO nanocrystals (1.9 µM) in 1:1 THF:toluene with 5 mmol (77 x 10^4 equiv/NC) of ethanol with irradiation for 1 – 3 hours.

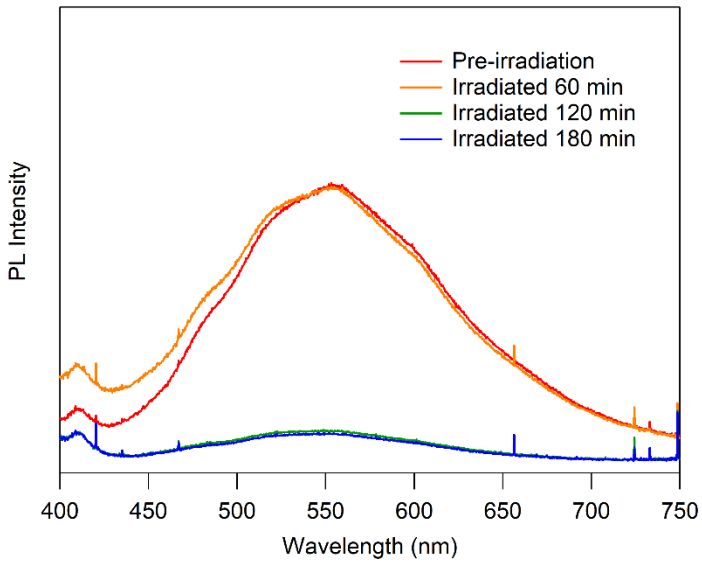

Figure 5.30 Photoluminescence spectra of ZnO nanocrystals (1.9 µM) in 1:1 THF:toluene with 5 mmol (77 x 10^4 equiv/NC) of ethanol with irradiation for 1 – 3 hours. An excitation wavelength of 365 nm was used.

Preliminary studies probing evidence of photoinduced ET with a molecular acceptor, methyl viologen (MV^{2+}), with the reduced ZnO QDs were subsequently performed. UV-Vis absorption studies of ZnO QDs with excess methyl viologen and ethanol show the expected excitonic bleach following

irradiation at 369 nm for 30 minutes from filling of the VB hole by ethanol (Figure 5.31). However, unexpectedly the presence of a small amount of the reduced $MV^{\cdot+}$ radical cation was detected in the sample with the ZnO QDs prior to irradiation (Figure 5.31 inset). Following irradiation, the spectral handles of the $MV^{\cdot+}$ radical cation disappeared and absorbance features of an unknown impurity appeared. As such, it was clear that persisting photoactive impurities limited these preliminary experiments despite multiple recrystallizations of the methyl viologen. Looking forward, repeated rigorous purification steps may be required to achieve reliable data with the ZnO QDs system.

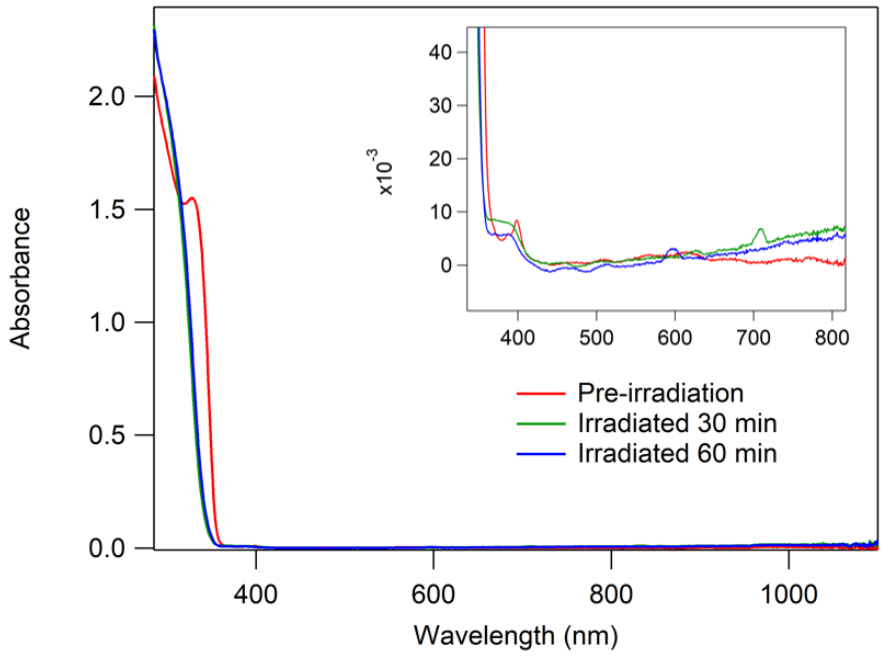

Figure 5.31 UV-Vis absorption spectra of ca. 2.3 µM ZnO QDs in 1:1 THF:toluene with 0.8 M ethanol and excess methyl viologen prior to irradiation, and then after irradiation at 369 nm for 30 minutes. Inset: Zoom-in on region showing the expected spectral handles of $MV^{\cdot+}$ radical cation at 398 nm and ca. 620 nm in the pre-irradiation trace, as well as the observation of an unknown impurity at 382 nm following irradiation.

5.3 Conclusions and Outlook

In conclusion, approaches towards designing and experimental system to probe the Marcus Inverted region in photoinduced ET from QDs to molecular acceptors were explored. First, a wide range of outer-sphere reductants and QD materials (CdE, E = Se, S) were screened for compatibility and

evidence of charge transfer. Limitations of these materials and reagents were discussed after evaluating preliminary optical studies with UV-Vis absorbance and photoluminescence spectroscopies. Subsequently we designed a revised system employing a wider band gap material, ZnO. Stable ZnO NCs capped were prepared and ethanol confirmed to function as an effective and irreversible valence band hole quencher upon NC photoexcitation. This work provides the basis for future research that will probe whether, by eliminating the Auger-assisted charge transfer mechanism, the inverted region can be observed in charge transfer from QDs to molecular acceptors.

Moving forward in this project, there are several considerations to keep in mind regarding system design and experimental setup. In regards to system design, it is of interest to eventually expand the driving force ($-\Delta G°$) range in order to adequately probe the existence of the inverted region. Therefore, driving force can be varied by preparing a range of ZnO QD sizes to vary the band edge potentials; it is important to keep in mind, however, the small Bohr radius of ZnO (2.87 nm) which limits the size of nanocrystals that experience quantum confinement in this material.[7] Alternatively, one could expand the library of molecular acceptors used to vary the reduction potential of the molecular acceptors. Depending on solubility and compatibility, it may be necessary to vary the ZnO capping ligands and solvent combinations to achieve a wider driving force range.

There are also important factors to consider in the experimental setup for measuring the rate of charge transfer from ZnO QDs to molecular acceptors. We anticipate that hole trapping and ET will occur on the picosecond timescale; therefore, it will be necessary to use the Dempsey laboratory ultrafast table setup (not fully operational at the time this was written). In these time-resolved spectroscopy studies, it will be of interest to carefully adjust the laser power to try to achieve only one exciton per QD prior to ET in order to avoid further complications from Auger-related processes.[24] Finally, a combination of UV-Vis absorbance spectroscopy and NMR spectroscopy should be employed to ensure that there is no unexpected ground-state reactivity.[20]

5.4 Experimental Details

Synthesis and Purification of CdSe QDs. Batches of CdSe quantum dots were synthesized as previously reported by a heat-up method adding Se powder to a $Cd(oleate)_2$ solution in 1-octadecene.[27,28] Specific sizes were targeted by adjusting the solution temperature and amount of time the QDs were allowed to grow before stopping the reaction by cooling the solution to RT. QDs were then purified by repeated precipitation and centrifugation steps to isolate the QDs from unreacted starting material and excess solvent as previously reported with minor variations.[27,28] QD sizes were determined by the empirical relationship between QD diameter and the energy of the excitonic absorption feature.[29]

Synthesis of CdS QDs. The CdS quantum dots were synthesized following literature procedure.[30] CdO (361 mg, 2.81 mmol), oleic acid (4.4 mL, 13.9 mmol), and 1-octadecene were combined in a 3-neck round bottom flask with stir bar and stirred under vacuum for 15-20 minutes at room temperature to degas. The solution was then heated to ~100 ℃ under vacuum and then heated under nitrogen further to 200 ℃. To remove excess steam that built up during the reaction, the flask was cooled back down to 100 ℃ and alternated between nitrogen and vacuum for 10 minutes. The flask was then returned to nitrogen and heated to 260 ℃. Over the course of 1 hour, the solution changed from a heterogeneous red mixture to clear and colorless. The temperature was again lowered to 100 ℃ and cycled between vacuum and N_2 to remove excess water. Meanwhile, a solution of sulfur powder in 8 mL octadecene were added to a two-neck pear-shaped flask and stirred under vacuum, cycling with nitrogen three times. The solution was then placed under nitrogen flow and heated in an oil bath to 120 ℃ to incorporate the sulfur powder into solution. The sulfur mixture stirred at that temperature under nitrogen for 2 hours. The flask with $Cd(oleate)_2$ was adjusted to a temperature of 246 ℃ under N_2. A 10 mL glass syringe with long luer-lock needle was degassed five times before drawing up the sulfur solution and injecting into the $Cd(oleate)_2$. Upon injection, the solution went from colorless to light yellow to darker yellow over the course of 10 seconds. The solution grew at 222 ℃ for 2 minutes. After 2 minutes the heating mantle was removed, the

flask placed in a RT water bath and 4 mL ODE at RT injected. After cooling to 50 ℃ the flask was opened to air and the solution placed in a 50 mL centrifuge tube with 15 mL acetone and left overnight.

Purification of CdS QDs. The CdS QDs were purified according to a modified literature procedure.[30] The crude reaction mixture was divided among six centrifuge tubes (7.5 mL/tube) and 5 mL acetone added. These were mixed by pipette and centrifuged for 10 min at 9000 rpm. This first centrifugation step yielded a yellow pellet and clear supernatant. The supernatant was discarded. 13 mL acetone were added to the yellow pellet and these were mixed by pipette and sonicated, leaving a white pulp-like precipitate and yellow tinted pellet, and these were centrifuged. The clear supernatant resulting was decanted off and left a yellow and white precipitate. 10 mL toluene was added to each tube in an effort to dissolve the QDs and separate from the white precipitate. These were mixed by pipette and sat for 2 hours. This left a very viscous solution with a pulp-like solid. These were sonicated, 3 mL acetone added and then centrifuged. This yielded a white pellet with light yellow supernatant. The supernatant was decanted off and solvent removed by rotary evaporation, leaving a yellow residue. The residue was diluted in 11 mL toluene and then left for several days. The toluene solution was divided among six centrifuge tubes and 11 mL acetone added. These were mixed by pipette and then centrifuged for 10 min at 8600 rpm. This step yielded a clear supernatant and pale yellow/white precipitate. The supernatant was decanted off and the precipitate dispersed in 2 mL toluene and precipitated with 11 mL acetone. This was mixed by pipette and sonicated until well incorporated, then centrifuged. The precipitation with acetone was repeated a total of five times. The remaining precipitate was dispersed in pentane and then dried under vacuum to isolate the purified CdS QD solid.

Synthesis of ZnO Nanocrystals. ZnO nanocrystals were synthesized following literature procedure.[31] Initial synthesis attempts resulted in unstable ZnO solid, and the synthetic approach was modified following an informal discussion with Prof. Murielle Delley in Fall 2020 (University of Basel, Switzerland). The following advice was given at this informal chat:

(1) Use fresh bottles of DMSO and ethanol (water buildup in solvent is problematic)

(2) Use ethyl acetate as antisolvent for purification, it works better than heptane

(3) Do dodecylamine capping on the same day as the synthesis

(4) Do not let ZnO pellets dry in between steps! Keep them in solution and remove solvent immediately prior to capping with dodecylamine

(5) Long-term storage in air (even in lab freezer) leads to colloidal instability

Based on these discussions, ZnO nanocrystals were synthesized using the following procedure. $Zn(acetate)_2 \cdot 2H_2O$ (513.2 mg, 2.34 mmol) was added to a 125 mL Erlenmeyer flask with stir bar and dissolved in 15 mL DMSO and ~7.5 mL ethanol (200 proof, anhydrous). The solution stirred at RT to fully dissolve the solid for ca. 20 min. Meanwhile, $[Me_4N][OH] \cdot 5H_2O$ (728 mg, 4.02 mmol) was weighed out in the glovebox into a 50 mL Erlenmeyer flask. It was taken out of the glovebox and 8 mL of ethanol (200 proof, anhydrous) was added. This solution was swirled by hand to fully dissolve the solid. Both flasks were submerged in ice in a dewar to cool for 30 minutes. The base solution was added dropwise (by pipette) to the Zn solution with stirring. The solution remained clear and colorless as the base solution was added over the course of 2 minutes. **Note: If base is added too quickly to the zinc solution a white precipitate appears. This is not desirable**. The solution stirred in the ice bath for ~63 minutes. After this time, 60 mL of ethyl acetate was added to crash out the NCs (*a large excess is needed. If the NCs don't visibly precipitate, keep adding more ethyl acetate*).

Purification and Ligand Capping of ZnO Nanocrystals. **Note: Purification needs to be done on the same day as the synthesis. Do not leave the crude reaction mixing**. The crude reaction mixture was divided among 6 glass test tubes and centrifuged for 10 minutes. This gave great separation and the clear supernatant was discarded. The remaining white pellets were dissolved in 3 mL ethanol. *Getting the white solid to dissolve took a combination of aggressive pipetting and sonicating, but it should go fully back into solution (clear and colorless rather than a milky white suspension)*. 10 mL ethyl acetate was added to each tube to precipitate the QDs. This precipitated the QDs in three of the test tubes well, but the other

three did not crash out. Those three tubes were each divided in half with three new test tubes and ~7 mL ethyl acetate added to those tubes to get them to precipitate out. This worked fine, and then all 9 test tubes were centrifuged. The clear supernatant was discarded and the pellets again dissolved in 1-2 mL of ethanol, and then crashed with ~10 mL ethyl acetate. Again, there were three tubes that didn't precipitate any NCs, so those were temporarily abandoned. The precipitated NCs in the six successful tubes sat in solution for a few minutes while the dodecylamine was prepared. Dodecylamine in a 20 mL vial was heated to ~115 ℃ in an oil bath until it was molten and allowed to equilibrate at that temperature for 20-30 minutes. The tubes containing the precipitated nanocrystals were centrifuged. The supernatant was discarded and immediately after ~1 mL of molten dodecylamine added to each tube. These were mixed by aggressive pipetting to fully dissolve the white zinc oxide pellet in DDA and then combined into one test tube and allowed to rest for 5 minutes at RT. After resting, the solution was divided into two test tubes and each crashed with ~10 mL ethanol and centrifuged. This resulted in a small white pellet and a cloudy supernatant. To try to salvage any NCs in the supernatant, the supernatants from these test tubes were transferred to two new test tubes and more ethanol added to try to precipitate any remaining NCs, and then centrifuged again. The second centrifugation did not give good separation. The supernatant was discarded and all the pellets dissolved in toluene (total volume of 5-10 mL used). The toluene solution was transferred to a 100 mL round bottom flask and solvent removed by rotary evaporation. The colorless solid residue remaining was brought into the glovebox immediately afterward. The solid in the flask was dispersed in 10 mL toluene, transferred to a 20 mL vial and stored in the glovebox freezer. There were a couple of grainy bits that were not soluble but this worked well for the most part.

ICP-Mass Spectrometry to Determine Concentration of ZnO: To prepare samples for ICP-MS, the procedure by Valdez et al was followed.[32] A 100 µL aliquot of the ZnO suspension in toluene was transferred to a 20 mL vial and removed from the glovebox. In the fume hood, the solvent was allowed to evaporate over several days to leave a dry white solid. After two days, the solid sample was pyrolyzed in a box furnace for 2 hours at 500 ˚C. The pyrolyzed sample was digested in 0.5 mL of nitric acid (trace

metal grade) for several hours and then diluted to 5 mL with a 2% nitric acid solution. Samples for ICP-MS were then prepared from this 5 mL solution by serial dilution with the 2% nitric acid solution (Table 5.3). Standard solution samples were also prepared using a commercial ICP standard (10 µg/mL zinc ions) diluted in 2% nitric acid solution to have standards at [Zn] = 1 ppm, 500 ppb, 250 ppb, 100 ppb, 50 ppb, 25 ppb, 10 ppb and 5 ppb.

Table 5.3 Summary of ZnO NC samples prepared for ICP-MS analysis and results

Sample	Contents in 10 mL centrifuge tube	Concentration of Zn ions (ng/mL) determined by ICP-MS[a]
1	100 µL of 5 mL digested NC + 9.9 mL acid solution	- (too concentrated for calibration curve)
2 (1/10 of Sample 1)	1 mL of Sample 1 + 9 mL acid solution	39.463
3 (1/100 of Sample 1)	1 mL of Sample 2 + 9 mL acid solution	6.854
4 (1/500 of Sample 1)	2 mL of Sample 3 + 8 mL acid solution	3.817
5 (1/1000 of Sample 1)	1 mL of Sample 3 + 9 mL acid solution	- (too dilute for calibration curve)

a. Samples run by Dr. Marina Sokolsky, Director of UNC Nanomedicines Characterization Core Facility (NCore)

Following the approach of Mayer and coworkers,[32] we determined the approximate concentration of ZnO NCs in the stock solution as shown below through a combination of ICP-MS and insight gained about NC size from UV-Vis absorption spectroscopy.

$$[NC] = \frac{Total\ [Zn]}{\#\ Zn\ atoms/NC}$$

$$\#\ Zn\frac{atoms}{NC} = \frac{(2)(^4/_3\,\pi r^3)}{V}$$

Based on UV-Vis absorption spectroscopy, the radius (r) of the NCs was determined to be approximately 17.25 Å.[26] Given that the unit cell volume (V) of wurtzite ZnO is 47.66 Å^3, there are on average 902 Zn atoms/NC.

From dilution of Sample 2, we determine that the approximate total [Zn] in the 0.5 mL sample to be 394630 µg/L. Converting this to moles of Zn:

$$\frac{394630\ \mu g}{L} \times \frac{1\ g}{10^6\ \mu g} \times \frac{mol\ Zn}{65.4\ g} \times (500\ \times 10^{-6} L) = 3\ \times 10^{-6}\ mol\ Zn$$

Therefore,

$$\frac{3\ \times\ 10^{-6}\ mol\ Zn}{902\ Zn\frac{atoms}{NC}} = 3.3\ \times\ 10^{-9}\ mol\ NCs\ in\ 100\ mL\ aliquot$$

So, the approximate concentration of nanocrystals in the stock solution is

$$[NC] = \frac{3.3\ \times 10^{-9} mol\ NC}{100\ \mu L} = 33\ \mu M\ ZnO$$

Zinc Oxide Photodoping. Samples of ZnO nanocrystals in 1:1 toluene:THF were photodoped by irradiation for a specified amount of time in the presence of ethanol under an inert environment using a UV lamp (370 nm, Kessil lamp at 100% intensity borrowed from Alexanian lab in UNC Chemistry department). It is critical to use Kontes cuvettes under an inert atmosphere to achieve photodoping as oxygen is expected to quench accumulated conduction band electrons.[16] The setup is shown for reference

in Figure 5.32. If irradiating for long periods of time (>30 minutes), sample heating can be mitigated by moving setup into the fume hood and/or blowing with a fan.

Figure 5.32 (left) UV irradiation setup in dark cardboard box lined with aluminum foil and Kontes cuvette with sample held ~1 cm from lamp. (right) Upon turning the lamp on, visible emission of the ZnO nanocrystals is evident, indicating successful excitation with irradiation.

Synthesis of CoCp(dppbz). Synthesis was performed according to an adapted literature procedure.[15] Briefly, $CoCp(CO)_2$ (50 µL, 0.374 mmol), 1,2-bis(diphenylphosphino)benzene (151 mg, 0.338 mmol) and 5 mL toluene were combined in a 25 mL Schlenk bomb flask with a stir bar in an inert atmosphere glovebox. On a Schlenk line, the flask side arm was degassed by three cycles of alternating vacuum and nitrogen. After the final cycle the flask was opened to nitrogen and the solution heated to reflux (ca. 115 ℃). The solution refluxed with stirring under nitrogen for 2 hours. After this time, the solution was cooled to room temperature. The flask was then closed and brought back into the glovebox where solvent was removed under vacuum. The resulting product was a dark red powder with a slight hint of green precipitate (possibly some oxidized product). The complex was characterized by ^{1}H NMR (Figure 5.33).

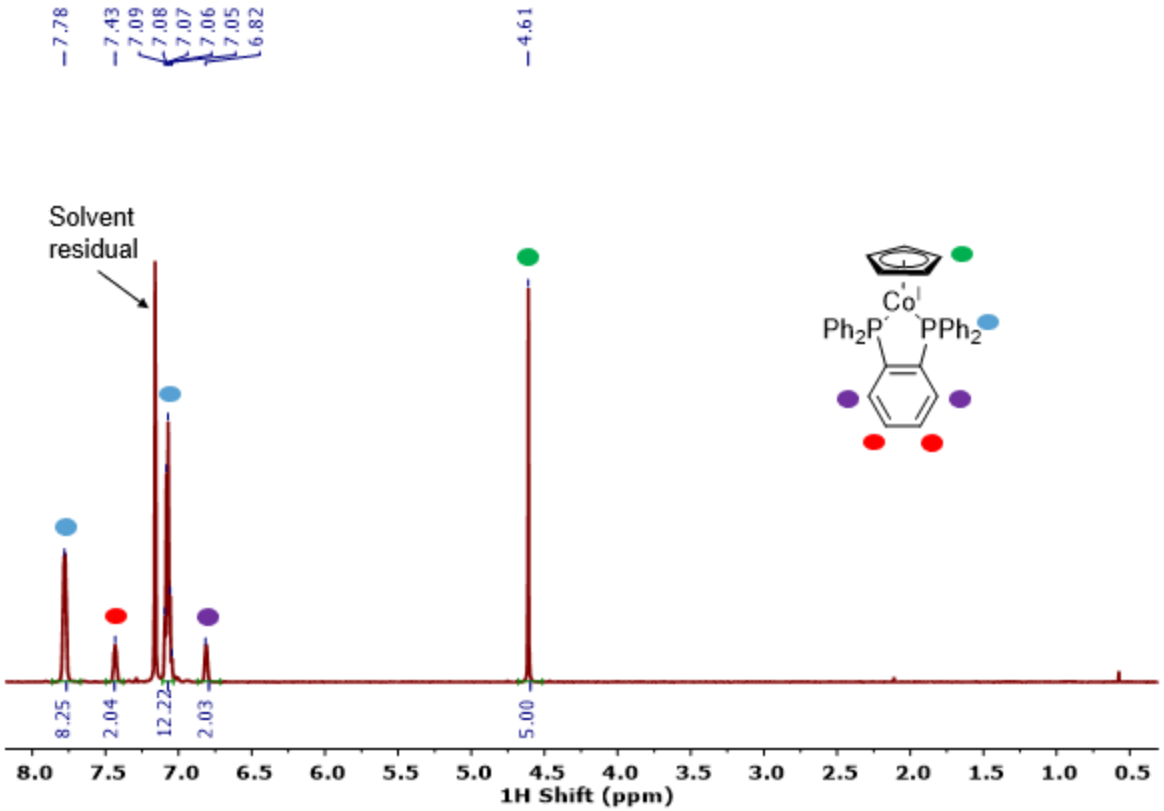

Figure 5.33 ^{1}H NMR spectrum of purified CoCp(dppbz) in benzene-d_6.

Synthesis of Cr(bpy)$_3^{2+}$. The compound was synthesized following literature procedure.[13] All synthesis steps were performed in a dry nitrogen-filled glovebox. $[Cr(CH_3CN)_4][BF_4]_2$ (80.7 mg, 0.207 mmol) in was dispersed in ~7 mL dry acetonitrile to yield a blue solution. This was added to 2,2'-bipyridyl (112 mg, 0.717 mmol), and upon addition the solution immediately turned to a dark purple color. The solution was mixed by hand for 5 minutes to ensure all reagents mixed completely. The reaction mixture was then precipitated from solution with 5x excess diethyl ether yielding a purple solid. The product was filtered over a frit and washed with a large excess of diethyl ether to remove uncoordinated 2,2'-bipyridyl (3 x 6 mL, 2 x 10 mL). The dark purple solid was collected and dried under vacuum.

Salt metathesis of $Cr(bpy)_3^{2+}$. A salt metathesis reaction was performed in order to improve solubility of $Cr(bpy)_3^{2+}$ in less polar solvents to ensure compatibility with oleate-capped QDs. The $[Cr(bpy)_3][BF_4]_2$ product (13.07 mg, 0.0188 mmol) and sodium tetrakis[3,5-bis(trifluoromethyl)phenyl]borate (Na[BArF]) (33.5 mg, 0.0378 mmol) were combined in 9 mL dry acetonitrile and stirred for 30 minutes at RT in the glovebox. The resulting mixture was then passed through a microfiber glass filter paper pipette plug and rinsed with 1 mL acetonitrile. There was a very fine white precipitate observed on the pipette (presumably $NaBF_4$ that had crashed out). The filtered acetonitrile $Cr(bpy_3)^{2+}$ solution was pumped down to remove solvent under vacuum. The solid dissolved nicely in 10 mL DCM with a good amount of a clear/white fine precipitate (excess $NaBF_4$). The solution was filtered again over a filter paper pipette plug and rinse with DCM, then solvent removed under vacuum to leave a nice crystalline solid that was fully soluble in THF. The solution was redispersed in DCM and filtered a final time to ensure that residual $NaBF_4$ was removed from solution.

Salt metathesis of MV^{2+}. Methyl viologen hexafluorophosphate ($[MV][PF_6]_2$) (51.8 mg, 0.109 mmol) and sodium tetrakis[3,5-bis(trifluoromethyl)phenyl]borate (Na[BArF]) (197 mg, 0.222 mmol) were combined in ~14 mL dry dichloromethane in a 25 mL Schlenk flask in a nitrogen-filled glovebox. The heterogeneous white suspension was allowed to stir overnight at room temperature under a nitrogen environment. The flask was then heated to reflux (45 °C) under active nitrogen flow on the Schlenk line and stirred vigorously for 1 hour. Notably, not all of the white solid suspension went fully into solution. The solution was then allowed to cool to RT and solvent removed under vacuum. The dry white powder was then returned to a nitrogen-filled glovebox, suspended in DCM and filtered over a microfiber filter paper pipette plug. Solvent was then removed under vacuum to yield a white powder. ^{1}H and ^{31}P NMR analysis of the crude filtered product (Figure 5.34 – Figure 5.35) indicated the successful preparation of $[MV][BArF]_2$ with excess Na[BArF] and unknown impurities present. To purify, the solid was recrystallized by slow diffusion of pentane into a concentrated DCM solution twice; however, photoactive impurities persisted.

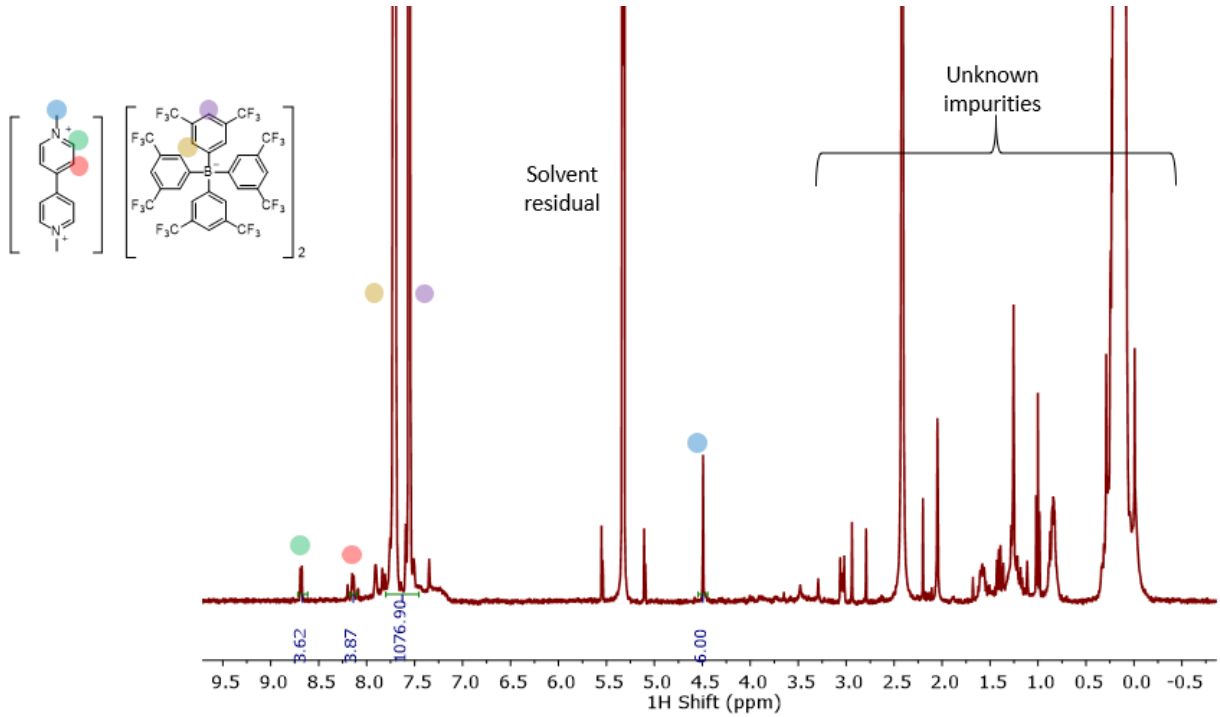

Figure 5.34 ^{1}H NMR spectrum of [MV][BArF]$_2$ reaction product in dichloromethane-d_2.

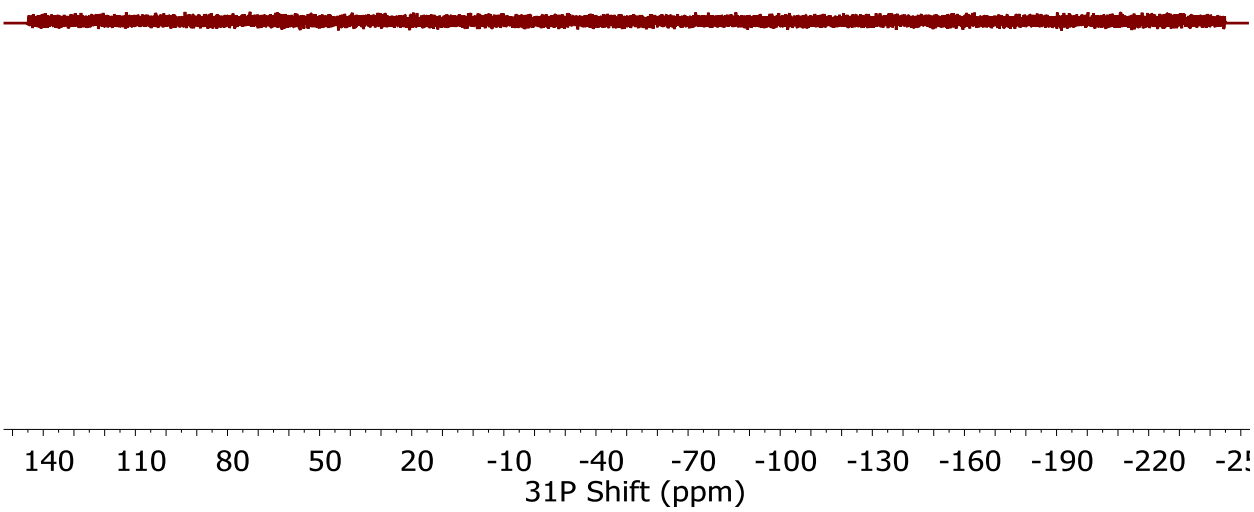

Figure 5.35 $^{31}P\{^{1}H\}$ NMR spectrum of [MV][BArF]$_2$ reaction product in dichloromethane-d_2. The absence of any hexafluorophosphate resonances indicate the successful removal of Na[PF_6] in the salt metathesis reaction.

REFERENCES

(1) Zhu, H.; Yang, Y.; Wu, K.; Lian, T. Charge Transfer Dynamics from Photoexcited Semiconductor Quantum Dots. *Annu. Rev. Phys. Chem.* **2016**, *67*, 259–281.

(2) Piechota, E. J.; Meyer, G. J. Introduction to Electron Transfer: Theoretical Foundations and Pedagogical Examples. *J. Chem. Educ.* **2019**, *96*, 2450–2466.

(3) Tvrdy, K.; Frantsuzov, P. A.; Kamat, P. V. Photoinduced Electron Transfer from Semiconductor Quantum Dots to Metal Oxide Nanoparticles. *Proc. Natl. Acad. Sci.* **2011**, *108*, 29–34.

(4) Zigler, D. F.; Morseth, Z. A.; Wang, L.; Ashford, D. L.; Brennaman, M. K.; Grumstrup, E. M.; Brigham, E. C.; Gish, M. K.; Dillon, R. J.; Alibabaei, L.; et al. Disentangling the Physical Processes Responsible for the Kinetic Complexity in Interfacial Electron Transfer of Excited Ru(II) Polypyridyl Dyes on TiO2. *J. Am. Chem. Soc.* **2016**, *138*, 4426–4438.

(5) Zhu, H.; Yang, Y.; Hyeon-Deuk, K.; Califano, M.; Song, N.; Wang, Y.; Zhang, W.; Prezhdo, O. V.; Lian, T. Auger-Assisted Electron Transfer from Photoexcited Semiconductor Quantum Dots. *Nano Lett.* **2014**.

(6) Olshansky, J. H.; Ding, T. X.; Lee, Y. V.; Leone, S. R.; Alivisatos, A. P. Hole Transfer from Photoexcited Quantum Dots: The Relationship between Driving Force and Rate. *J. Am. Chem. Soc.* **2015**, *137*, 15567–15575.

(7) Ghosh, S.; Ghosh, M.; Kumar, P.; Sarkar, A. S.; Pal, S. K. Quenching of the Excitonic Emission of ZnO Quantum Dots Due to Auger-Assisted Hole Transfer to CdS Quantum Dots. *J. Phys. Chem. C* **2016**, *120*, 27717–27723.

(8) Zhu, H.; Yang, Y.; Hyeon-Deuk, K.; Califano, M.; Song, N.; Wang, Y.; Zhang, W.; Prezhdo, O. V.; Lian, T. Auger-Assisted Electron Transfer from Photoexcited Semiconductor Quantum Dots. *Nano Lett.* **2014**, *14*, 1263–1269.

(9) Olshansky, J. H.; Balan, A. D.; Ding, T. X.; Fu, X.; Lee, Y. V.; Alivisatos, A. P. Temperature-Dependent Hole Transfer from Photoexcited Quantum Dots to Molecular Species: Evidence for Trap-Mediated Transfer. *ACS Nano* **2017**, *11*, 8346–8355.

(10) McArthur, E. A.; Morris-Cohen, A. J.; Knowles, K. E.; Weiss, E. A. Charge Carrier Resolved Relaxation of the First Excitonic State in CdSe Quantum Dots Probed with Near-Infrared Transient Absorption Spectroscopy. *J. Phys. Chem. B* **2010**, *114*, 14514–14520.

(11) Tseng, H. W.; Wilker, M. B.; Damrauer, N. H.; Dukovic, G. Charge Transfer Dynamics between Photoexcited CdS Nanorods and Mononuclear Ru Water-Oxidation Catalysts. *J. Am. Chem. Soc.* **2013**, *135*, 3383–3386.

(12) Malicki, M.; Knowles, K. E.; Weiss, E. A. Gating of Hole Transfer from Photoexcited PbS Quantum Dots to Aminoferrocene by the Ligand Shell of the Dots. *Chem. Commun.* **2013**, *49*, 4400–4402.

(13) Cabrera, P. J.; Yang, X.; Suttil, J. A.; Brooner, R. E. M.; Thompson, L. T.; Sanford, M. S. Evaluation of Tris-Bipyridine Chromium Complexes for Flow Battery Applications: Impact of Bipyridine Ligand Structure on Solubility and Electrochemistry. *Inorg. Chem.* **2015**, *54*, 10214–10223.

(14) Connelly, N. G.; Geiger, W. E. Chemical Redox Agents for Organometallic Chemistry. *Chem. Rev.* **1996**, *96*, 877–910.

(15) Elgrishi, N.; Kurtz, D. A.; Dempsey, J. L. Reaction Parameters Influencing Cobalt Hydride Formation Kinetics: Implications for Benchmarking H 2 -Evolution Catalysts. *J. Am. Chem. Soc.* **2017**, *139*, 239–244.

(16) Cohn, A. W.; Janßen, N.; Mayer, J. M.; Gamelin, D. R. Photocharging ZnO Nanocrystals: Picosecond Hole Capture, Electron Accumulation, and Auger Recombination. *J. Phys. Chem. C* **2012**, *116*, 20633–20642.

(17) Schrauben, J. N.; Hayoun, R.; Valdez, C. N.; Braten, M.; Fridley, L.; Mayer, J. M. Titanium and Zinc Oxide Nanoparticles Are Proton-Coupled Electron Transfer Agents. *Science (80-.).* **2012**, *336*, 1298–1301.

(18) Schimpf, A. M.; Gunthardt, C. E.; Rinehart, J. D.; Mayer, J. M.; Gamelin, D. R. Controlling Carrier Densities in Photochemically Reduced Colloidal ZnO Nanocrystals: Size Dependence and Role of the Hole Quencher. *J. Am. Chem. Soc.* **2013**, *135*, 16569–16577.

(19) Sharma, S. N.; Pillai, Z. S.; Kamat, P. V. Photoinduced Charge Transfer between CdSe Quantum Dots and p -Phenylenediamine. *J. Phys. Chem. B* **2003**, *107*, 10088–10093.

(20) Zhao, F.; Li, Q.; Han, K.; Lian, T. Mechanism of Efficient Viologen Radical Generation by Ultrafast Electron Transfer from CdS Quantum Dots. *J. Phys. Chem. C* **2018**, acs.jpcc.8b06551.

(21) Lennox, J. C.; Dempsey, J. L. Influence of Proton Acceptors on the Proton-Coupled Electron Transfer Reaction Kinetics of a Ruthenium–Tyrosine Complex. *J. Phys. Chem. B* **2017**, *121*, 10530–10542.

(22) Vaid, T. P.; Sanford, M. S. An Organic Super-Electron-Donor as a High Energy Density Negative Electrolyte for Nonaqueous Flow Batteries. *Chem. Commun.* **2019**, *55*, 11037–11040.

(23) Kubiak, C. P.; Broeker, G. K.; Granger, R. M.; Lemke, F. R.; Morgenstern, D. A. Patterned Imaging of Palladium and Platinum Films. In *Photosensitive Metal-Organic Systems*; Serpone, K. and, Ed.; Washington, DC, 1993; pp 165–184.

(24) Aguirre, M. E.; Municoy, S.; Grela, M. A.; Colussi, A. J. Low Intensity, Continuous Wave Photodoping of ZnO Quantum Dots – Photon Energy and Particle Size Effects. *Phys. Chem. Chem. Phys.* **2017**, *19*, 4494–4499.

(25) Knowles, K. E.; Tagliazucchi, M.; Malicki, M.; Swenson, N. K.; Weiss, E. A. Electron Transfer as a Probe of the Permeability of Organic Monolayers on the Surfaces of Colloidal PbS Quantum Dots. *J. Phys. Chem. C* **2013**, *117*, 15849–15857.

(26) Reid, P. J.; Fujimoto, B.; Gamelin, D. R. A Simple ZnO Nanocrystal Synthesis Illustrating Three-Dimensional Quantum Confinement. *J. Chem. Educ.* **2014**, *91*, 280–282.

(27) Knauf, R. R.; Lennox, J. C.; Dempsey, J. L. Quantifying Ligand Exchange Reactions at CdSe Nanocrystal Surfaces. *Chem. Mater.* **2016**, *28*, 4762–4770.

(28) Hartley, C. L.; Dempsey, J. L. Electron-Promoted X-Type Ligand Displacement at CdSe Quantum Dot Surfaces. *Nano Lett.* **2019**, *19*, 1151–1157.

(29) Jasieniak, J.; Smith, L.; Van Embden, J.; Mulvaney, P.; Califano, M. Re-Examination of the Size-Dependent Absorption Properties of CdSe Quantum Dots. *J. Phys. Chem. C* **2009**, *113*, 19468–19474.

(30) Nepomnyashchii, A. B.; Harris, R. D.; Weiss, E. A. Composition and Permeability of Oleate Adlayers of CdS Quantum Dots upon Dilution to Photoluminescence-Relevant Concentrations. *Anal. Chem.* **2016**, *88*, 3310–3316.

(31) Valdez, C. N.; Schimpf, A. M.; Gamelin, D. R.; Mayer, J. M. Proton-Controlled Reduction of ZnO Nanocrystals: Effects of Molecular Reductants, Cations, and Thermodynamic Limitations. *J. Am. Chem. Soc.* **2016**, *138*, 1377–1385.

(32) Valdez, C. N.; Braten, M.; Soria, A.; Gamelin, D. R.; Mayer, J. M. Effect of Protons on the Redox Chemistry of Colloidal Zinc Oxide Nanocrystals. *J. Am. Chem. Soc.* **2013**, *135*, 8492–8495.

APPENDIX A : ADDITIONAL DETAILS AND CHARACTERIZATION FOR CHAPTER 2

A.1 Experimental Methods

A.1.1 General Considerations

All syntheses and titration experiments were performed using standard air-free Schlenk techniques or carried out in a dry, nitrogen-filled glovebox (M. Braun) unless noted otherwise. Anhydrous THF was collected from a dry solvent system and purified over an alumina column under an argon atmosphere (Pure Process Technologies) and stored in a nitrogen-filled glovebox over 3Å molecular sieves. Solvents were tested with ketyl radical to confirm dryness prior to use. THF-d_8 (D, 99.5%) was purchased from Cambridge Isotope Laboratories in 1 g ampoules and dried over alumina immediately before use.

A.1.2 Nanocrystal Characterization

QD size and molar extinction coefficient were determined using the empirical relationship between energy of the excitonic absorption feature and nanocrystal diameter reported by Jasieniak et al.[1] UV-Vis absorption spectra were measured on an Agilent Cary 60 spectrophotometer or an Ocean Optics Flame UV-Vis spectrometer with a DH-mini light source. Emission spectra were measured using an Ocean Optics LLS spectrometer with excitation light provided by a 455 nm LED source. Samples for TEM analysis were prepared by drop casting dilute solutions of nanocrystals in pentane on lacey carbon film 400 mesh copper TEM grids. The grids were then dried under vacuum to remove any excess solvent and run on a JEOL 2010F-FasTEM with 200 kV accelerating voltage.

A.1.3 UV-Vis Absorption Spectroscopy Titrations

UV-Vis absorption spectra were collected on an Agilent Cary 60 spectrophotometer at a scan rate of medium unless noted otherwise. Samples of CdSe QDs in THF were prepared in a nitrogen-filled glovebox and added to a custom-made 1-cm path length quartz cuvette with an adapted 14/20 glass joint

top and equipped with a micro-stir bar. The cuvette was capped with a rubber septum and secured with a layer of electrical tape and copper wire under an inert atmosphere. Appropriately diluted solutions of $Na[C_{10}H_8]$ in THF were prepared (see below, Preparation of Redox Reagents) and collected in a 250 µL gas-tight locking Hamilton syringe with a 4-inch long needle kept locked and the needle stuck into a rubber septum. This air-tight assembly was then taken out of the glovebox and absorption spectra measured of the solution of QDs alone, and upon addition of reductant. The sample was stirred following addition of $Na[C_{10}H_8]$, and in between additions the syringe needle was locked to ensure there was no dripping or accidental addition.

A.1.4 ^{1}H NMR Spectroscopy Titrations

^{1}H NMR experiments were run using 8 scans with d1 time of 7.5 seconds on 500 or 600 MHz Bruker NMR spectrometers unless otherwise noted. An internal standard of 1,3,5-trimethoxybenzene was used in all samples to quantify ligand coverage. All titration samples were prepared under an inert atmosphere in J-Young NMR tubes and aliquots of reductant were added in a nitrogen-filled glovebox. For ^{1}H NMR titration studies, though the appearance of naphthalene serves as confirmation of electron transfer from the radical anion $Na[C_{10}H_8]$, the integrals of the corresponding naphthalene proton resonances may only be used for absolute quantification if an appropriately long d1 delay time is used (d1 = 155 seconds), as determined by an inversion recovery experiment (Figure 2.7).

A.1.5 ATR-FTIR Titrations

FTIR measurements were collected using a Bruker Alpha I FTIR in ATR mode with a diamond crystal using a resolution of 4 cm^{-1} with 24 scans. Samples for FTIR analysis were prepared in a nitrogen-filled glovebox by adding aliquots of reductant to samples of a divided stock solution of CdSe QDs in THF. After addition of reductant under an inert atmosphere, samples were opened to air and solutions

drop cast onto a crystal of FTIR under ambient conditions and allowed to dry before collecting the measurement.

A.1.6 Synthesis of OA-Capped CdSe QDs

3.4 nm CdSe nanocrystals capped with oleate ligands were synthesized following a modified literature procedure.[2] CdO (321 mg, 2.5 mmol) and 1.8 mL oleic acid (5.6 mmol) were added to a 50 mL three-neck round bottom flask with 16 mL octadecene and stirred under vacuum for 30 min. The flask was then placed under nitrogen and heated to 230 ºC until the solution became clear and colorless. The flask was then cooled to 80 ºC while alternating between vacuum and nitrogen for 10 min to remove water formed in situ. After the final cycle, the flask was placed back under nitrogen and heated to 125 ºC and Se powder (104 mg, 1.3 mmol) was added. The flask continued to heat to a growing temperature of 220 ºC at which point the solution went from a heterogeneous mixture to a homogeneous yellow, then orange, and finally dark red solution. The nanocrystals continued to grow for 40 min at 220 ºC before the flask was cooled by removal of the heating mantle and addition of 10 mL of toluene to quench growth.

A.1.7 Purification of OA-Capped CdSe QDs

The nanocrystal solution was divided among four test tubes (~7 mL each) and 5 mL acetone added to each. The solutions were mixed and then centrifuged at 2500 rpm for 10 min, yielding a red supernatant and white pellet. The supernatant was decanted off and excess solvent removed by rotary evaporation. The concentrated solution was divided among six test tubes (3.5 mL each) and 8 mL acetone added to each prior to centrifuging for 15 min at 2500 rpm. This step yielded a clear supernatant and dark red pellet of nanocrystals. The supernatant was decanted off, and the pellets dispersed in 11 mL acetone and sonicated prior to centrifuging again to isolate the nanocrystals. Following this step, the acetone supernatant was decanted off and 6 mL DCM added to each tube and the samples sonicated. These were then centrifuged for 20 min at 2500 rpm, leaving a red supernatant with white solid collected at the top of

the solution. This mixture was filtered through celite and washed with DCM (3 x 10 mL), and the solvent was removed by rotary evaporation. The resulting red residue was dissolved in toluene and divided among six test tubes (1 mL/tube) and 11 mL acetone added to precipitate the nanocrystals prior to centrifugation. The samples were then repeatedly resuspended in toluene and precipitated by addition of acetone and centrifuged until the sample consistently showed a clear supernatant with cleanly separated red pellet. The nanocrystals were then dispersed in pentane, transferred to a vial, and dried via evaporation overnight. Purified nanocrystals were then stored dry in a nitrogen-filled glovebox.

A.1.8 Preparation of sodium oleate salt (Na[oleate])

Sodium oleate (Na[oleate]) was prepared following a literature procedure.[3] Sodium hydroxide (0.73 g, 18.2 mmol) was dissolved in 70 mL of 200-proof ethanol and stirred at room temperature until fully incorporated into solution. Oleic acid (5.75 mL, 18.1 mmol) was added slowly to the ethanol solution, yielding immediate formation of a waxy white solid. The reaction mixed overnight, and the white solid was then dried under vacuum and stored in a desiccator under ambient conditions.

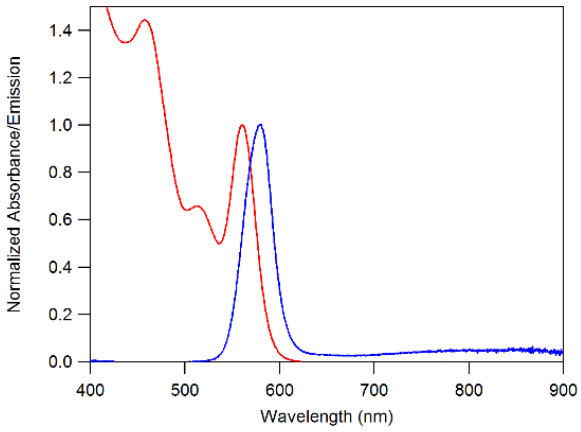

Figure A.1.1 Normalized absorbance (red) and emission (blue) spectra of 3.4 nm CdSe QDs in toluene (λ_{exc} = 455 nm).

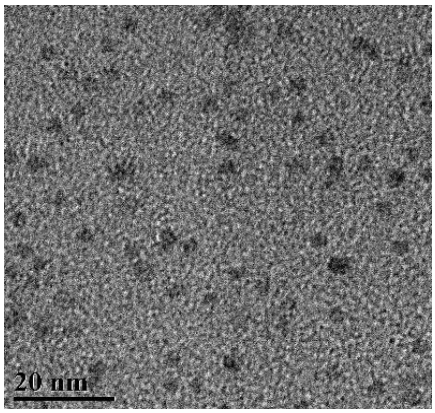

Figure A.1.2 TEM image of 3.4 nm CdSe QDs.

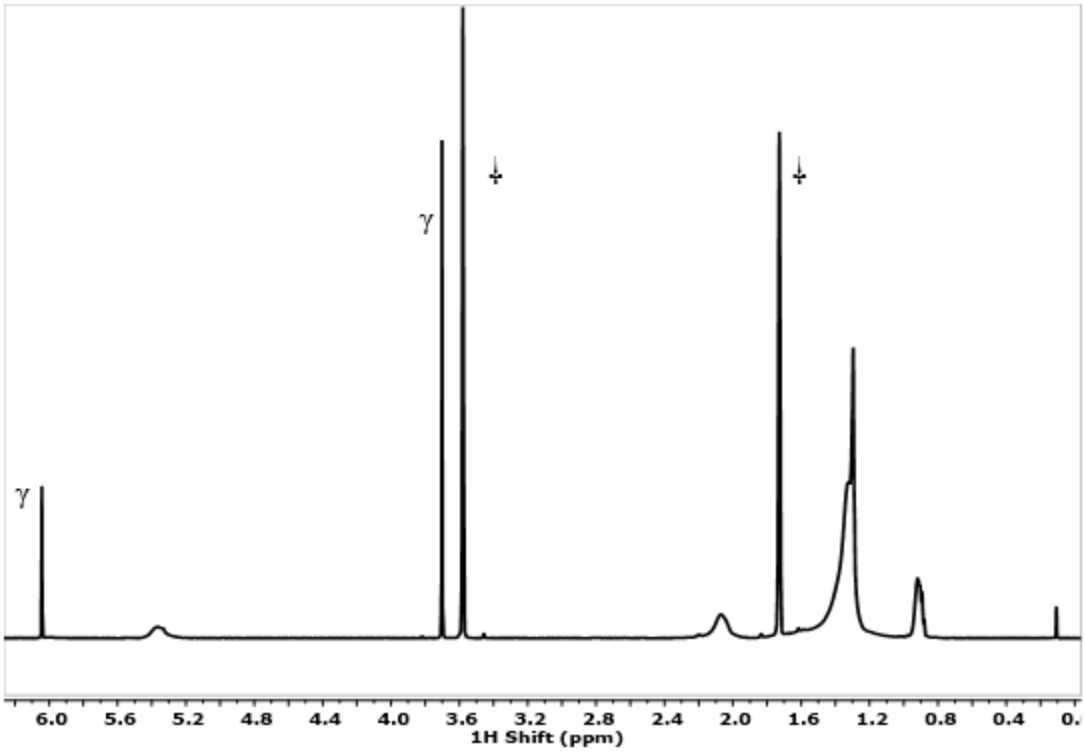

Figure A.1.3 ^{1}H NMR spectrum of 109 μM 3.4 nm CdSe QDs in THF-d_8. Ligand coverage was determined to be approximately 3.4 oleate ligands per nm^2 using an internal standard of 1,3,5-trimethoxybenzene (γ). Solvent residuals are marked with a ⏚ symbol.

A.1.9 Preparation of Redox Reagents

Preparation of sodium naphthalenide ($Na[C_{10}H_8]$)

Solutions of reductant were prepared day-of for each experiment in a nitrogen-filled glovebox following a common literature procedure.[4] A naphthalene solution (153 mg, 1.19 mmol) was prepared in 3 mL dried and deoxygenated THF or THF-d_8 and added to a slight excess of sodium metal (40 mg, 1.74 mmol). Upon addition of the naphthalene solution to sodium metal, there was an immediate color change from clear to dark forest green. The solution was stirred with a glass-coated stir bar at room temperature for a minimum of 2-3 hours prior to use. The concentration of the $Na[C_{10}H_8]$ solution was confirmed by UV-Vis absorbance spectroscopy unless otherwise noted and stock solutions were diluted in THF to achieve a desired concentration.[5]

Note on the sensitivity of this reductant: We note that $Na[C_{10}H_8]$ serves as an effective one-electron donor in this model system due its strong reducing nature and the formation of benign naphthalene upon its oxidation. However, it is *extremely* air and moisture-sensitive, and must be handled only under thoroughly inert conditions with very dry solvents. Upon preparing solutions of $Na[C_{10}H_8]$, the naphthalene solution should *immediately* turn dark green upon addition to sodium metal.[4] A delay in coloration of the solution indicates that the solvent is not completely dried, and dilution with that same solvent risks unintentional quenching of the radical anion.[4] Because of its sensitivity, the concentration of the reductant solution must be confirmed by UV-Vis absorption spectroscopy for quantitative studies.[4,5] Similarly, it is important that the QD solution to be reduced is free of impurities that might quench $Na[C_{10}H_8]$ in order to ensure precision and reproducibility in doping studies.

Preparation of ferrocenium tetrakis[3,5-bis(trifluoromethyl)phenyl]borate ($[Fc][BAr^F_4]$)

$[Fc][BAr^F_4]$ was prepared using literature procedure.[6] Briefly, $[Fc][BF_4]$ (50 mg, 0.183 mmol) and $Na[BAr^F_4]$ (162 mg, 0.183 mmol) were combined with 12 mL of dichloromethane in a 25 mL Schlenk flask under a nitrogen atmosphere. The flask was heated to reflux and stirred under nitrogen for 30 minutes. The solution was then cooled to room temperature and the solvent removed under vacuum. In

a nitrogen-filled glovebox, the blue solid was dissolved in 8 mL DCM and filtered through a microfilter pipette plug. The [Fc][BAr^F_4] was further extracted with ~2 mL diethyl ether. The resulting blue solution was concentrated to approximately 2 mL under vacuum and the product precipitated with 15 mL of pentane. The blue solid was filtered and washed with pentane (5 x 2 mL) and dried under vacuum. The product was then recrystallized by slow diffusion of pentane into a concentrated DCM solution. ATR-FTIR: 1352, 1276, 1119 cm^{-1}.

A.1.10 Fitting UV-Vis Spectra to Quantify ⟨n⟩

Absorbance spectra were fit using the method of Shim et al. to estimate the number of electrons in the $1S_e$ state.[7–9] The $1S_e \leftarrow 1S_{h3/2}$, $1S_e \leftarrow 2S_{h3/2}$, and $1P_e \leftarrow 1P_{h3/2}$ features were fit to gaussian curves and an exponential curve was added to account for in the increased absorbance at high energies (Figure S4). The parameters used to fit this exponential curve were typically held constant across a given data set, and a second exponential curve was added to account for the lower energy absorbance feature observed upon QD reduction. The area of the excitonic absorbance feature at each addition of reductant was then used to quantify CB electrons using the expression $\langle n \rangle = \frac{-2\Delta A}{A_0}$ where $\langle n \rangle$ is the number of electrons in the $1S_e$ state and A_0 is the area of the excitonic absorbance feature in the absence of reductant.[7–9] ΔA is the difference between A_0 and the area, A, of the $1S_e$ feature of the doped QDs.

A.2 Additional Experimental Results

Table A.2.1 Estimated number of CB electrons based on UV-Vis data corresponding to Figure 2.1.

Equivalents of $Na[C_{10}H_8]$ added (per mol QD)	Estimated Number of Electrons in $1S_e$ state, $\langle n \rangle$
QD only	0

5	0
10	0.05
20	0.28
40	0.61
60	1.1
80	1.2
100	1.3

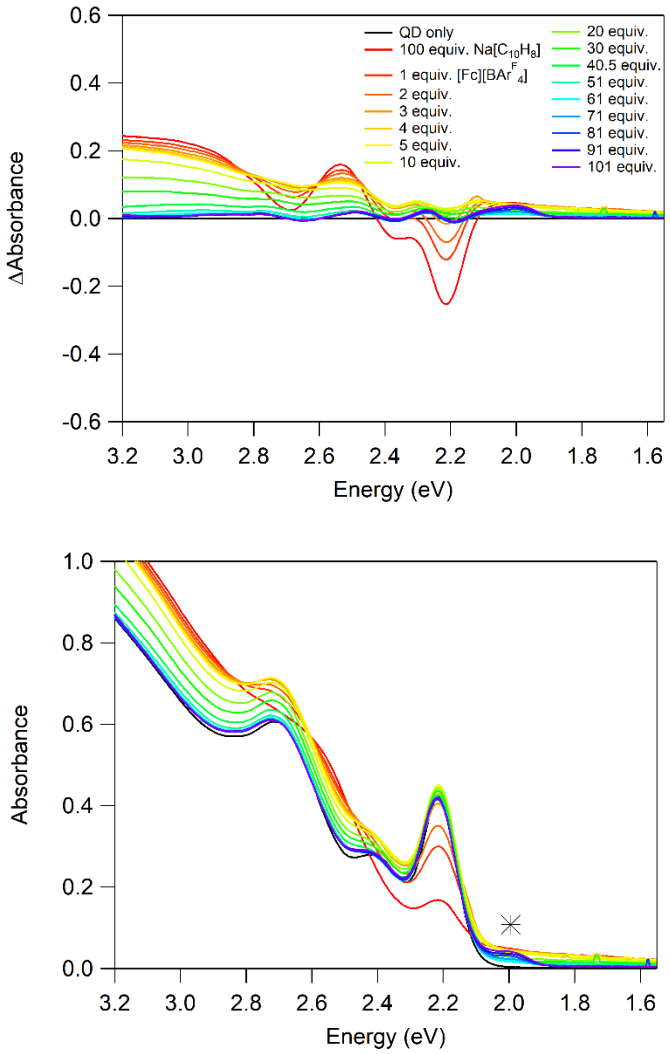

Figure A.2.1 (Top) Figure 2.1c from the chapter 2 with a full legend upon addition of aliquots of $[Fc][BAr^F_4]$ to a solution of 2 µM 3.4 nm QDs in THF reduced with 100 equivalents of $Na[C_{10}H_8]$. (Bottom) Enlarged inset from Figure 2.1, showing the absorbance spectra of the reversibility study. The legend for the bottom plot is the same as that shown for the top figure. Oxidation of the reduced QDs shows good reversibility with addition of Fc^+, demonstrated by the close overlay of the original trace

(black) with the final trace after re-oxidation. Addition of more than ~50 equivalents of oxidant shows the growth of an absorbance feature attributable to unreacted [Fc][BAr^F_4] (*).

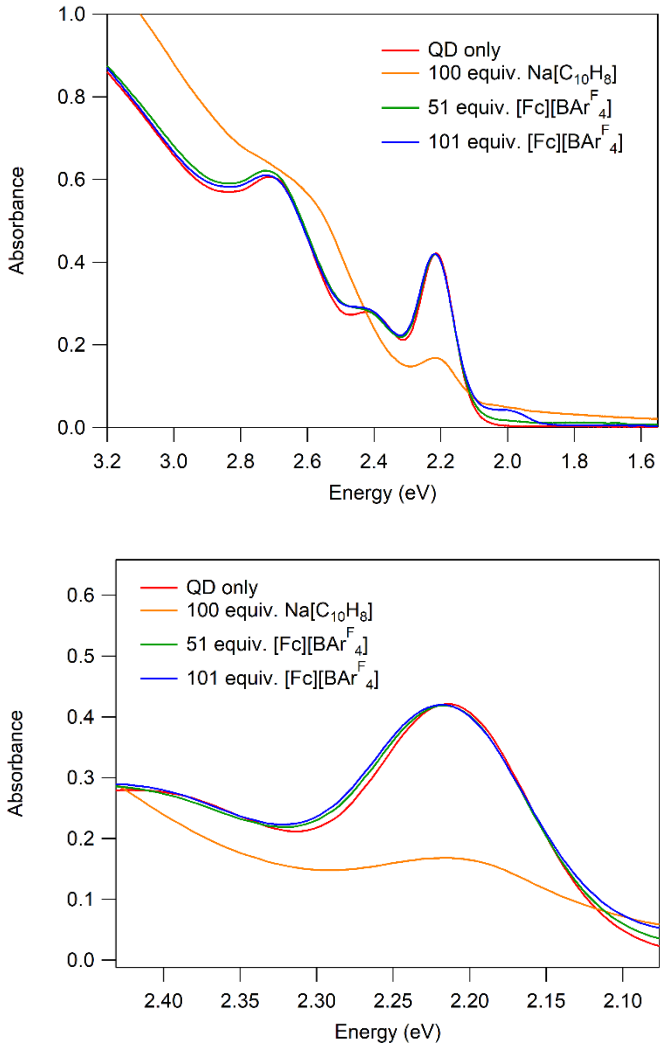

Figure A.2.2 (Top) Figure 2.1c from chapter 2 showing traces of QD only, upon addition of 100 equivalents of Na[$C_{10}H_8$] and then with approximately 51 and 101 equivalents of [Fc][BAr^F_4]. (Bottom) The same spectrum, zoomed in on the excitonic absorbance feature to show differences in the reduced and oxidized traces compared with the QD only trace. Upon addition of reductant there is a slight red shift in addition to the excitonic bleach, in agreement with previous reports and may be suggestive of surface charging in the reduced QDs.[7–9] Upon re-oxidation and recovery of the excitonic absorbance feature, we observe a ~0.008 eV (~1 nm) blue shift in comparison to the original spectrum. This slight shift may be indicative of changes in surface composition but do not suggest substantial change in the size of the nanocrystals.

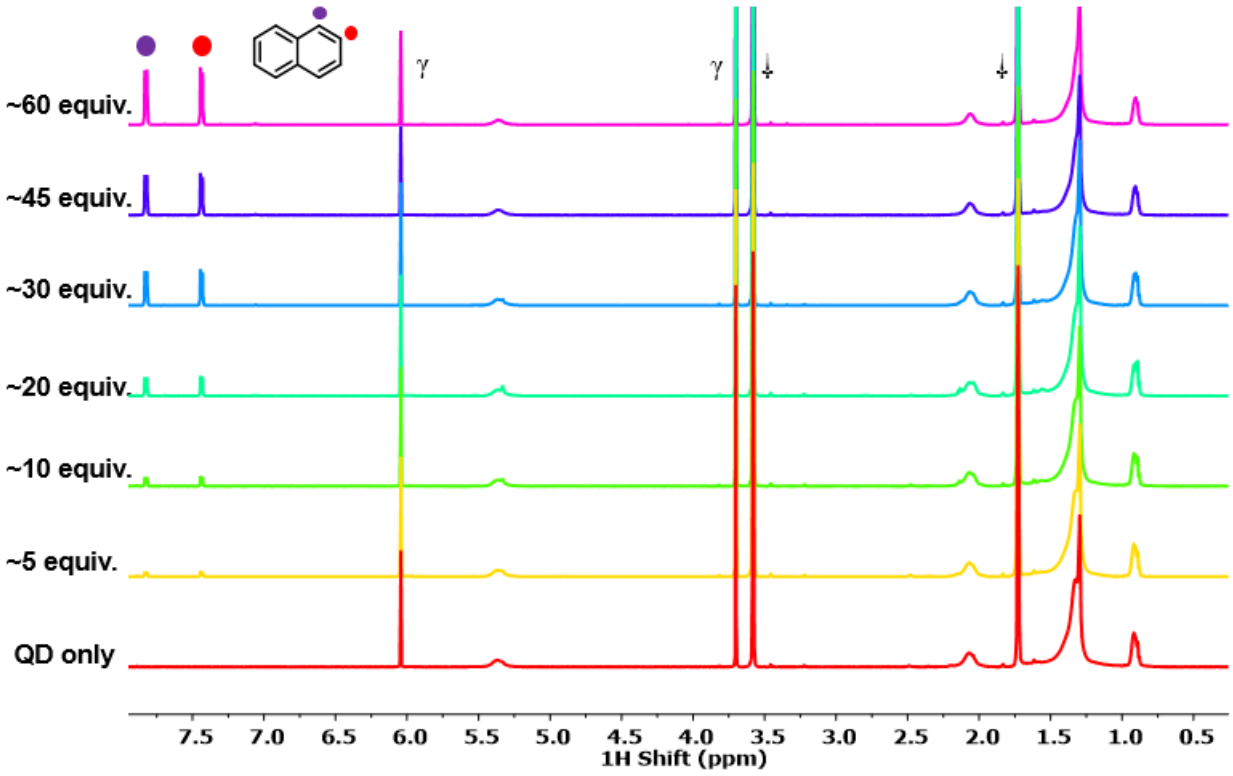

Figure A.2.3 Full stacked ^{1}H NMR spectra corresponding to Figure 2.4 in the chapter 2 for a solution of 112 µM 3.4 nm CdSe QDs in THF-d_8 with added aliquots of Na[$C_{10}H_8$]. An internal standard of 1,3,5-trimethoxybenzene was used (γ). Solvent residuals are marked with a ⏚ symbol.

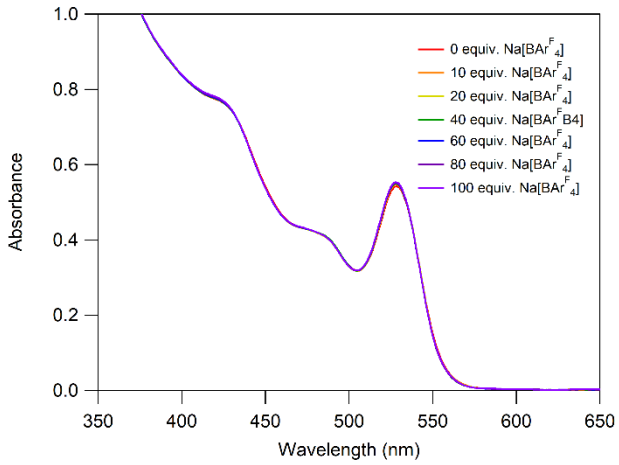

Figure A.2.4 UV-Vis absorbance spectra of similarly prepared and purified 3.2 µM 2.7 nm CdSe QDs with addition of Na[BAr^F_4] in THF. Though this control study was performed on a QD size different from the batch of focus, its results should not be affected by changes in QD reduction potentials with size as it involves no redox reactivity.

Table A.2.2 The effect of dilution on a sample of similarly prepared and purified 72.5 µM 2.4 nm CdSe QDs in THF-d_8 monitoring the free versus bound oleate ligand coverage. The percentage of free oleate ligands relative to total integrated ligands based on the alkene resonance does not change significantly upon dilution at typical volumes of aliquots employed in reductive titration studies (less than 200 µL). Though this control study was performed on a QD size different from the batch of focus, its results should not be affected by changes in QD reduction potentials with size as it involves no redox reactivity.

Volume of THF-d_8 added to NMR Sample	**Percentage of Free Oleate Ligands**
Initial 600 µL sample	3.2%
50 µL	3.1%
100 µL	3.6%
200 µL	3.5%
400 µL	3.6%
2400 µL	5.8%

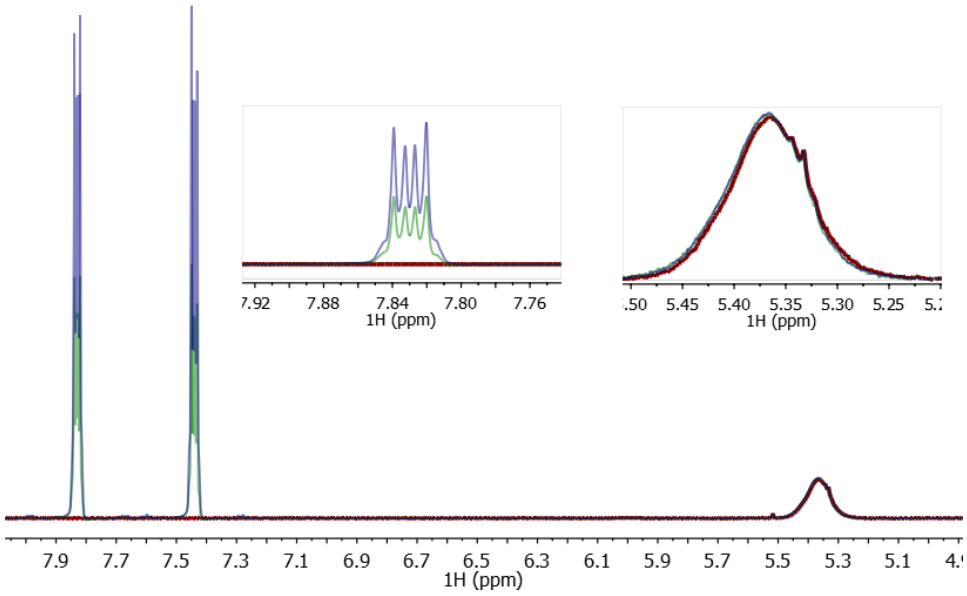

Figure A.2.5 ^{1}H NMR spectra of similarly prepared and purified 72 µM 2.7 nm CdSe QDs in THF-d_8 (red) with addition of 50 equivalents (green) and 100 equivalents (blue) of naphthalene. Insets show growth of naphthalene resonances (left) and no change in the ratio of bound to free oleate ligands using the alkene resonance (right). Though this control study was performed on a QD size different from the batch of focus, its results should not be affected by changes in QD reduction potentials with size as it involves no redox reactivity.

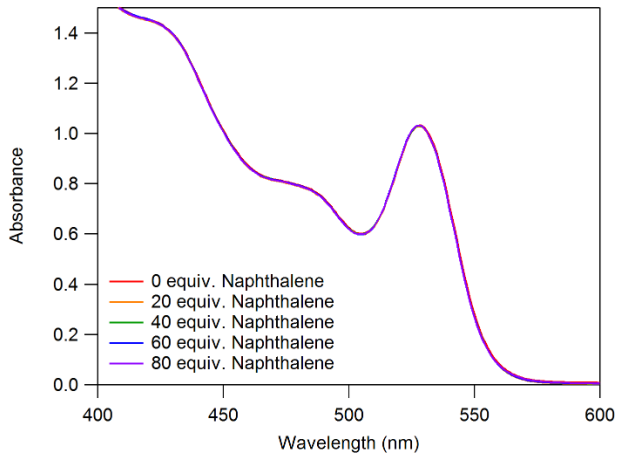

Figure A.2.6 UV-Vis absorbance spectra of similarly prepared and purified 6 µM 2.7 nm CdSe QDs with addition of naphthalene in THF. Though this control study was performed on a QD size different from the batch of focus, its results should not be affected by changes in QD reduction potentials with size as it involves no redox reactivity.

Table A.2.3 The time-dependence of a similarly prepared and purified sample of 72.5 µM 2.4 nm CdSe QDs in THF-d_8 monitoring free versus bound oleate ligand coverage in solution. The percentage of free oleate ligand relative to total integrated ligands does not change with time, illustrating that ligand loss is not promoted by samples sitting in THF-d_8 during long NMR titration experiments. Though this control study was performed on a QD size different from the batch of focus, its results should not be affected by changes in QD reduction potentials with size as it involves no redox reactivity.

Time After Sample Preparation	**Percentage of Free Oleate Ligands**
0 min	3.3%
60 min	3.5%
120 min	3.2%
180 min	3.3%

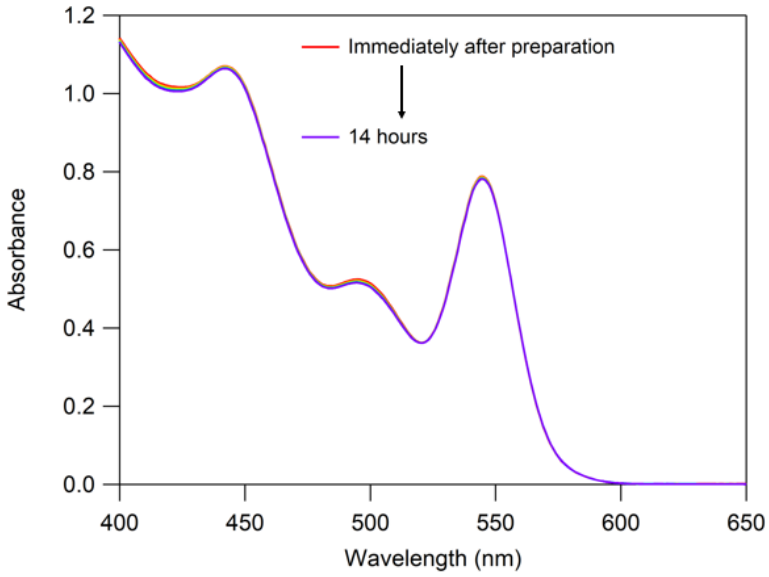

Figure A.2.7 UV-Vis absorbance spectra of similarly prepared and purified 4.3 µM 3.1 nm CdSe QDs monitoring change in time for up to 14 hours in THF. There is not a significant change observed with time following sample preparation. Though this control study was performed on a QD size different from the batch of focus, its results should not be affected by changes in QD reduction potentials with size as it involves no redox reactivity.

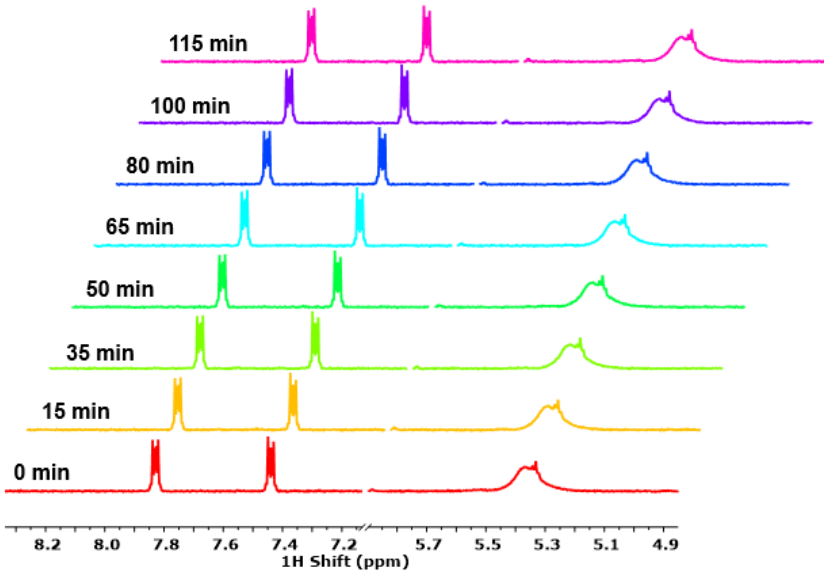

Figure A.2.8 ^{1}H NMR spectra of 82 µM 3.4 nm CdSe QDs with ~12 equiv. Na[$C_{10}H_8$] in THF-d_8 over time. The ratio of bound to free oleate ligands and integration of naphthalene resonances does not change significantly with time from 0 to 115 min.

Table A.2.4 Equivalents of naphthalene and percentage of free oleate ligands upon addition of ~12 equiv. $Na[C_{10}H_8]$ in THF-d_8 over 115 minutes corresponding to Figure A.2.8.

Time After Addition of $Na[C_{10}H_8]$	**Approximate Equiv. Naphthalene (per mole QD)**	**Percentage of Free Oleate Ligands**
0 min	11.8	4.9%
15 min	11.7	4.8%
35 min	11.7	4.4%
50 min	11.8	4.9%
65 min	11.8	4.6%
80 min	11.8	5.0%
100 min	12.0	5.3%
115 min	11.7	3.8%

REFERENCES

(1) Jasieniak, J.; Smith, L.; Van Embden, J.; Mulvaney, P.; Califano, M. *J. Phys. Chem. C* **2009**, *113* (45), 19468−19474.

(2) Knauf, R. R.; Lennox, J. C.; Dempsey, J. L. *Chem. Mater.* **2016**, *28* (13), 4762−4770.

(3) Parmentier, D.; Metz, S. J.; Kroon, M. C. *Green Chem.* **2013**, *15* (1), 205−209.

(4) Connelly, N. G.; Geiger, W. E. *Chem. Rev.* **1996**, *96* (2), 877−910.

(5) Szwarc, M. Carbanions, Living Polymers, and Electron Transfer Processes.; Interscience Publishers: New York, 1968.

(6) Chávez, I.; Alvarez-Carena, A.; Molins, E.; Roig, A.; Maniukiewicz, W.; Arancibia, A.; Arancibia, V.; Brand, H.; Manuel Manríquez, J. *J. Organomet. Chem.* **2000**, *601* (1), 126−132.

(7) Shim, M.; Guyot-Sionnest, P. *Nature* **2000**, *407*, 981−983.

(8) Shim, M.; Wang, C.; Guyot-Sionnest, P. *J. Phys. Chem. B* **2001**, *105* (12), 2369−2373.

(9) Rinehart, J. D.; Schimpf, A. M.; Weaver, A. L.; Cohn, A. W.; Gamelin, D. R. *J. Am. Chem. Soc.* **2013**, *135* (50), 18782−18785.

(10) Tsui, E. Y.; Carroll, G. M.; Miller, B.; Marchioro, A.; Gamelin, D. R. *Chem. Mater.* **2017**, *29* (8), 3754−3762.

APPENDIX B : ADDITIONAL DETAILS AND CHARACTERIZATION FOR CHAPTER 3

B.1 Experimental Details

B.1.1 Isolation of a Proposed [$CoCp_2$][OA]

All manipulations and purifications performed in a dry nitrogen-filled glovebox

1) A solution of 3.7 nm PbS QDs (12.9 μM) in 7.5 mL toluene was combined with ~500 eq. $CoCp_2$ in toluene (4.8 mL of 0.01 M solution) and stirred at RT overnight.

2) Toluene solvent was removed under vacuum leaving a dry QD solid.

3) The solid was dispersed in pentane and sonicated.

4) The pentane solution was filtered through a glass microfiber filter paper pipette plug and then washed with toluene (~2 – 3 mL x 3 times)

5) Acetonitrile (5 mL) was run through the filter paper pipette plug to extract a pale-yellow product that was then dried under vacuum and analyzed by ^{1}H NMR and UV-Vis absorbance spectroscopy.

B.1.2 Conversion of Reduction Potential to Energy

Reduction potential of redox-active chemical probes were first converted from V vs. Fc+/0 to V vs. NHE. This value was then converted to energy (eV) vs. vacuum.

Example calculation for $CoCp_2$ ($E^{o\prime}$ = −1.3 V vs. $Fc^{+/0}$):

$$E^{\circ\prime} = -1.33\ V\ vs.\ Fc^{\frac{+}{0}} + 0.63\ V = -.7\ V\ vs.\ NHE$$

$$Energy\ vs\ Vacuum = -4.5 - \left(E^{\circ\prime}, V\ vs.\ NHE\right)$$

$$= -4.5 - (-0.7\ V\ vs.\ NHE) = -3.8\ eV\ vs.\ vacuum$$

B.2 Additional Experiments

B.2.1 Variable Temperature ^{1}H NMR Experiment

The broadness of the diamagnetic $[CoCp_2]^+$ feature (6.2 ppm) could arise from this species being in dynamic electronic exchange with excess paramagnetic $CoCp_2$ in solution. To test the possibility of dynamic exchange, ^{1}H NMR spectra monitoring the $CoCp_2$ and $[CoCp_2]^+$ features at −52 ppm and 6.2 ppm, respectively, were collected at temperatures ranging from −50 ˚C to 80 ˚C (Figure S7 – S10). At high temperatures, both features shift downfield while at lower temperatures they shift upfield. The observed peak position shift with temperature is likely a result of increased paramagnetism at lower temperatures.[4] The correlated shift of the two peaks with varying temperature may be consistent with slow exchange between $CoCp_2$ and $[CoCp_2]^+$ on the NMR spectroscopy timescale.

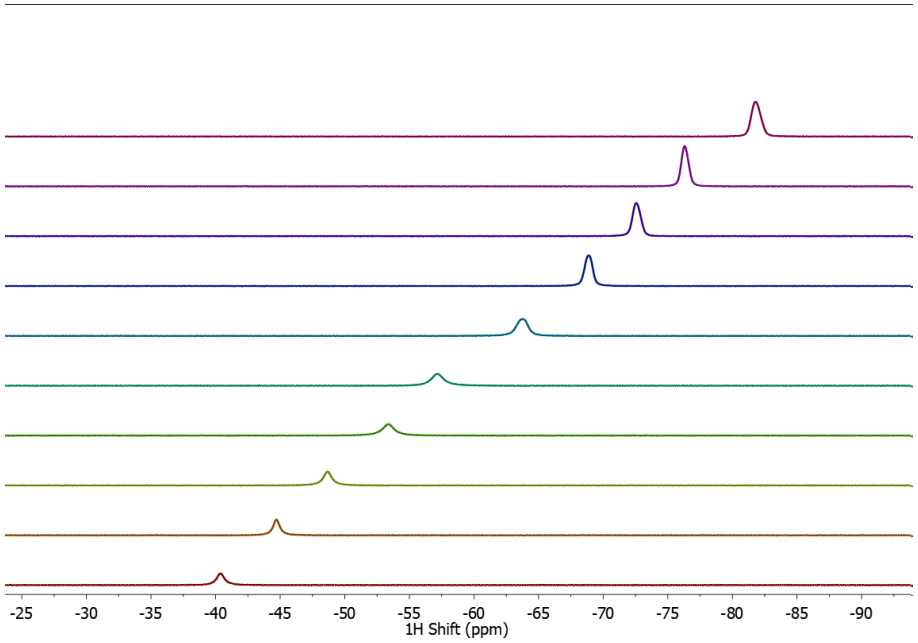

Figure B.2.1 ^{1}H NMR spectra of 4.7 nm QDs (19.6 µM) in toluene-d_8 with 500 eq. $CoCp_2$ at varying temperatures ranging from approximately 80 ˚C (maroon) to −30 ˚C (purple) monitoring the paramagnetic $CoCp_2$ resonance.

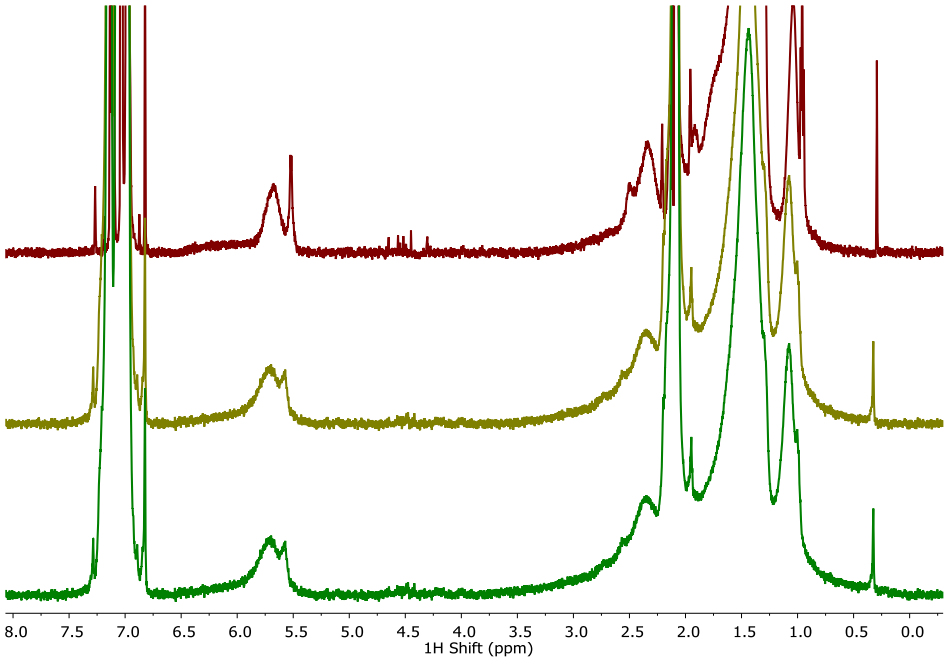

Figure B.2.2 ^{1}H NMR spectra of 4.7 nm QDs (19.6 µM) in toluene-d_8 with 500 eq. $CoCp_2$ at varying temperatures ranging from approximately −50 ˚C (green), to −30 ˚C (gold) to −10 ˚C (maroon).

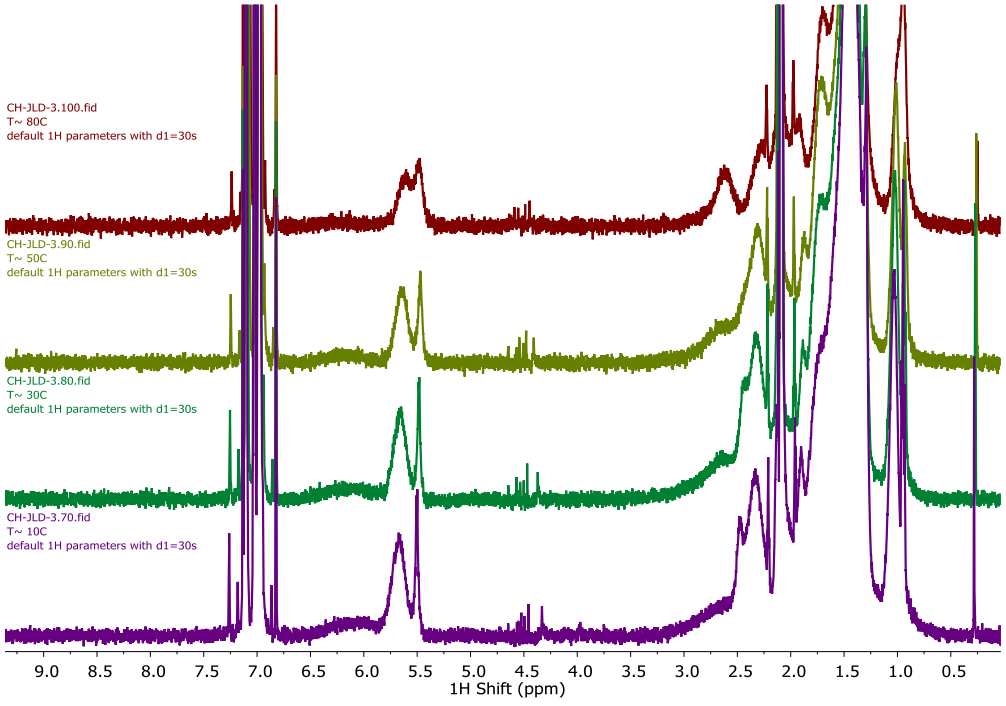

Figure B.2.3 ^{1}H NMR spectra of 4.7 nm QDs (19.6 µM) in toluene-d_8 with 500 eq. $CoCp_2$ at varying temperatures ranging from approximately 10 ˚C (violet) to 80 ˚C (maroon).

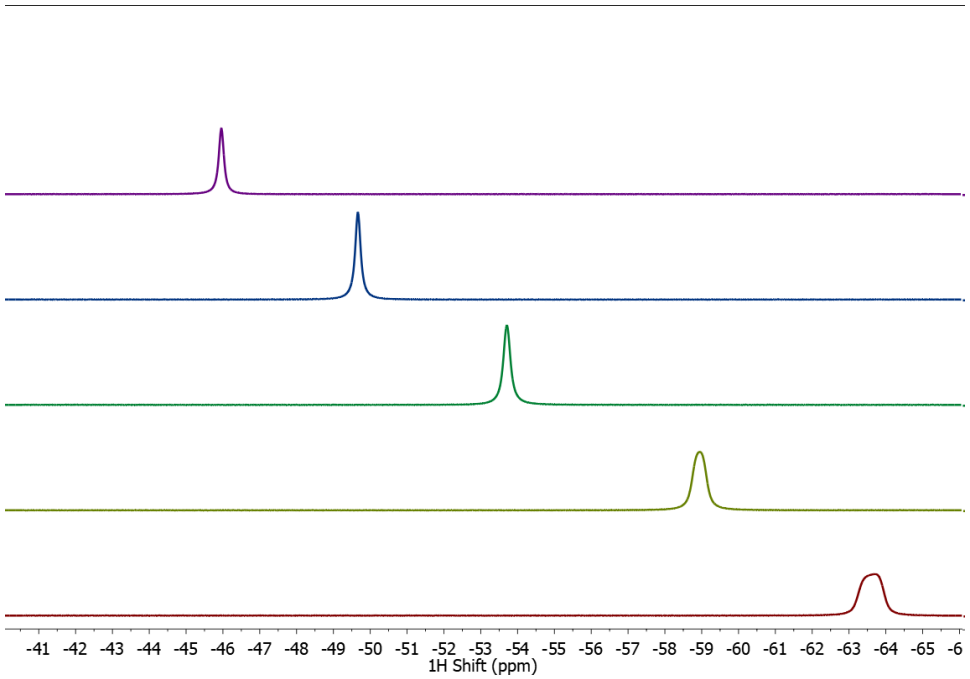

Figure B.2.4 ^{1}H NMR spectra of 50 mM $CoCp_2$ in toluene-d_8 at varying temperatures ranging from approximately −30˚C (red) to 30˚C (purple) monitoring the paramagnetic $CoCp_2$ resonance.

B.2.2 NMR Titrations with Added $CoCp_2$

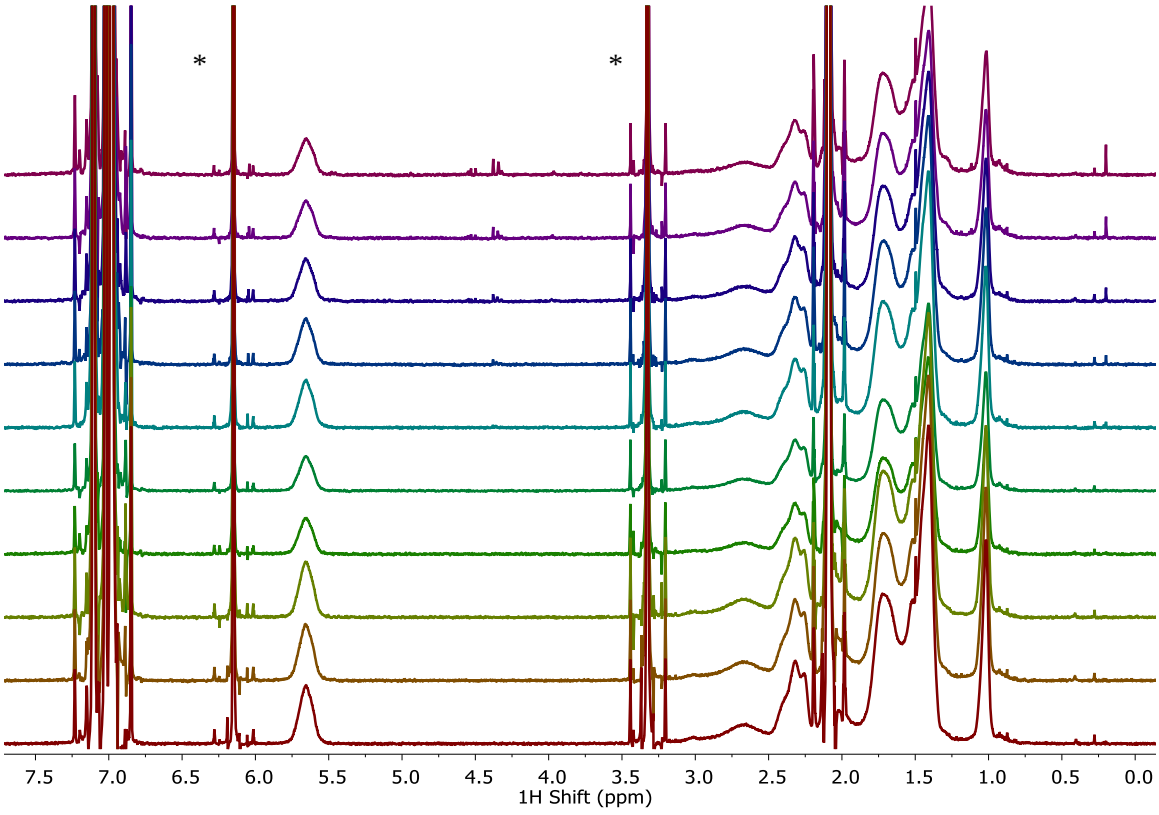

Figure B.2.5 ^{1}H NMR titration of 27.7 µM PbS QDs (2.6 nm) with 0 (red), 25 (orange), 50 (gold), 75 (light green), 100 (dark green), 200 (teal), 350 (blue), 500 (dark blue), 750 (purple), and 1000 (magenta) eq. $CoCp_2$ added in toluene-d_8. (*) denotes internal standard 1,3,5-trimethoxybenzene. NMR spectra collected on 600 MHz NMR with cryoprobe utilizing d1 delay of 30 seconds with 12 scans.

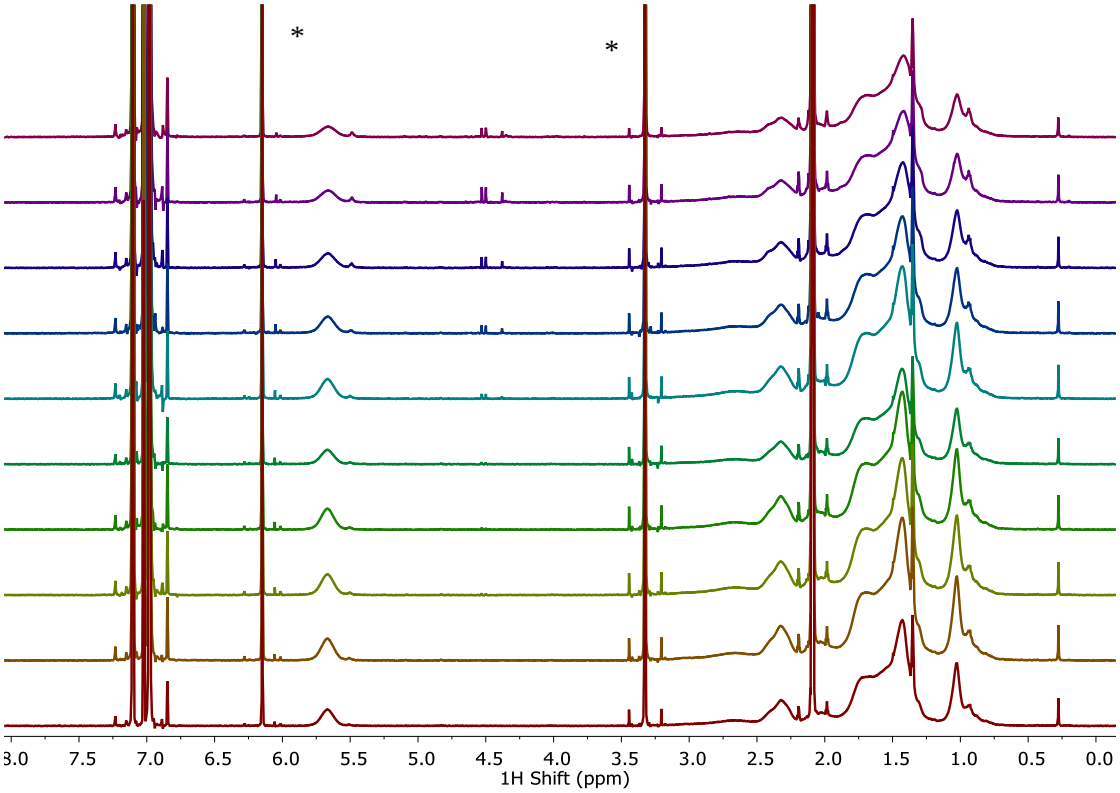

Figure B.2.6 ^{1}H NMR titration of 27.7 µM PbS QDs (3.8 nm) with 0 (red), 25 (orange), 50 (gold), 75 (light green), 100 (dark green), 200 (teal), 350 (blue), 500 (dark blue), 750 (purple), and 1000 (magenta) eq. $CoCp_2$ added in toluene-d_8. (*) denotes internal standard 1,3,5-trimethoxybenzene. NMR spectra collected on 600 MHz NMR with cryoprobe utilizing d1 delay of 30 seconds with 12 scans.

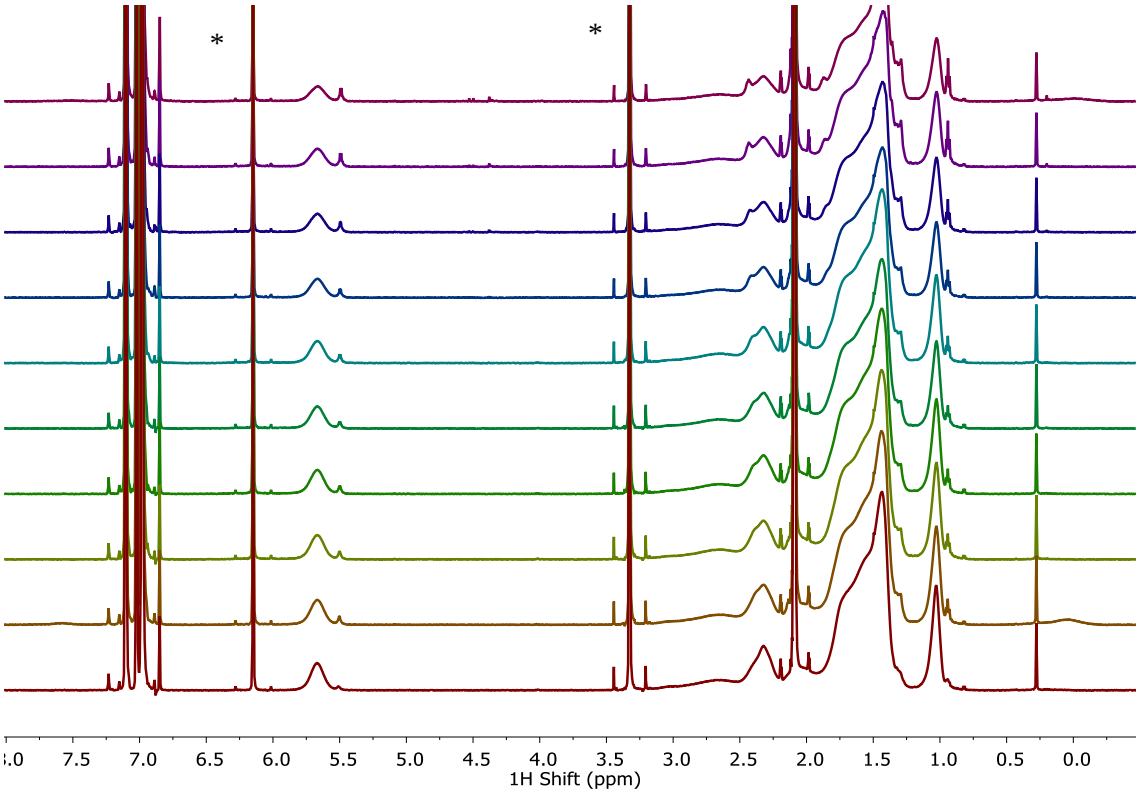

Figure B.2.7 ^{1}H NMR titration of 27.7 µM PbS QDs (4.1 nm) with 0 (red), 25 (orange), 50 (gold), 75 (light green), 100 (dark green), 200 (teal), 350 (blue), 500 (dark blue), 750 (purple), and 1000 (magenta) eq. $CoCp_2$ added in toluene-d_8. (*) denotes internal standard 1,3,5-trimethoxybenzene. NMR spectra collected on 600 MHz NMR with cryoprobe utilizing d1 delay of 30 seconds with 12 scans.

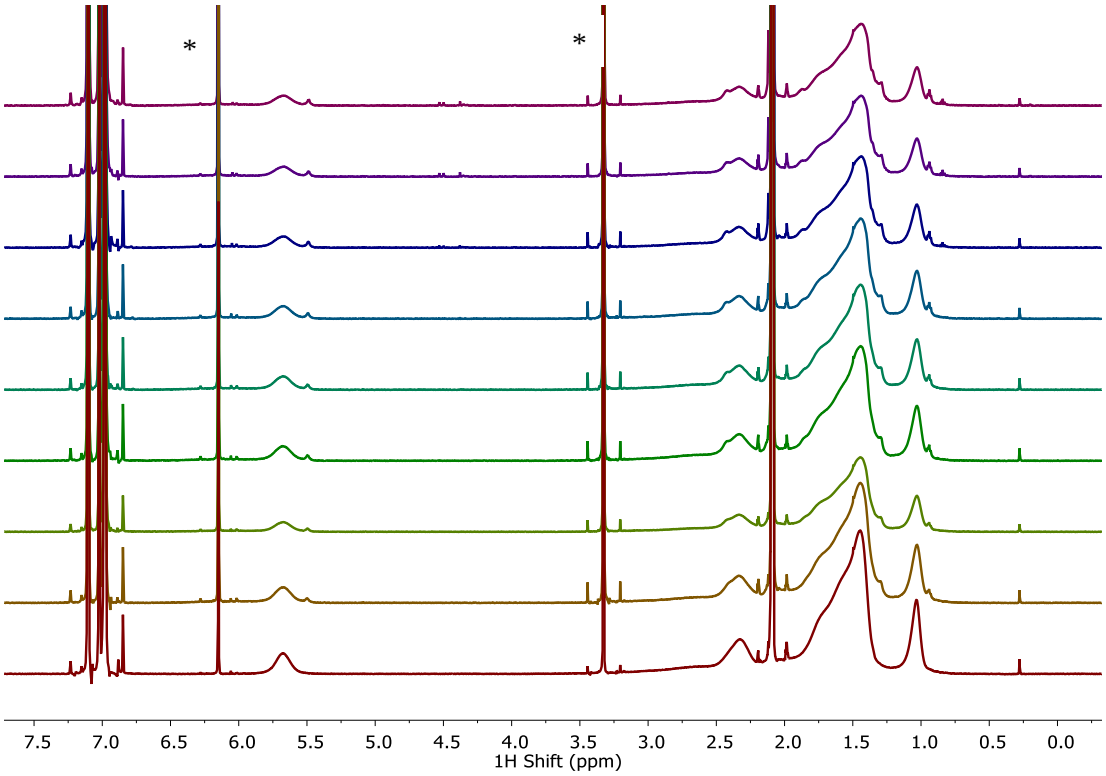

Figure B.2.8 ^{1}H NMR titration of 27.7 µM PbS QDs (4.9 nm) with 0 (red), 25 (orange), 50 (gold), 75 (light green), 100 (dark green), 200 (teal), 350 (blue), 500 (dark blue), 750 (purple), and 1000 (magenta) eq. $CoCp_2$ added in toluene-d_8. (*) denotes internal standard 1,3,5-trimethoxybenzene. NMR spectra collected on 600 MHz NMR with cryoprobe utilizing d1 delay of 30 seconds with 12 scans.

B.2.3 Oxidative Redox Probe Studies with PbS QDs

To complement studies employing reductive chemical probes, experiments were conducted with a well-known ground-state oxidant of PbS QDs, tetracyanoquinodimethane (TCNQ). This worked aimed to investigate the reactivity of the surface upon oxidation, and specifically whether we could observe evidence for the oxidation of underpassivated S^{2-} moieties to form disulfide defects. These studies largely reproduce what has been shown in previous works by other groups.[7,8] Efforts to directly observe evidence of disulfide formation were ultimately inconclusive, but these attempts are summarized below.

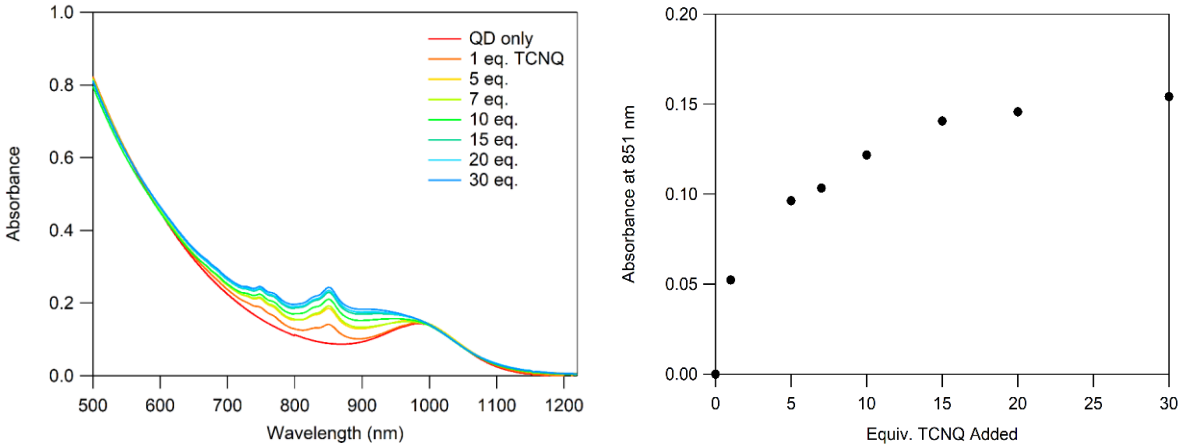

Figure B.2.9 (*Left*) UV-Vis-NIR absorbance spectrum of 3.4 µM PbS QD (2 µM) in chloroform with added excess TCNQ. Samples were equilibrated for 12 hours before measurement. (*Right*) Monitoring absorbance at 851 nm to track appearance of TCNQ radical anion.

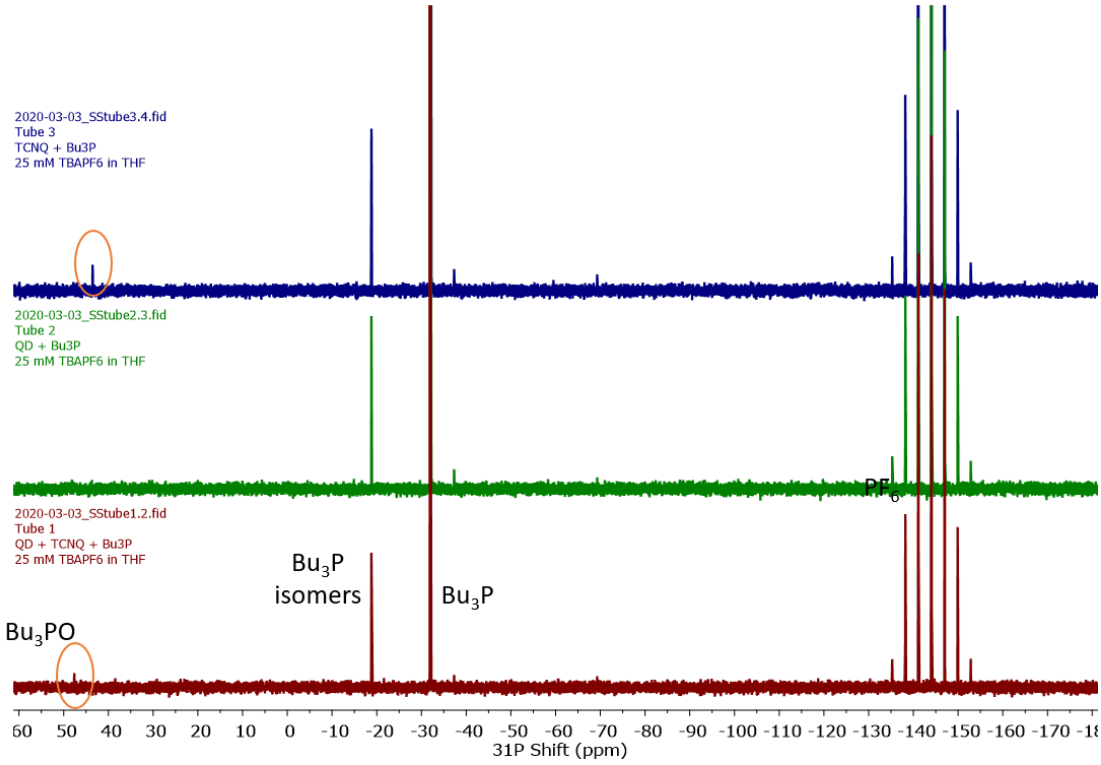

Figure B.2.10 PbS QDs (3.7 nm, ~50 µM) in 25 mM $[Bu_4N][PF_6]$ in tetrahydrofuran with: 1000 eq. Bu_3P and 50 eq. NaOH in H_2O and excess TCNQ (red); QDs with 1000 eq. Bu_3P and NaOH (no TCNQ) (green); and Bu_3P with NaOH and TCNQ (no QD) (blue). This study shows that there is background reactivity of Bu_3P with TCNQ. Therefore, reactivity of Bu_3P with disulfides that may form on the QD surface from reacting with TCNQ cannot be probed in situ. Future efforts to use Bu_3P as a probe of disulfides on TCNQ-treated QDs should be first rigorously isolated from excess TCNQ to avoid this background reactivity.

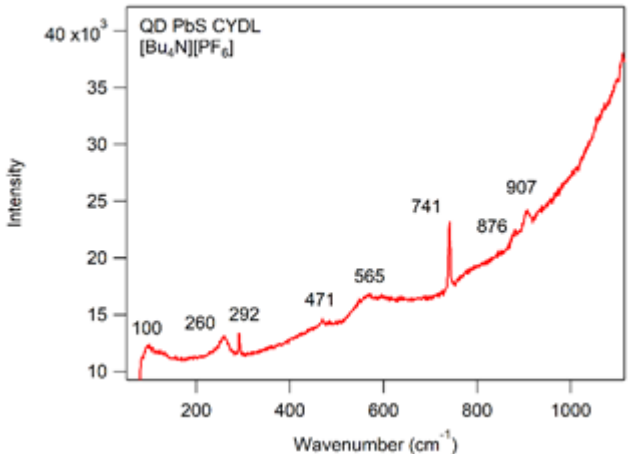

Figure B.2.11 Raman spectrum of 3.4 nm QDs drop cast from a 41 µM solution in chloroform with excess $[Bu_4N][PF_6]$ onto a glass slide for analysis. Raman microscope was run at 10% power using the 633 nm laser, a 30 sec integration time, and collecting 20 accumulations. Samples were equilibrated for 3 hours in solution prior to drop casting on glass slide.

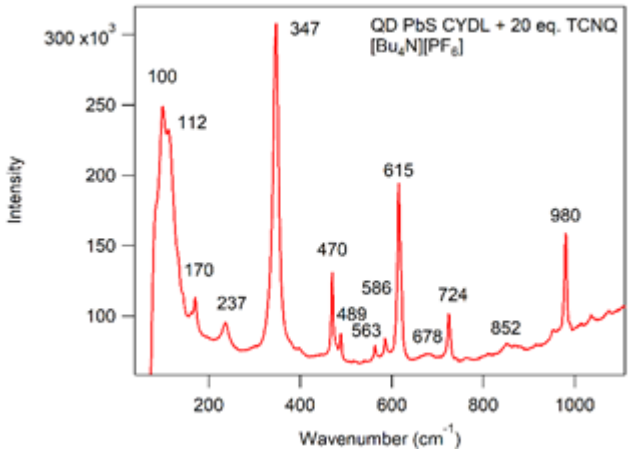

Figure B.2.12 Raman spectrum of 3.4 nm QDs drop cast from a 41 µM solution in chloroform with 20 eq. TCNQ added and excess $[Bu_4N][PF_6]$ onto a glass slide for analysis. Raman microscope was run at 10% power using the 633 nm laser, a 30 sec integration time, and collecting 20 accumulations. Samples were equilibrated for 3 hours in solution prior to drop casting on glass slide. Peaks at 347, 615, 980 cm^{-1} are attributed to $TCNQ^{x-}$.[9, 10] The peak at 470 cm^{-1} may be indicator of disulfides present, though a small feature at this same shift is observed in a Raman spectrum of $[Bu_4N][PF_6]$ alone.[11-13]

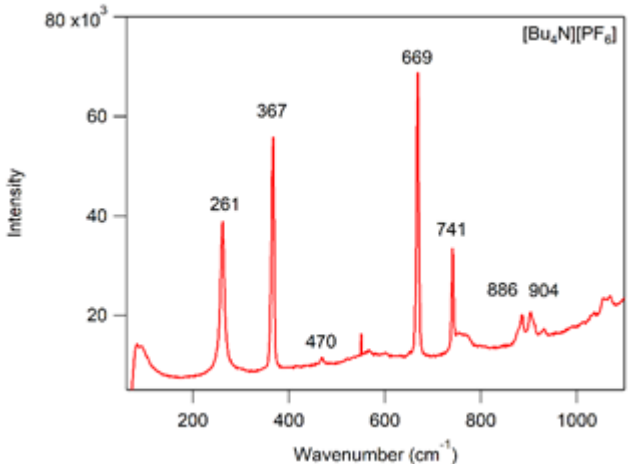

Figure B.2.13 Raman spectrum of $[Bu_4N][PF_6]$ drop cast from chloroform solution onto a glass microscope slide. Raman microscope was run at 10% power using the 633 nm laser, a 30 sec integration time, and collecting 20 accumulations.

REFERENCES

(1) Pivrikas, A. How to convert redox potential vs NHE to energy in absolute scale https://almantaspivrikas.blogspot.com/2013/07/how-to-convert-redox-potential-vs-nhe_15.html.

(2) Zoski, C. *Handbook of Electrochemistry*, 1st ed.; Elsevier Science, 2006.

(3) Dang, Z.; Shamsi, J.; Palazon, F.; Imran, M.; Akkerman, Q. A.; Park, S.; Bertoni, G.; Prato, M.; Brescia, R.; Manna, L. *In Situ* Transmission Electron Microscopy Study of Electron Beam-Induced Transformations in Colloidal Cesium Lead Halide Perovskite Nanocrystals. *ACS Nano* **2017**, *11*, 2124–2132.

(4) Pagels, N.; Prosenc, M. H.; Heck, J. An *ansa*-Cobaltocene with a Naphthalene Handle: Synthesis and Spectroscopic and Structural Characterization. *Organometallics* **2011**, *30*, 1968–1974.

(5) Zherebetskyy, D.; Scheele, M.; Zhang, Y.; Bronstein, N.; Thompson, C.; Britt, D.; Salmeron, M.; Alivisatos, P.; Wang, L. Hydroxylation of the Surface of PbS Nanocrystals Passivated with Oleic Acid. *Science* **2014**, *344*, 1380–1384.

(6) Kim, T.-G.; Zherebetskyy, D.; Bekenstein, Y.; Oh, M. H.; Wang, L.-W.; Jang, E.; Alivisatos, A. P. Trap Passivation in Indium-Based Quantum Dots through Surface Fluorination: Mechanism and Applications. *ACS Nano* **2018**, *12*, 11529–11540.

(7) Knowles, K.E.; Malicki, M.; Parameswaran, R.; Cass, L.C.; Weiss, E.A. Spontaneous Multielectron Transfer from the Surfaces of PbS Quantum Dots to Tetracyanoquinodimethane. *J. Am. Chem. Soc.* **2013**, *135*, 7264–7271.

(8) Edme, K.; Bettis Homan, S.; Nepomnyashchii, A.B.; Weiss, E.A. Ultrafast exciton decay in PbS quantum dots through simultaneous electron and hole recombination with a surface-localized ion pair. *Chemical Physics* **2016**, *471*, 46–53.

(9) Kamitsos, E.I.; Risen, W.M. Raman studies in CuTCNQ: Resonance Raman spectral observations and calculations for TCNQ ion radicals. *J. Chem. Phys.***1983**, *79*, 5808.

(10) Grossel, M.C.; Weston, S.C. A Truly Isolated $TCNQ^{-}$ Dimer? *Chem. Mater.***1996**, *8*, 977-980.

(11) Blackburn, J.L.; Chappell, H.; Luther, J.M.; Nozik, A.J.; Johnson, J.C. Correlation between Photooxidation and the Appearance of Raman Scattering Bands in Lead Chalcogenide Quantum Dots. *J. Phys. Chem. Lett.* **2011**, *2*, 599-603.

(12) Li, X.; McNaughter, P.D.; O'Brien, P.; Minamimoto, H.; Murakoshi, K. Photoelectrochemical Formation of Polysulfide at PbS QD-Sensitized Plasmonic Electrodes. *J. Phys. Chem. Lett.* **2019**, *10*, 5357-5363.

(13) Li, W.; Seal, D. Role of S/Se ratio in chemical bonding of As-S-Se glasses investigated by Raman, x-ray photoelectron, and extended x-ray absorption fine structure spectroscopies. *J. Appl. Phys.* **2005**, *98*, 053503.

APPENDIX C : ADDITIONAL DETAILS AND CHARACTERIZATION FOR CHAPTER 4

C.1 Additional Experimental Procedures

C.1.1 Details of Advanced NMR Methods and Relaxation Studies.

Proton and relaxation studies were carried out either on a Bruker 600 Avance NEO spectrometer equipped with a cryoQNP cryoprobe or Bruker 600 Avance III equipped with a cryoQCI cryoprobe. All DOSY experiments were run on a Bruker 600 Avance system. Samples were thermoregulated at 25 ^{o}C and allowed to equilibrate 5 minutes before NMR acquisition. NMR processing was performed in MNOVA, and spectra were baseline corrected with a Whittaker smoother. While the exact baseline correction parameters vary from experiment to experiment, care was taken not to over-correct the broad QD features using large filters and smooth factors (exemplum: filter 111, smooth factor 16,384,000).

C.1.2 Preparation of lead (II) dodecanethiolate complex.

Lead (II) dodecanethiolate was prepared following a modified literature procedure.[1] $Pb(oleate)_2$ (76.4 mg, 0.0992 mmol) and 1-dodecanethiol (60 µL, 0.25 mmol) were combined with 10 mL toluene in a 50 mL round bottom flask equipped with a stir bar. The heterogeneous white solution stirred under nitrogen for 15 minutes before heating to reflux. The solution stirred under reflux for 40 minutes, after which point the heat was removed and the solution cooled to room temperature. The solution was allowed to continue to stir at room temperature overnight, during which the solution changed from white to yellow in color. The crude reaction product was transferred to three centrifuge tubes (3 mL/tube) and centrifuged for 5 minutes at 8600 rpm. The resulting clear and colorless supernatant was discarded leaving a solid yellow precipitate. The solid was resuspended in toluene and then centrifuged again to isolate a fine yellow powder. The powder was dried under high vacuum and then characterized by XPS. Poor solubility in organic solvents inhibited characterization by NMR spectroscopy.

C.1.3 Precipitation Procedure for Isolating Displaced Toluate from Reduced Toluate/Oleate-PbS QDs.

A 150 µM solution ($9 \cdot 10^{-8}$ mol) of toluate/oleate-PbS QDs in toluene-d_8 was prepared in an inert-atmosphere glovebox, and 500 eq. $CoCp_2$ added (300 µL aliquot of a 150 mM stock solution, $4.5 \cdot 10^{-5}$ mol). The solution was allowed to react for four days under inert atmosphere shielded from light. A ^{1}H NMR spectrum of the sample was collected before precipitation. Inside of the glovebox, the sample was then divided between two 5 mL centrifuge tubes (~400 – 450 µL/tube) and filled to 5 mL total volume with acetonitrile to precipitate the QDs. The samples were then centrifuged at 9200 rpm for 5 minutes, yielding a dark brown precipitate of QDs and a light brown supernatant. The precipitated QDs were dried under vacuum and then dispersed in toluene-d_8 for post-precipitation analysis. Portions of the resulting supernatant (3 mL) were transferred to two new centrifuge tubes and 2 mL acetonitrile added for a total volume of 5 mL/tube, and the samples centrifuged for 7 minutes. This second centrifugation produced a lightly colored brown-orange supernatant with a dark brown QD precipitate. The supernatant was transferred to a vial and solvent removed under vacuum, revealing a yellow-grey crystalline solid. The solid was redispersed in 10 mL of 1:1 acetone:acetonitrile, divided between two centrifuge tubes and centrifuged for 10 minutes, resulting in a small amount of dark brown precipitate. The supernatant from this final centrifugation step was transferred to a 20 mL vial and solvent removed under vacuum. The sample was then dispersed in acetonitrile-d_3 and analyzed by ^{1}H NMR spectroscopy. This procedure was repeated on a sample of toluate/oleate-PbS QDs without added $CoCp_2$ to ensure that free toluate ligand was not displaced by the precipitation procedure.

C.2 Example Calculation of Extinction Coefficient at 400 nm

First, a sample of QDs with known volume (600 µL) but unknown concentration was prepared in a 2 mm cuvette. Although the concentration was unknown, rough calculations of the anticipated QD concentration allowed for preparation of a sample for UV-Vis and ICP-MS analysis. The QD

concentrations selected in this study both i) provide absorbance spectra with observable excitonic peaks and ii) allow for few serial dilutions to achieve Pb concentrations appropriate for ICP-MS.

A UV-Visible absorbance spectrum was collected and the A_{400} value was determined as shown:

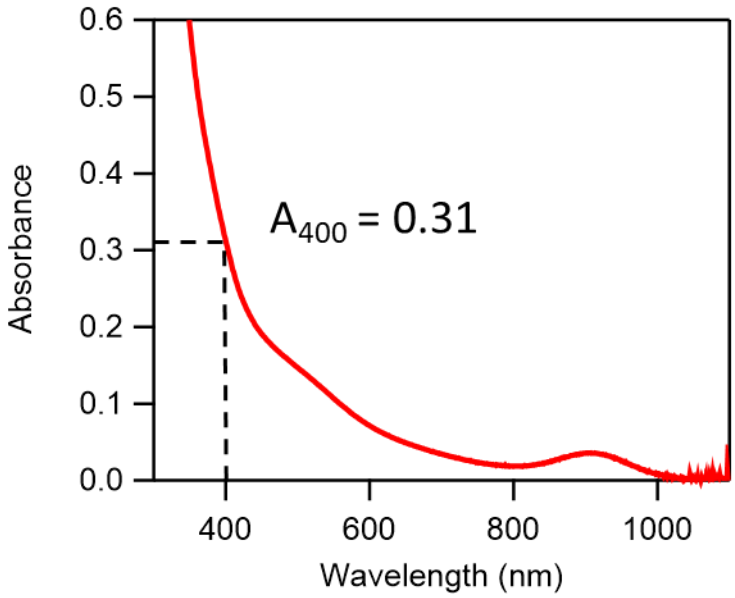

The contents of the cuvette were carefully and completely rinsed with pentane into a 20 mL scintillation vial and allowed to evaporate in a fume hood under air stream (previously, rotary evaporation had caused the sample to bump, which disrupted quantitative transfer and analysis of the sample). Next, the sample was pyrolyzed in the same vial in a box furnace at 450 ℃ for 30 min and allowed to cool to room temperature. Then, 0.5 mL of TraceMetals grade HNO_3 was added to the sample and allowed to digest for a minimum of 4 hours. The sample was diluted with Millipore water and filtered through a pipette filter into a 10 mL volumetric flask to remove insoluble pyrolyzed organic particulates. The sample was transferred to a 15 mL centrifuge tube, and serial dilutions were performed to attain a concentration 250× more dilute than the initial sample. Pb concentrations of the 250× diluted samples were measured between 30 and 60 ppb Pb by ICP-MS.

The sample given in the UV-Vis spectrum above is from the oleate-PbS-2 QD batch, and had a Pb concentration of 42 ppb. Since this sample had been diluted by 250x, the product of 42 x 250 yields

the Pb concentration of the initial sample prepared in the 10 mL volumetric flask, $1.0 \cdot 10^4$ ppb Pb.

Converting from ppb Pb to moles of Pb yields $5.1 \cdot 10^{-7}$ mol total Pb, as follows:

$$1.0 \cdot 10^4 \text{ ppb} = \frac{1.0 \cdot 10^4 \text{ µg}}{1 \text{ L}} * \frac{1 \text{ g}}{10^6 \text{µg}} * \frac{1 \text{ mol Pb}}{207.2 \text{ g}} * \frac{1 \text{ L}}{1000 \text{ mL}} * 10 \text{ mL}$$
$$= 5.1 \cdot 10^{-7} \text{ mol Pb in volumetric flask}$$

Using Equation 4.2 gives the total number of Pb and S ions in each QD:

$$\text{N} = \frac{4\pi}{3}\left(\frac{2.9}{0.593}\right)^3 = 493 \text{ total Pb} + \text{S per QD}$$

The Pb:S ratio for this set of QDs is 2.12 Pb:S. This is used to solve for one variable, Pb:

$$2.12 = \frac{\text{Pb}}{\text{S}}$$

$$2.12\text{S} = \text{Pb}$$

The equation for total atoms is:

$$\text{Pb} + \text{S} = \text{N}$$

Substituting 2.12S into the equation for total number of atoms allows one to solve for S:

$$2.12\text{S} + \text{S} = \text{N}$$

$$3.12\text{S} = 493$$

$$\text{S} = 158$$

Next, Pb per QD is calculated:

$$493 - 158 = 335 \text{ Pb}$$

The next step in the calculation of the concentration of QDs in the cuvette is to combine the molar ratio of 335 Pb ions per QD with the total moles of Pb determined via ICP-MS:

$$5.1 \cdot 10^{-7} \text{mol Pb} \times \frac{1 \text{ mol QD}}{335 \text{ mol Pb}} \times \frac{1}{0.0006 \text{ L}} = 2.5 \cdot 10^{-6} \text{ M} = \text{c}$$

With the concentration of QDs, $2.5 \cdot 10^{-6}$ M, and the A_{400} value of 0.31 from the UV-Vis spectrum above, Beer's law (Equation 4.1) is finally employed to determine the molar extinction coefficient at 400 nm:

$$\varepsilon_{400} = \frac{A_{400}}{\text{bc}} = \frac{0.31}{(0.2 \text{ cm}) \times (2.5 \cdot 10^{-6} \text{ M})} = 6.2 \cdot 10^{5} \text{ M}^{-1}\text{cm}^{-1}$$

C.3 Note on fitting method used in toluate/oleate-PbS NMR spectra

Due to the overlapping nature of both the bound and free toluate peaks as well as the oleate and $CoCp^{+}_{2}$ peaks, a strategy different from the other systems was used to obtain consistent integrations for each bound and free ligand species. First, a multipoint baseline correction was applied to each toluate-containing spectrum studied herein, taking care to avoid over-baselining the toluate and $CoCp^{+}_{2}$ features. The region between 9.5 and 6.4 did not contain any points, nor did the region between 6.0 and 4.7 ppm. Next, the bound and free toluate resonances near 8.3 ppm were deconvoluted by fixing the bound feature to 8.2 ppm and allowing a sharp, downfield peak to float. Qualitatively, upon fitting multiple spectra between 4 and 123 hours of reaction, we observed that increasing the area attributed to the free toluate species over time described the data well. However, we recognize that choices in baseline selection and peak position locking are subjective and may not accurately represent the true chemical nature of the bound and free toluate species. We thus ascribe an error of 10% to the value of free toluate species liberated, 27%. To further verify that fitting the toluate feature to bound and free species can be justified, we carried out chemical separation methods to analyze the supernatant of this reaction (discussed in Chapter 4).

C.4 Additional Studies with Decamethylcobaltocene ($CoCp^*_2$)

Preliminary ^1H NMR studies with the stronger reductant $CoCp^*_2$ and the oleate-PbS QD systems unexpectedly indicated the displacement of approximately two oleate ligands per equivalent of $CoCp^*_2$ added (Table C.4.1)—full consumption of $CoCp^*_2$ was confirmed by a lack of a paramagnetic NMR feature at 45 ppm. Based on charge balance, we would expect that only one X-type oleate ligand would be displaced per equivalent of $CoCp^*_2$ added. However, the 2:1 ratio of oleate loss suggested instead possible Z-type ligand ($Pb(oleate)_2$) displacement. Additionally, in these NMR samples we observed evidence of a fine black precipitate (likely precipitated QDs) over time, consistent with instability from significant degree of ligand loss. Similarly, UV-Vis studies showed overall instability with an increase in baseline and slight blue shift upon addition of $CoCp^*_2$, consistent with surface etching and Z-type ligand loss (Figure C.4.1).[2]

Table C.4.1 NMR studies with oleate-PbS-3 show a 2:1 ratio of displaced oleate ligands per equivalent of $CoCp^*_2$ added

Sample	Bound OA/QD	Free OA/QD	Total OA ligands
QD only	179	0	179
10 equiv. $CoCp^*_2$	159 ± 2	21 ± 0.7	180 ± 2
20 equiv. $CoCp^*_2$	142 ± 5	39 ± 0.8	181 ± 4
50 equiv. $CoCp^*_2$	92 ± 1	92 ± 0.6	185 ± 2

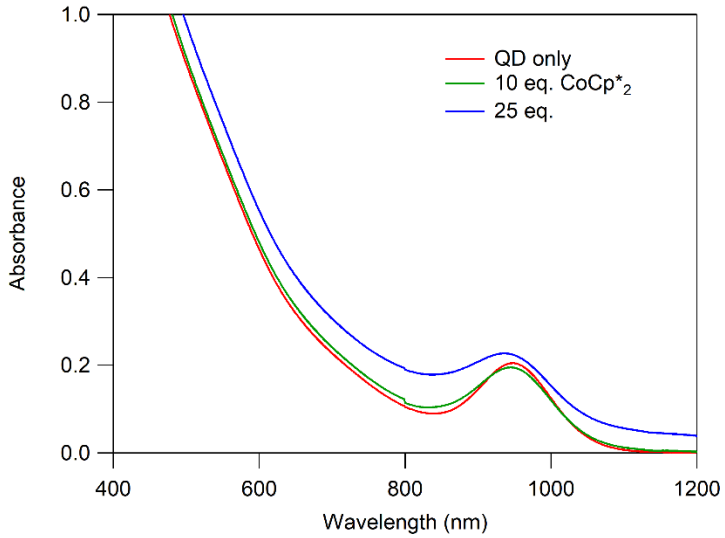

Figure C.4.1 UV-Vis-NIR absorption spectrum of oleate-PbS-3 in toluene (2.5 µM) with added $CoCp^*_2$

To probe whether there was evidence for Z-type loss by other methods, we turned to XPS spectroscopy. Using XPS, we aimed to monitor whether there was a change in Pb:S ratio in isolated QDs after reacting with excess $CoCp^*_2$. Data showed that there was a measurable decrease in the average Pb:S ratio, which could be indicative of Z-type ligand loss from reaction with $CoCp^*_2$ (Table C.4.2).

Table C.4.2 XPS data for oleate-PbS-1 upon isolation after reacting with $CoCp^*_2$

	Spot	Pb atomic %	S atomic %	Pb:S ratio	AVERAGE	STANDARD DEV.
QD only	**A1**	7.51	3.77	1.99	1.96	0.043
	A2	7.32	3.79	1.93		
Crashed QDs	**A1**	8.05	4.57	1.76	1.75	0.110
	A2	7.86	4.75	1.65		
	B1	7.87	4.67	1.69		
	B2	7.78	4.07	1.91		
50 equiv $CoCp^*_2$	**A1**	9.63	6.49	1.48	1.56	0.098
	A2	9.08	6.11	1.49		
	B1	9.49	5.61	1.69		
	B2	9.55	6.1	1.57		

C.4.1 Hypothesis on Z-type displacement from $CoCp^*_2$ addition

From the perspective of maintaining charge balance at the QD surface, it is not obvious why surface reduction to induce neutral Z-type ligand displacement. Rather, we hypothesized that this observation could be attributed to steric bulkiness of $CoCp^*_2$. Unlike in the case of the more moderately reducing $CoCp_2$, it is likely the $CoCp^*_2$ is able to favorably reduce the QD conduction band edge state in addition to reducing surface ions. In the case of reduction of the QD band edge state—and subsequent formation of QD^-— a counterion ($[CoCp^*_2]^+$) must ion pair with the QD and maintain close proximity to the nanocrystal core.[3] The steric bulkiness of the $[CoCp^*_2]^+$ at the surface could thereby lead to displacement of Z-type ligands from physical crowding. Indeed, such ligand displacement has been proposed in other systems whereupon redox-active molecules adsorb or closely associate with the QD surface.[4,5] Alternatively, it is conceivable that reduction of spectroscopically silent states by the strongly reducing $CoCp^*_2$ leads to surface rearrangement that could result in some Z-type ligand displacement.

We attempted to probe possibility of steric crowding by reducing the QDs with $CoCp^*_2$ in the presence of Na[BArF]. Our hypothesis was that, if Z-type displacement is indeed induced by steric crowding effects at the surface from the decamethylcobaltocenium cation, that the presence of a smaller cation, Na^+, in solution that could ion pair with QD^- instead could lessen these effects. This experiment, performed with oleate-PbS-3 is shown in Figure C.4.2 and the amount of ligand loss per QD quantified in Table C.4.3. The results of this work showed a decrease in the amount of displaced oleate ligand in the presence of Na[BArF], supporting the possibility that steric crowding by the $[CoCp^*_2]^+$ leads to some Z-type ligand displacement in combination with the above work. However, the inconsistency of the absolute quantification of oleate ligands in this study led us to only use this experiment to draw qualitative conclusions regarding support of our hypothesis.

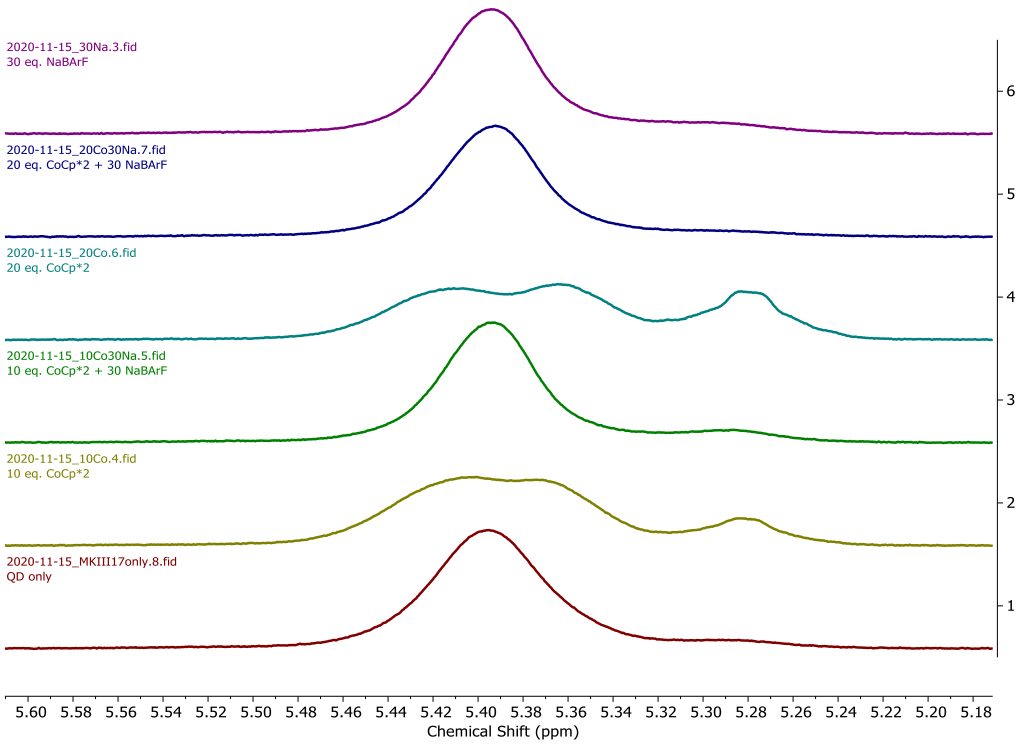

Figure C.4.2 Stacked ^{1}H NMR spectra of oleate-PbS-3 QDs focused in on the oleate alkene proton handle region of a sample of QD only (red), 10 eq. $CoCp^{*}_{2}$ (yellow), 10 eq. $CoCp^{*}_{2}$ and 30 eq. Na[BArF] (green), 20 eq. $CoCp^{*}_{2}$ (teal), 20 eq. $CoCp^{*}_{2}$ and 30 eq. Na[BArF] (blue), 30 eq. Na[BArF] (purple) in 1:1 THF-d_8:toluene-d_8.

Table C.4.3 Quantification of ligand displacement with $CoCp^{*}_{2}$ added in presence of Na[BArF] in 1:1 THF-d_8:toluene-d_8.

Sample	**Bound OA/QD**	**Free OA/QD**	**Free OA/QD minus QD only free**	**Total OA ligands**	**BAr^{F}_{4}/QD**

QD only	184	5	-	188	0
10 eq $CoCp^*_2$	162	23	18	184	0
10 eq $CoCp^*_2$ + 30eq $Na[BAr^F_4]$	174	12	8	186	29
20 eq $CoCp^*_2$	140	47	42	186	0
20 eq $CoCp^*_2$ + 30eq $Na[BAr^F_4]$	169	4	-1	173	29
30 eq $Na[BAr^F_4]$	170	14	9	184	29

REFERENCES

(1) Giansante, C. Surface Chemistry Control of Colloidal Quantum Dot Band Gap. *J. Phys. Chem. C* **2018**, *122*, 18110–18116.

(2) Kessler, M. L.; Dempsey, J. L. Mapping the Topology of PbS Nanocrystals through Displacement Isotherms of Surface-Bound Metal Oleate Complexes. *Chem. Mater.* **2020**, *32*, 2561–2571.

(3) Valdez, C. N.; Delley, M. F.; Mayer, J. M. Cation Effects on the Reduction of Colloidal ZnO Nanocrystals. *J. Am. Chem. Soc.* **2018**, *140*, 8924–8933.

(4) Knowles, K. E.; Malicki, M.; Parameswaran, R.; Cass, L. C.; Weiss, E. A. Spontaneous Multielectron Transfer from the Surfaces of PbS Quantum Dots to Tetracyanoquinodimethane. *J. Am. Chem. Soc.* **2013**, *135*, 7264–7271.

(5) Peterson, M. D.; Jensen, S. C.; Weinberg, D. J.; Weiss, E. A. Mechanisms for Adsorption of Methyl Viologen on CdS Quantum Dots. *ACS Nano* **2014**, *8*, 2826–2837.